METABOLIC ENGINEERING ANALYSIS OF POST-BURN HEPATIC HYPERMETABOLISM

by

KYONGBUM LEE

B.S., Chemical Engineering, 1995
Stanford University

Submitted to the Department of Chemical Engineering
in partial fulfillment of the requirements for the degree of

DOCTOR OF PHILOSOPHY

at the

MASSACHUSETTS INSTITUTE OF TECHNOLOGY

February 2002

© Massachusetts Institute of Technology 2001
All rights reserved.

ARCHIVES
MASSACHUSETTS INSTITUTE OF TECHNOLOGY
FEB 2 8 2002
LIBRARIES

Signature of Author_____
Department of Chemical Engineering
October 30, 2001

Certified by_____
Martin L. Yarmush
Helen Andrus Benedict Professor of Surgery and Bioengineering, Harvard Medical School
Thesis Supervisor

Certified by_____
Gregory N. Stephanopoulos
Professor of Chemical Engineering
Thesis Supervisor

Accepted by_____
Daniel Blankschtein
Chairman, Committee for Graduate Students

METABOLIC ENGINEERING ANALYSIS OF POST-BURN HEPATIC HYPERMETABOLISM

by

KYONGBUM LEE

Submitted to the Department of Chemical Engineering on November 13th, 2001 in partial fulfillment of the requirements for the degree of Doctor of Philosophy in Chemical Engineering

ABSTRACT

Metabolic engineering refers to the directed improvement of product formation or cellular properties through the modification of specific biochemical reactions or introduction of new ones with the use of recombinant DNA technology. It has been used to investigate and modify intermediary metabolism in a variety of microbial organisms of biotechnological interest. An emerging area of application for metabolic engineering is medicine, in particular the study of metabolic disorders, where analysis and manipulation of metabolic pathways have obvious relevance.

Central to metabolic engineering is the notion that metabolism results from the concerted and coordinated activities of biochemical pathways connected through shared intermediates in the form of common reactants, products, and catalysts. According to this "metabolic network" concept, an enhanced understanding of metabolism and cellular function is obtained by considering the component biochemical reactions together, rather than individually. In this light, this thesis work was motivated by the idea that the application of metabolic engineering analysis to biological systems relevant to human disease has the potential to provide valuable insight into the biochemical underpinnings behind metabolic disorders. In the present dissertation, this idea was explored by investigating a metabolic disorder known clinically as hypermetabolism that is associated with the systemic inflammatory response to severe injury.

At the whole body level, hypermetabolism is characterized by elevated resting energy expenditure and increased turnover of proteins, fatty acids, and carbohydrates. If this state persists over a period of days to weeks, the patient is predisposed to muscle wasting, progressive organ dysfunction, multiple organ failure, and ultimately death. Unfortunately, existing nutritional therapies are inadequate for preventing the onset of persistent hypermetabolism, because many of the mechanistic details of this process are poorly understood. An important player in the hypermetabolic response to injury is the liver, which responsible for synthesizing healing factors from muscle protein derived amino acids, converting carbohydrate and lipid fuel resources to useful energy substrates, and eliminating waste products generated by these processes. In order to better understand the biochemical underpinnings behind injury derived hypermetabolism in the liver, the following specific aims were addressed: 1) to develop and validate tissue and organ models of injury for the liver; 2) to delineate activity changes in the major metabolic pathways in the liver during the developmental period of hypermetabolism; and 3) to build diagnostic tools for detecting and grading the injury derived metabolic abnormalities in the liver.

A particularly useful metabolic engineering tool is metabolic flux analysis (MFA), which refers to a methodology whereby intracellular reaction fluxes are estimated using a stoichiometric model for the major intracellular reactions and applying mass balances around intracellular metabolites. A powerful feature of this methodology is its ability to consider cellular biochemistry in terms of a network of reactions. Stoichiometric and mass balance considerations quantify the degree of engagement of each metabolic pathway participating in overall cellular activity, which paints a comprehensive picture of cellular metabolism.

MFA was used in conjunction with a burned rat perfused liver model to estimate injury induced changes in liver central carbon flux distribution. By developing a perfused liver model, liver intrinsic changes induced by burn injury could be studied in isolation from systemic influences. In order to employ MFA, a network model of liver central carbon metabolism was formulated based on published knowledge. In an exploratory study, the network and perfused liver models were used to compare intracellular fluxes in livers isolated from burn and sham-burn animals at the onset of whole body hypermetabolism. The model predictions resulting from this study regarding burn induced activation of several intracellular pathways were validated by isotopic tracer experiments and enzymatic assays.

The next step in the thesis work expanded on the above study to perform comprehensive metabolite measurements on livers perfused at various times during the first week of burn injury. MFA on these data identified reaction groups which were significantly activated by burn injury: fatty acid oxidation, gluconeogenesis, pentose phosphate pathway (PPP), tricarboxylic acid (TCA) cycle, and urea cycle. An important discovery was that these reaction groups were activated or repressed differentially with respect to time after injury. Gluconeogenesis remained unchanged except a slight increase on day 4 post-burn, fatty acid oxidation peaked on day 3, PPP and urea cycle fluxes were significantly elevated by day 2 post-burn, and TCA cycle fluxes continued to rise throughout the week-long study period. Energy balances based on the flux estimates revealed a significant gap between predicted adenosine triphosphate (ATP) production and demand. In light of the activation of the PPP and its intimate involvement in oxygen free radical metabolism, the ATP gap pointed to the induction of an oxidative stress sensitive mitochondrial respiratory uncoupler UCP2, which was subsequently confirmed by Western blot analysis.

The role of endogenous oxidative stress agents in mediating hepatic hypermetabolism was examined in more detail using a stable hepatocyte culture system. In combination with glucagon, which is known to increase substrate loading into hepatocytes, reactive oxygen species (ROS) significantly elevated oxygen uptake and induced UCP2 expression. This effect was dampened by the addition of antioxidants or an inhibitor of a PPP enzyme. ROS also adversely affected cell viability, which was attenuated by glucagon. These results supported a role for ROS in mediating inflammation derived hepatic hypermetabolism, and the potential for therapeutic benefits of antioxidants.

The final chapter of this thesis proposed a general strategy for building robust diagnostic tools. The strategy, termed metabolic profiling, was formulated based on the notion that composite analysis of multidimensional metabolite data yields superior classification of metabolic states over the single marker approach. The success of the proposed classification technique, Fisher's Discriminant Analysis (FDA), as applied to the perfused liver data presented in this thesis, strongly correlated with the number of metabolite measurements. This result reinforced the notion that cellular metabolism is best described by many, rather than a few, measured parameters. Furthermore, combining the measured metabolite exchange rates with flux

estimates enhanced FDA performance, which underscored the idea that the calculated fluxes contain additional, valuable information pertinent to delineating metabolic states in complex biological systems.

Thesis Supervisors: Gregory N. Stephanopoulos
Professor of Chemical Engineering
Massachusetts Institute of Technology

Martin L. Yarmush
Helen Andrus Benedict Professor of Surgery and Bioengineering
Harvard Medical School

ACKNOWLEDGEMENTS

First specific thanks go to my thesis advisors, Maish and Greg. Maish's passion for research has been a constant source of inspiration. I thank him for his vision, sense of mission, creative insights, motivation, and support. Greg deserves thanks for his direction, countless particulars, and patient guidance. I thank both for not only being there to guide my research, but also my outlook on science and academia, the pitfalls and the glory.

There has been no one more crucial to my laboratory work than my committee member Francois Berthiaume. I thank him for the tissue culture lessons, assay consultations, sharing his bench experiences, and in general helping me realize my experimental plans. Arul Jayaraman also deserves thanks for patiently teaching molecular biology techniques to a complete novice.

The acknowledgements would not be complete without mentioning my laboratory mates, fellow students and others, past and present: Joseph Ledoux and Howard Davis for setting standards of excellence, Stelios Andreadis and Christina Chan for their intellectual input, and Yoon H. Kang for encouragement and support not to mention the daily cups of coffee. Special thanks goes to S. Patrick Walton for his ever-present cheerfulness, intellectual and emotional support, and friendship worth far more than this thesis.

Finally, I want to thank my family, especially Mom and Dad, who have inspired me to seek and befriend scholars and scholarship, while giving unconditional love and support through all times. I thank you, my wife, for your understanding, words of comfort and motivation, and loving care.

I am probably forgetting some people who decidedly deserve gratitute, because there were so many who helped me through the past six years. My deepest appreciation and affection to you all.

TABLE OF CONTENTS

LIST OF FIGURES AND TABLES

CHAPTER 1. METABOLIC ENGINEERING IN BIOMEDICINE

1.1 Overview

The manipulation of metabolic pathways for improved production of biochemical compounds using microorganisms, despite many success, remained essentially a random process, relying on chemical mutagenesis, until the introduction of recombinant DNA technology (popularly called genetic engineering) in the late 1970's. This significant development in molecular biology presented the opportunity to introduce heterologous genes and regulatory elements [1], and made possible the targeted modification of specific enzymes in metabolic pathways [2]. The integration of genetic engineering into bioprocess technology has been described by a variety of terms in the literature, including molecular breeding, pathway engineering, cell engineering, and metabolic engineering [2]. In this dissertation, the term metabolic engineering is used, because it best describes the integrative nature of the field and encompasses the diverse array of tools developed in the field for analysis and manipulation of cellular metabolism.

Metabolic engineering has been defined as the directed improvement of product formation or cellular properties through the modification of specific biochemical reactions or introduction of new ones with the use of recombinant DNA technology [2]. It is an interdisciplinary field, which builds on the concepts and techniques developed in many areas of science and engineering, including biochemistry, analytical chemistry, cell biology, genetic engineering, chemical engineering, and systems analysis. The areas of application have been equally diverse [3, 4]. Biotechnological applications have included: improved production of chemicals already produced by the host organism [5], extended substrate range for growth and product formation [6], addition of new catabolic activities for degradation of toxic chemicals [7-9], synthesis of biopolymers [10], production of chemicals new to the host organism [11, 12], or entirely novel, as is the case with polyketides [13, 14], and modification of general cell properties, such as the ability to withstand hypoxic fermentation conditions [15] and prevention of overflow metabolism [16]. Other recent applications include synthesis of chiral intermediates for pharmaceutical production [17, 18] and variable composition copolymers in plants [19-21]. The wide range of applicability of metabolic engineering extends also to the types of cells, and

have included prokaryotes such as *E. coli*, eukaryotic microorganisms such as yeast, transformed mammalian cell lines such as Chinese Hamster Ovary (CHO) cells, and numerous plant systems.

1.2 Motivation and Objective

Central to metabolic engineering is the notion that metabolism results from the concerted and coordinated activities of biochemical pathways connected through shared intermediates in the form of common substrates, cofactors and allosteric regulators. According to this "metabolic network" concept, an enhanced understanding of metabolism and cellular function is obtained by considering the component biochemical reactions together, rather than individually [22]. As such, metabolic engineering encompasses diverse issues, including pathway modification, analysis of network control, evaluation of data quality, and quantification of metabolic flux. In order to address these issues, metabolic engineers have developed various frameworks and tools that allow quantitative and systematic investigation of cellular metabolism. These analytical components of metabolic engineering are general in nature, and in principle applicable to not only microorganisms, but also more complex systems such as primary cells of higher organisms, tissues, and organs.

In this regard, medicine, where the analysis of metabolic pathways has obvious relevance, presents a novel area of opportunity for metabolic engineering. Potential areas of application include optimization of engineered tissue function, rational design of nutritional therapies, diagnosis of metabolic disorders, monitoring disease progression, and investigation of metabolic disease mechanisms. As an illustration of the potential for metabolic engineering in biomedicine, consider tissue engineering, which uses cells or tissues together with natural or synthetic extracellular components to develop implantable parts or extracorporeal devices for restoring or replacing function [23]. Investigators in this discipline have traditionally relied on measuring one or a few markers for assessing cell or tissue performance and viability. Usually, performance markers have been one or two enzymes or protein products unique to the cell or tissue of interest, such as acetylcholine receptor level for neurons, creatine kinase and lactate dehydrogenase activities for cardiomyocytes [24], cytochrome P450 activity for hepatocytes [25], or insulin secretion rate for pancreatic islet cells [26]. Viability has typically been measured by such generic gross indices as total ATP [27] and protein content [25]. However,

complex biological functions involve multiple gene products, either because this affords greater efficacy and higher quality control, or a single protein cannot provide the required function [28]. This is especially true for metabolic activity, which results from the concerted action of a host of biochemical reactions. As cell or tissue functions such as synthesis, secretion, and drug clearance intimately depend on metabolic parameters such as reduction potential, energy level, and substrate supply, methods for studying and modifying cell or tissue metabolic behavior could be very useful for optimizing performance. Boyce et al. [29] reported that irrigation of cultured skin grafts with topical nutrients promoted engraftment as well as epithelial and connective tissue regeneration, suggesting presence of proper metabolic substrates may be critical for *in vivo* performance of engineered skin. Naughton et al. [30] showed that implanting dermal tissue with a defined range of metabolic activity dramatically improved healing of diabetic foot ulcers. Recent isolation of neural stem cells and advances in genetic manipulation have also increased prospects for engineering neural tissue that either express heterologous or overexpress endogenous enzymes, which could compensate for either genetic or trauma-related metabolic deficiencies [31]. In some applications, such as hepatic tissue engineering, assessing metabolic activity is especially crucial, as the primary function of artificial liver support is preservation of whole body metabolic homeostasis [32]. In addition to improving *in vivo* performance, rational manipulation of cellular metabolism helps optimize *in vitro* culture conditions. It has been long recognized that the effective removal of harmful metabolites accumulating in culture is critical for maintaining long-term tissue viability [33]. In the bioprocess literature, the application of metabolic engineering to rational medium design for increasing productivity of animal cell cultures has already been well documented [34].

In light of the aforementioned concepts and examples, this thesis is motivated by the idea that the application of metabolic engineering analysis to medicine has the potential to provide valuable insights into the biochemical underpinnings behind human disease processes. Specifically, this idea is explored by performing an integrated metabolic analysis of post-burn hypermetabolism, which is a metabolic disorder associated with the whole body inflammatory response to severe burn injury. To the best knowledge of the author, this thesis work represents the first such undertaking. In this respect, the thesis has dual objectives:

1. **to elucidate the biochemical underpinnings behind injury derived metabolic alterations by performing an integrated metabolic analysis as afforded by the application of metabolic engineering frameworks and tools;**
2. **to demonstrate the utility of the "metabolic network" concept and the systems analysis approach in studying cellular metabolism in tissues relevant to understanding and treating human disease.**

In achieving these objectives, one metabolic engineering analysis tool, called metabolic flux analysis (MFA), figures prominently. MFA refers to a methodology whereby intracellular fluxes are calculated from metabolite and isotopic tracer measurements based on a stoichiometric model for the major intracellular reactions using balance equations around intracellular metabolites and their isotopic isomers [35].

1.3 Metabolic Flux Analysis

Among the tools available to the metabolic engineer, presumably the most useful one for biomedical applications is metabolic flux analysis (MFA). MFA has also been referred to as stoichiometric balancing [36], metabolite balancing, and metabolic flux balancing [37], especially in the earlier bioprocess engineering literature, where metabolite measurements provided the dominant experimental input. In recent years, it has become widely accepted that using isotopic tracers is advantageous in, even necessary for, obtaining robust estimates of intracellular fluxes and resolving complex metabolic systems. Thus, MFA applications which involve the analysis of both metabolites and isotopic tracers have been featured more and more prominently in the published literature.

One of the earliest applications of MFA was to the derivation of fermentation equations used to predict product yield and selectivity in cultures of butyric acid bacteria by Papoutsakis [36]. In another important early work, Holms [38] examined the relationship between the fluxes through the pathways of central carbon metabolism and the conversion efficiency of acetate to biomass in *E. coli*. In both of these works, of central importance was the concept of a biochemical network, or the interrelations between metabolites, which the authors argued could be studied by formulating balance equations around the metabolites that are derived from known

stoichiometric relationships. Since these early works, MFA has been used to study pathway interactions in a variety of biological systems. Vallino and Stephanopoulos [39, 40] applied MFA to estimate flux distributions in the primary metabolic network of *Corynebacterium glutamicum* under various perturbed states. Based on the flux distribution data, they were able to attribute the limitations in lysine yield to network rigidity [41] at either the phosphoenolpyruvate (PEP) or pyruvate (PYR) branch point. Jørgensen et al. [42] showed that penicilin formation in *Penicilium chrysogenum* is accompanied by a large flux through the pentose phosphate pathway due to a large requirement for nicotinamide-adenine dinucleotide phosphate (NADPH) used in the biosynthesis of cysteine. Pons et al. [43] found that choice of carbon source significantly influenced growth of *Corynebacterium melassecola*. By calculating flux distributions in a recombinant, riboflavin-producing *Bacillus subtilis* strain, Sauer et al. determined that riboflavin formation is limited by the fluxes through the biosynthetic rather than the central carbon pathways.

In principle, the application MFA to medically relevant systems is straightforward, as the basic biochemistry of mammalian tissue bears close resemblance to those found in microorganisms and, as it will be seen, the modeling framework is essentially system independent. However, in practice, the extension of MFA to tissues presents a number of challenges. While the central carbon biochemistry is similar between biotechnologically relevant systems such as bacteria, yeast, and transformed cell lines, and the medically relevant systems such as primary cultures, isolated organs, extracorporeal devices, and *in vivo* models, there are a number of important differences in experimental condition and cellular organization, as well as subtle biochemical differences, which impact the implementation of MFA. Microorganisms and transformed cells can be cultured in media with one or a few substrates, which greatly simplifies model formulation and reduces the number of measurements. Tissue systems, particularly those *in vivo*, cannot be subjected to the same treatment. Even those systems in more experimentally controllable settings such as extracorporeal, engineered tissues or perfused organs, cannot be maintained in minimal media without quickly losing viability or sacrificing physiological relevance. Prokaryotic organisms like bacteria lack subcellular organelles. In contrast, eukaryotic systems are highly compartmentalized. Multiple pools of the same metabolite may exist within a eukaryotic cell, along with intracellular transport systems not found in most microbes. For example, cells in the mammalian heart and liver transfer electrons from cytoplasmic NADH onto

mitochondrial NADH by an enzymatic shuttle system involving malate and aspartate dehydrogenases [44]. The parenchymcal cells of the liver also possess specialized metabolic pathways such as the urea cycle, which are not present in most microorganisms. Tissues, especially those in the intact body, have only limited observability compared to microorganism cultures. Bacteria, yeast, and cell lines are grown fed-batch reactors, chemostats, or hollow fiber reactors, where obtaining medium samples and metabolite measurements without disruption of culture is straightforward. Most *in vivo* systems are inaccessible to such direct measurements.

The effect of the above mentioned complexities is to increase the number of unknown fluxes and reduce the number of possible measurements, adding to the total degrees of freedom. While it is still possible to resolve tissue metabolic networks with conventional MFA tools relying on metabolite measurements, the results from such studies are subject to uncertainties, because of the many assumptions and few, if any, redundant constraints. It has been suggested that additional constraints may be introduced based on biochemical theory, such as co-factor balances and irreversibility of certain reactions [45], but these ideas have yet to be validated experimentally. The preferable alternative to using more assumptions is to increase the number of measurements and measurement derived constraints. In the experimental approach, the method of choice has been use of isotopic tracers, in particular metabolite analogs labeled with ^{14}C or ^{13}C. Isotopic tracers have been used for tissue metabolism studies for several decades. Biochemists and physiologists have used isotopically labeled substrates in a variety of applications, including estimation of *in vivo* metabolite production rates [46], quantification of fluxes through the TCA cycle and gluconeogenesis in perfused organs [47], and investigation of changes to substrate turnover during inflammation [48]. While these works have focused on specific pathways, and performed without reference to MFA *per se*, their significance in calculation of intracellular fluxes through large scale metabolic networks in tissue is obvious. Thus, the integration of biochemical tracer techniques tailored for physiology into the MFA framework presents a challenging but promising opportunity to develop a powerful set of tools for investigating the metabolism systems relevant to the medical field.

In light of the above motivation, the remainder of this chapter examines basic concepts and equations used in MFA as well as popular strategies currently used for estimating metabolic fluxes with isotopic tracers. The chapter also summarizes notable applications of MFA and isotopic tracer analysis to medically relevant systems. Finally, the chapter concludes with a few

examples illustrating the role metabolic engineering, in particular MFA, may play in studying, diagnosing, and developing therapies for metabolic disorders. Before proceeding with these discussions, the overall strategy followed by more or less all MFA applications is briefly summarized at this point (Figure 1-1).

MFA begins with the formulation of a model network that consists of reactions selected from the published literature, which are thought to collectively represent the major biochemical processes in the system of interest. Except in a few very recent cases involving optimization studies, most published model networks have included on the order of 100 reactions, even though a typical cell carries out thousands of biochemical reactions, mainly because of practical limitations regarding measurement availability.

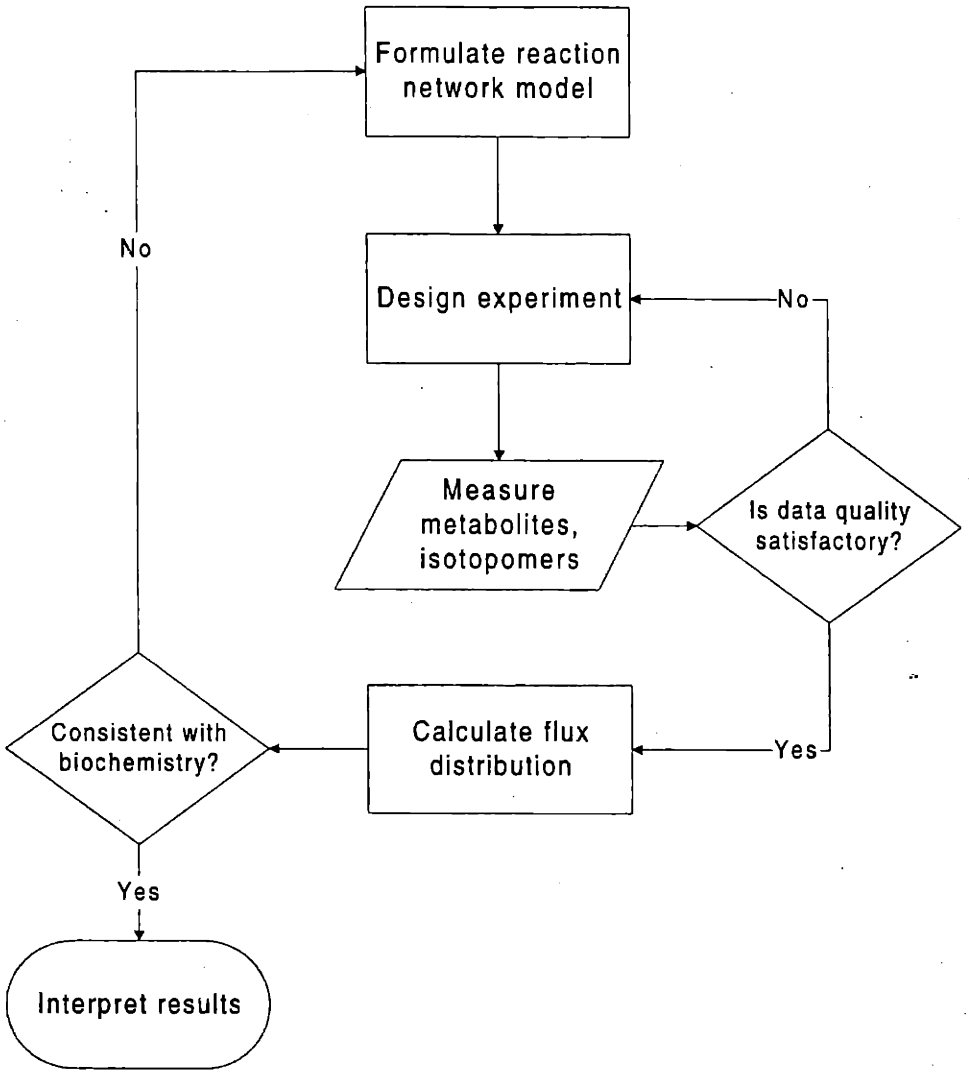

Figure 1-1. Schematic overview of metabolic flux analysis.

The first step is to formulate the model network by deciding which reactions should be included. The second step determines the necessary number and type of measurements. The number depends on the number of unknown fluxes to be calculated. The types of possible measurements include metabolite concentrations, isotopic enrichment in extracellular metabolites, and intracellular isotopic isomer distribution. After conducting the measurements, data quality is checked against statistical distributions using mass balance derived constraints. Experimental design is revised and measurements performed until data is reasonably free of gross or systematic errors. Fluxes are calculated from equations which relate the unknown fluxes to the metabolite or isotopomer measurements. These equations are derived from reaction and/or carbon atom transfer stoichiometry. Finally, the results are checked and validate against published values and known biochemistry. If the results are inconsistent, the model network may need to be modified, and the entire process repeated.

Fortunately, not all reactions have the same quantitative significance. According to the notion of biochemical time hierarchy proposed by Reich [49], biochemical reactions can be classified into one of three groups [50]: (a) rapid reactions whose time scale for reaching a state indistinguishable from the steady state is very much shorter than the time scale of observation, (b) reactions whose time scale for approaching a steady state is close to the time scale of observation, and (c) reactions that cause significant changes in concentrations on time scales longer than that of the observation. Processes in the first group include ionic equilibrium and binding of substrates and effectors by enzymes. The third group includes depletion of a pool of metabolite, synthesis or degradation of the common part of a coenzyme group, or the synthesis or degradation of an enzyme. Intermediary metabolism, which provides fuel, energy equivalents (e.g. ATP, GTP), reducing equivalents (e.g. NADH, NADPH), and basic building blocks (amino acids) for growth and maintenance, belongs to the second group. Therefore, for practical purposes, the quantitatively important aspects of a metabolic system can be reasonably modeled by including only these reactions, which number on order of 100 [49]. Once the reactions have been chosen, usually a schematic of the model network is drawn as a directed graph in order to facilitate visualization and subsequent modification.

The choice of the model also determines the necessary number and type of measurements. Smaller networks, where the aim is to estimate only net fluxes, can usually be resolved using metabolite concentration measurement data. Complex networks that include numerous branch points, cyclic pathways, and reversible steps require additional information supplied by isotopic tracer experiments.

Finally, constraint equations are written and solved, which relate the measured data to the unknown fluxes based on reaction stoichiometry and biochemistry. Here, the biochemistry of a reaction refers to the correspondence of carbon atom positions between substrate and product molecules. As it will be evident, the conservation of this correspondence in biochemical reactions is crucial in labeling experiments. It should be noted that the three step procedure outlined here is in many instances iterative. For example, during the process of fitting the experimental data to the model equations, irreconcilable inconsistencies may arise that reflect measurement errors, false judgment regarding choice of reactions, or incorrect stoichiometry and biochemistry. In this case, the experiments may need to be repeated, or, if it has been ascertained that the source of error lies elsewhere, the structure of the model network could be modified,

until a consistent set of model equations and experimental data is obtained. In this light, it is always beneficial to have as many constraint equations and measurements as possible, which allows rigorous statistical treatment of both model and data.

1.3.1 Metabolite balancing

The most basic flux estimation technique is the metabolite or material balance method [37]. In this approach, the constraint equations are derived directly from reaction stoichiometry. The stoichiometric relationships between the participating reactions is typically summarized in a stoichiometric matrix $\boldsymbol{S}$, where the element s_{ij} in the ith row and jth column refers to the stoichiometric coefficient of the ith metabolite in the jth reaction. For example, consider the reaction network described by Table 1-1A and Figure 1-2. The corresponding stoichiometric matrix is shown in Table 1-1B. Since there are four intracellular metabolites involved in eight reactions, the stoichiometric matrix has dimensions 4×8.

Once the stoichiometric matrix has been formulated, the metabolite balances are easily written using matrix notation. Let $\boldsymbol{v}$ and $\boldsymbol{x}$ be vectors whose elements v_j and x_i refer to the flux through the jth reaction and the intracellular concentration of the ith metabolite, respectively. For a stoichiometric matrix which has dimensions $M \times N$, the corresponding vectors $\boldsymbol{v}$ and $\boldsymbol{x}$ have dimensions $N \times 1$ and $M \times 1$. In the case of the example network shown in Figure 1-2A, $\boldsymbol{v}$ and $\boldsymbol{x}$ have dimensions 8×1 and 4×1, respectively. Using the stochiometric matrix and these vectors, the metabolite balance equations are written as follows:

$$\frac{d\boldsymbol{x}}{dt} = \boldsymbol{S}\boldsymbol{v} \tag{1-2}$$

In the case of the current example, Equation 1-2 summarizes the following system of equations:

$$\frac{dA}{dt} = F1 - F3 - F4 \tag{1-3a}$$

$$\frac{dB}{dt} = F2 + F3 - F5 \tag{1-3b}$$

$$\frac{dC}{dt} = F5 - F6 - F8 \tag{1-3c}$$

$$\frac{dD}{dt} = F4 + F6 - F7 \tag{1-3d}$$

Table 1-1A. Reaction Stoichiometry for Example Network

Reaction No.	Stoichiometry
F1	A uptake
F2	B uptake
F3	A $\rightarrow$ B
F4	A $\rightarrow$ D
F5	B $\rightarrow$ C
F6	C $\rightarrow$ D
F7	C output
F8	D output

Table 1-1B. Stoichiometric Matrix for Example Network

	F1	*F2*	*F3*	*F4*	*F5*	*F6*	*F7*	*F8*
A	1	0	-1	-1	0	0	0	0
B	0	1	1	0	-1	0	0	0
C	0	0	0	0	1	-1	-1	0
D	0	0	0	1	0	1	0	-1

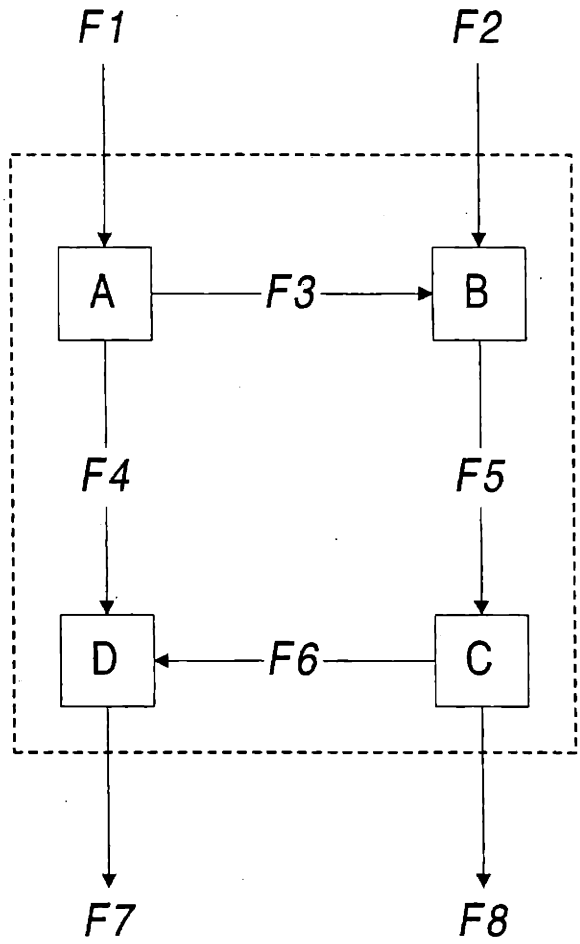

Figure 1-2. Directed graph representation of example network.
A, B, C, and D are intracellular metabolites. F1, F2, F7, and F8 are rates of uptake or output of metabolites A, B, C, and D, respectively. F3 through F6 denote intracellular reactions. If all of the metabolite uptake and output rates measurable, the system is exactly determined, as there are four unknowns and four linearly independent equations. If an additional flux through one of the intracellular reactions is measurable, then the system is overdetermined, giving rise to redundant constraints useful for consistency checks. If one of the metabolite uptake and output rates are not measurable, then the system is underdetermined, and there is an infinite number of solutions.

It is generally accepted that there is a very high turnover of the intracellular pools of most metabolic intermediates, especially those participating in central carbon metabolism. The pathways of central carbon metabolism in most prokaryotic and mammalian cells include glycolysis, glycogen synthesis, pentose phosphate pathway (PPP), tricarboxylic acid (TCA) cycle, fatty acid synthesis and oxidation, amino acid synthesis and degradation, etc. A few specialized cells, such hepatocytes in the mammalian liver also include urea cycle and gluconeogenesis. As a result of the high turnover, the concentrations of the metabolites in these pathways rapidly adjust to new levels even after large perturbations in the cellular environment is experienced by the cells. Therefore, the (pseudo) steady-state assumption applies to the balances in Equation 1-2:

$$\frac{d\boldsymbol{x}}{dt} = 0 = \boldsymbol{S}\boldsymbol{v} \tag{1-4}$$

In the case of the current example, the steady-state assumption linearizes the system of equations in 1-3a through 1-3d. Using the above defined stoichometric matrix (Figure 1-2B) and vectors, these linear equations are succinctly expressed as follows:

$$\begin{bmatrix} dA/dt \\ dB/dt \\ dC/dt \\ dD/dt \end{bmatrix} = 0 = \begin{bmatrix} 1 & 0 & -1 & -1 & 0 & 0 & 0 & 0 \\ 0 & 1 & 1 & 0 & -1 & 0 & 0 & 0 \\ 0 & 0 & 0 & 0 & 1 & -1 & -1 & 0 \\ 0 & 0 & 0 & 1 & 0 & 1 & 0 & -1 \end{bmatrix} \begin{bmatrix} F1 \\ F2 \\ F3 \\ F4 \\ F5 \\ F6 \\ F7 \\ F8 \end{bmatrix} \tag{1-5}$$

In order to solve the system of linear equations represented by Equation 1-4 it is customary to first partition the stochiometric matrix $\boldsymbol{S}$ and the metabolic flux vector $\boldsymbol{v}$ into known and unknown components [35]:

$$\boldsymbol{S}\boldsymbol{v} = 0 = \boldsymbol{S}_m\boldsymbol{v}_m + \boldsymbol{S}_c\boldsymbol{v}_c \tag{1-6}$$

where $\boldsymbol{v}_m$ and $\boldsymbol{v}_c$ are the vectors of measured and unknown reaction fluxes, respectively, and $\boldsymbol{S}_m$ and $\boldsymbol{S}_c$ contain the stoichiometric coefficients of the corresponding reactions. Rearranging,

$$\boldsymbol{S}_c\boldsymbol{v}_c = -\boldsymbol{S}_m\boldsymbol{v}_m \tag{1-7}$$

Equation 1-8 can be solved for $\boldsymbol{v}_c$ explicitly in terms of the elements of $\boldsymbol{v}_m$ by simple matrix inversion if $\boldsymbol{S}_c$ is a square matrix.

$$v_c = -S_c^{-1} S_m v_m \tag{1-8}$$

Equation 1-9 represents the exactly determined case where the number reaction fluxes in the model metabolic network equals the number of linearly independent balance equations plus the number of measurements. In the current example, this would be the case if two of the five reaction fluxes, e.g. F1 and F2, are experimentally determined. In this case, S_c has full rank, which is also equal to the number of elements in v_c.

If the number of fluxes in the model is less than the number of linearly independent balance equations plus the number of measurements, the system is overdetermined, and there exist extra constraints that can be used for testing the consistency of the overall balances, the accuracy of the flux measurements, the validity of the pseudo steady- state assumption, and ultimately, the calculation of more accurate values for the unknown intracellular fluxes. In the current example, this would be the case if in addition to the two reaction fluxes F1 and F2, a third flux, e.g. F3, could be experimentally determined. A brief description of the systematic procedure for using redundant constraints for error checking and measurement correction as proposed by Wang and Stephanopoulos [51] is given in the subsequent chapter. If it is determined that no gross measurement errors are present, then the overdetermined system is may be solved by a least-squares approach:

$$v_c = -(S_c^T S_c)^{-1} S_c^T S_m v_m \tag{1-9}$$

If the number of fluxes in the model is greater than the number of linearly independent balance equations plus the number of measurements, the system is underdetermined, and an infinite number of solutions exist. In the current example, this would be the case if none or only one of the reaction fluxes were experimentally determined. In this case, an optimization approach may be taken, where objectives functions are formulated, which are linear combinations of all or some of the unknown variables. Mathematically, this is expressed as follows:

$$\max_{v_c} c^T v_c \tag{1-10a}$$

subject to

$$S_c v_c = -S_m v_m \tag{1-10b}$$

$$v_c \geq b \tag{1-10c}$$

$$v_c \geq -d \tag{1-10d}$$

where the vector $\boldsymbol{c}$ specifies which unknown flux vector elements are to be maximized (or minimized) and the vectors $\boldsymbol{b}$ and $\boldsymbol{d}$ provide the lower and upper bounds for the unknown fluxes. Solutions to linear optimization problems such as that described by Equation 1-11 are easily obtained by published methods, such as the simplex algorithm, which can be found in standard optimization textbooks [52].

It should be note that solutions to metabolic flux problems based on optimization strategies are strongly depend on the assumed nature of the cellular metabolic activity and the formulation of the objective function. Provided such a function can be specified, it is possible to obtain a unique solution for the intracellular fluxes that optimizes the objective function subject to the constraints of the metabolite balances. In the case of microorganisms or cell line cultures, a commonly chosen objective function is maximal growth. For example, Savinell and Palsson [53, 54] use the linear optimization approach in conjunction with experimental measurements to study the interactions of nutrients and the demand for intermediates for growth in hybridoma cells. However, for individual cells in a multicellular organism, the choice of objective function is not as clear, which is the case in medically relevant systems. A mammalian cell may need to secrete a particular protein, store substrates for energy production, metabolize chemicals toxic to the rest of the body, in addition to growing efficiently in a controlled manner, as part of its role in the larger body. A realistic objective function requires these myriad of objectives to be weighted properly, which introduces additional parameters that are difficult obtain experimentally. Thus, the optimization approach is more suited to exploring the capacities of metabolic networks to get a qualitative understanding of how metabolic systems respond to hypothetical scenarios rather than determining actual flux distributions.

Unfortunately, the case of the underdetermined network is a common occurrence, especially in the metabolism of medically relevant systems, which are in general more complex due to cellular compartmentalization and added branch points. In order to fully resolve such metabolic networks, additional measurements are needed. The most prominent method involves using isotopically labeled metabolite analogs as tracers.

1.3.2 Overview of isotopic tracer methods

Isotopic tracer methods are based on the notion that the activities of metabolic pathways can be determined by providing substrates enriched in a carbon isotope (typically ^{13}C or ^{14}C) and

analyzing the distribution of the isotopes in metabolic intermediates. Isotopically labeled substrates are chemically indistinguishable from normal substrates, and they are metabolized by the same sequence of reactions as their unlabeled analogs. Substrate cycling, asymmetrical splits in pathways, and reversibility of reactions produce metabolic intermediates that differ in the number of labeled carbons or the position of the label. Isotopic isomers which differ by the number of labeled carbons are called mass isotopomers while isotopic isomers which differ by the position of the label are called positional isotopomers. Given a particular input tracer or set of input tracers, the steady-state distribution of the isotopomers is a function of the relative fluxes through the reactions which produce the isotopomers. Therefore, using an appropriately formulated metabolic network model, equations can be written that relate isotopic enrichment in metabolic intermediates to metabolic fluxes.

One of the earliest efforts to obtain metabolic fluxes using isotopic tracers was performed by Weinman et al. [55], whose equations describing the production of $^{14}CO_2$ or [^{14}C]glucose were derived from convergent geometric series. Rognstad and Katz [56] avoided using these often unwieldy geometric series equations by invoking an isotopic steady-states assumption in calculating the rate of pyruvate entry into the TCA cycle relative to its flux through gluconeogenesis. Under the isotopic steady-state assumption, the inflow of isotopic material into a metabolite pool equals the outflow of isotopic material from that pool. Kelleher [57, 58] expanded on the works by Rognstad and Katz to include multiple tracer inputs and outputs into and out of the TCA cycle, expressing the steady-state relationships between metabolic fluxes and isotopic enrichment in terms of specific activity (SA) equations:

$$SA_p = \frac{\sum_{i=1}^{m} (SA \cdot F_{pi})}{\sum_{i=1}^{m} F_{pi}} \tag{1-11}$$

In Equation 1-12, representative of the balances appearing in [57, 58], the enrichment of metabolite p (SA_p) at isotopic steady-state equals the ratio of the total isotopic flux to the total carbon (labeled and unlabeled) flux into pool p. The total fluxes are found by summation across all metabolites i (1 through m) from which reaction fluxes enter the pool p.

Since the early works of Weinman et al. [55] and Rognstad and Katz [56], numerous analytical and numerical modeling approaches have been proposed for the estimation of intracellular metabolic fluxes using isotopic enrichment data. Broadly, these approaches fall into

the following two categories based on the nature of the experimental data to be modeled. One approach models the dynamics of isotopic enrichment observed over a period of time while the other describes the isotopomer distribution at isotopic steady-state. In both approaches, differential equations are written that describe the production of (mass or positional) isotopomers of metabolites included in the model metabolic network subsequent to the introduction of the input tracer(s). In the steady-state models, the time derivative are set to zero, and the differential equations become algebraic equations. One notable alternative to these two strategies is the syntactic method proposed by Cohen and Bergman [59, 60]. In this approach, which combines a rule-based description of biochemical reactions with a stochastic model of chemical kinetics, the parameter of interest is the mean residence time of a particular carbon atom of a reactant molecule within the model metabolic network. Here, the residence time refers to the time it takes for the carbon atom of interest to traverse the entire network. This parameter, obtained by fitting exponential functions to time-dependent isotopic enrichment data, gives an estimate for the dominant rate constant for the metabolic process under investigation. This elegant approach greatly simplifies the formulation of model equations while describing an important characteristic of a metabolic network. However, it is only applicable to cyclical pathways, where a carbon atom can return to its pool of origin. Nevertheless, the syntactic method has many attractive features, such as the ability to estimate absolute fluxes and to infer information about metabolite pool sizes [61].

1.3.3 Kinetic models

To date, nuclear magnetic resonance (NMR) spectroscopy remains the most widely used method for measuring the kinetics of isotopic enrichment in the intact tissue despite the drawback of low sensitivity, chiefly because of its nondestructive nature. The most commonly used label in NMR spectroscopy applications to metabolic flux analysis is the stable isotope ^{13}C, which is safe for even clinical applications and has a low natural abundance (1.1 %). Unfortunately, due to the low sensitivity of NMR spectroscopy, ^{13}C isotopomers are only discernible in NMR spectra if their tissue concentrations exceed 0.5 mM. Most metabolic intermediates are normally present below this level, and hence irresolvable by NMR spectroscopy even when the ^{13}C enrichment is unity, unless the signals are acquired over an excessively long period of time [49]. The major exceptions are the five amino acids alanine,

aspartate, glycine, glutamate and glutamine, which add up to about 80 % of the free cytosolic amino acid pool [49]. In addition to being present in relatively high concentrations, glutamate and aspartate are in exchange with α-ketoglutarate and oxaloacetate, respectively, which are key intermediates of the TCA cycle and gluconeogenesis. Consequently, many kinetic flux estimation models use the isotopic enrichment data of these two amino acid pools as the major measured inputs.

In an important early work, Chance et al. [62] used 176 differential equations to describe the production of positional isotopomers of TCA cycle intermediates following the introduction of [2-^{13}C]acetate or [3-^{13}C]pyruvate in the perfused rat heart. The experimental input used for flux estimation was ^{13}C spectra of glutamate isotopomers in tissue extracts obtained at various times after tracer injection. This work was later extended to include glycolysis and the malate-aspartate shuttle, which led to a model with 340 differential equations [63]. The models presented in these works contained large numbers of equations, because a separate equation described each reaction between two particular isotopomers. The number of possible ^{13}C isotopomers for a given metabolite is given by 2^n, where n is the number of carbon atoms in the metabolite. For example, the above approach required a total of 32 differential equations to describe the interconversion between α-ketoglutarate and glutamate via one aminotransferase reaction. A compartmental modeling approach was proposed by Yu et al. [64, 65], who estimated TCA cycle flux parameters in the perfused rabbit heart by analyzing the isotopic enrichment kinetics for carbon atoms in selected, rate-limiting metabolite pools of the TCA cycle. This treatment resulted in a more compact model involving only nine equations, and yielded TCA cycle flux estimates similar to those by [62] and [63].

Aside from the above mentioned experimental limitation associated with ^{13}C NMR spectroscopy, the major drawback of the kinetic modeling approach is that it requires knowledge of metabolite pool sizes. As ^{13}C NMR spectra only contain information regarding relative enrichments of carbon atoms within a given molecule, the fractional enrichment of each isotopomer has to be multiplied by the respective metabolite pool size in order to trace the flow of label. While it is possible to obtain tissue concentrations for many metabolites from the published literature, there are uncertainties associated with flux estimates based on these values, since sample variations can be significant in biological systems, and as averages, the literature values may not reflect the concentrations in the particular sample being analyzed [62]. A more

reliable approach is to perform enzymatic assays parallel to the ^{13}C NMR experiments [62]. However, this process is time-consuming and requires extraction of tissue samples, which undermines the noninvasive feature of ^{13}C NMR spectroscopy. Furthermore, the experimentally found concentrations are still subject to errors inherent to enzymatic assays. Based on sensitivity analyses using simulated results, Yu et al. [66] concluded that the estimated fluxes were relatively insensitive to variations in pool sizes of most metabolites, except those metabolites whose isotopic enrichment kinetics are directly measured by NMR spectroscopy. For example, in determining TCA cycle fluxes, even small variations in the assumed glutamate pool size strongly influenced the predicted labeling patterns, and in turn the calculated flux values. In order to reduce the uncertainties associated with pool size measurement errors, Chatham et al. [63] and Yu et al. [66] proposed including a "metabolic cost" term in the objective function of the non-linear regression that fits the predicted enrichment curves to the measured spectra. For example, in [66], the cost function was the difference between the measured and predicted oxygen uptake rates, with the predicted value expressed as function of the estimated flux parameters.

Despite the drawbacks mentioned above, kinetic isotopomer modeling, coupled with dynamic ^{13}C NMR spectroscopy, remains an attractive approach for flux estimation, because the method does not require steady-state metabolic or isotopic conditions, and allows for the dynamic study of metabolic systems, which is particularly useful for investigating metabolic stresses in intact tissues [67]. For example, Cohen et al. [68] used nondestructive ^{13}C NMR methodology to monitor metabolic fluxes in the perfused liver of obese mice treated with leptin. Recent advances in NMR technology has also enabled the *in vivo* observation of large, polymeric metabolites in selected tissues, such as glycogen in the liver or skeletal muscle, at resolutions comparable to those obtained *in vitro* or in extracts [69]. However, for applications where detailed analysis of intermediary metabolism is desired, isotopomer measurements are still conducted in extracts [70], which negates the noninvasiveness advantage of the kinetic modeling approach. Therefore, in applications where extracts are available (via biopsies), or cells are exposed, such as *ex vivo* engineered tissues, an alternative approach based on steady-state models has been used more frequently, because of the superior resolution of the associated experimental method and the flexibility of these mature models that can accommodate large, complex metabolic networks.

1.3.4 Steady-state models

Steady-state isotopomer analysis is analogous to metabolite balancing in that intracellular fluxes are estimated using steady-state mass balances, except that by using isotopic tracers, many more additional constraints can be generated to improve the resolvability of the model metabolic network. As alluded to earlier, the metabolite balancing approach sometimes leads to underdetermined algebraic systems, especially when there are large numbers of branch points and cyclic pathways [71]. Furthermore, reversible reactions are entirely irresolvable by metabolite balancing alone, as this method estimates only net fluxes. Introducing isotopic tracers expands the number of available measurements, and hence constraints, which can be used to resolve more complex networks as well as quantify exchange fluxes between metabolites participating in reversible reactions. On the other hand, introducing isotopic tracers also adds complexity to the model formulation, as the numbers of equations required to relate the steady-state distribution of isotopomers to metabolic fluxes is very large. The model construction is further complicated by the dependence of the isotopomer distribution on reversible reactions. The distribution of isotopomers is also influenced by the choice of the tracer, both in terms of the position(s) of the label and the metabolite, and therefore, depending on the chemical reactions occurring in the metabolic network, differently labeled substrates are required to obtain informative measurements from a tracer experiment. In order to optimize the type and degree of tracer labeling and thereby maximize the information yield, it is often useful to perform *a priori* sensitivity analyses which test the stability of estimated flux parameters with respect to various tracers using simulated data [72].

These considerations regarding the formulation of complex model equations and the choice of appropriate tracer labeling have been facilitated by recent introductions of computational tools and formalisms. Zupke et al. [73, 74] proposed a method involving atom mapping matrices (AMMs), which effectively separated the chemical reaction details of isotopomer formation from composing the structure of the metabolic network model. Using binary indexing to enumerate isotopomers, an AMM specifies the transfer of carbon atoms from reactant to product in a corresponding biochemical reaction. Thus, AMMs allow straightforward derivation of isotopomer balances from metabolite balances. Similar approaches have been suggested by several other authors [75-77].

Flux estimation by isotopomer analysis proceeds iteratively, which, combined with the complexity of the model equations, prohibits analytical solutions. In general, simulation models are used to predict isotopomer distributions as a function of a given set of intracellular fluxes, which are then compared with the experimental data. The best estimate for the fluxes are obtained by minimizing the deviation between the calculated and measured isotopomer distributions [78]. This strategy, shown schematically in Figure 1-6, is usually applied iteratively, and has been used with minor modifications by a number of researchers in a variety of systems. The implementation, while in principle straightforward, requires rigorous statistical treatment of both experimental data and the algorithm, because of the large number of variables involved, which are often nonlinearly dependent on the measured data [79]. To this end, Wiechert and de Graaf [80, 81] proposed an elegant, generally applicable formalism for sensitivity analysis, computation of confidence regions, and parameter identifiability analysis. Central to this formalism was the notion that both structural network properties [82] as well as quantitative assumptions regarding measured data and fluxes could be expressed as linear equality or inequality constraints using matrix algebra and a formal language developed specifically for metabolic network modeling. By defining accessible labeling states with equality and inequality constraints, theoretical boundaries can be established around possible isotopomer distributions, and hence flux solutions, aiding in the experimental design and reducing computation time.

In addition to computational strategies, several recent advances have also been made in isotopomer measurement techniques. Unlike kinetic models, which require knowledge of metabolite pool sizes, the only experimental input to steady-state isotopomer models is fractional enrichment or isotopomer distribution data. As the steady-state approach has been applied to systems where tissues are exposed or extracts are available, these measurements have been performed using both gas chromatography-mass spectrometry (GC-MS) as well as NMR spectroscopy. Traditionally, MS has been perceived to be a more sensitive method than NMR spectroscopy, able to detect ^{13}C labeling patterns of metabolites present at low cellular levels (< 0.5 mM) [47]. On the other hand, ^{13}C NMR spectroscopy presents a simpler measurement tool than GS-MS, which requires multiple chemical derivation steps prior to the analysis. Fortunately, recent progress in two-dimensional (2D) NMR spectroscopy has led to the development of an analytical technique, termed 2D heteronuclear correlation spectroscopy (COSY), which can efficiently determine the labeling patterns of amino acids from a single measurement on crude

biomass (protein) hydrolisates [83]. Amino acids in biomass hydrolisates are abundantly present, and the ability to use the isotopomer distribution patterns of these compounds avoids the need to measure the isotopomer distribution patterns of central carbon metabolism intermediates, which are present at low cellular levels and therefore more difficult to obtain. Moreover, unlike GC-MS, which distinguishes only mass isotopomers, 2D ^{13}C-NMR spectra also contains information regarding the relative amounts of positional isotopomers, and in principle can be used to acquire constraints on all of the 2^n isotopomers of a *n* carbon molecule [78]. One remaining limitation of 2D ^{13}C-NMR is that for larger, nearly symmetrical metabolites, it can only quantify subsets of isotopomers, because certain nuclear spin couplings, parameters essential to the isotopomer analysis from 2D ^{13}C-NMR spectra, appear identical or are irresolvable. For example, GC-MS, while somewhat tedious in its application, has no such limitations regarding the size and symmetry of the metabolite. To date, the most complete approach to determining the isotopic labeling state of a metabolite is to use both GC-MS and 2D ^{13}C-NMR, as they yield complementary experimental data from which robust, tracer independent flux estimates may be obtained [84].

1.3.5 Extension to tissue systems

Significant advances in computational methods and analytical techniques have led to the maturation of steady-state isotopomer analysis as a robust tool for intracellular flux estimation applicable to even large complex metabolic networks. However, there remain a number of obstacles to extending this method to systems relevant to the study of human disease, such as whole body animal models or perfused organs. The ultimate output of the afore mentioned analysis is not a set of absolute fluxes, but a flux distribution, because the experimental input, an isotopomer distribution, is only a function of the relative activities of metabolic pathways. In order to infer absolute values, which is crucial for sample and treatment comparisons in physiological studies, the absolute value of at least one flux in the metabolic network must be experimentally obtained. This is a straightforward matter for a bioreactor culture, where the absolute rate of uptake or release of a metabolite can easily be found by multiplying the concentration gradient across the reactor inlet and outlet by the dilution rate. Even for a perfused organ, the exchange rate of a metabolite may be determined from a measured concentration time profile. However, *in vivo* tissue systems are not amenable to these approaches, because they are

physically inaccessible and directly or indirectly interact with various other tissues and organs in the body.

In order to address these obstacles, biochemists, organ chemists, and physiologists have developed several tracer methods for metabolic flux estimation that are specifically tailored for *in vivo* applications. An excellent review of techniques for measuring the turnover rate, or rate of *de novo* synthesis, of a single metabolite in a particular tissue or organ is provided by Wolfe [85, 86]. In this application, the stable or radioactive tracer analog of the metabolite of interest is infused at a constant rate into the body following a priming dose injected as bolus. The corresponding metabolic flux, or to use the terminology in this literature, the rate of appearance (Ra), is found from the tracer dilution data using mass balances drawn around the plasma compartment. For example, Hellerstein et al. [87] estimated the rate of glucose production in the liver by measuring the steady-state plasma dilution of the tracer [1-H^3]glucose. Once the *in vivo* turnover rate of a metabolite is known, absolute values for tissue or organ specific intracellular fluxes associated with the production or consumption of the metabolite may be calculated using the isotopomer models described above, provided the tissue or organ isotopomer distribution can be measured.

In situations where the desired intracellular fluxes involve physiological polyermerization reactions, several techniques specifically developed for this application may be used in conjunction with the steady-state isotopomer modeling method. In general, these techniques proceed by introducing a monomer substrate enriched with a stable isotope (usually ^{13}C) into the cell, tissue or organ and then analyzing the relative abundance of the polymerization product isotopomers. From this data, estimates may be obtained for the relative contributions of the pathways that led to the formation of the polymer using algebraic equations. One of the earliest versions of this technique was employed by Kalderon et al. [46, 88-90] in order to probe glycogen formation from gluconeogenesis derived glucose precursors in patients with glycogen storage disease. Since then, several researchers have developed useful extensions which incorporate probabilistic models into the data analysis. Currently, the two most popular versions are mass isotopomer distribution analysis (MIDA) and isotopomer spectral analysis (ISA).

MIDA, which was originally conceived by Strong et al. [91] and subsequently expanded by Hellerstein et al. [92-95] and Lee et al. [96, 97], estimates biosynthetic rates by fitting mass isotopomer distribution frequency data to a probabilistic model. It has long been established that

the inference of biosynthesis using tracers requires accurate experimental determination of the isotopic enrichment of the "true" precursor pool, denoted "*p*" in the literature. The "true" precursor is the actual monomer substrate which enters the product at the site of synthesis. In practice, isolating the putative precursor and determining its enrichment is very challenging, because of intracellular inhomogeneities such as subcellular compartmentation, formation of enzyme-substrate complexes, etc. MIDA calculates the precursor enrichment *p* by comparing the measured product isotopomer distribution with a calculated binomial probability expressed as a function of *p* [93]. It has been shown that the mathematical estimate of *p* by MIDA remains valid even if there are multiple anatomical or functional pools of precursors. Once *p* is known, both fractional synthesis, or *de novo* synthesis of labeled polymer during a tracer experiment, and the absolute rate of total endogenous polymer production can be calculated from tracer dilution kinetics.

In principle, MIDA is applicable to the study of both very long polymers such as proteins as well as simple dimers such as glucose. Glucose can be considered a dimer formed from the condensation of two triose phosphate (TP) subunits, dihydroxyacetone phosphate (DHAP) and glyceraldehyde 3-phosphate (GAP). MIDA has been suggested as an attractive alternative for investigating hepatic gluconeogenesis, because it can avoid certain artifacts associated with the other methods, such as isotope exchange, which leads to underestimation of glucose production rates [98]. In practice, the validity of MIDA as a tool for studying glucose metabolism is still subject to debate. In a study involving intravenous infusion of two different tracers, Neese et al. reported that both tracer experiments yielded identical values for hepatic gluconeogenesis in the fasted rat [99]. However, in a similar experiment, Previs et al. [100] found significant variations depending on whether labeled lactate or glycerol was infused. This result was ascribed to heterogeneous zonation of glycerol metabolism across the liver lobule. Further more, it was concluded while labeled lactate was a suitable substrate for MIDA of GNG *in vivo*, this was not the case in a perfused liver, presumably because labeled lactate and pyruvate are not fully equilibrated. It is clear that although MIDA is conceptually sound, care must be taken in interpreting its results, because of system specific nuances such as heterogeneous zonation across an organ.

A method conceptually similar to MIDA is isotopomer spectral analysis (ISA), which is a method developed by Karroubi et al. [101] in order to measure lipid biosynthesis in cells. Many

biosynthesis reactions occur by condensations of the type $nA \rightarrow 1B$, where n is the number of A molecules needed to synthesize one molecule of B. ISA utilizes the discrete spectrum of isotopomer abundance and the multinomial probability distribution to estimate two key parameters associated with the biosynthesis. These parameters are dilutions of the immediate precursor and the newly synthesized product in the sampled compartment. Since its first application to palmitate synthesis in 3T3-L1 cells [101], ISA has been employed in a variety of situations, including cholesterol synthesis in HepG2 human hepatoma cell line [102], acetoacetate metabolism in AS-30D hepatoma [103], and acetyl-L-carnitine flux to lipids in 3T3-L1 and HepG2 cells [104]. The advantage of ISA is that it is applicable to all condensation type reactions, including polymerization, and to situations where multiple fluxes need to be estimated from a single experiment [102].

Thus far, this section has summarized the basic ideas behind popular MFA methods used in both the bioprocess and physiology literature (Table 1-2). The methods covered here have been developed either for microorganisms or specific tissue or organ pathways, and therefore, in their present form, are not wholly adequate for biomedical applications, where the aim is to quantify intracellular fluxes through tissue metabolic networks. On the other hand, the mathematical formalisms developed by bioprocess engineers and *in vivo* tracer techniques used by biochemists and physiologists are complementary, and carefully integrated, could resolve even large, complex metabolic systems pertinent to medicine. The remainder of this chapter highlights representative examples from published MFA applications to tissue, organ, and *in vivo* systems.

Table 1-2. Methods for Metabolic Flux Analysis

Method	Measurement / Analytical Technique	Typical Application	Comments
Metabolite balancing	Extracellular metabolite concentration by HPLC, enzymatic assays, or GC-MS	Microbial central carbon metabolism	Simple to apply, very few assumptions required; limited resolution
Linear optimization	None required, extracellular metabolite concentration by HPLC, enzymatic assays, or GC-MS useful	Nutrient requirement under assumed objective, such as maximal growth	Explores metabolic capacity; difficult to find realistic objectives for higher organisms
Enrichment dynamics	Enrichment kinetics of intracellular metabolites by ^{13}C-NMR	TCA cycle fluxes in perfused organ	Estimates absolute fluxes in intact tissue; need to know metabolite pool sizes
Isotopomer distribution analysis	Fractional enrichment or relative isotopomer concentrations of intracellular metabolites by ^{13}C NMR, 2D ^{13}C-NMR, or GC-MS	Complex networks containing cyclical pathway and multiple branch points	Only input is isotopomer distribution data; large computational cost, obtaining complete isotopomer distribution experimentally challenging
MIDA	Relative abundance of mass isotopomers of biopolymers by GC-MS	Synthesis of carbohydrate biopolymers	Tracer independent results; limited to polymerization form identical subunits
ISA	Relative abundance of mass isotopomers of biopolymers by GC-MS	Synthesis of lipid biopolymers	Applicable to all condensation reactions; validated solely in vitro, estimate only relative fluxes
Tracer dilution	Extracellular concentration of labeled tracer by GC-MS or radiometric assay	Whole body metabolite turnover	Clinical relevance; unsuitable for network analysis

1.4 Metabolic Flux Analysis in Biomedicine

1.4.1 Cell and organ physiology

An important aspect of tumor biology has been understanding the ability of tumors to adapt to adverse growth environments such as hypoxia or hypoglycemia. It has been suggested that the energy metabolism of tumors is altered in such a way as to accommodate high levels of anaerobic metabolism and alternate substrate utilization. Using ISA and a model of metabolism around the TCA cycle, Holleran *et al.* [103] investigated the quantitative importance of acetoacetate and glucose in energy production in AS-30D hepatoma cells. The study showed that addition of acetoacetate diverted pyruvate from pyruvate dehydrogenase (PDH) to pyruvate carboxylation while addition of a nonmetabolized analog of acetoacetate increased the oxidation of glucose via PDH. Without added acetoacetate, glucose supplied 65% of the acetyl-CoA used for *de novo* lipogenesis, but in the presence of high levels of acetoacetate, glucose was replaced by acetoacetate as the dominant lipogenic precursor. These findings suggested that AS-30D cells have a large capacity for acetoacetate utilization for *de novo* lipogenesis, enabling increased fat storage compared to nontransformed cells, which could aid survival under cachexic conditions. In a study involving rat brain tumor (C6 glioma) cells by Portai *et al.* [105], flux distributions calculated using ^{1}H-^{13}C-NMR data showed low pyruvate carboxylase (PK) activity and efflux of carbon moieties from the TCA cycle, suggesting suppressed glutamine synthesis. In the follow-up publication, Portai *et al.* [106], reported that glutamine and glucose are metabolized complementarily in C6 glioma cells, where glutamine is utilized for anaplerosis but not as fuel, whereas the majority of glucose is oxidized, with only tiny amounts entering anaplerotic pathways. In a similar set of experiments, Bouzier *et al.* [107] showed that unlike normal astrocytes, C6 glioma cells preferentially use lactate as a substrate for aerobic metabolism. These examples illustrate the usefulness of MFA in characterizing important physiological differences between tumors and their normal counterparts in intact cells, which could form a basis for better understanding tumor metabolism and controlling tumor growth in the human body.

MFA has also been used to characterize the effects of acute metabolic stresses. Malloy et al. [108] used a TCA cycle isotopomer model in conjunction with a perfused heart to show a protective role for aspartate and glutamate during ischemia-reperfusion, as these two metabolites can help prevent a dramatic reduction in TCA cycle intermediate levels. In a similar perfused

heart model, Laplante *et al.* [109] established that the mechanism of cardiomyocyte viability protection by fumarate during ischemia or hypoxia involves its conversion to succinate via the reversible enzyme succinate dehydrogenase. In another similar study, Sumegi et al. [110] showed that lipoamide, a chemical thought to enhance recovery after myocardial infarction, almost entirely prevents the switch from lactate to acetate oxidation observed in ischemic heart tissue, pointing to a potential biochemical mechanism for the physiologic activity of this agent.

1.4.2 Metabolic disorders

One of the earliest direct applications of isotopomer analysis to studying metabolic disorders concerned glycogen storage disease (GSD). In a series of tracer experiments involving ^{13}C labeled glucose, Kalderon et al. [46, 88-90] studied the effect of GSD types I and III (GSD-I and –II) on hepatic glucose storage and utilization. In children with GSD-I, the glucose isotopomer distributions in the plasma mirrored that of the infused tracer, indicating that glucose recycling was absent. In contrast, the plasma glucose isotopomer distribution was significantly altered in control and GSD-III subjects. The absence of recycled glucose in plasma eliminated gluconeogenesis as a mechanism for glucose production in GSD-I patients, and pointed instead at a functional deficiency in a gluconeogenic enzyme. In GSD-III patients, the opposite was true, as gluconeogenesis was found to be the dominant route for glucose production. A promising extension to these findings is the minimally invasive detection of metabolic disorders using isotopomer analysis. As the differences in glucose recycling between GSD-I, GSD-II, and normal subjects were deduced from differences in plasma glucose isotopomer distributions, conversely, defects in glucose metabolism may be detected simply by performing NMR spectroscopy or GC-MS on drawn blood samples.

Another metabolic disorder studied frequently with isotopic tracer analysis is diabetes. In a series of extensive studies in perfused livers, Cohen et al. [111-113] found that concomitant activation and repression pyruvate carboxylase and pyruvate kinase, respectively, prevent back conversion of phosphoenolpyruvate to pyruvate, leading to the enhanced gluconeogenesis found in some diabetic patients. More recently, Peroni et al. [114] demonstrated that the increased gluconeogenic contribution to hepatic glucose production in streptozotocin-diabetic rats depended on the whole body nutritional state, as isotopic tracer experiments showed that gluconeogenic flux increased relative to control in the post-absorptive state but not in the fasted

state. In a clinical study, Tayek and Katz [115] compared the relative contributions of gluconeogenesis and glycogenolysis to post-absorptive hepatic glucose production in normal volunteers and non-insulin-dependent diabetes mellitus (NIDDM) patients. They found that while total glucose production was elevated in NIDDM patients compared to control subjects, fractional contribution of gluconeogenesis was comparable, raising doubts about the widely-held notion that synthesis of hepatic glycogen is seriously impaired in NIDDM. This was not the case for insulin-dependent-diabetes mellitus, as Landau et al. [116] showed using a similar approach that the contribution of gluconeogenesis to glucose production is significantly less in IDDM patients than in normal subjects.

Finally, the above results, coupled with the minimally invasive nature of performing NMR spectroscopy or GC-MS on drawn blood samples, hint at possible diagnostic tests based on isotopomer distribution analysis of one or more plasma metabolites. In an early utilization of this notion, Gopher et al. [117] proposed a isotopomer analysis based procedure for detecting hereditary fructose intolerance (HFI), which has traditionally been diagnosed by liver biopsy. HFI subjects, who lack the ability to degrade fructose-1 phosphate by aldolase B action, if continuously exposed to fructose during infancy, may develop liver cirrhosis and mental retardation, and risk high chance of mortality. In the isotopomer analysis approach, the hepatic fructose metabolizing pathways in potential HFI children are probed using ^{13}C labeled fructose, and checked for any defects by analyzing plasma glucose isotopomer distributions. This procedure was validated by an experiment where nasogastric infusion of D-[U-^{13}C]fructose into healthy and HFI children and subsequent analysis of plasma glucose isotopic enrichment confirmed that conversion of fructose to glucose was significantly lower in HFI children. Interestingly, it was also found that the generally accepted pathway of fructose conversion to glucose via fructose-1 phosphate aldolase accounted for only ½ of the total even in normal subjects. Thus, the study concluded that a direct pathway must exist which converts fructose to fructose-1,6 bisphosphate, for example via a particular isoform of phosphofructokinase.

In addition to plasma samples, metabolites excreted in bodily fluids may also be used as input to isotopomer analysis models to quantify organ specific metabolic fluxes. For example, one technique termed "chemical biopsy" [118] takes advantage of the known biochemistry of xenobiotic conjugation the liver and the subsequent excretion of the conjugation product in urine. This method was first validated by Magnusson et al. [119], who obtained detailed estimates for

TCA cycle fluxes by analyzing the ^{14}C distribution of xenobiotic conjugate phenylacetate-glutamine in urine samples of human volunteers orally administered phenylacetate and infused with [3-^{14}C]lactate. The glutamine component of the conjugate is synthesized from the TCA cycle intermediate α-ketoglutarate via glutamate without rearrangement of carbons, thus providing a direct look at the labeling state of α-ketoglutarate in the liver. Recently, Jones et al. [120] improved on the method by substituting [3-^{14}C]lactate with a stable tracer, [U-^{13}C] propionate, which is quantitatively extracted into the liver from portal circulation.

1.5 Concluding Remarks

This introductory chapter began with a motivation for metabolic engineering analyses in medicine, with particular emphasis on MFA as a promising tool for studying, diagnosing, and identifying therapeutic targets for metabolic disorders. It then gave a survey of basic concepts and techniques commonly used in MFA, followed by examples from the literature highlighting the use of isotopic tracers in studies involving medically relevant systems. In this concluding section, the discussion focuses on defining crucial areas in need of further research. Specifically, MFA in biomedicine could significantly benefit from progress in the following three areas: implementation and integration of MFA models into computer software; development of physiologically relevant tissue and organ experimental systems; and improving sensitivity and throughput of analytical techniques.

In the past, MFA models have been relatively small, including on the order of 10 to 100 equations, either because of limited availability of metabolite measurements or because they focused on specific pathways such as TCA cycle and gluconeogenesis. With the recent progress in analytical techniques and development of mathematical formalism, it has become possible to build larger, more comprehensive models encompassing most of the known reactions in central carbon metabolism as well as reversible reaction steps. As model networks and corresponding equations expand further in size and complexity, the need is growing for software implementations. Ideally, MFA software integrates the various steps, such as model construction tracer selection, equation formulation, flux calculation, consistency check, and sensitivity analysis into one easy-to-use package with a graphical interface. In this way, network models are built and modified rapidly, and data presentation and analysis is simplified. Furthermore, the

investigator can take better advantage of the rapidly growing number of available on-line biochemical databases in searching for novel pathways and validating reaction stoichiometry. Finally, software implementation also affords better experimental design, particularly in choosing tracers and type of measurements. As alluded to earlier, the amount of information that can be obtained from a labeling experiment depends strongly on the input tracer as well as the isotopomer measurements. For example, simulating various scenarios of flux distributions through the pentose phosphate pathway, Follstad and Stephanopoulos [121] found that measuring the isotopic enrichment of the hexose pool (glucose 6-phosphate and fructose 6-phosphate) and erythrose 4-phosphate is more useful than measuring the enrichment of the pentose pool (ribulose 5-phosphate, ribose 5-phosphate, and xylulose 5-phosphate). The authors ascribed this results to the sensitivity of the hexose pool isotopomer distribution pattern to variations in the rates of reversible reactions. Simulations such as these are very valuable in maximizing the informational content of each experiment, and could easily be performed by software implementations of metabolic network models.

Extension of MFA to medically relevant systems could also benefit from development of new or refinement of existing experimental models. These models need to combine controllability and observability with physiological relevance. While fed-batch or chemostat reactors adequately address these needs for suspended microorganism cultures, they are not suitable for anchorage dependent tissue cultures. For some tissue types, such as those in the liver, heart, kidney, and pancreas, there are existing options such as perfused organs and bioreactors, which offer the advantage of flow over traditional dish and plate cultures. However, the physiological relevance of these systems still need to be fully validated. One way to improve relevance is by designing better media, which more closely mimic *in vivo* substrate composition, hormone levels and soluble messenger milieu.

Finally, in order to fully realize the potential of MFA in medicine, techniques are need for sensitive and rapid detection of both metabolites and isotopomers. While traditional enzymatic assays for metabolites are sensitive and specific, they are tedious and time-consuming. Recently, researchers in plant physiology have published several novel chromatographic methods for rapid screening of metabolites in leaf extracts, which could readily be adopted for applications in culture media, bodily fluids, and tissue homogenates. A number of advances have also been made in improving isotopomer detection *in vivo* and *in vitro*. One hindrance to

dynamic ^{13}C NMR for *in vivo* applications has been the poor resolution of multilinear resonances, which are critical sources of information for isotopomer distribution analysis. This problem was at least partially addressed in a series of publications by Sherry et al.[122], who showed that ^{13}C homonuclear decoupling of a five carbon metabolite C3 resonance collapses nine-line C4 and C2 resonances into well-resolved three-line multiplets. The difficulty in obtaining clear *in vivo* NMR spectra can be avoided in certain situations by utilizing methods for noninvasive sampling of tissue metabolites. One such method involving xenobiotic chemicals samples the glutamate pool in the liver, and has already mentioned [119]. Another, involving plasma fraction of very low density lipoprotein (VLDL) has been suggested by Wykes et al. [123]. VLDL is rapidly processed to particles of higher density, apolipoprotein B (apoB) within the liver. VLDL has a very fast turnover rate, so that during the course of a tracer experiment lasting less than 12 hrs, full isotopic equilibrium is reached between the tracer and the hepatic apoB pool. At this point, the isotopic enrichment of amino acids in VLDL directly defines the isotopic enrichment of corresponding metabolites in the liver from which they are derived. Thus, pyruvate, α-ketoglutarate, and oxaloacetate enrichments may be assayed by analyzing apoB bound alanine, glutamate, and aspartate, respectively. A serious limitation to isotopomer detection *in vitro* as well as *in vivo* has been the low abundance of labeled primary metabolites in sample extracts. As mentioned briefly in a previous section, one promising approach to overcoming this obstacle has been to recover labeled amino acids by hydrolyzing protein, which is abundantly present in most cells [83]. The notion of utilizing products of anabolic pathways can be extended to other central carbon metabolites, as most are stored in polymeric compounds such as glycogen, membrane lipids, and nucleic acids. Techniques to isolate and hydrolyze these molecules have been available for some time [83, 124, 125]. For instance, glycerol has been extracted from lipids [126] and ribonucleotides from RNA and DNA [127]. These and aforementioned advances have made possible the collection of a formerly unattainable amount of high-precision isotopomer distribution data.

If continued progress is made in the above defined computational, experimental, and analytical areas, MFA could a powerful tool for noninvasively obtaining quantitative, comprehensive information regarding cell and tissue metabolism. As hinted at throughout this chapter, potential areas of application include: investigation of basic cell and organ physiology, optimization of engineered tissue function, detection and diagnosis of metabolic disorders,

identification of therapeutic targets, evaluation of drug effects on metabolism, finer stratification of disease states, and design of novel treatment strategies for metabolic disorders, including rational nutritional support for critically ill patients and tailored diet regimen for patients suffering from chronic diseases such as diabetes, obesity, and cancer. It is the hope of the author to illustrate the aforementioned ideas with the experiments and analyses presented in the remainder of this dissertation, which deal with the study of injury induced hypermetabolic response in the liver.

1.6 Specific Aims

The overall objective of this thesis was to integrate metabolic engineering principles and tools with cell biology, biochemistry, and physiology concepts and techniques in order to achieve an improved understanding of the mechanisms underlying injury derived metabolic perturbations in an organ central to whole-body regulation of metabolic homeostasis. To this end, the following specific aims were addressed:

1. **to develop and validate an experimental model of injury for the liver**
2. **to delineate the metabolic flux distribution in the liver during the onset of the inflammatory response to injury**
3. **to build diagnostic tools for detecting and grading injury derived metabolic abnormalities**
4. **to identify potential target pathways for therapeutic intervention**

CHAPTER 2. POST-BURN HYPERMETABOLISM IN THE PERFUSED LIVER

2.1 Introduction

Injury elicits dramatic acute and chronic changes in whole body metabolism, which are general with respect to type of insult and correlate with the severity of the injury. As originally described by [128], the metabolic response to injury is biphasic. The early or ebb phase lasts about 24 hours and is characterized by decreased intravascular volume, poor tissue perfusion, low cardiac output and relative hypometabolism where total oxygen consumption is below normal levels [129]. It is followed by a flow phase, where patients exhibit increased resting energy expenditure, hyperglycemia, and net proteolysis of myofibrillar protein in muscle. This hypermetabolic and hypercatabolic state can persist for several weeks and even months [130]. While hypermetabolism is thought to be beneficial for the short term in that it mobilizes host resources in order to aid in wound healing, if persistent, it is associated with the development of cell and organ injury, progressive multiple organ dysfunction syndrome and, eventually, death [131, 132].

In recent years, the liver has been recognized to play an active role in the pathogenesis of hypermetabolism. In addition to generating acute phase proteins early after injury [133], the liver is the major and only site of increased *de novo* glucose and urea synthesis, respectively, during the flow phase [134, 135]. Sustained elevation of liver amino acid transporter activity has been also reported [136], which supports the notion that hypermetabolism associated muscle wasting reflects an increased amino acid demand in the liver. Furthermore, the liver itself undergoes dramatic changes during prolonged hypermetabolism, as there is a decline in ATP and glutathione content [137], accompanied by worsening liver dysfunction which culminates in a fall in glucose synthesis and amino acid oxidation [138]. Unfortunately, the biochemical mechanisms behind the hypermetabolic response to injury remain unclear, and thus far, attempts at modulating this response have been largely unsuccessful.

As a preliminary step toward understanding hypermetabolism in the liver, we previously used an established model of rodent thermal injury [139] in conjunction with an isolated perfused liver model to assess the metabolic adaptations occurring in the liver during hypermetabolism [140]. We found that burn injury increased hepatic urea production, oxygen consumption, and net uptake of gluconeogenic amino acids, but did not significantly affect net glucose output.

That hepatic glucose output was unaltered despite increased uptake of gluconeogenic amino acids seemed incongruous, especially since subsequent ^{13}C isotopomer studies [74, 141] revealed that burn injury increased carboxylation of pyruvate, which is the first step of gluconeogenesis. One explanation for this discrepancy could be substrate cycling between the pathways of gluconeogenesis and glycolysis and a cycle involving breakdown and synthesis of stored triglycerides (TGL), as previously proposed by Wolfe *et. al.* [48]. On the other hand, the presence of futile substrate cycles in non-thermogenic tissue such as the liver is still subject to debate, given the reciprocal regulation of gluconeogenesis and glycolysis [142] and β-oxidation and fatty acid synthesis [143]. Alternatively, the increased amino acid influx could be used for the synthesis of acute phase proteins such as plasma C-reactive protein [144] and fibrinogen [145]. However, other proteins (negative acute-phase proteins) such as albumin [145] and transferrin [144] are produced at depressed rates during the hypermetabolic state. Furthermore, a significant fraction of the amino acids taken up by the liver in the burn condition is deaminated and oxidized rather than incorporated into protein, as evidenced by the large increase in urea production.

In order to elucidate the fate of glucose and amino acids in liver, we used metabolic flux analysis to determine the effect of burn injury on the flux distribution through the major pathways in the liver associated with carbohydrate, fatty acid, and amino acid metabolism. Metabolic flux analysis [146] refers to a methodology whereby intracellular fluxes are calculated using a stoichiometric model for the major intracellular reactions and applying mass balances around intracellular metabolites. This approach allows a large number of metabolite measurements to be used simultaneously in formulating a comprehensive model of metabolism. To date, metabolic flux analysis has been primarily used to study systems relevant to biotechnology and bioprocess engineering [147]. In this study, we formulated a stoichiometric balance model of hepatic intermediary metabolism involving the pathways of gluconeogenesis, pentose phosphate shunt (PPP), amino acid degradation, oxygen consumption, ketone body production, and fatty acid oxidation. These balance equations were applied to metabolite data obtained from perfused rat livers 3 days post burn and previously published by Yamaguchi *et al.*[140] in combination with new data.

2.2 Materials and Methods

2.2.1 Chemicals

Unless otherwise noted, all chemicals were purchased from Sigma Chemical Co. (St. Louis, MO). [1-^{14}C]glucose (54.5 Ci/mmol) was purchased from New England Nuclear Life Science Products (Boston, MA). [6-^{14}C]glucose (56 mCi/mmol) and $NaH^{14}CO_3$ (54 mCi/mmol) were purchased from ICN Biomedicals (Irvine, CA).

2.2.2 Burn injury model

Male Sprague-Dawley rats (Charles River Laboratories, Boston, MA) weighing 150 ~ 200 g were housed in a temperature (25 °C) and light-controlled room (12-hour light-dark cycle). The animals were cared for in accordance with the National Research Council guidelines. Experimental protocols were approved by the Subcommittee on Research Animal Care, Committee on Research, Massachusetts General Hospital. Water and rat chow were provided *ad libitum*. Animals were individually housed and allowed to adjust to their new surroundings for at least 2 days before receiving treatment. On the day of treatment, animals were randomly divided into two groups, burned and sham-burned. Burn and sham-burn procedures were carried out as described previously [140]. Briefly, the burn injury consisted of a full-skin thickness scald-burn of the dorsum, calculated to be ~ 20 % of the rat's total body surface area (TBSA), induced by immersing the designated area in boiling water for 10 seconds. Rats were resuscitated with two intraperitoneal injections of sterile saline solution (1.5 mL/kg/% TBSA), one immediately after burn and one within 8 hours of burn. The mortality rate of this treatment was negligible. Sham-burn animals were treated identically except that they were immersed into a 37 °C water bath.

2.2.3 Liver perfusion

Perfusions for metabolite data collection were performed in a recirculating system as described previously [140] (Figure 2-1). Minor modifications were made for the radioactive tracer experiments. As suggested by Kuehn and Scholz [148], livers were perfused in single-pass mode in order to present a constant fraction of labeled glucose to the liver and prevent reincorporation of labeled bicarbonate.

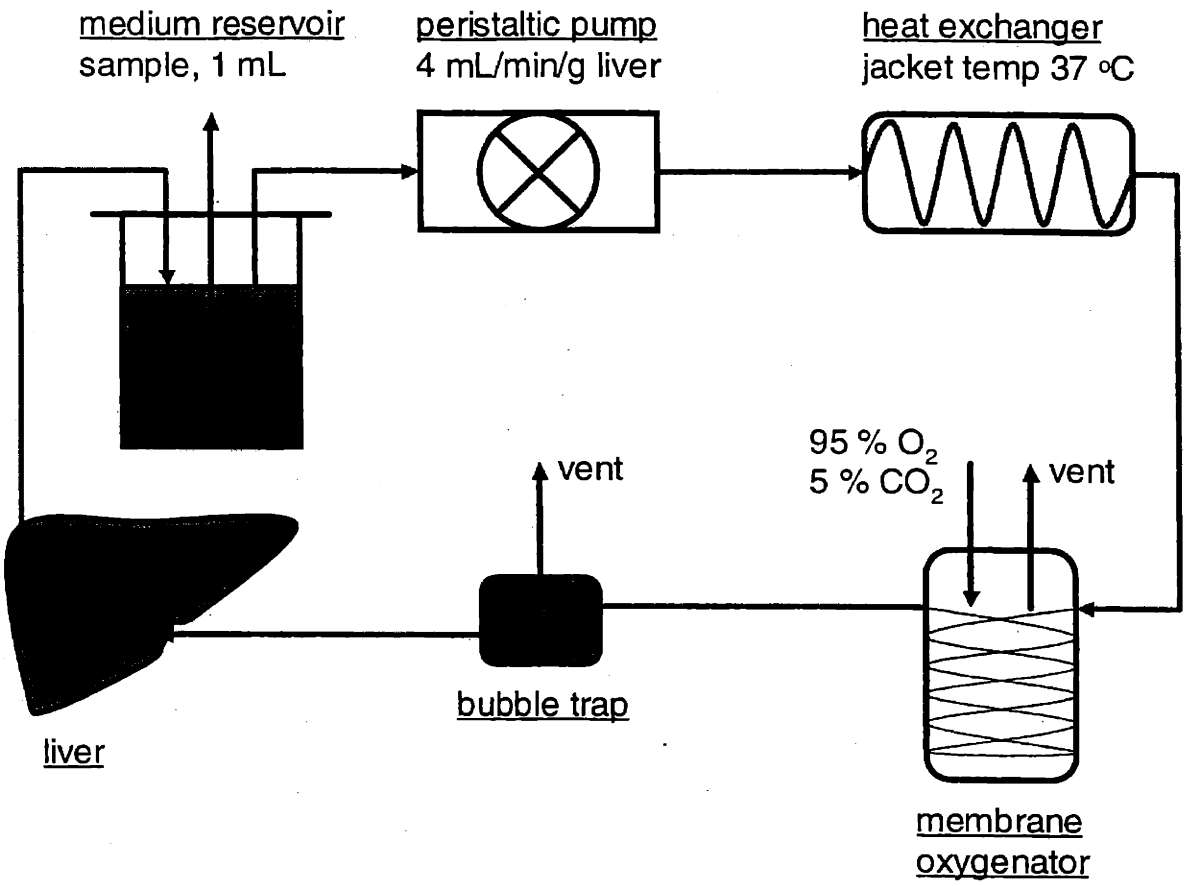

Figure 2-1. Recirculating liver perfusion system

The experimental system described in [140] and used for metabolite data collection in work presented in this chapter and throughout the dissertation is shown for reference. Medium reservoir holds perfusate composed of minimal essential medium (MEM) supplemented with bovine serum albumin (BSA), lactate, pyruvate, and amino acids. The medium substrate concentrations were designed to resemble those in the rat portal vein during the post-absorptive period (see Table 3-1). Perfusion medium was delivered by a peristaltic pump at 4 mL/min/g fresh liver. Medium was warmed to 37°C by a heat exchanger, gassed with artificial atmosphere (95 % O2 / 5 % CO2), and vented, before entering the liver via a catheter cannulated into the portal vein. After emerging from the liver via a catheter placed into the *vena cava*, medium reentered the reservoir. Samples (1 mL) were drawn from the reservoir at timed intervals during the perfusion and later assayed for metabolites.

Clark-type oxygen sensing electrodes in flow-through modules were connected to the perfusion circuit (Lazar Inc., Brea, CA) at the inlet and outlet of the liver for continuous monitoring of oxygen consumption. Perfusion flow rates were maintained at 20 mL/min (2.72 ± 0.07 mL/min/g liver) by a peristaltic pump. The perfusion lasted 60 minutes and was divided into three phases, where time zero is taken to be the moment the portal vein was connected to the perfusion circuit. The first phase (I) lasted 30 minutes during which time the liver was washed of residual blood and allowed to reach a metabolic steady state as determined by monitoring oxygen consumption. During this phase, effluent perfusate was collected at 15, 20, 25, and 30 minutes after the start of perfusion. At the end of phase I, the liver was perfused for 15 minutes with medium containing 0.05 μCi/mL of either labeled D-[1-^{14}C]glucose or D-[6-^{14}C]glucose. During this second phase (II), effluent was collected every 60 seconds. The third phase (III) lasted another 15 minutes during which time the liver was again perfused with unlabeled medium. During phase III, samples were collected at 2 minute intervals. At the end of the perfusion, the whole liver was quickly excised, blotted, weighed, and frozen in liquid nitrogen. Livers were stored at -80 °C and the effluent perfusate samples were refrigerated.

2.2.4 $^{14}CO_2$ measurement

$^{14}CO_2$ was trapped and measured using a modified version of the technique of Gaines *et al.* [149]. 200 μL of sample was added to a 1.5 mL Eppendorf microcentrifuge tube, which was then placed in a 20 mL glass scintillation vial containing 1 mL of 1 N $NaOH_{(aq)}$. The vial was then closed with a self-sealing septum. 400 μL of 6 N $HCl_{(aq)}$ was injected by syringe through the septum into the Eppendorf tube. After 6 hours of incubation at room temperature, the septum was removed, the Eppendorf tube discarded, and 20 mL of scintillation fluid (Ultima Gold, Packard Instrument Co., Meriden, CT) added. The vials were recapped and radioactivity was counted in a Beckman LS 6000 IC scintillation counter (Beckman Instruments, Palo Alto, CA).

2.2.5 Metabolite assays

Amino acids were fluorescently labeled (AccQ·Tag, Waters Corporation., Milford, MA), separated by HPLC (Model 2690, Waters), and quantitated by fluorescence measurement (Model 474, Waters). Glucose, lactate, and urea were measured by commercially available colorimetric enzymatic assay kits (Sigma Diagnostics, Sigma Chemical Co.). Ketone bodies were measured

by a modified version of the Wilson assay [140]. Dissolved oxygen and carbon dioxide were measured with an automated blood gas analyzer (Model 238, Bayer Corporation, Norwood, MA).

2.2.6 Enzyme activity measurements

All enzyme activities were measured in liver crude extracts prepared in the following manner. From each frozen liver, an entire lobe (ca. 1.0 g) was broken off and minced in 10 mL of ice-cold buffer (50 mM potassium phosphate, pH 7.5, containing 1 mM EDTA) using a Potter-Elevehjem tissue grinder (Wheaton, Millville, NJ). This homogenate was diluted 10-fold in the same buffer. The diluted homogenate was centrifuged at 8,500 × g and 4 °C for 10 minutes. The supernatant was collected and kept on ice. Samples not assayed immediately were stored at –80 °C. Glucose-6-phosphate dehydrogenase (G6PDH) and glutathione reductase (GR) activities were measured using commercial kits (Sigma Diagnostics 345-A, Sigma Chemical Co., St. Louis, MO and OXIS International Inc., Portland, OR, respectively).

2.2.7 Calculation of intracellular fluxes

A network model of liver metabolism was constructed based on known stoichiometric relationships between the reactions of intermediary metabolism. The pathways included in the model are: (a) TCA cycle, (b) urea cycle, (c) pentose phosphate pathway (PPP), (d) gluconeogenesis, (e) β-oxidation, (f) amino acid oxidation, and (g) ketone body synthesis. Pathways (a), (b), and (c) are always active, while (d) ~ (g) are active in the fasted state. The following pathways are inhibited by fasting and therefore were not included in the model: (h) glycogen synthesis, (i) fatty acid synthesis, and (j) irreversible, energy requiring steps in *de novo* amino acid biosynthesis. An example of pathway (j) is synthesis of proline from glutamate via glutamate kinase and pyrroline carboxylate reductase. The strictly glycolytic enzymes, hexokinase, phosphofructokinase, and pyruvate kinase, are also assumed to be inhibited. While these enzymes are likely to be expressed to some degree at all times, this assumption was necessary in order to avoid including cycles irresolvable by metabolite balancing. Finally, flux through pyruvate dehydrogenase (PDH) was assumed to be negligible based on the results of a previous study using ^{13}C isotopomer analysis of TCA cycle intermediates showing that flux through PDH accounts for less than 10 % of the net total flux into the acetyl-CoA pool [141]. Table 2-1 lists the stoichiometry and the relevant enzymes of the reactions included in the model.

The calculation of intracellular fluxes follows the procedure described in the previous chapter and by Zupke et al. [150], with minor modifications. Briefly, the stoichiometric coefficients of the reactions in Table 2-1 were collected into a matrix **S**, where element s_{ij} holds the coefficient of metabolite i in reaction j. Table 2-2 lists the metabolites around which balances were written. The balance equations are succinctly written in matrix form:

$$\frac{dx}{dt} = Sv \tag{2-1}$$

where each element x_i of $\boldsymbol{x}$ is the intracellular concentration of metabolite i and element v_j of $\boldsymbol{v}$ is the net flux through reaction j. Assuming the liver was in a metabolic steady state during the perfusion,

$$Sv = 0 \tag{2-2}$$

Equation 2 was rearranged by separating $\boldsymbol{v}$ into measured and unknown components $\boldsymbol{v}_m$ and $\boldsymbol{v}_c$, respectively, and partitioning **S** into corresponding parts S_m and S_u, respectively:

$$Sv = S_m v_m + S_u v_u \tag{2-3}$$

Combining Equations 2-2 and 2-3, we obtained the following:

$$S_c v_c = -S_m v_m \tag{2-4}$$

In the present model, there are 35 linear constraints which could be used to calculate 32 unknown reaction fluxes. Thus, the measurements could be tested for presence of any gross errors by the mass balance method of Wang and Stephanopoulos [51]. The method uses the redundant constraints in conjunction with an error variance-covariance matrix $\boldsymbol{F}$ to calculate a test function (h), which represents the weighted square of the residuals of the constraints. In the present study, measurement errors were assumed to be uncorrelated and $\boldsymbol{F}$ was estimated by a diagonal matrix whose diagonal entries are the animal-to-animal variances associated with each measurement. For normally and randomly distributed errors, h follows the chi-square (χ^2) distribution. The null hypothesis is that the amount of errors present in the measurements is significant with a confidence level of 1 - θ, where θ is a parameter which expresses the tail area probability of a χ^2 distribution. The hypothesis is rejected if $h < \chi^2_{1-\theta}(m)$, where m represents the number of redundant constraints. If $h > \chi^2_{1-\theta}(m)$, it is concluded with (1 - θ) × 100 % level confidence that either gross or systematic error is present in the data. In this case, a systematic approach also outlined in Wang and Stephanopoulos [51] may identify the source(s) of the error(s) and find better estimates for the measurements. The h values computed for the

metabolite measurement sets collected in these studies are shown in the last row of Table 2-3. Comparing the test function (h) values with standard chi-square (χ^2) distribution values at various confidence levels for 3 degrees of freedom, it could not be concluded at 95 % confidence level that any gross errors were present in the measurements. Thus, the quality of this data were deemed to be satisfactory, and the measurements were used without any subsequent adjustments for the calculation of unknown fluxes v_c.

In order to evaluate the uncertainty in the flux estimates, Equation 2-4 was scaled by the variances of the measurements [150]:

$$D_{ij} = \frac{S_{ij}}{\sigma_i}, b_i = \frac{r_i}{\sigma_i}, \boldsymbol{r} = -\boldsymbol{S}_m \boldsymbol{v}_m \tag{2-5}$$

where σ_i^2 is the variance of r_i. This transformation takes into account differences in the uncertainties of the various measurements and is equivalent to solving Equation (2-4) by weighted least squares:

$$\boldsymbol{v}_c = (\boldsymbol{D}^T \boldsymbol{D})^{-1} \boldsymbol{D}^T \boldsymbol{b} \tag{2-6}$$

The matrix $(\boldsymbol{D}^T\boldsymbol{D})^{-1}$ is the variance-covariance matrix of the flux vector $\boldsymbol{v}_c$, and its ith diagonal element holds the variance of v_i. The elements of $\boldsymbol{v}_m$ are measured rates of metabolite uptake or release by the liver (Table 2-3), obtained from previously published data [140] and additional experiments performed in this study. Two measurement vectors $\boldsymbol{v}_m$ were constructed, corresponding to one $\boldsymbol{v}_m$ each for burn and sham-burn conditions. Tests of statistical significance between fluxes were performed by the t-test based on either measured or estimated variances. All other tests of statistical significance were performed using the Excel 97 ANOVA data analysis tool (Microsoft Corp., Redmond, WA).

2.3 Results

In order to determine the effect of burn injury on intracellular fluxes in the perfused liver, rates of change of extracellular metabolites were obtained from Yamaguchi *et al.* [140] and additional measurements performed in this study. These data are shown in Table 2-3. The calculated intracellular fluxes are listed according to their reaction numbers in Table 2-4, where the numbering scheme refers to that in Table 2-1.

Table 2-1. Reaction Stoichiometry of Hepatic Central Carbon Metabolism

Reaction	Enzyme(s)	Stoichiometry
1	glucose-6-Pase	glucose-6-P → glucose + Pi
2	phosphohexose isomerase	fructose-6-P ↔ glucose-6-P
3	fructose-1,6-$p_2$ase	fructose-1,6-P_2 → fructose-6-P + Pi
4	2 steps	2 glyceraldehyde-3-P ↔ fructose-1,6-P_2
5	4 steps	PEP + NADH + ATP ↔ glyceraldehyde-3-P + Pi + NAD^+ + ADP
6	PEPCK	oxaloacetate + GTP ↔ PEP + GDP + CO_2
7	PC	pyruvate + CO_2 + ATP → oxaloacetate + ADP + Pi
8	LDH	lactate + NAD^+ ↔ pyruvate + NADH
9	citrate synthase	oxaloacetate + acetyl-CoA → citrate
10	several, including ICDH	citrate + NAD^+ ↔ α-ketoglutarate + CO_2 + NADH
11	α-ketoglutarate dehydrogenase	α-ketoglutarate + NAD^+ → succinyl-CoA + CO_2 + NADH
12	succinyl-CoA synthetase & SCCDH	succinyl-CoA + Pi + GDP + FAD ↔ fumarate + GTP + $FADH_2$
13	fumarase	fumarate ↔ malate
14	malate dehydrogenase	malate + NAD^+ ↔ oxaloacetate + NADH
15	arginase	ARG → urea + ornithine
16	cabamoyl-P synthetase I & ornithine transcabamylase	ornithine + (CO_2 + NH_4^+ + 2 ATP) ↔ citrulline + 2 ADP + 2 Pi
17	argininosuccinate synthetase & argininosuccinase	citrulline + ASP + ATP → ARG + fumarate + AMP + Ppi
18		ARG uptake
19		NH_4^+ output
20		ornithine output
21		citrulline output
22	ALA aminotransferase & GLU dehydrogenase	ALA + NAD^+ → pyruvate + NH_4^+ + NADH
23		ALA output
24	SER dehydratase	SER → NH_4^+ + pyruvate
25		SER uptake
26	transaminase, 3-mercaptopyruvate sulfurtransferase, GLU dehydrogenase	CYS + NAD^+ + SO_3^{2-} → pyruvate + thiosulfate + NH_4^+ + NADH
27		CYS output
28	SER hydroxymethyl transferase	THR + NAD^+ → GLY + acetyl-CoA + NADH
29	GLY synthase	GLY + NAD^+ + H_4folate ↔ N^5,N^{10}-CH_2-H_4folate + NADH + CO_2 + NH_4^+
30		GLY uptake
31	7 steps	VAL + α-ketoglutarate + 3 NAD^+ + FAD → GLU + 3 NADH + $FADH_2$ + 2 CO_2 + propionyl-CoA
32	6 steps	ILE + α-ketoglutarate + 2 NAD^+ + FAD → GLU + 2 NADH + $FADH_2$ + CO_2 + propionyl-CoA + acetyl-CoA
33	6 steps	LEU + α-ketoglutarate + NAD^+ + FAD + ATP → GLU +

		NADH + $FADH_2$ + ADP + Pi + acetoacetate + acetyl-CoA
34	3 steps	propionyl-CoA + ATP + CO_2 → succinyl-CoA + AMP +Ppi
35	8 steps	LYS + 2 α-ketoglutarate + NADPH + 4 NAD^+ + FAD → 2 GLU + $NADP^+$ + 4 NADH + 2 CO_2 + $FADH_2$ + acetoacetyl-CoA
36	phenylALA hydroxylase	PHE + H_4biopterin + O_2 → H_2biopterin + TYR
37	5 steps	TYR + NAD^+ + 2 O_2 → NH_4^+ + CO_2 + fumarate + acetoacetate + NADH
38		TYR output
39	GLU dehydrogenase	GLU + NAD^+ ↔ α-ketoglutarate + NH_4^+ + NADH
40		GLU output
41	glutaminase	GLN → GLU + NH_4^+
42	3 steps	PRO + 0.5 O_2 + 0.5 NAD^+ + 0.5 $NADP^+$ → GLU + 0.5 NADH + 0.5 NADPH
43	4 steps	HIS + H_4folate → NH_4^+ + N^5-formiminoH_4folate + GLU
44	5 steps	MET + ATP + SER + NAD^+ → PPi + Pi + adenosine + CYS + NADH + CO_2 + propionyl-CoA
45	ASP aminotransferase	ASP + NAD^+ ↔ oxaloacetate + NH_4^+ + NADH
46		ASP uptake
47	asparaginase	ASN → ASP + NH_4^+
48	7 × 4 steps	palmitate + 7 ATP + 7 FAD + 7 NAD^+ → 8 acetyl-CoA + 7 $FADH_2$ + 7 NADH + 7 AMP + 7 PPi
49	thiolase	2 acetyl-CoA ↔ acetoacetyl-CoA
50	2 steps	acetoacetyl-CoA → acetoacetate
51		acetoacetate production
52	β-hydroxybutyrate dehydrogenase	acetoacetate + NADH ↔ β-OH-butyrate + NAD^+
53		NADH + 0.5 O_2 → NAD^+
54		$FADH_2$ + 0.5 O_2 → FAD
55		O_2 uptake
56	G6PDH + 3 steps	glucose-6-P + 2 $NADP^+$ → ribulose-5-P + CO_2 + 2 NADPH
57	phosphopentose isomerase	ribulose-5-P ↔ ribose-5-P
58	epimerase	ribulose-5-P ↔ xylulose-5-P
59	transketolase & transaldolase	ribose-5-P + xylulose-5-P ↔ erythrose-4-P + fructose-6-P
60	transketolase	erythrose-4-P + xylulose-5-P ↔ fructose-6-P + glyceraldehyde-3-P
61		CO_2 output

Table 2-2. Key Intermediates in Hepatic Central Carbon Metabolism

No.	Metabolite
1	glucose-6-P
2	fructose-6-P
3	fructose-1,6-P_2
4	glyceraldehyde-3-P
5	PEP
6	pyruvate
7	oxaloacetate
8	NADH
9	acetyl-CoA
10	citrate
11	α-ketoglutarate
12	succinyl-CoA
13	fumarate
14	$FADH_2$
15	malate
16	arginine
17	ornithine
18	NH_4^+
19	citrulline
20	aspartate
21	alanine
22	glutamate
23	serine
24	cysteine
25	glycine
26	propionyl-CoA
27	acetoacetate
28	acetoacetyl-CoA
29	O_2
30	tyrosine
31	ribulose-5-P
32	ribose-5-P
33	xylulose-5-P
34	erythrose-4-P
35	CO_2

Table 2-3. Measured Metabolite Exchange Rates

Rxn. No.	Metabolite	Net Uptake Rate, μmol/g liver/hr	
		Burn	Sham-burn
1	Glucose	-8.4 ± 1.2	-7.8 ± 1.2
8	Lactate	18.5 ± 2.8	21.1 ± 3.2
15	Urea	-18.5 ± 0.4*	-12.2 ± 0.6
18	Arginine	2.3 ± 0.6	2.3 ± 0.4
19	NH_4^+	-0.5 ± 0.1*	-0.3 ± 0.06
20	ornithine	-0.9 ± 0.2*	-2.6 ± 0.7
21	citrulline	0.0 ± 0.0*	0.2 ± 0.1
23	Alanine	0.3 ± 0.6*	-4.2 ± 2.4
25	Serine	2.5 ± 0.7	3.6 ± 1.1
27	Cysteine	-0.1 ± 0.01*	-0.2 ± 0.03
28	threonine	0.2 ± 0.04	-0.1 ± 0.4
30	Glycine	1.2 ± 0.2*	-0.3 ± 0.2
31	Valine	-0.3 ± 0.04	-0.3 ± 0.1
32	isoleucine	-0.2 ± 0.03*	-0.1 ± 0.03
33	Leucine	-0.4 ± 0.1*	-0.2 ± 0.04
35	Lysine	-0.05 ± 0.01*	0.4 ± 0.09
36	phenylalanine	0.5 ± 0.1*	0.3 ± 0.02
38	tryrosine	-0.1 ± 0.04	-0.1 ± 0.02
40	glutamate	-2.8 ± 0.3*	-4.8 ± 1.3*
41	glutamine	21.3 ± 4.2*	14.0 ± 2.8*
42	Proline	0.9 ± 0.2	1.3 ± 0.3
43	histidine	0.7 ± 0.1*	1.2 ± 0.2
44	methionine	0.2 ± 0.03*	0.1 ± 0.02
46	aspartate	0.2 ± 0.1	0.02 ± 0.1
47	asparagine	8.4 ± 1.1*	4.4 ± 0.3
51	acetoacetate	-6.8 ± 2.1	-3.5 ± 0.4
52	3-OH-butyrate	-6.2 ± 1.9	-2.5 ± 0.3
55	O_2	193.8 ± 10.2*	72.6 ± 1.8*
61	CO_2	112.9 ± 30.9*	23.1 ± 11.9*

Metabolite measurements corresponding to reactions 8, 19, 35, 40, 41, 43, 44, 48, and 61 were performed in this study. All other measurements were obtained from Yamaguchi et al. [140]. Values are reported as mean ± SE. Number of livers per group were 3 in this study and 7 in Yamaguchi et al [140]. *Significantly different from sham burn group ($p < 0.05$) as analyzed by *t*-test.

In Table 2-4, a negative value indicates that the calculated flux is opposite to the assumed direction. In general, the calculated fluxes were consistent with the assumed directions, with the exception of reactions 22, 26, 29, and 45 for the sham burn group and reaction 45 for the burn group. These reactions are reversible and are catalyzed by aminotransferases; the negative flux values indicate that the reactions proceed in the direction of amino acid formation from the corresponding ketoacids.

In our model, the number of unknown fluxes to be estimated was 32 and the number of linearly independent stoichiometric constraint equations was 35. Therefore, there were three redundant equations with which we could test the statistical consistency of each measurement vector v_m. The value of the chi-square (χ^2) distribution function with three degrees of freedom and 95 % tail area probability, or $\chi^2_{0.05}(3)$, is 7.82. The test function (h) values were 6.03 and 5.20, respectively, for the burn and sham-burn v_m. Since $h < \chi^2_{0.05}(3)$ in both cases, the measurements were considered consistent with the assumed biochemistry. Consequently, all of the measurements shown in Table 2-3 were included in our flux estimation. In both groups, the relative errors estimated for the calculated fluxes were generally similar to the relative errors associated with the measurements. Comparing mean flux values, statistically significant differences were found for gluconeogenesis (reactions 2 ~ 6), the TCA cycle (9 ~ 14), urea cycle (16 and 17), transamination of alanine, cysteine, glycine, tyrosine, and aspartate (22, 26, 29, 37, and 45), β-oxidation (48), electron transport (53 and 54), and the PPP (56 ~ 60).

These and other key fluxes are shown on a simplified graph in Figure 2-2, where amino acid degradation pathways have been grouped according to their points of entry into the TCA cycle and gluconeogenesis. The important metabolites around which there is a significant change in flux distribution are discussed below. The flux of amino acids away from pyruvate in the sham-burn condition was reversed by burn injury, resulting in a net influx of amino acid derived 3-carbon moieties into the pyruvate pool. The oxidation of lactate to pyruvate was not significantly altered by burn injury while the net carboxylation of pyruvate to oxaloacetate was increased significantly from 10.1 to 23.1 μmol/hr/g liver. Aspartate transamination, the other major route of amino acid entry into the oxaloacetate pool, proceed in the direction of aspartate formation in both burn and sham-burn conditions, with burn injury increasing this flux from 5.3 to 9.4 μmol/hr/g liver.

Table 2-4. Calculated Intracellular Fluxes

Rxn. No.	Net Flux, μmol/hr/g liver					
	Burn			Sham-burn		
2	57.3	±	12.8*	12.6	±	8.3
3	25.0	±	4.1*	10.3	±	2.7
4	25.0	±	4.1*	10.3	±	2.7
5	33.9	±	4.0*	19.5	±	2.9
6	33.9	±	4.0*	19.5	±	2.9
7	19.2	±	2.8*	8.7	±	3.2
9	54.6	±	4.6*	17.1	±	1.6
10	54.6	±	4.6*	17.1	±	1.6
11	60.6	±	4.2*	23.0	±	1.4
12	61.3	±	4.2*	23.5	±	1.4
13	78.6	±	4.2*	33.3	±	1.4
14	78.6	±	4.2*	33.3	±	1.4
16	16.9	±	0.1*	9.7	±	0.1
17	16.9	±	0.1*	9.6	±	0.1
22	0.1	±	0.6*	-9.3	±	2.1
24	2.0	±	0.7	2.4	±	1.0
26	0.1	±	0.0*	-0.1	±	0.0
29	1.4	±	0.2*	-0.6	±	0.6
34	0.7	±	0.1	0.5	±	0.1
37	0.4	±	0.1*	0.2	±	0.0
39	6.8	±	3.2	7.4	±	2.0
45	-9.4	±	1.2*	-5.3	±	0.4
48	10.0	±	0.8*	3.4	±	0.2
49	13.2	±	3.9	5.3	±	0.7
50	13.2	±	3.9	5.7	±	0.7
53	244.3	±	13.5*	93.4	±	2.8
54	132.4	±	6.9*	48.6	±	2.0
56	48.5	±	13.3*	3.5	±	8.6
57	16.2	±	4.4*	1.2	±	2.9
58	32.3	±	8.9*	2.3	±	5.8
59	16.2	±	4.4*	1.2	±	2.9
60	16.2	±	4.4*	1.2	±	2.9

Data shown are fluxes calculated by Equation 2-6 ± SE. Errors were estimated as described in **Materials and Methods**. *Significantly different from sham burn group ($p < 0.05$) as analyzed by *t*-test using the estimated deviations.

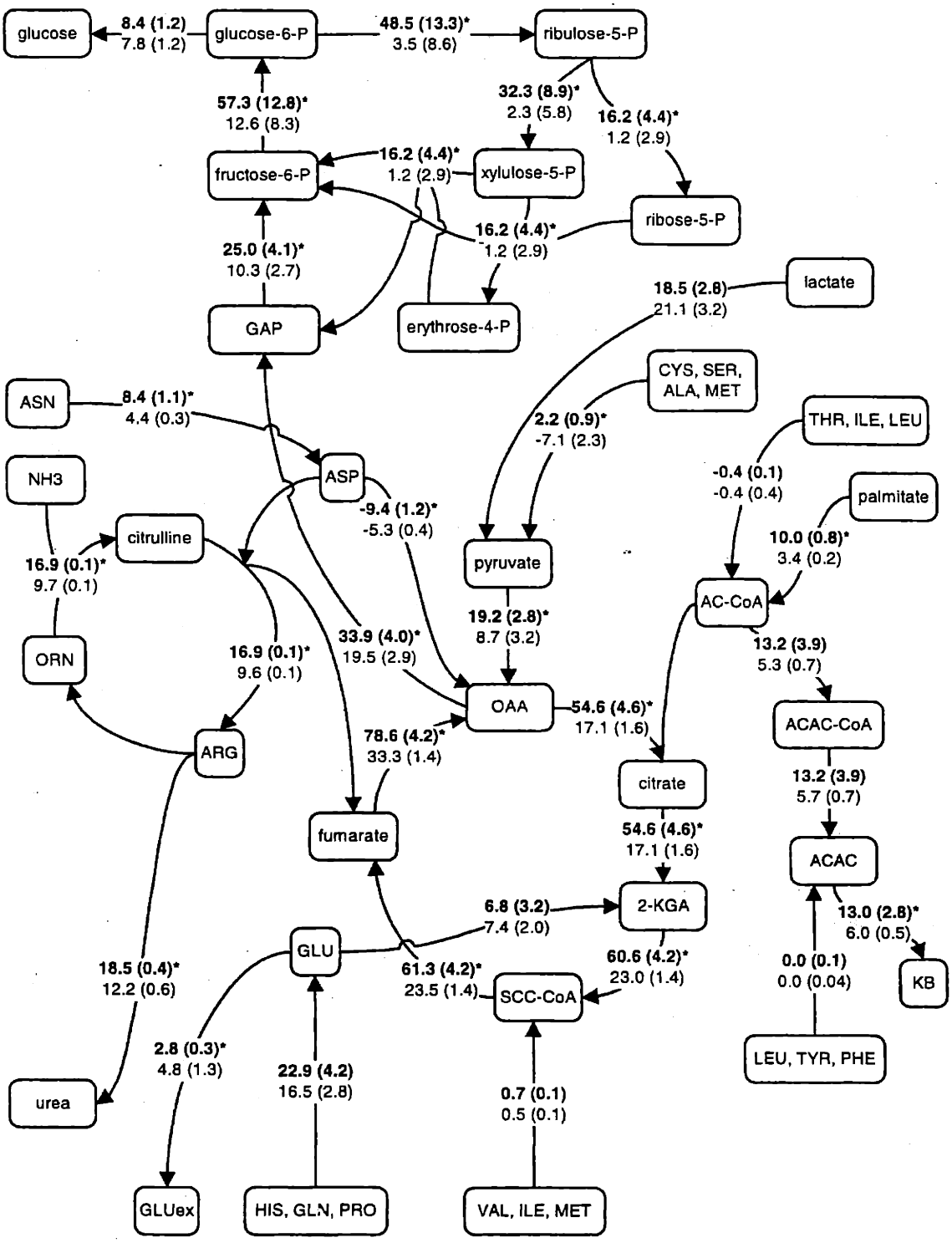

Figure 2-2. Effect of burn injury on hepatic fluxes.
Selected fluxes calculated from averaged measurements of 7 independent perfusions are shown on a simplified network graph.

Figure 2-2. legend continued.

For clarity, some non-branching pathways are combined. Arrows indicate assumed direction of reaction. Some metabolite names have been abbreviated: G3P, glyceraldehyde-3-phosphate, OAA, oxaloacetate; 2-KGA, α-ketoglutarate; SCC-CoA, succinyl-Coenzyme A; H4F, N^5,N^{10}-methylene-tetrahydrofolate; Ac-CoA, acetyl-CoA; AcAc-CoA. acetoacetyl-CoA; ACAC, acetoacetate; KB, ketone bodies (acetoacetate + β-hydroxybutyrate); PROP-CoA, propinoyl-CoA, ORN, ornithine. Amino acids have been abbreviated using the standard three letter convention. Extracellular metabolites which are transported across the cell membrane and feed into branch points in the network are denoted by the subscript *ex*. Amino acid degradation pathways are grouped according to the points of entry into the TCA cycle, gluconeogenesis, or ketone body synthesis. Reaction numbers refer to those listed in Table 1. Flux values for the burn condition are shown in bold, SE in parentheses. *Significantly different from sham burn group ($p < 0.05$) as analyzed by *t*-test.

Aspartate, also formed by transamination of asparagine, is an intermediate of the urea cycle which reacts with citrulline to form arginine and fumarate via two successive steps catalyzed by argininosuccinate synthetase and argininosuccinase (reaction 17). Fumarate, an intermediate of the TCA cycle, is converted to oxaloacetate by fumarase and malate dehydrogenase (reactions 13 and 14). These urea and TCA cycle fluxes were increased significantly by burn injury from 9.6 and 33.3 to 16.9 and 78.6 μmol/hr/g liver, respectively. Consequently, there was a net increase in total flux into oxaloacetate in the burn condition, which is reflected in an elevated PEPCK flux (reaction 6).

Contributions to TCA cycle intermediates from other gluconeogenic amino acids were essentially unaffected by injury, despite the significantly higher uptake of glutamine, histidine, and methionine. There was, however, a 1.9-fold increase in fatty acid oxidation to acetyl-CoA in the burn condition, which paralleled the increase in the TCA cycle fluxes by burn injury. Finally, the largest fractional changes were estimated for the PPP fluxes (reactions 56 ~ 60). Interestingly, the increase in the PPP flux in the burn condition was such that glucose output remains nearly constant despite the increased flux to G6P. Thus, a greater fraction of flux from gluconeogenic substrates to the hexose-6-phosphate pool (F6P and G6P) was diverted into the PPP in the burn condition. The data show that 85 % of the phosphohexose isomerase flux (reaction 2) entered the PPP in the burn compared to 28 % in the sham-burn condition. Moreover, the incremental uptake in gluconeogenic amino acids (8.9 μmol/hr/g liver) induced by burn injury accounted for 80 % of the incremental carbon flux delivered to the triose phosphate pool (14.4 μmol/hr/g liver).

In order to confirm that the PPP is differentially activated by burn injury, we independently estimated the flux through this pathway by measuring the conversion rate of exogenously added [1-^{14}C]glucose into $^{14}CO_2$. In the liver, glucose is taken up and rapidly phosphorylated to G6P by glucokinase. As an initial step of the PPP, G6P is converted to 6-P-gluconate, which is then irreversibly decarboxylated by 6-P-gluconate dehydrogenase at the C-1 position to produce CO_2. Therefore, at steady state, the rate of [1-^{14}C]glucose conversion into $^{14}CO_2$ is proportional to the PPP flux. We detected significantly higher amounts of $^{14}CO_2$ in the effluent of the burn compared to the sham-burn livers ($p < 0.05$, ANOVA) (Figure 2-3).

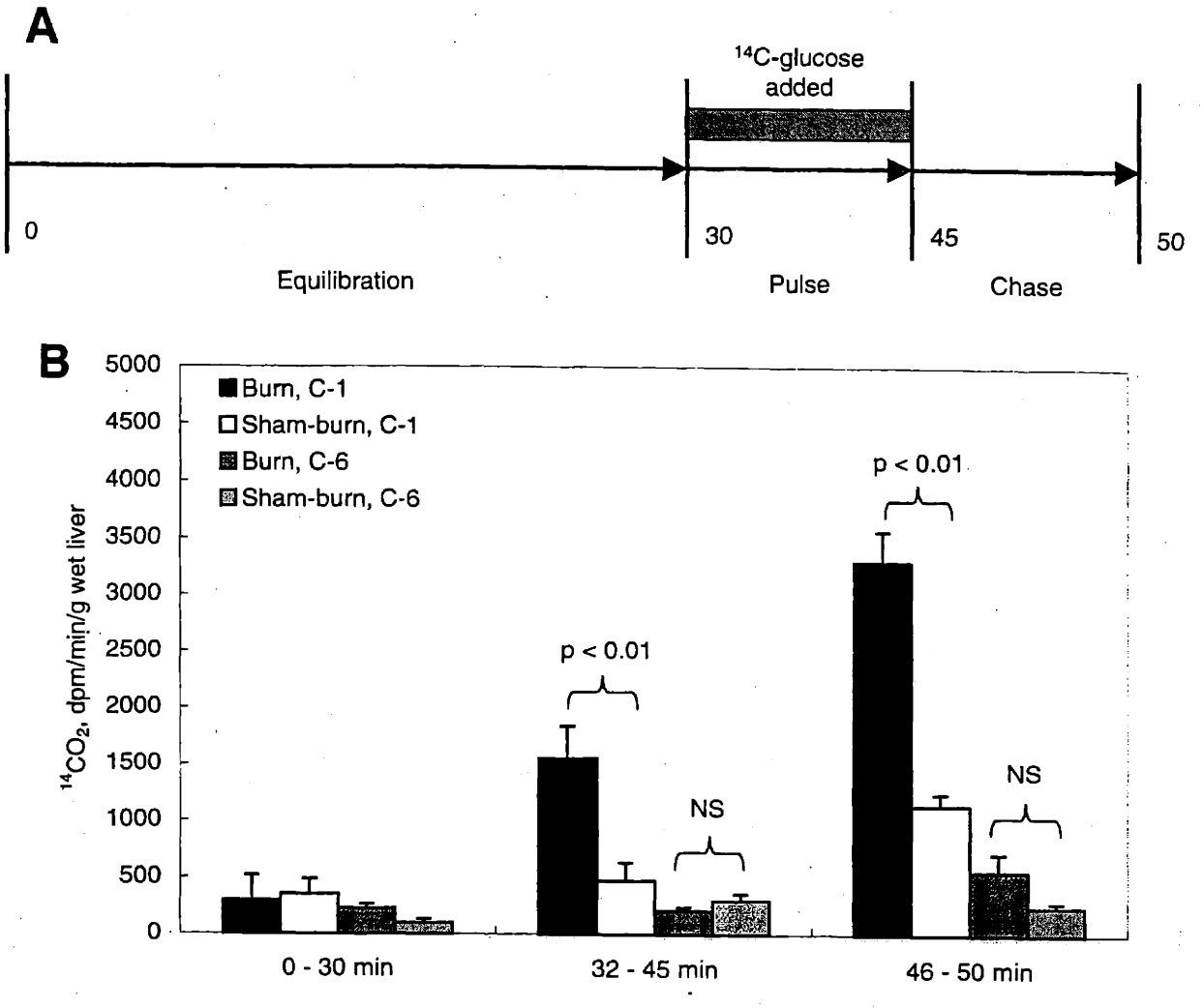

Figure 2-3. $^{14}CO_2$ evolution from [^{14}C]glucose in perfusion effluent.
Schematic of the experiment (A): 0 - 30 minutes: initial equilibration period; 30 – 45 minutes: labeled glucose infusion period; 45 – 50 minutes: chase period. After 50 minutes, $^{14}CO_2$ activity in the effluent began to decrease. $^{14}CO_2$ collected in the effluent. C-1 refers to [1-^{14}C]glucose and C-6 to [6-^{14}C]glucose. Each data point in (B) represents the average of three liver perfusion experiments ± SE. NS: not significant.

In the control experiment, when [6-^{14}C]glucose was used, radioactivity measurements of evolved CO_2 did not produce readings above background in neither the burn nor the sham-burn condition. Unlike [1-^{14}C]glucose, [6-^{14}C]glucose generates $^{14}CO_2$ mainly via glycolysis to [1-^{14}C]pyruvate, followed by decarboxylation by PDH, processes which are presumably inhibited in the fasted state.

Since G6PDH catalyzes the rate-controlling step in the PPP, we measured G6PDH activities in homogenized liver samples. G6PDH activity increased by 45 % in response to burn injury (Figure 2-4). G6PDH activity is also regulated by the ratio of free cytosolic [NADPH] to [$NADP^+$], NADPH being a potent inhibitor of G6PDH [151]. We measured the activity of the GR, the most significant consumer of cytosolic NADPH [152]. Burn injury increased hepatic GR by 29 % (ANOVA, $p < 0.05$) (Figure 2-4).

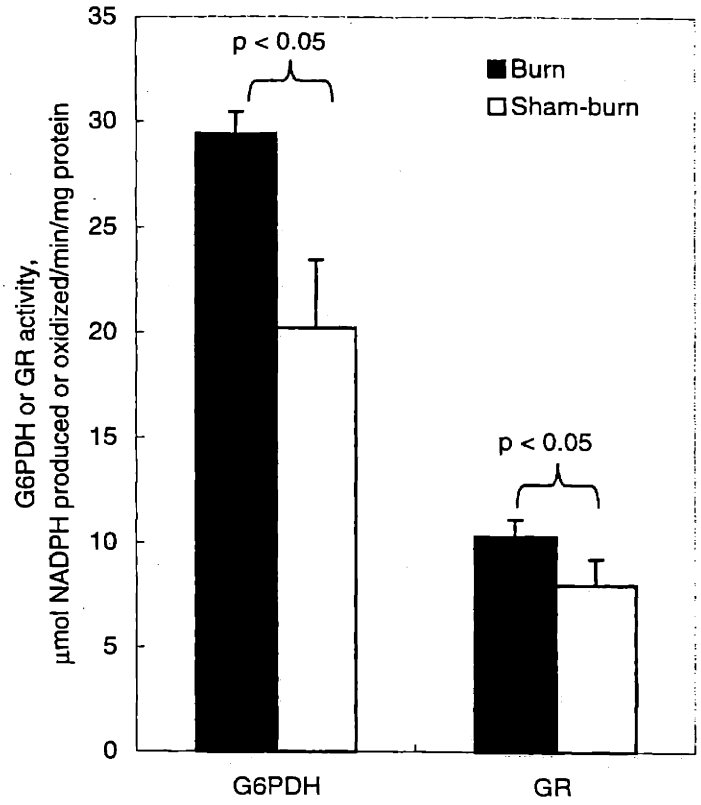

Figure 2-4. Liver glucose-6-phosphate dehydrogenase and glutathione reductase activities. G6PDH and GR activities were measured in crude extracts prepared from livers perfused 3 days after sham-burn or burn treatment. Data shown are the average of 3 livers ± SE. Tests of statistical significance were performed by ANOVA, with $p < 0.05$ considered significantly different.

2.4 Discussion

In this chapter, we investigated the metabolic adaptations of liver as part of the hypermetabolic response to injury. Major hurdles in understanding the role of the liver in the onset and maintenance of hypermetabolism include (1) the difficulty in isolating changes intrinsic to the liver from confounding systemic changes and (2) the complexity of metabolic changes associated with hypermetabolism. We addressed these shortcomings through the use of an isolated perfused liver model and a stoichiometric balance model which takes into account the interdependence between pathways through common intermediates and co-factors. The latter, which included all of the major pathways for carbohydrate, amino acid, and fatty acid catabolism, was used in conjunction with previously published data [140] and metabolite measurements obtained in this study to estimate intracellular fluxes. We found that several pathways were significantly activated by burn injury, including mitochondrial electron transport, the TCA and urea cycles, transamination of gluconeogenic amino acids to pyruvate, and the PPP. The increase in flux through the PPP was confirmed by ^{14}C tracer experiments and was correlated with increases in the activities of G6PDH and GR, both of which may contribute to increasing flux through PPP.

Our model system exhibited many of the clinical features associated with hypermetabolism, including elevated urea production, uptake of amino acids, and consumption of oxygen, although increased output of glucose was not observed. The latter finding contrasts with the results of *in vivo* isotopic tracer studies, where endogenous glucose production was found to be significantly elevated in hypermetabolic burn patients [48]. This discrepancy suggests that the observed elevation in gluconeogenesis in human studies is probably regulated by factors outside the liver. These factors may include the increased delivery of gluconeogenesis precursors from other tissues/organs, particularly skeletal muscle [153, 154], or the immediate effect of various stress hormones and cytokines in circulation [129]. These circulating factors were not added to our perfusate, as we were interested in the adaptations intrinsic to the liver. The plasma concentrations of glucagon and corticosterone, known stimulators of gluconeogenesis *in vivo*, are significantly elevated during systemic inflammation [155], and it is likely that these soluble mediators play a significant role in determining glucose output from the perfused liver as well. On the other hand, the uptake of gluconeogenic amino acids was

increased by burn injury even in the absence of these hormones, suggesting that not all of the enhanced amino acid uptake is to increase glucose output.

Metabolic flux analysis, which balances the major input and output metabolites according to well-known stoichiometric constraints, was able to systematically identify pathway fluxes which were activated by burn injury. While the biochemistry of hepatic central carbon metabolism is well characterized, due to the complexity and the large number of reactions present in the liver, some judgment was involved in choosing which pathways to include in the stoichiometric model. Most of the assumptions regarding the choice of reactions relied on accepted knowledge of liver biochemistry. *De novo* protein synthesis in the perfused liver was neglected due to the difficulty in quantitatively measuring this parameter. The validity of this assumption was tested by drawing a nitrogen (N) balance around the liver, which accounted for N in amino acids, urea, and ammonia (Table 2-5).

In both burn and sham-burn conditions, the majority of N taken up by the liver was released into the medium in the form of urea, amino acids, and ammonia. The remainder is likely to be primarily incorporated into proteins, as nucleotide synthesis is not expected to contribute significantly to the nitrogen balance since the livers were not regenerating. The total amount of N not accounted for by small metabolites included in the model was ~ 15 μmol/hr/g liver (29% of total N uptake) in the sham-burned rat liver. In normal rat liver, albumin and fibrinogen secretion together account for 43 % of the total hepatic protein production [156, 157] with rates of 0.74 mg/hr/g liver and 0.06 mg/hr/g liver, respectively [158-160]. Assuming a N content of 16 % by weight, this corresponds to 9 - 10 μmol N/hr/g liver, or about 2/3 of the predicted N for protein synthesis. Based on the N balance, N flow into protein synthesis is doubled in the burn case, corresponding to 45 % of the total N uptake. Thus protein synthesis is a significant nitrogen sink, which may impact on the calculated fluxes. In order to estimate the effect of protein synthesis on the calculated fluxes, the metabolite balance model was recast by including an equation for amino acid incorporation into protein, where the stoichiometry was determined by using albumin as a "model" protein (see Table 6A for amino acid composition of albumin). Based on the N content of albumin and the N balance, protein output rates were set to 0.02 and 0.04 μmol/hr/g liver for the sham-burn and burn livers, respectively.

Table 2-5. Nitrogen Balance in the Perfused Liver

Metabolite	N / Metabolite	N Uptake, μmol/hr/g liver	
		Burn	Sham-burn
Urea	2	-37.0 ± 0.8	-24.4 ± 1.2
Arginine	3	6.9 ± 1.8	6.9 ± 1.2
NH_4^+	1	-0.5 ± 0.1	-0.3 ± 0.1
Ornithine	1	-0.9 ± 0.2	-2.6 ± 0.7
Citrulline	2	0.0 ± 0.0	-0.4 ± 0.2
Alanine	1	0.3 ± 0.6	-4.2 ± 2.4
Serine	1	2.5 ± 0.7	3.6 ± 1.1
cysteine	1	-0.1 ± 0.0	-0.2 ± 0.0
threonine	1	0.2 ± 0.0	-0.1 ± 0.4
glycine	1	1.2 ± 0.2	-0.3 ± 0.2
valine	1	-0.3 ± 0.0	-0.3 ± 0.1
isoleucine	1	-0.2 ± 0.0	-0.1 ± 0.0
leucine	1	-0.4 ± 0.1	-0.2 ± 0.0
lysine	2	-0.1 ± 0.0	0.8 ± 0.2
phenylalanine	1	0.5 ± 0.1	0.3 ± 0.0
tryrosine	1	-0.1 ± 0.0	-0.1 ± 0.0
glutamate	1	-2.8 ± 0.3	-4.8 ± 1.3
glutamine	2	42.6 ± 8.4	28.0 ± 5.6
proline	1	0.9 ± 0.2	1.3 ± 0.3
histidine	3	2.1 ± 0.3	3.6 ± 0.6
methionine	1	0.2 ± 0.0	0.1 ± 0.0
aspartate	1	0.2 ± 0.1	0.0 ± 0.1
asparagine	2	16.8 ± 2.2	8.8 ± 0.6
	Total	32.0 ± 4.3*	15.4 ± 4.1

Data shown are measured rates of uptake of nitrogen (N) containing metabolites multiplied by corresponding numbers of N. *Significantly different from sham burn group ($p < 0.05$) as analyzed by *t*-test.

As shown in Table 6B, the adjustment resulting from the inclusion of protein synthesis mainly attenuated the estimated differences in flux through gluconeogenesis and the PPP between the burn and sham-burn livers. For example, the adjusted fractional increase in the PPP flux in the burn was 6.6, down from 13.0 in the original calculation, presumably because peptide synthesis demanded amino acid carbon moieties away from gluconeogenesis at greater rates in the burn than in the sham-burn livers. On the other hand, albumin has a relatively high frequency of alanine residues, which also was found to be a major gluconeogenic substrate in this study, and thus the degree of attenuation in PPP activation predicted by the protein synthesis adjustment is likely to be less with a more realistic protein amino acid composition. Thus, while adding a reaction for protein synthesis could improve the material balance model, this would require that the residue compositions of the various proteins secreted by the liver be known.

It is a well-established limitation of metabolite balancing that when the number of branching points in the metabolic network becomes large, as is the case in the present model, redundant or excess constraints are needed to establish reliability [45]. This is especially important when choices have to be made regarding the reactions to be included in the model, either because the biological system has not yet been fully characterized or the stoichiometry is to complex and simplifying assumptions are necessary in order to avoid singularities such as futile cycles. Thus, while application of metabolite balancing to simpler systems such as *E. coli* is straightforward given a sufficient number of measurements, more complex eukaryotic systems require additional assumptions regarding the structure of the metabolic network. For example, the liver expresses enzymes for both gluconeogenesis and glycolysis, and selection of gluconeogenesis over glycolysis was based on physiological considerations. Typically, additional constraints arise from cofactor (e.g. NADH, CoA-SH) and energy balances or experimental data obtained by isotopic tracer studies [124], where tracer experiments are most useful when assumptions regarding the biochemistry need to be checked, since cofactor and energy balances still rely on the validity of the assumed structure of the metabolic network

Table 2-6A. Rat Albumin Amino Acid Composition

Amino acid	Frequency	Number of N / residue
Ala	61	61
Arg	24	72
Asn	20	40
Asp	32	32
Cys	35	35
Gln	25	50
Glu	57	57
Gly	17	17
His	25	75
Ile	13	13
Leu	56	56
Lys	53	106
Met	6	6
Phe	26	26
Pro	30	30
Ser	24	24
Thr	33	33
Trp	1	2
Tyr	21	21
Val	35	35
Total	584	791

Source: GenBank accession number *ABRTS;* PID *g72101*

Table 2-6B. Protein Output Adjusted Fluxes

Rxn. No.	Net Flux, µmol/hr/g liver					
	Burn			Sham-burn		
2	52.6	±	9.8	15.1	±	8.1
3	23.4	±	2.9	11.2	±	2.6
4	23.4	±	2.9	11.2	±	2.6
5	32.3	±	2.7	20.5	±	2.7
6	32.3	±	2.7	20.5	±	2.7
7	15.0	±	2.8	10.7	±	3.3
9	54.1	±	4.2	18.1	±	1.3
10	54.1	±	4.2	18.1	±	1.3
11	68.8	±	4.2	26.7	±	1.2
12	66.4	±	4.2	25.3	±	1.2
13	82.3	±	4.2	34.3	±	1.2
14	82.3	±	4.2	34.3	±	1.2
16	17.4	±	0.1	9.8	±	0.1
17	17.4	±	0.1	9.7	±	0.1
22	-2.2	±	0.6	-6.4	±	2.2
24	1.5	±	0.7	2.9	±	1.1
26	-1.5	±	0.0	-0.9	±	0.0
29	-0.6	±	0.2	-1.4	±	0.4
34	-2.5	±	0.0	-1.4	±	0.1
37	-1.5	±	0.1	-0.7	±	0.0
39	5.3	±	1.2	4.6	±	1.5
45	-10.9	±	1.1	-6.4	±	0.3
48	12.4	±	0.8	4.8	±	0.2
49	20.4	±	4.0	8.8	±	0.7
50	18.1	±	4.0	8.2	±	0.7
53	241.4	±	13.7	91.8	±	2.8
54	146.0	±	7.0	55.4	±	1.8
56	43.7	±	10.5	5.8	±	8.5
57	14.6	±	3.5	1.9	±	2.8
58	29.2	±	7.0	3.9	±	5.7
59	14.6	±	3.5	1.9	±	2.8
60	14.6	±	3.5	1.9	±	2.8

Fluxes were calculated as described in Table 2-4 legend, with an additional equation describing the incorporation of amino acids into protein.

. In the present study, there were three equality constraints in excess of the number required to uniquely determine the system, two of which stemmed from co-factor balances around NADH and $FADH_2$. Thus, we attempted to validate our flux estimates using experimental means, at least for the PPP. While the results of the radioactive tracer experiments qualitatively corroborated the findings of metabolite balancing, the degree of activation estimated by the latter was ~ 6.5 times greater than the former. In light of the previous discussion regarding the N balance, it is possible that this discrepancy is due to over-estimation by metabolite balancing, although it is difficult to determine for certain, as the tracer method estimated only relative changes in the PPP flux. In order to obtain absolute fluxes from the $^{14}CO_2$ data, the fractional enrichment of the intracellular G6P pool has to be known, which we were not able to measure at the time of this study.

There was good quantitative agreement between the sham-burn PPP flux (3.5 μmol/hr/g liver) and values reported in the literature for similar conditions. In perfused livers from 24-hr fasted rats, Brigelius [161] estimated substrate flux through the PPP to be 2.16 μmol/hr/g liver, which increased to 3.36 μmol/hr/g liver upon addition of the oxidant *t*-butyl-hydroperoxide. In a similar system, Kuehn and Scholz [148] found the PPP flux to increase with perfusate glucose concentration from 1.68 to 7.26 μmol/hr/g liver, with a value of 2.94 μmol/hr/g liver at the physiological fasting blood glucose concentration of 5 mM. On the other hand, our calculated values for the TCA cycle fluxes were higher than those reported in the literature. Combining metabolite measurements and analysis of ^{13}C labeling pattern of glutamate, Large *et. al.* [162] estimated the flux through citrate synthase (reaction 9 in our model) in perfused livers from 48-hour starved rats to be 4.2 ~ 5.4 μmol/hr/g liver, which is roughly one third of our estimate (17.1 μmol/hr/g liver); however, addition of glucagon (10^{-7} M) increased citrate synthase flux to 13.7 ~ 16.5 μmol/hr/g liver, closer to our value. The sensitivity of the TCA cycle to variations in perfusate composition (both hormones and substrates) may explain some of the discrepancies between these studies. Implicit in our calculation was the assumption that all of the oxygen consumed is used as electron acceptor in the mitochondrial electron transport chain. Non-mitochondrial respiration accounts for 22 % of total oxygen consumption by resting hepatocytes [163] and 20 % in the perfused liver [164]. Consequently, the current calculations, where TCA cycle reactions are stoichiometrically related to oxygen uptake, may overestimate these fluxes. On the other hand, this would not affect the relative TCA cycle flux increase predicted in

response to burn, as TCA cycle fluxes are linearly related to measured oxygen consumption rates in the stoichiometric balance model.

Two important findings of this study are that (1) amino acids provide the main source of carbon for the incremental portion of the gluconeogenic flux in the burn condition, and (2) that the glucose produced is diverted into the PPP, so that the same net glucose output is observed in the burn and sham-burn conditions. This is consistent with the increase in glucose substrate cycling in burn patients reported by Wolfe *et al.* [48], which is based on the differential loss of deuterated label from infused [6,6-$^2H_2$]glucose and [2-$^2H_1$]glucose as their carbon moieties undergo glycolysis or gluconeogenesis. In particular, a glucose molecule that cycles through the glucose (glucose to G6P and back to glucose) or fructose cycle (fructose 1-phosphate to fructose 1,6-bisphosphate and back to fructose 1-phosphate) in the liver loses the deuterium at position 2 but retains the label at position 6, whereas ^2H in the 6 position of glucose can be lost at two possible sites in the process of gluconeogenesis. However, as Wolfe [165] points out, any [2-$^2H_1$]G6P that enters the PPP also loses its label. Thus, the difference in glucose Ra determined with [6,6-$^2H_2$]glucose and [2-$^2H_1$]glucose could reflect not only rates of glucose and fructose cycling, but also cycling of glucose moieties through the PPP.

In the liver, the PPP is the main source of cytosolic NADPH [166], a cofactor for fatty acid synthesis, mixed function oxidation, and recycling of endogenous anti-oxidants. Among the latter, the recycling of the ROS scavenger glutathione (GSH) by glutathione reductase is quantitatively the most significant reaction, as the maximal rate of NADPH consumption by GR is 5 to 8 fold that of other NADPH dependent reactions [152]. The [NADPH]/[NADPH + $NADP^+$] ratio and PPP activity are sensitive to inducers of oxidative stress in isolated rat hepatocytes [167, 168] and in perfused rat livers [169]. Furthermore, it has been reported that increased flux through the PPP is an important adaptive response to oxidative stress in various liver-derived cell types [170, 171]. Thus, PPP stimulation by burn injury may reflect an increased NADPH demand by ROS scavenging pathways. Lending support to this hypothesis are findings of increased lipid peroxidation in liver after burn injury [172, 173]. The increase in both G6PDH and GR activities by burn injury may also indicate a metabolic adaptation similar to those described above. Moreover, the increase in GR activity found here (29 %) agrees with that reported by Sabeh *et al.* [173] for a comparable model of burn injury. Our measurements also showed a greater uptake of glycine in the burn condition (Table 2-3), which is noteworthy

considering that glutathione is a tri-peptide composed of glutamate, cysteine, and glycine. Glutathione is synthesized from its constituent amino acids in two steps, where glycine is added to γ-glutamylcysteine in the second step by glutathione synthetase. It is possible that the increased net influx of glycine into the liver contributed to additional synthesis of GSH in response to oxidative stress. In an animal model similar to ours, Lalonde et al. [137] found total liver glutathione to be significantly increased by burn injury.

A potential source of ROS is the increase in flux through the electron transport chain (reactions 53 and 54) and the TCA cycle. It has been shown that the leakage of ROS from various pathways is a normal occurrence of oxidative metabolism [174, 175], particularly in the mitochondria [176, 177], especially when the respiratory chain is highly reduced and its activity is dependent on ADP availability [178, 179]. Consistent with this notion is our finding that the ratio of excreted acetoacetate to β-hydroxybutyrate is lowered from 1.4 to 1.1 by burn injury (Table 3), which indicates an accumulation of NADH relative to NAD^+ in the mitochondria. The ratio of acetoacetate to β-hydroxybutyrate, which are formed in the mitochondria and freely cross both the mitochondrial and cytoplasmic membranes, is directly proportional to the mitochondrial $[NAD^+]/[NADH]$ ratio [180].

In conclusion, we found metabolic flux analysis to be useful in studying metabolic adaptations to stress in intact organs such as the isolated perfused liver. Our results suggest that amino acids are used as substrates for gluconeogenesis to provide glucose to the PPP in the hypermetabolic liver. The parallel induction of G6PDH and GR also supports the notion that increased glutathione turnover, for example because of oxidative stress, is a major factor governing the increased demand for NADPH derived from the PPP. We also observed an increase turnover of reducing equivalents (e.g. NADH and $FADH_2$) which reflects an increased demand for mitochondrial energy production. Given that mitochondrial energy metabolism generates significant amounts of ROS, it is plausible that the induction of gluconeogenesis and the PPP is an endogenous protective mechanism which helps maintain cellular integrity during hypermetabolism. At which point in the time course of host response to injury this occurs and whether this is reversible by infusion of exogenous anti-oxidants or anti-oxidant precursors warrants further investigation.

CHAPTER 3. DYNAMICS OF THE HEPATIC METABOLIC RESPONSE TO BURN INJURY: AN INTEGRATED ANALYSIS

3.1 Introduction

Severe injury leads to a hypermetabolic state, which features increased turnover of protein, fatty acid, and carbohydrates at the whole body level [48, 181, 182]. Concomitant with these changes are also an increased resting energy expenditure and a negative nitrogen balance [183]. The hypermetabolic state may persist from days to weeks or even months, in which case patients often exhibit complications such as infections and multiple organ dysfunction syndrome (MODS), which could threaten recovery and survival [131, 132]. It has been thought that the hypermetabolic response aids the wound healing process by supplying energy, substrates, and healing factors to the wound site. Over the last 5 ~ 10 years, this traditional view has been challenged and modified by observations that hypermetabolism persists even in the face of aggressive nutritional support and long after wound closure [184, 185]. Furthermore, the notion that increased amino acid turnover is indicative of increased protein synthesis is inconsistent with the associated urea nitrogen loss, as the latter is a measure of amino acid catabolism rather than protein synthesis.

An important player in systemic hypermetabolism is the liver, where many of the acute phase reactants, most of the *de novo* glucose, and all of the urea is synthesized. Thus, understanding the biochemical underpinnings of the hypermetabolic response in the liver may lead to a better understanding at the systemic level and ultimately provide clues for limiting its deleterious consequences. As a first step toward identifying the driving forces of hepatic hypermetabolism, we had previously developed a perfused liver model of burn-injury associated hepatic hypermetabolism [186]. In conjunction with a stoichiometric network model, we used the perfused liver model to characterize the effects of burn injury on liver metabolism on day 4 after burn injury, which corresponded to the peak activity level of the host metabolic response during the first week after the injury. Comparing livers from burn and sham-burn treated animals, we found that burn injury significantly increased the uptake of amino acids and the fluxes through several intracellular pathways, including the TCA cycle, urea cycle, and PPP. The aim of the present study was to expand upon these earlier findings, and to probe, in greater detail, the

biochemical mechanisms underlying the progression of hepatic hypermetabolism during the first week of burn injury.

3.2 Materials and Methods

3.2.1 Chemicals.

Unless otherwise noted, all chemicals were purchased from Sigma-Aldrich Chemical Co. (St. Louis, MO). [U-^{14}C]leucine (300 mCi/mmol) and [U-^{14}C]glutamine (300 mCi/mmol) were purchased from New England Nuclear Life Science Products (Boston, MA).

3.2.2 Animals.

Male Sprague-Dawley rats (Charles River Laboratories, Boston, MA) weighing 150 ~ 200 g were housed in a temperature (25 °C) and light-controlled room (12-hour light-dark cycle). The animals were cared for in accordance with the National Research Council guidelines. Experimental protocols were approved by the Subcommittee on Research Animal Care, Committee on Research, Massachusetts General Hospital. Water and rat chow were provided ad libitum. Animals were individually housed and allowed to adjust to their new surroundings for at least 2 days before receiving treatment. On the day of treatment, animals were randomly divided into two groups, burned and sham-burned. Burn and sham-burn procedures were carried out as described by Yamaguchi et al. [140] and in Chapter 2.

3.2.2 Liver perfusion

Liver perfusions were performed 1, 2, 3, 4, and 7 days after burn or sham-burn treatment. Rats were fasted 24 hours prior to the perfusions in order to deplete liver glycogen stores. The perfusion method has been described previously [140] and diagrammed in Chapter 2. A detailed description of the basal perfusion medium is given in Table 3-1. For determination of secreted protein flux, livers were perfused with medium containing [U-^{14}C]leucine. In order to allow sufficient uptake of leucine by the liver, additional unlabeled leucine was added to the basal medium so that the final leucine concentration was 0.71 mM, which is approximately five times the plasma concentration [187]. Livers were washed with ca. 300 mL of the leucine enriched medium in single-pass mode before the perfusion circuit was closed. At time zero, which was taken to be the moment recirculation was started, 40 μCi of [U-^{14}C]leucine was mixed into the

medium reservoir, which contained ca. 200 mL of the leucine enriched medium. The perfusion lasted 2 hours, during which time 2 mL samples were taken at $t = 0$, 30, 60, 90, and 120 min. At the end of all perfusions, livers were quickly excised, blotted, weighed, and frozen in liquid nitrogen. Livers were stored at -80 °C and the medium samples were refrigerated until assays could be performed. Metabolite assays on the medium samples were performed as described in Chapter 2.

3.2.3 Western blot analysis

Livers previously frozen were ground in liquid nitrogen and lysed for the detection of UCP2 by sonication on ice in a lysis buffer containing Triton X-100. Proteins were separated on 12 % Tris-HCl polyacrylamide gels (Bio-Rad, Hercules, CA) and transferred to polyvinylidine difluoride membranes (Bio-Rad). Membranes were blocked for 45 min. at room temperature in buffer containing Tris-buffered saline (TBS), 0.2 % Tween-20, and 5 % powdered milk (w/v). Membranes were then incubated with rabbit anti-mouse antibody to UCP2 (Chemicon, CA) in blocking buffer overnight at 4 °C. After 3 washes with TBS-Tween-20 (TBS-T), the membranes were incubated with goat anti-rabbit IgG conjugated with horseradish peroxidase (Santa Cruz Biotechnology, Santa Cruz, CA) for 1 hr. at room temperature. After washing again in TBS-T, the membranes were developed with a chemiluminescence enhancer (Pierce, Rockford, IL) and exposed on an imaging screen (Bio-Rad). Protein bands were quantified by image analysis and expressed in arbitrary units relative to background.

3.2.4 Determination of specific activities in secreted liver proteins

Proteins in medium samples were concentrated for specific activity measurement using centrifugal filter devices with a nominal MW cut-off of 3 kD (Millipore, Bedford, MA). Filter assemblies containing 500 µL sample were centrifuged at 10,000 × g for 30 minutes at room temperature. The filters were then removed from the vials containing the permeates, inverted, placed in fresh vials and centrifuged at 1,000 × g for 5 minutes to collect the retentates. Permeate and retentate volumes were measured and their radioactivity counted in a Beckman LS 6000 IC scintillation counter (Beckman Instruments, Palo Alto, CA). The concentrations of labeled proteins in the samples were determined from the volume and radioactivity measurements using mass balances.

Table 3-1. Perfusion Medium Composition

Metabolite	Concentration
Amino Acids	*MM*
Alanine	0. 48
Arginine	0. 72
Asparagine	0. 78
Aspartic Acid	0. 06
Cystine	0. 13
Gutamic Acid	0. 33
Glutamine	2. 00
Glycine	0. 38
Histidine	0. 27
Isoleucine	0. 40
Leucine	0. 40
Lysine	0. 50
Methionine	0. 10
Phenylalanine	0. 19
Proline	0. 42
Serine	0. 63
Threonine	0. 40
Tryptophan	0. 05
Tyrosine	0. 29
Valine	0. 39
Carbohydrates	*mM*
Glucose	5. 6
Lactate	5. 0
Pyruvate	0. 5
Protein	*g/L*
Bovine Serum Albumin	30
Salts and Vitamins	*g/L*
Calcium Chloride 2 H_2O	0. 265
Choline Chloride	0. 001
Folic acid	0. 001
Magnesium Sulfate	0. 09767
myo-Inositol	0. 002
Niacinamide	0. 001
Pantothenic acid (hemicalcium)	0. 001
Phenol Red	0. 011
Potassium Sulfate	0. 4
Pyridoxal HCl	0. 001
Rriboflavin	0. 0001
Sodium Bicarbonate	2. 2
Sodium Chloride	6. 8
Sodium Phosphate monobasic	0. 122
Thiamine HCl	0. 001

Assuming that the low-molecular metabolites are free to cross the filter membrane,

$$L_P = L_R \tag{3-1}$$

where L_P and L_R are concentrations of labeled low-molecular metabolites in the permeate and retentate fractions, respectively. The radioactivity count (C), volume (V), and labeled macromolecule concentration (M) are related by the following equations:

$$C_P = V_P(M_P + L_P) \tag{3-2}$$

$$C_R = V_R(M_R + L_R) \tag{3-3}$$

where the subscript P or R denotes permeate or retentate. Since macromolecules cannot pass through the filter membrane,

$$M_P = 0 \tag{3-4}$$

and the labeled macromolecule concentration is related to radioactivity and volume as follows:

$$C_P/V_P = L_P = L_R \tag{3-5}$$

$$C_R/V_R = C_P/V_P + M_R \tag{3-6}$$

$$M_T V_T = V_R M_R + V_P M_P = V_R M_R \tag{3-7}$$

$$M_T = \frac{V_R}{V_T}\left(\frac{C_R}{V_R} - \frac{C_P}{V_P}\right) \tag{3-8}$$

where M_T and V_T refer to the concentration of labeled proteins in the original sample and the total (permeate + retentate) sample volume, respectively. Total protein output was calculated by normalizing M_T with respect to leucine enrichment in the medium (E):

$$E = \frac{[Leu^*]}{[Leu + Leu^*]} \tag{3-9}$$

where *Leu* and *Leu** refer to unlabeled and labeled leucine, respectively.

3.2.5 Discriminant analysis

In order to determine whether the livers perfused on different days after the burn or sham-burn treatment exhibited distinct metabolic phenotypes, as judged by a composite measure based on many measured metabolic parameters, a multivariate statistical analysis technique

called Fisher's Discriminant Analysis (FDA) was applied to the measurements. For samples divided *a priori* into different groups and described by a multi-dimensional set of variables, FDA derives linear combinations of the variables that define a new set of coordinate axes so that sample projection onto the new coordinate space maximizes the ratio of between-group to within-group variances. In the present study, time concentration profile measurements were performed for 25 metabolites in 42 perfusion experiments. The concentration profiles were linearly regressed to ontain rates of metabolite uptake or output by the liver, and arranged into a $M \times N$ data matrix with the variables (exchanged rates) in columns ($N = 25$) and samples (livers) in rows ($M = 42$). Assuming that time between sham-burn treatment and perfusion did not have significant effects, all livers isolated from sham-burned animals were considered together as a single sham-burn control group. Thus, there was a total of 6 treatment groups: sham-burn control, post-burn day 1, post-burn day 2, post-burn day 3, post-burn day 4, and post-burn day 7. Liver samples were projected onto a three-dimensional (3D) FDA space by a mathematical procedure as spectral decomposition, which is described in detail elsewhere [188]. From Figure 3-1, it can be seen that our initial assumption regarding treatment groups was statistically valid, as the liver sample projections formed clearly discernable clusters that corresponded to their respective treatment groups. In particular, all sham-burn livers projected closely to each other.

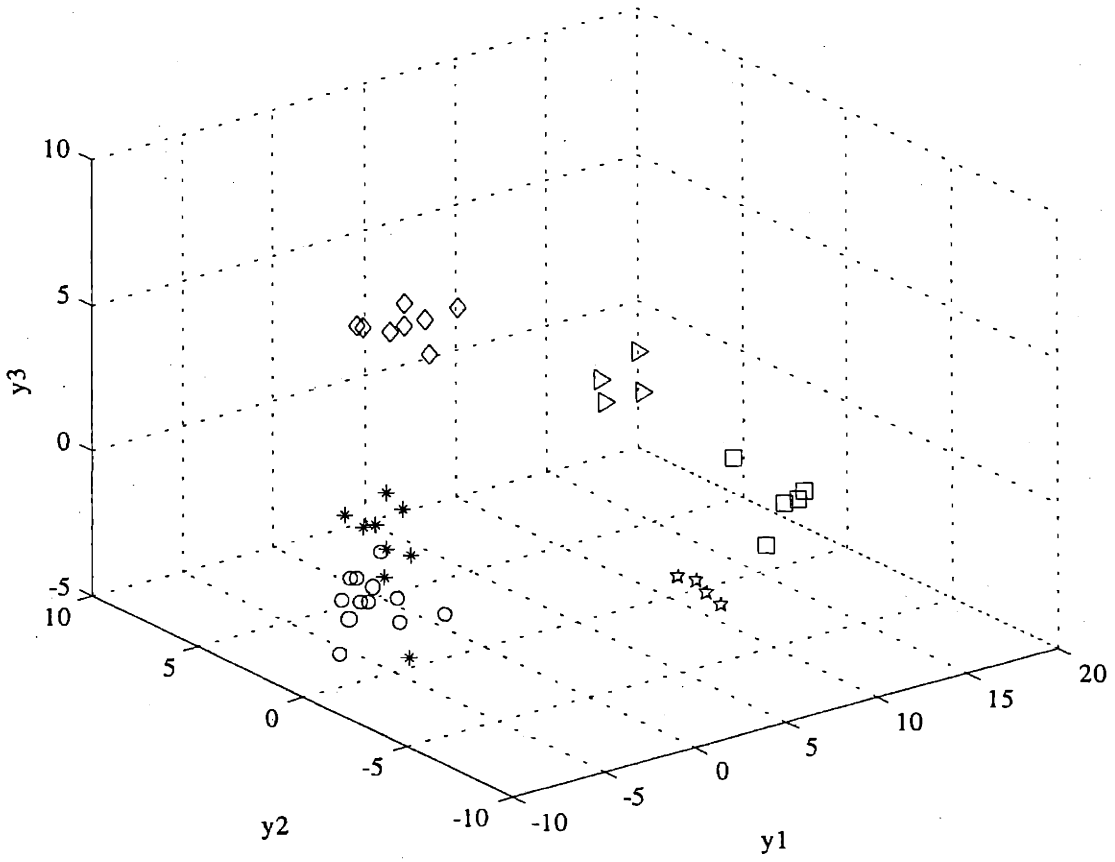

Figure 3-1. FDA projection of measured metabolite exchange rates.
Projection of measured metabolite exchange rates into a three-dimensional discriminant score space (*y1-y2-y3*). Each data point in the plot corresponds to one liver sample. Symbols denote liver sample treatment group membership: ○, sham-burn control; ✳, day 1 post-burn; ▷, day 2 post-burn; ✱, day 3 post-burn; □, day 4 post-burn; and ◇, day 7 post-burn.

3.2.6 Calculation of intracellular fluxes

A network model of liver metabolism was formulated as described in Chapter 2, with minor modifications. Table 3-2 lists the stoichiometry and the relevant enzymes of the reactions included in the model, which is shown graphically in Figure 3-2. As before, the stoichiometric coefficients were collected into a matrix S whose ith row, jth column element is the coefficient of metabolite i (Table 3-3) in reaction j. Once again, the steady state metabolite balance was written in matrix form:

$$Sv = 0 \tag{3-10}$$

where v is a vector whose jth element holds the net flux through reaction j. The left hand side of Equation 10 was rearranged by separating v into measured and unknown components, v_m and v_u, respectively, and partitioning matrix S into S_m and S_c, where S_m and S_c contain the stoichiometric coefficients of measured and unknown reactions, respectively.

$$Sv = 0 = S_m v_m + S_c v_c \tag{3-11}$$

$$S_u v_u = -S_m v_m \tag{3-12}$$

In this model version, the number of linearly independent balance equations (38) exceeded the number of unknown fluxes (35). Thus, there were redundant equations, and the macroscopic balance method of Wang and Stephanopoulos [51] was used again in order to test for the presence of any systematic or gross errors. The h values computed for the metabolite measurement sets collected in these studies are shown in the last row of Table 3-4. Comparing the test function (h) values with standard chi-square (χ^2) distribution values at various confidence levels for 3 degrees of freedom, it could not be concluded even at 75 % confidence level that any gross errors were present in the measurements. Thus, the quality of this data were deemed to be satisfactory, and the measurements were used without any subsequent adjustments for the calculation of unknown fluxes (v_c).

$$v_c = -(S_c^T S_c)^{-1} S_c^T S_m v_m \tag{3-13}$$

Variances for v_c were computed from variances associated with v_m [189]:

$$\mathrm{VAR}(v_{c_i}) = \sum_{j=1}^{K} B_{ij}^2 \mathrm{VAR}(v_{m_j}),\ i = 1 \ldots L \tag{3-14}$$

where $B \equiv -(S_u^T S_u)^{-1} S_u^T S_m$, K is the number of measured rates, and L the number of unknown reaction fluxes.

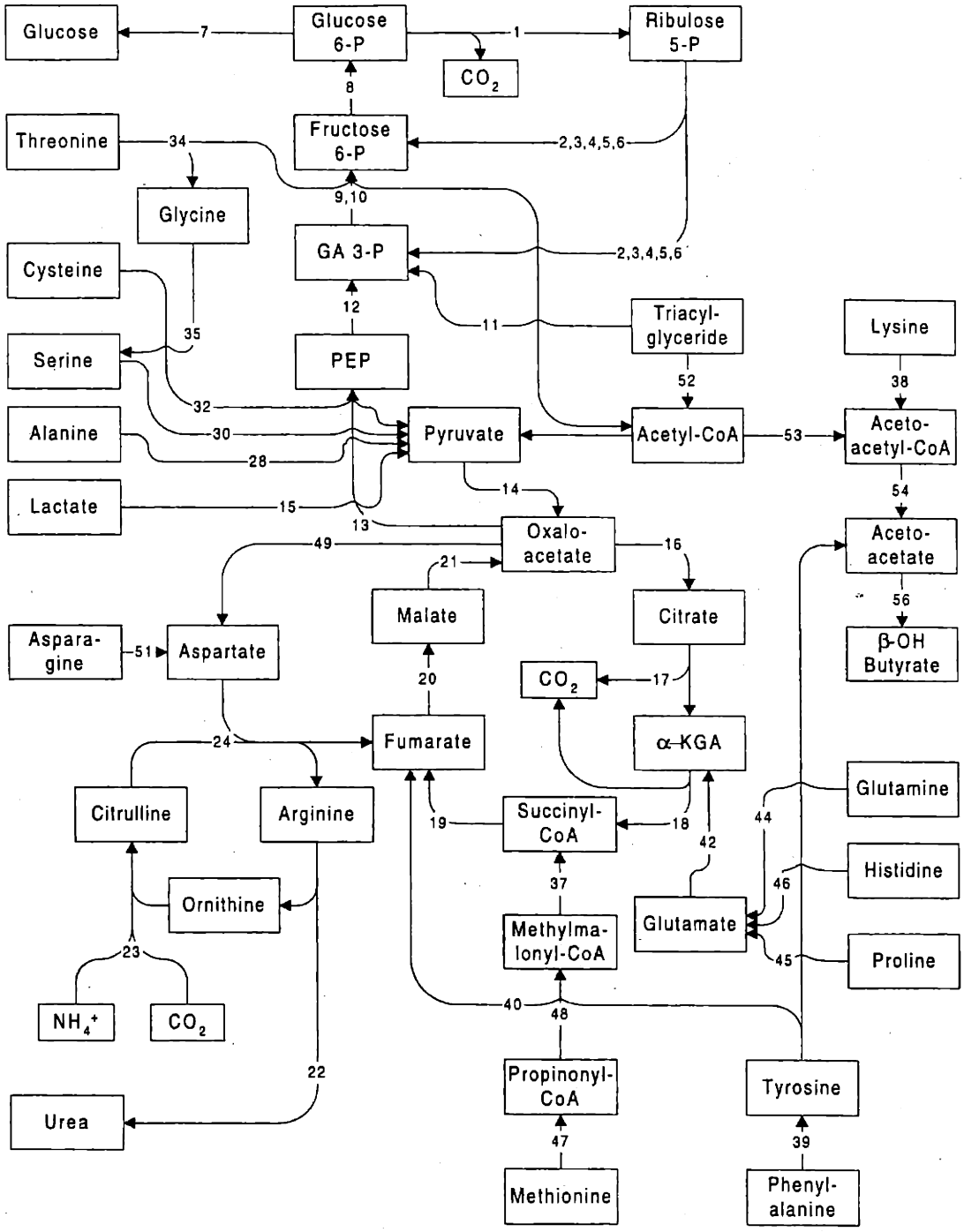

Figure 3-2. Hepatic metabolic network.
Stoichiometric model used to formulate metabolite balances. Some non-branching metabolite nodes have been omitted for clarity. Arrows indicate assumed direction of reaction. Numbers on arrows refer to reactions numbers in Table 2. Abbreviations: GA 3-P, glyceraldehyde-3-phosphate, PEP, phosphoenol pyruvate, α-KGA, α-ketoglutarate; and CoA, coenzyme A.

Table 3-2. Reaction Stoichiometry

No.	Enzymes	Stoichiometry
1	glucose 6-P DH, 6-P gluconolactonase, and P-gluconate DH	glucose 6-P + 2 $NADP^+$ → ribulose 5-P + CO_2 + 2 NADPH
2	ribose 5-P pentose isomerase	ribulose 5-P ↔ ribose 5-P
3	ribulose-P 3-epimerase	ribulose 5-P ↔ xylulose 5-P
4	transketolase	ribose 5-P + xylulose 5-P ↔ sedoheptulose 7-P + glyceraldehyde 3-P
5	transaldolase	sedoheptulose 7-P + glyceraldehyde 3-P ↔ fructose 6-P + erythrose 4-P
6	transketolase	erythrose-4-P + xylulose-5-P ↔ fructose-6-P + glyceraldehyde-3-P
7	glucose-6-phosphatase	glucose 6-P → glucose + Pi
8	phosphohexose isomerase	fructose 6-P ↔ glucose 6-P
9	fructose bisphosphatase	fructose 1,6-P_2 → fructose 6-P + Pi
10	triose-P isomerase, fructose bisphosphatase aldolase	2 glyceraldehyde-3-P ↔ fructose-1,6-P_2
11	lipase, glycerol kinase, glycerol-P DH, triose-P isomerase	palmitoylglycerol + ATP + NAD^+ → 3 palmitate + glyceraldehyde-3-P + ADP + Pi + NADH
12	enolase, phosphoglycero-mutase, 3-phosphoglycerate kinase, glyceraldehyde DH	PEP + NADH + ATP ↔ glyceraldehyde-3-P + Pi + NAD^+ + ADP
13	phosphoenolpyruvate carboxykinase	oxaloacetate + GTP ↔ PEP+ GDP + CO_2
14	pyruvate carboxylase	pyruvate + CO_2 + ATP → oxaloacetate + ADP + Pi
15	lactate DH	lactate + NAD^+ ↔ pyruvate + NADH
16	citrate synthase	oxaloacetate + acetyl-CoA → citrate + CoA-SH
17	aconitase, isocitrate DH,	citrate + NAD^+ ↔ α-ketoglutarate + CO_2 + NADH
18	α-ketoglutarate DH system	α-ketoglutarate + NAD^+ → succinyl-CoA + CO_2 + NADH
19	succinyl-CoA synthetase, succinate DH	succinyl-CoA + Pi + GDP + FAD ↔ fumarate + GTP + $FADH_2$
20	fumarase	fumarate ↔ malate
21	malate DH	malate + NAD^+ ↔ oxaloacetate + NADH
22	arginase	arginine → urea + ornithine
23	carbonate dehydratase, carbamoyl-P synthetase, ornithine carbamoyl transferase	ornithine + CO_2 + NH_4^+ + 2 ATP ↔ citrulline + 2 ADP + 2 Pi
24	argininosuccinate synthase, argininosuccinate lyase	citrulline + aspartate + ATP → arginine + fumarate + AMP + 2 Pi
25		arginine uptake
26		NH_4^+ output
27		ornithine output
28	alanine aminotransferase, glutamate DH	alanine + NAD^+ ↔ pyruvate + NH_4^+ + NADH
29		alanine uptake
30	serine dehydratase	serine → NH_4^+ + pyruvate
31		serine uptake
32	cysteine transaminase, glutamate DH, 3-mercaptopyruvate sulfurtransferase	cysteine + NAD^+ + H_2SO_3 ↔ pyruvate + $H_2S_2O_3$ + NH_4^+ + NADH
33		cysteine uptake
34	threonine 3-DH	threonine + NAD^+ → glycine + acetyl-CoA + NADH

35	glycine DH, aminomethyltransferase, dihydrolipoyl DH)	2 glycine + NAD^+ ↔ serine + NADH + CO_2 + NH_4^+
36		glycine uptake
37	methylmalonyl-CoA-epimerase and methylmalonyl-CoA-mutase	(S)methylmalonyl-CoA ↔ succinyl-CoA
38	saccharopine DH, aminoadipate semialdehyde DH, 2-aminoadipate transaminase, glutamate DH, α-ketoglutarate DH, glutaryl-CoA-DH, enoyl-CoA hydratase, 3-hydroxy-acyl-CoA DH	lysine + 5 NAD^+ + CoA-SH + FAD → 5 NADH + 2 NH_4^+ + 2 CO_2 + $FADH_2$ + acetoacetyl-CoA
39	phenylalanine 4-mono-oxygenase	phenylalanine + tetrahydrobiopterin + O_2 → dihydrobiopterin + tyrosine
40	tyrosine transaminase, glutamate DH, 4-hydroxyphenylpyruvate dioxygenase, homogenisate 1,2 dioxygenase, maloyl acetoacetate isomerase, fumaryl acetoacetase	tyrosine + NAD^+ + 2 O_2 → NH_4^+ + NADH + CO_2 + fumarate + acetoacetate
41		tyrosine uptake
42	glutamate DH	glutamate + NAD^+ ↔ α-ketoglutarate + NADH + NH_4^+ (When the direction of catalysis is biosynthesis of glutamate, NADPH is the reductant.)
43		glutamate output
44	glutaminase	glutamine → glutamate + NH_4^+
45	proline oxidase, 1-pyrroline-5-carboxylate DH	proline + 0. 5 O_2 + NAD^+ → glutamate + NADH
46	histidine ammonia lyase, urocanate hydratase, imidazole propionase, glutamate formimino-transferase	histidine + THF → NH_4^+ + 2-formimino-THF + glutamate
47	methionine adenosyl-transferase, DNA methyltransferase, adenosyl homocysteinase, cystathione lyase, pyruvate DH	methionine + 2 ATP + serine + NAD^+ + CoA-SH → PPi + Pi + adenosine + cysteine + NADH + CO_2 + propionyl-CoA
48	propinoyl-CoA carboxylase	propinoyl-CoA + ATP + CO_2 → (S)methylmalonyl-CoA + ADP + Pi
49	aspartate aminotransferase, glutamate DH	aspartate + NAD^+ ↔ oxaloacetate + NADH + NH_4^+
50		aspartate output
51	asparaginase	asparagine → aspartate + NH_4^+
52	β-oxidation	palmitate + ATP + 7 FAD +7 NAD^+ + 8 CoA-SH → 8 acetyl-CoA + AMP + 2 Pi + 7 $FADH_2$ + 7 NADH
53	thiolase, hydroxymethylglutaryl-CoA-synthetase, hydroxymethylglutaryl-CoA-cleavage enzyme	2 acetyl-CoA → acetoacetate + 2 CoA-SH
54	acetoacetyl-CoA hydrolase	acetoacetyl-CoA → acetoacetate + CoA-SH
55		acetoacetate output

56	β-hydroxybutyrate DH	acetoacetate + NADH ↔ β-OH-butyrate + NAD^+
57	complexes I, II, III, and IV	NADH + H^+ + ½ O_2 → NAD^+ + H_2O
58	complexes II, III, and IV	$FADH_2$ + ½ O_2 → FAD + H_2O
59		O_2 uptake
60		CO_2 output

Table 3-3. Reaction Network Metabolites

Row Number in Stoichiometric Matrix	Metabolite
1	Glucose 6-P
2	Ribulose 5-P
3	Ribose 5-P
4	Xylulose 5-P
5	Sedoheptulose 7-P
6	Glyceraldehyde 3-P
7	Fructose 6-P
8	Erythrose 4-P
9	Fructose bisphosphate
10	PEP
11	NADH
12	Oxaloacetate
13	CO_2
14	Pyruvate
15	Acetyl-CoA
16	Citrate
17	2-Oxoglutarate
18	$FADH_2$
19	Succinyl-CoA
20	Fumarate
21	Malate
22	Arginine
23	Orinithine
24	NH_4^+
25	Citrulline
26	Aspartate
27	Alanine
28	Glutamate
29	Serine
30	Cysteine
31	Glycine
32	Methylmalonyl-CoA
33	Acetoacetate
34	Acetoacetyl-CoA
35	O_2
36	Tyrosine
37	Propinoyl-CoA
38	Palmitate

3.2.7 Statistical analysis.

Tests of statistical significance between calculated fluxes was performed using the *t*-test based on variances estimated by Equation 3-14. All other tests of statistical significance were performed using the MS Excel ANOVA data analysis tool (Microsoft Corp., Redmond, WA). The sensitivity of the calculated fluxes to measurement error and noise was gauged by calculating the condition number of the stoichiometric matrix $\boldsymbol{S}$.

3.2.8 Hierarchical clustering.

The pooled (measured and calculated) reaction fluxes were clustered using an agglomerative technique that forms average linkages between clusters. This technique starts with each cluster comprising of exactly one object and then progressively combines the two nearest clusters until there is just one cluster left consisting of all the objects. In the present case, an object refers to a vector of reaction fluxes of a perfused liver, and the metric for determining the degree of nearness (or similarity) was a modified correlation coefficient between the objects or clusters. Correlation coefficients between clusters of objects were computed by first averaging the fluxes of the objects comprising each cluster and then treating the cluster as an object. The clustering procedure was implemented using a publicly available software developed and distributed by Eisen et al. [190]. Before applying the software, all burn condition fluxes were normalized with respect to the sham-burn control fluxes, which were taken to be the zero time points. The normalized flux values were then log (base 2) transformed, except when the results of normalization were negative. In these cases, the object or vector containing these elements was dropped from the analysis. The log transformation allowed the visualization of activation and repression in a symmetrical fashion about the zero axis, e.g. two-fold activation is equal to1, no change 0, and two-fold reduction -1.

3.3 Results

In prior work, we had developed a perfused liver model of burn-injury associated hepatic hypermetabolism [186], and also formulated and validated a metabolite balance mathematical model of hepatic central carbon metabolism. Using these tools, we characterized the effect of burn injury on liver metabolism on day 4 after burn injury, which corresponded to the peak activity level of the host metabolic response during the first week after the injury. Comparing

livers from burn and sham-burn treated animals, we found that burn injury significantly increased the uptake of amino acids and the fluxes through several intracellular pathways, including the TCA cycle, urea cycle, and PPP.

In order to better identify the progression of hepatic hypermetabolism, in the present study, we examined the first week of hypermetabolism in more detail. For each time point, concentration time profiles of all medium metabolite components were determined by periodic sampling of the perfusate reservoir, and through linear regression analysis we obtained rates of metabolite exchange. Figure 3-3 shows several representative metabolite concentration profiles. In this case, glucose, lactate, urea, and 3-OH-butyrate curves for a burn and a sham-burn liver on days 1 and 4 are shown, representing key metabolites in hexose, triose, amino acid, and fatty acid metabolism, respectively. The concentration profiles of all of the metabolites followed a linear time course as judged by their R^2 values (0. 9 or greater), indicating that within the prescribed time we were operating at steady state.

Given that the metabolite exchange rates for sham-burn livers varied insignificantly with respect to time after treatment (see **Materials and Methods**, Figure 3-1), the sham-burn metabolite exchange rates were averaged across the entire sham-burn treatment group irrespective of the time between treatment and perfusion. The sham-burn control group, thus, refers to a single treatment group that includes all sham-burn livers examined in these experiments. All changes in metabolism for the burn livers are noted with respect to this treated, but unburned, "day 0 after burn" reference group. Accordingly, the metabolite exchange rates for the sham-burn control group are listed in a single column in Table 3-4, which summarizes the metabolite exchange rates measured in these experiments.

With respect to glucose and lactate, burn injury produced insignificant fluctuations in their exchange. In contrast, burn injury significantly increased the rate of exchange of nitrogen containing compounds by the liver. Urea output increased to 1.4 times above the sham-burn control one day after burn and remained elevated for the duration of the study period. The uptake of glucogenic amino acids followed a time course similar to that of urea output. Glutamine, arginine, and asparagine, which together comprised more than 77 % of the total net amino acid uptake (based on moles of carbon atom) for all of the livers, rose to 2.3, 1.6, and 2.6 times, respectively, above sham-burn control one day after burn and remained significantly higher throughout the first week after the injury. Interestingly, this trend was not observed for the

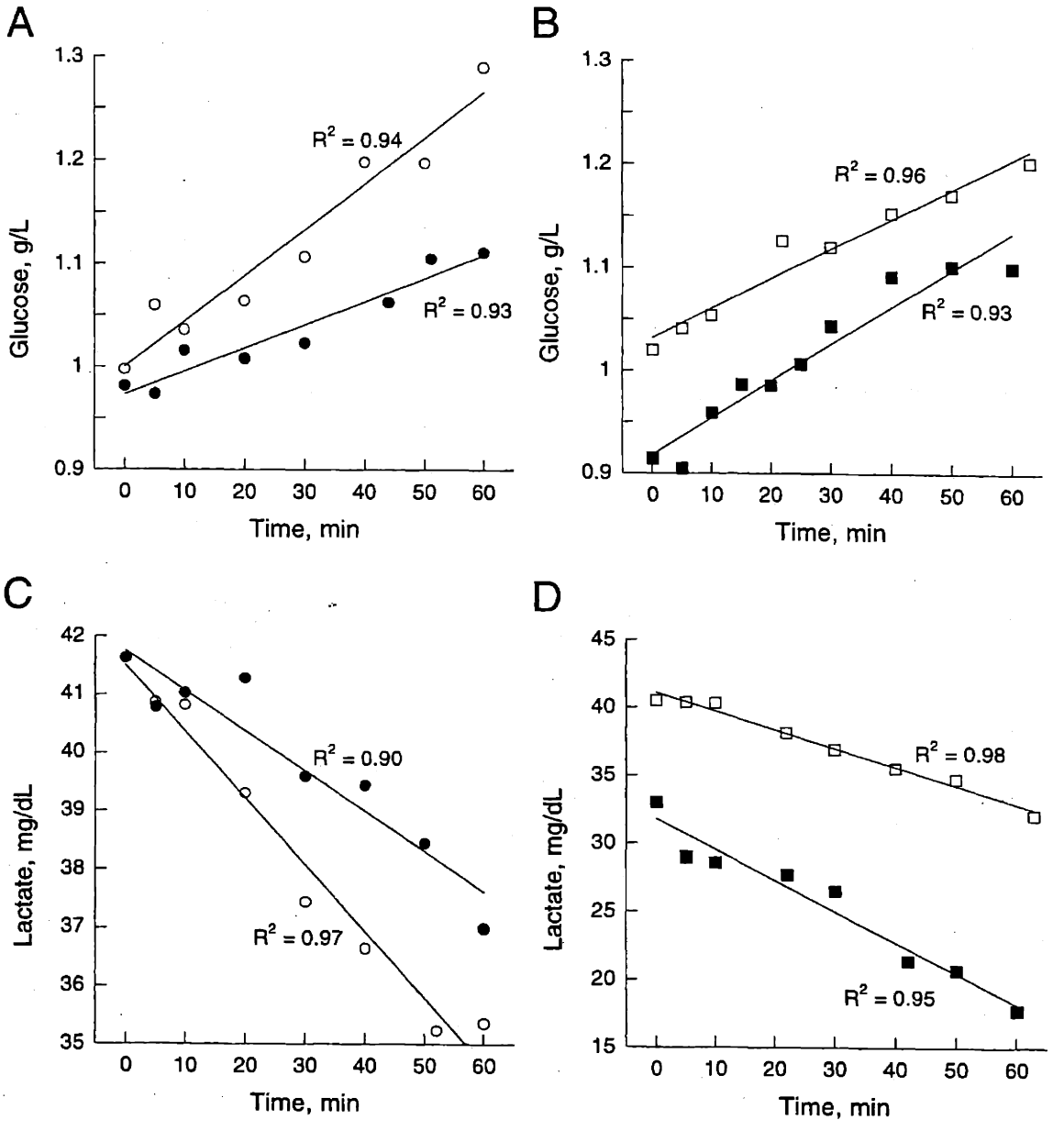

Figure 3-3. Metabolite concentration profiles in perfusion medium reservoir.
Representative profiles of glucose (A,B), lactate (C,D), urea (E,F), and 3-OH-butyrate (G,H) concentration changes in the perfusion medium reservoir are shown. Data in panels A, C, E, and G are taken from livers perfused 1 day after treatment. Data in panels B, D, F, and H are taken from livers perfused 4 days after treatment. Each data series refers to one perfused liver from either burn (●,■) or sham-burn (○,□) group.

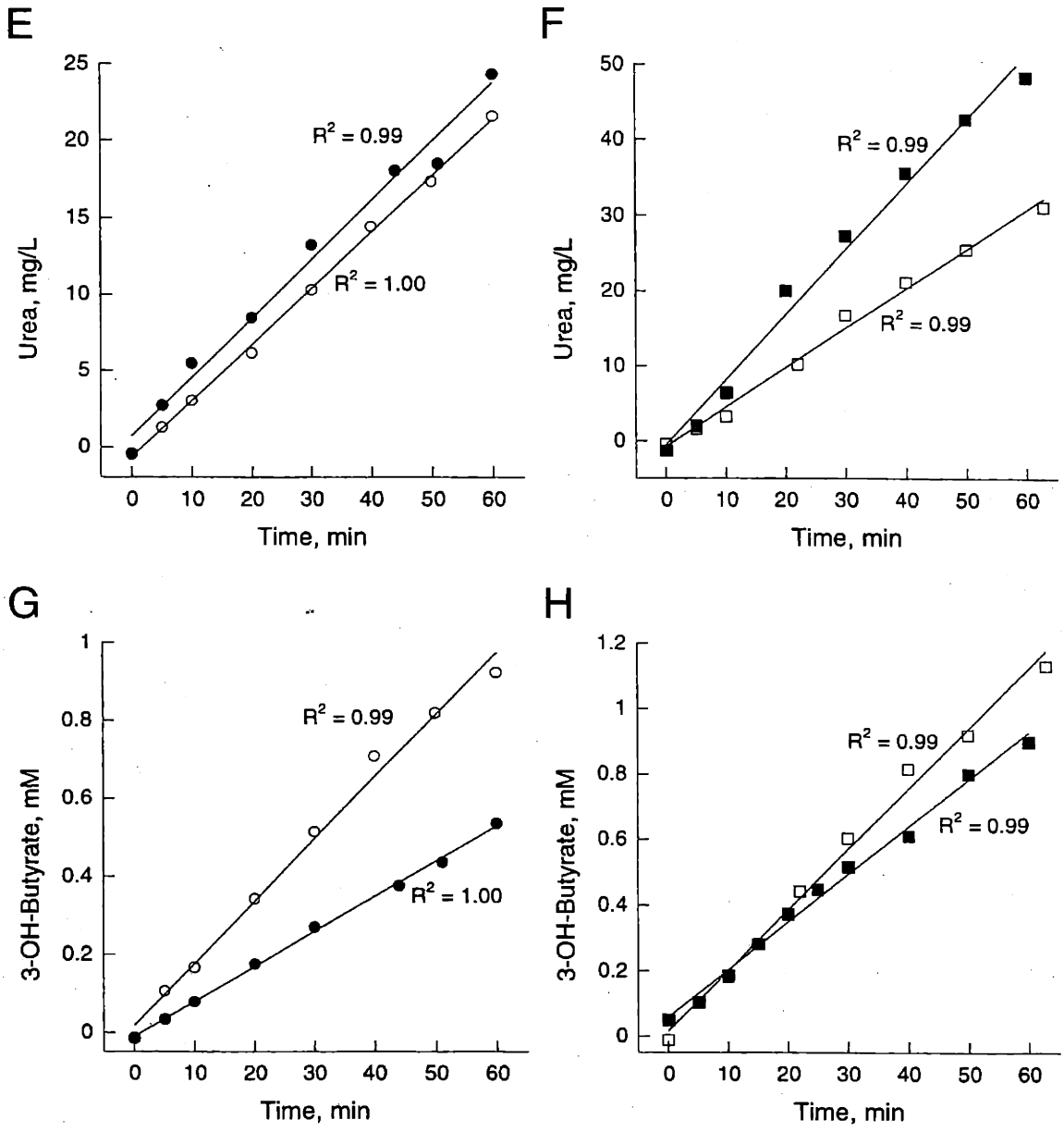

Figure 3-3. continued.

Table 3-4. Metabolite Exchange Rates

		Metabolite Exchange Rate, Day(s) After Treatment, μmol/g liver/hr					
Metabolite	No.	0 (Sham-burn) n = 12	1 n= 9	2 n = 4	3 n = 4	4 n = 5	7 n = 8
Gluconeogenesis							
Glucose	7	23.4 ± 2.5	24.8 ± 3.1	20.0 ± 2.6	26.3 ± 6.7	30.1 ± 3.0	23.1 ± 3.1
Lactate	15	-30.0 ± 2.4	-25.7 ± 2.9	-19.3 ± 5.5	-29.9 ± 8.5	-24.9 ± 3.8	-18.0 ± 2.9*
Urea Cycle							
Urea	22	23.3 ± 2.1	31.8 ± 2.6	43.1 ± 4.6*	34.9 ± 5.4	38.2 ± 8.1*	46.5 ± 2.6*
NH_4^+	26	2.6 ± 4.7	6.6 ± 5.8	8.1 ± 4.7	-0.7 ± 0.6	13.8 ± 3.4*	13.1 ± 5.8*
Orn	27	2.4 ± 0.5	3.3 ± 0.6	6.9 ± 1.5*	1.2 ± 0.6	4.2 ± 0.7	5.4 ± 0.6*
Glucogenic AA							
Arg	25	-4.5 ± 0.7	-7.0 ± 0.9	-11.8 ± 3.3*	-6.1 ± 1.6	-10.0 ± 0.8*	-9.1 ± 0.9*
Ala	29	0.1 ± 0.6	0.4 ± 0.7	1.9 ± 0.6*	-2.8 ± 2.0*	0.0 ± 0.5	0.6 ± 0.7
Ser	31	-2.3 ± 0.7	-3.4 ± 0.8	-3.5 ± 0.3	-4.3 ± 2.1	-4.0 ± 0.8	-4.5 ± 0.8
Cys	33	-0.4 ± 0.1	0.1 ± 0.1	-0.1 ± 0.3	0.6 ± 0.6	3.6 ± 3.0	-0.1 ± 0.1
Thr	34	-0.2 ± 0.4	-0.7 ± 0.5	-0.6 ± 0.3	-1.5 ± 1.4	-0.6 ± 0.5	-0.8 ± 0.5
Gly	36	-0.4 ± 0.4	-0.9 ± 0.5	-1.3 ± 0.1	-2.2 ± 1.4	-1.1 ± 0.3	-0.9 ± 0.5
Glu	43	2.4 ± 0.9	3.3 ± 1.1	3.6 ± 0.3	0.2 ± 1.7	2.0 ± 1.4	4.9 ± 1.1*
Gln	44	-7.6 ± 1.7	-17.1 ± 2.1*	-13.0 ± 0.3	-21.7 ± 9.5*	-17.6 ± 2.7*	-18.4 ± 2.1*
Pro	45	-0.1 ± 0.4	-1.0 ± 0.5	-1.1 ± 0.4	-2.0 ± 1.5	-1.6 ± 0.8	-0.5 ± 0.5
His	46	-0.2 ± 0.3	-0.8 ± 0.3	-0.6 ± 0.3	-1.2 ± 0.7	-0.6 ± 0.4	-0.5 ± 0.3
Met	47	-0.3 ± 0.1	-0.3 ± 0.2	-0.4 ± 0.1	-0.6 ± 0.3	-0.4 ± 0.1	-0.3 ± 0.2
Asp	50	0.1 ± 0.1	0.3 ± 0.2	1.0 ± 0.3*	-0.5 ± 0.3*	0.2 ± 0.1	0.4 ± 0.2*
Asn	51	-2.6 ± 0.9	-6.7 ± 1.1*	-7.4 ± 1.4*	-6.2 ± 2.5	-7.9 ± 1.9*	-6.2 ± 1.1*
Ketogenic AA							
Lys	38	-0.5 ± 0.6	-0.4 ± 0.7	-0.4 ± 1.0	-3.7 ± 2.3	-1.5 ± 0.9	-0.5 ± 0.7
Phe	39	-0.6 ± 0.2	-1.4 ± 0.2	-1.4 ± 0.4	-1.6 ± 0.6	-1.6 ± 0.3	-0.9 ± 0.2
Tyr	41	-0.1 ± 0.3	-0.7 ± 0.4	-0.3 ± 0.3	-1.0 ± 0.7	-0.4 ± 0.7	0.3 ± 0.4
Ketone Bodies							
ACAC	55	9.0 ± 1.2	8.3 ± 1.6	8.3 ± 2.0	7.1 ± 2.6	12.2 ± 2.6	6.7 ± 1.5
3-OH-Bt.	56	25.1 ± 1.7	18.2 ± 2.1	18.6 ± 5.8	30.8 ± 2.9	19.4 ± 5.9	22.1 ± 2.1
Respiration							
O_2	59	59.8 ± 4.1	62.4 ± 3.1	58.1 ± 1.9	92.5 ± 5.0*	98.3 ± 0.4*	92.9 ± 5.1*
CO_2	60	52.6 ± 5.5	76.5 ± 1.8*	81.3 ± 13*	99.5 ± 6.1*	121.2 ± 15.8*	87.9 ± 6.8*
Consistency Index		0.75	1.36	3.70	3.23	4.04	1.96

Metabolite exchanges rates were derived by linear regression of concentration profiles in the perfusion medium reservoir. Values are reported as mean ± SE. *Significantly different from the sham-burn control group ($p < 0.05$) as analyzed by *t*-test. Consistency indices were calculated for treatment group averages as described in **Materials and Methods.**

uptake of ketogenic amino acids, as the exchange rates of these metabolites remained statistically unchanged. Accordingly, acetoacetate and 3-OH-butyrate, the major end products of ketogenic amino acid catabolism, were also released by the liver at unchanged rates. Finally, burn injury heightened respiratory activity, albeit more slowly than the exchange of nitrogen containing metabolites. Oxygen uptake and net CO_2 output remained statistically unchanged until three days after burn, when they rose significantly to 1.5 times above sham-burn control. Taken together, these observations provide the following qualitative sequence of metabolic changes during the first week after burn injury (Figure 3-4). Shortly after the injury (1 ~ 2 days), both the uptake of glucogenic amino acids and output of urea were significantly increased and remained elevated. By the third day, the rate of liver respiration was significantly increased, which also remained elevated. On the other hand, the exchange of carbohydrate substrates, including glucose, lactate, and ketone bodies, remained virtually unaffected. In summary, data from the perfused liver experiments showed that the exchange rates of the various types of metabolic substrates are differentially affected by burn injury. We also noted that while the time course of metabolic changes in the perfused liver is similar to that observed in animal models and patient studies, there were important differences, especially with respect to glucose metabolism, as our results in the perfused liver are inconsistent with the notion that systemic hyperglycemia should be simply ascribed to increased gluconeogenesis in the liver.

The results presented above describe metabolic adaptations that occurred at the level of substrate exchange with the surrounding medium. In order to examine the time course of burn injury induced metabolic changes in the liver at the level of intracellular pathways, we applied our metabolic network model to the experimental data obtained in these studies. The qualities of both the model and the estimated fluxes were tested using sensitivity analysis and statistical hypothesis testing, respectively (see **Materials and Methods**), and were found to be satisfactory. The calculated fluxes are show in Table 3-5, which lists the reactions according to their number assignments in Table 3-2.

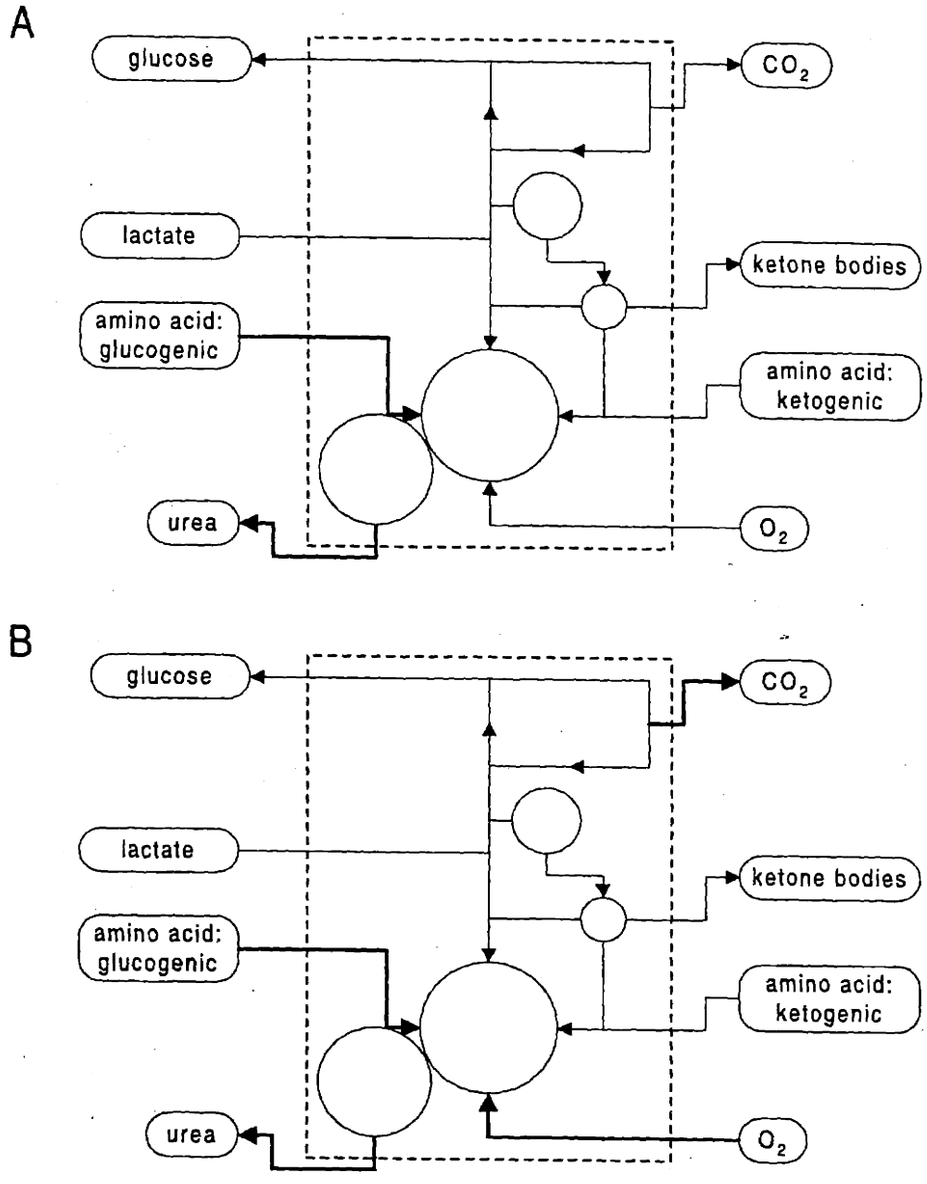

Figure 3-4. Two phases of metabolite exchange during the first week of hypermetabolism. The substrate exchange changes noted in Table 1 is summarized qualitatively as a schematic. **Bold** arrows indicate increased flux. During the first two days after burn injury, only glucogenic amino acid uptake and urea output are increased (A). Past the third day after burn injury, respiration (O_2 and CO_2 exchange) is also significantly increased.

Table 3-5. Calculated Intracellular Fluxes

Rxn. No.	Intracellular Flux, Day(s) After Treatment, μmol/g liver/hr					
	0 (Sham-burn)	1	2	3	4	7
	$n = 12$	$n = 9$	$n = 4$	$n = 4$	$n = 5$	$n = 8$
1	52.2 ± 6.7	65.6 ± 5.0	81.1 ± 13.8	78.9 ± 10.6	85.7 ± 17.1*	68.7 ± 4.8
2	16.4 ± 2.2	20.4 ± 1.7	25.6 ± 4.5	24.4 ± 3.7	26.7 ± 5.6	21.4 ± 1.6
3	37.1 ± 4.5	47.2 ± 3.3	57.5 ± 9.4*	56.9 ± 6.7*	61.6 ± 11.7*	49.4 ± 3.1
4	17.8 ± 2.2	22.4 ± 1.6	27.6 ± 4.6	27.0 ± 3.5	29.2 ± 5.8*	23.5 ± 1.6
5	19.7 ± 2.3	25.2 ± 1.7	30.4 ± 4.8*	30.5 ± 3.3*	32.9 ± 6.0*	26.3 ± 1.6*
6	20.8 ± 2.4	26.8 ± 1.7	32.0 ± 5.0*	32.5 ± 3.3*	34.9 ± 6.2*	27.9 ± 1.6*
8	73.9 ± 6.4	87.9 ± 4.6	98.6 ± 13.5	102.2 ± 9.9*	112.6 ± 16.8*	89.4 ± 4.3
9	31.9 ± 2.1	33.5 ± 2.1	33.9 ± 4.1	36.2 ± 4.8	41.8 ± 4.7*	32.7 ± 1.9
10	30.2 ± 2.0	31.1 ± 2.1	31.5 ± 4.0	33.1 ± 4.9	38.7 ± 4.5	30.2 ± 1.8
11	3.0 ± 0.2	2.5 ± 0.2	2.4 ± 0.4	3.4 ± 0.3	3.1 ± 0.4	3.2 ± 0.2
12	37.8 ± 2.8	34.6 ± 4.2	30.2 ± 5.1	32.3 ± 8.5	41.3 ± 4.4	31.0 ± 3.4
13	36.9 ± 2.7	33.2 ± 4.2	28.9 ± 5.2	30.6 ± 8.5	39.6 ± 4.4	29.7 ± 3.4
14	25.5 ± 3.1	11.3 ± 4.2*	8.2 ± 5.8*	6.8 ± 11.7*	9.5 ± 5.2*	8.1 ± 3.6*
16	1.3 ± 2.4	1.3 ± 2.1	1.3 ± 3.1	2.3 ± 5.0	8.6 ± 3.5	12.1 ± 1.6*
17	2.7 ± 2.4	3.3 ± 2.1	3.2 ± 3.0	4.8 ± 4.8	11.1 ± 3.4	14.0 ± 1.6*
18	7.3 ± 2.4	15.5 ± 2.0*	12.2 ± 3.0	22.7 ± 5.0*	26.2 ± 3.3*	26.0 ± 1.6*
19	10.2 ± 2.4	19.8 ± 2.2*	16.5 ± 3.0	28.3 ± 5.4*	31.8 ± 3.4*	30.4 ± 1.8*
20	30.5 ± 4.1	46.7 ± 3.5*	50.8 ± 6.2*	58.1 ± 7.5*	63.5 ± 9.2*	69.0 ± 3.9*
21	31.5 ± 4.1	48.3 ± 3.6*	52.4 ± 6.2*	60.1 ± 7.7*	65.6 ± 9.3*	70.6 ± 4.0*
23	18.9 ± 3.2	24.8 ± 2.6	32.5 ± 4.8*	28.1 ± 5.5	29.5 ± 8.1	37.7 ± 3.2*
24	20.5 ± 3.2	28.2 ± 2.7	34.7 ± 5.1*	33.9 ± 5.6	32.3 ± 8.1	40.4 ± 3.3*
28	-2.5 ± 0.6	-5.9 ± 1.1*	-6.1 ± 0.9*	-6.6 ± 3.0	-5.2 ± 1.1*	-5.2 ± 0.8*
30	-1.3 ± 1.1	-4.4 ± 1.5	-2.5 ± 1.1	-8.7 ± 4.0*	-3.5 ± 1.6	-1.9 ± 1.2
32	-1.7 ± 0.6*	-5.4 ± 0.9*	-3.8 ± 0.7	-9.5 ± 2.5*	-8.4 ± 2.8*	-4.2 ± 0.8*
35	-1.1 ± 0.3	-2.2 ± 0.6	-1.4 ± 0.4	-3.1 ± 1.5	-2.1 ± 0.6	-1.6 ± 0.4
37	2.0 ± 0.3	2.8 ± 0.4	2.9 ± 0.4	3.8 ± 0.8*	3.7 ± 0.5*	2.9 ± 0.4
40	-1.3 ± 0.7	-2.9 ± 0.9	-2.0 ± 0.8	-6.2 ± 2.5*	-2.6 ± 1.1	-3.5 ± 0.7
42	3.4 ± 1.5	10.5 ± 2.1*	7.2 ± 0.9	15.8 ± 7.7*	12.9 ± 2.7*	10.2 ± 1.9*
48	1.0 ± 0.2	1.3 ± 0.2	1.5 ± 0.2	2.0 ± 0.5*	1.8 ± 0.2*	1.4 ± 0.2
49	-20.0 ± 3.3	-26.9 ± 3.0	-32.2 ± 5.2	-36.1 ± 6.5*	-29.2 ± 8.3	-38.7 ± 3.5*
52	8.7 ± 0.7	7.1 ± 0.6	7.0 ± 1.2	9.9 ± 1.0	8.9 ± 1.3	9.1 ± 0.5
53	34.4 ± 3.1	28.2 ± 2.8	27.7 ± 6.2	39.3 ± 4.9	31.6 ± 6.5	30.9 ± 2.7
54	0.8 ± 0.5	0.8 ± 0.7	0.8 ± 1.0	4.3 ± 2.3*	2.1 ± 0.9	0.9 ± 0.1
57	52.3 ± 7.6	63.3 ± 5.4	55.2 ± 6.7	104.0 ± 10.1*	107.7 ± 6.5*	103.4 ± 2.8*
58	71.6 ± 4.5	69.7 ± 3.8	65.8 ± 6.1	101.2 ± 7.5*	95.1 ± 6.3*	94.5 ± 2.9*

Data shown are fluxes calculated by Equation 3-13 ± SE. Errors were estimated by Equation 3-14 as described in **Materials and Methods**. *Significantly different from sham-burn control group ($p < 0.05$) as analyzed by *t*-test using the estimated errors.

Like the measured metabolite exchanges rates, the intracellular fluxes were differentially affected by burn injury. Flux through the glucose 6-phosphate dehydrogenase reaction (reaction no. 1) rose to 1.4 times above the sham-burn control two days after burn, remained elevated until day four, and decreased to 1.2 times above the sham-burn control by day seven. Flux through pyruvate carboxylase (reaction no. 14) decreased to 50 % of the sham-burn control one day after burn, and continued to decline for the duration of the study period. Flux through malate dehydrogenase (reaction no. 21) rose to 1.4 times above the sham-burn control, and continued to increase steadily to 2.1 times above the sham-burn control by the end of the study period. As the afore illustrated diversity of the flux response profiles combined with the large number (60×6) of fluxes under consideration (Tables 3-4 and 3-5) prohibited a comprehensive analysis by visual inspection, the fluxes (measured and calculated) were subjected to a data dimensionality reduction analysis.

Hierarchical clustering identifies groups of reactions with similar activation or repression time profiles based on similarity measures between vectorized forms of reactions. The fluxes shown in Tables 3-4 and 3-5 were normalized with respect to sham-burn control levels, log (base 2) transformed, and clustered hierarchically by average linkage. The result, shown in Figure 3-4, includes 52 out of the 60 total reactions present in the metabolic network. The excluded reactions differed in their directions from the corresponding control reactions at some or all times after burn injury, and thus their normalized fluxes could not be log transformed. Interestingly, these reactions were all associated with the transport of amine compounds: ammonia output (reaction no. 26), alanine uptake (no. 29), cysteine uptake (no. 33), tyrosine uptake (no. 41), glutamate output (no. 43), and aspartate output (no. 50). From the dendogram, six physiologically recognizable, distinct reaction clusters were identified, denoted A ~ F. The choice regarding the number clusters was guided by statistics (see **Materials and Methods**) and decided by physiological intuition, an accepted procedure [191]. Referring to the reaction numbers in Table 3-2, the clusters were interpreted to correspond to the following reaction groups or pathways: A, TGL breakdown and ketone body formation; B, TCA cycle and respiration; C, amino acid uptake; D, urea cycle; E, PPP; and F, gluconeogenesis. In this context, the time profiles of the urea cycle and PPP most closely resembled each other, while that of gluconeogenesis was most distinct from the other pathways, which is reflected in the relative distances between the corresponding cluster nodes in the dendogram tree.

In order to better visualize the trends suggested by these groupings, the normalized, log transformed fluxes were plotted as a function of time in Figure 3-6. Once again referring to Table 3-2, fluxes through pathways associated with fatty acid oxidation (Figure 3-6A) showed a sharp, temporary increase on day 3 post-burn, which dissipated by day 7 post-burn. The reactions with the largest proportionate increase in flux were lysine oxidation and acetoacetate synthesis, rising to 7.4 and 2.4 times over sham-burn control. However, the absolute values of these fluxes were small compared to those through other reactions in this group, such as ketone body release and fatty acid breakdown, which remained relatively unchanged. In contrast, panels 5D and 5E show that burn injury increased fluxes through the urea cycle and PPP relatively rapidly to near maximal values by 2 days post-burn. However, while the urea cycle fluxes remained elevated throughout the first week after burn injury, the PPP fluxes declined after day 4. Fluxes through the TCA cycle and respiratory chain (Figure 3-6B) changed more slowly, increasing to near maximal values by day 4 post-burn. Reactions associated with amino acid uptake and catabolism (Figure 3-6C) responded to burn injury with mixed behavior, as these fluxes increased to maximal or near maximal values by day 3 post-burn, and declined by day 4 post-burn, but still remained elevated by day 7 post-burn compared to sham-burn control. Finally, consistent with the observations regarding glucose and lactate exchange by the liver, gluconeogenic reaction fluxes remained largely unaltered by burn injury, with the exception of day 4 post-burn, when fluxes through the reactions producing glucose 6-phosphate rose slightly to 1.25 times above sham-burn control.

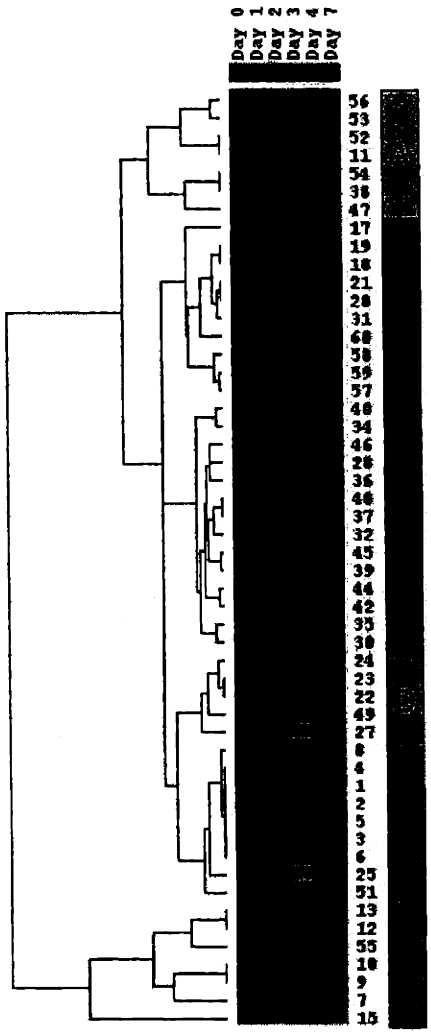

Figure 3-5. Hierarchical clustering of intracellular fluxes.

Calculated and measured fluxes were averaged for each group and normalized with respect to the sham-burn control flux averages. The normalized fluxes were $\log_2$ transformed and clustered using an agglomerative, average linkage technique using correlation as the similarity metric. Each colored square in the dendogram represents the logs transform value for one averaged, normalized reaction flux for a given treatment group. Repression is denoted by green, no change by black, activation by red, and missing value by gray, where the intensity of green or red corresponds to the degree of repression or activation. Numbers at the end of each reaction row refer to reaction numbers in Table 3-2. The dendogram tree shows the hierarchical relationships between reaction clusters, where the proximity of the branches corresponds to the similarity between objects. The colored letter blocks identify reaction group at the level of 6 clusters: A, TGL breakdown and ketone body formation; B, TCA cycle and respiration; C, amino acid uptake; D, urea cycle; E, PPP; and F, gluconeogenesis.

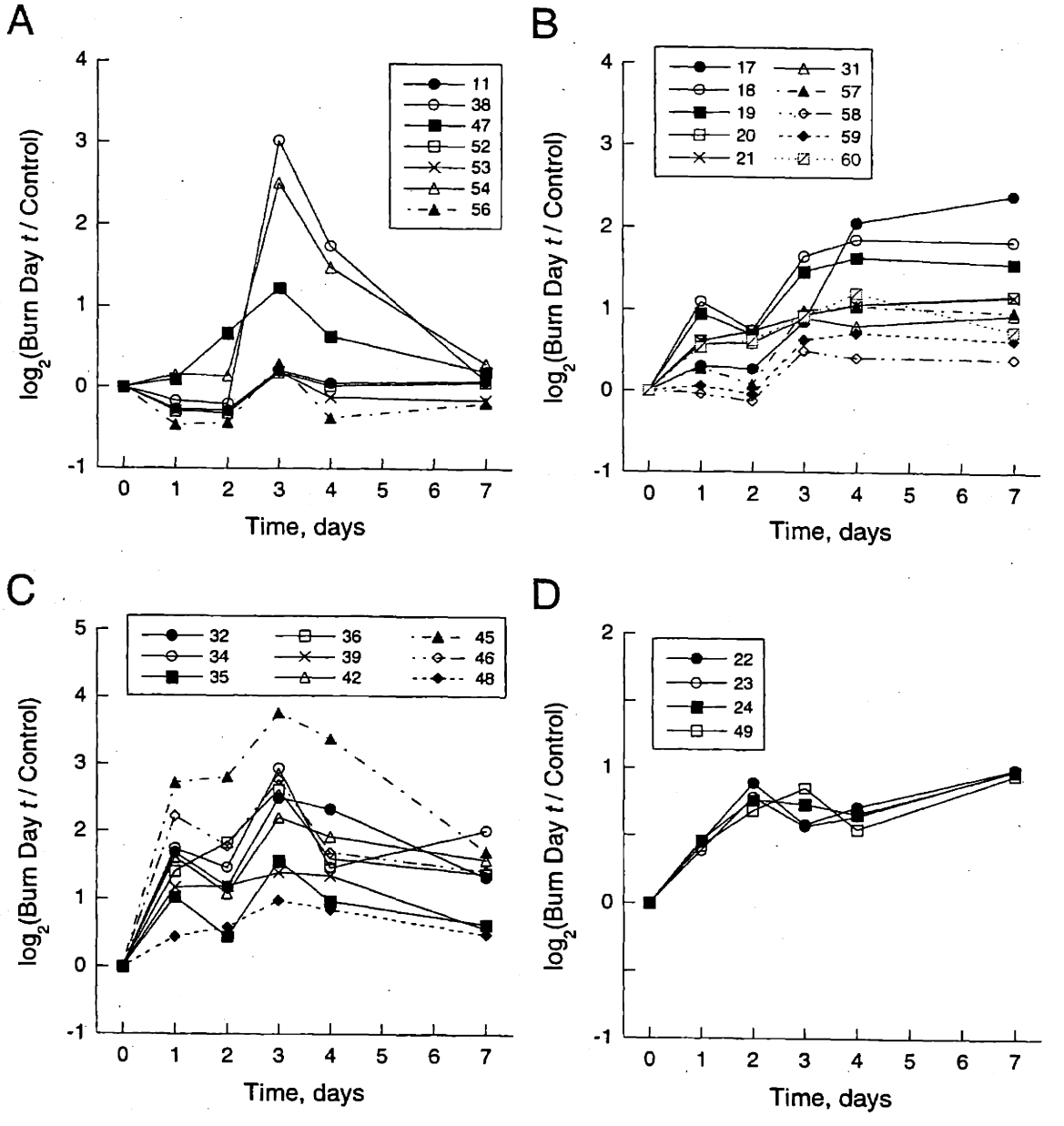

Figure 3-6. Time course of flux activation by burn injury.
Fluxes are plotted as against time after burn injury grouped according to the clusters in Figure 3-4: (A) TGL breakdown and ketone body formation; (B) TCA cycle and respiration; (C) amino acid uptake; (D) urea cycle; (E) PPP; and (F) gluconeogenesis. Each data point represents the normalized, $\log_2$ transformed average flux value for one reaction for a given treatment group. Error bars are omitted for clarity.

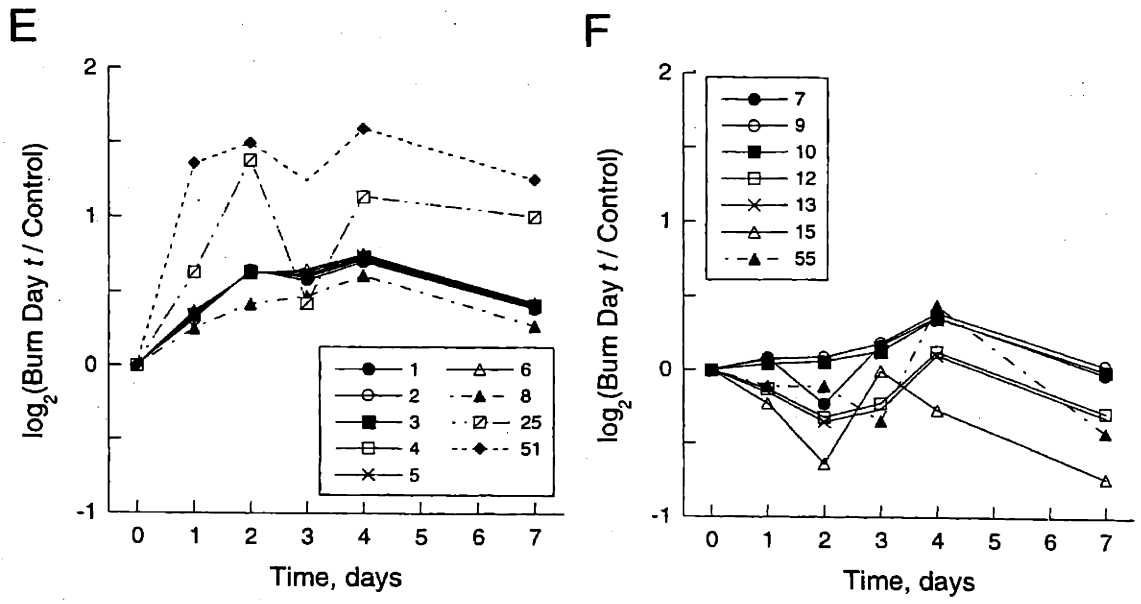

Figure 3-6. continued.

Taken together with the metabolite exchange data, the above observations pointed to a differential time response of metabolic pathways to burn injury. In order to see this more clearly, representative reaction time profiles for each of the pathway clusters were normalized to their respective internal maximum and plotted in Figure 3-7. Comparing panels A ~ F, it can be seen that the various pathways responded to burn injury in an asynchronous fashion. In particular, the time lag between the maximal induction of the TCA cycle (Figure 3-7B) (thought to be the major pathway in the liver (via electron transport) for producing ATP), and the major energy requiring pathways, (urea cycle and PPP) (panels D and E, Figure 3-7), suggested the presence of an energy gap, as the continuous increase in TCA cycle fluxes and oxygen uptake past 2 days post-burn was not matched by the ATP demand from urea, glucose, and ketone body synthesis (Table 3-6).

The gap between predicted ATP production and demand persisted even after accounting for ATP demand from increased secreted protein synthesis. Using [U-^{14}C]leucine as a tracer, the total rate of accumulation of secreted proteins in the perfusion medium was measured for livers perfused four days after burn or sham-burn treatment, which corresponded to the maximum of the predicted ATP gap. From Figure 3-8, it can be seen that burn injury increased the rate of leucine incorporation into protein 2.7 fold over the sham-burn control. However, the absolute values of these synthesis fluxes were small compared to the metabolic demands. Assuming that the average protein is 500 residues long, 4 high energy phosphate bonds are broken per one peptide bond formed [192], and leucine accounts for ca. 10 % of the residues, the ATP requirements for secreted protein synthesis for the sham-burn control and Burn Day 4 livers are 7 and 18 μmol/g liver/hr, respectively. As shown in Table 3-6, these values constituted less than 1 % of the predicted ATP gap between the burn (day 4) and the sham-burn control.

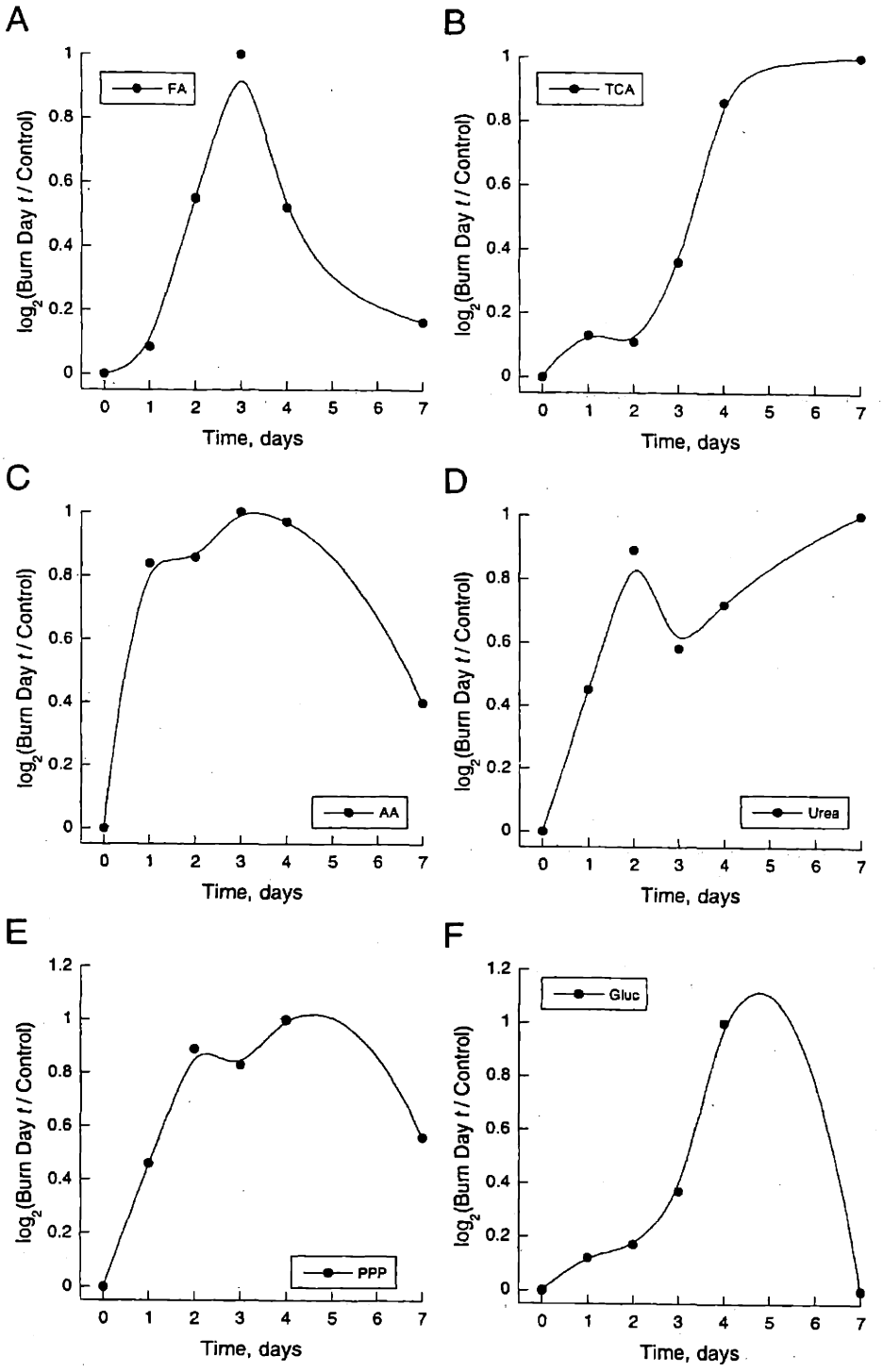

Figure 3-7. Representative time courses.
Representative reaction time courses from Figure 3-6 were normalized to their respective maxima and compared in corresponding panels (A) ~ (F). Error bars are omitted for clarity

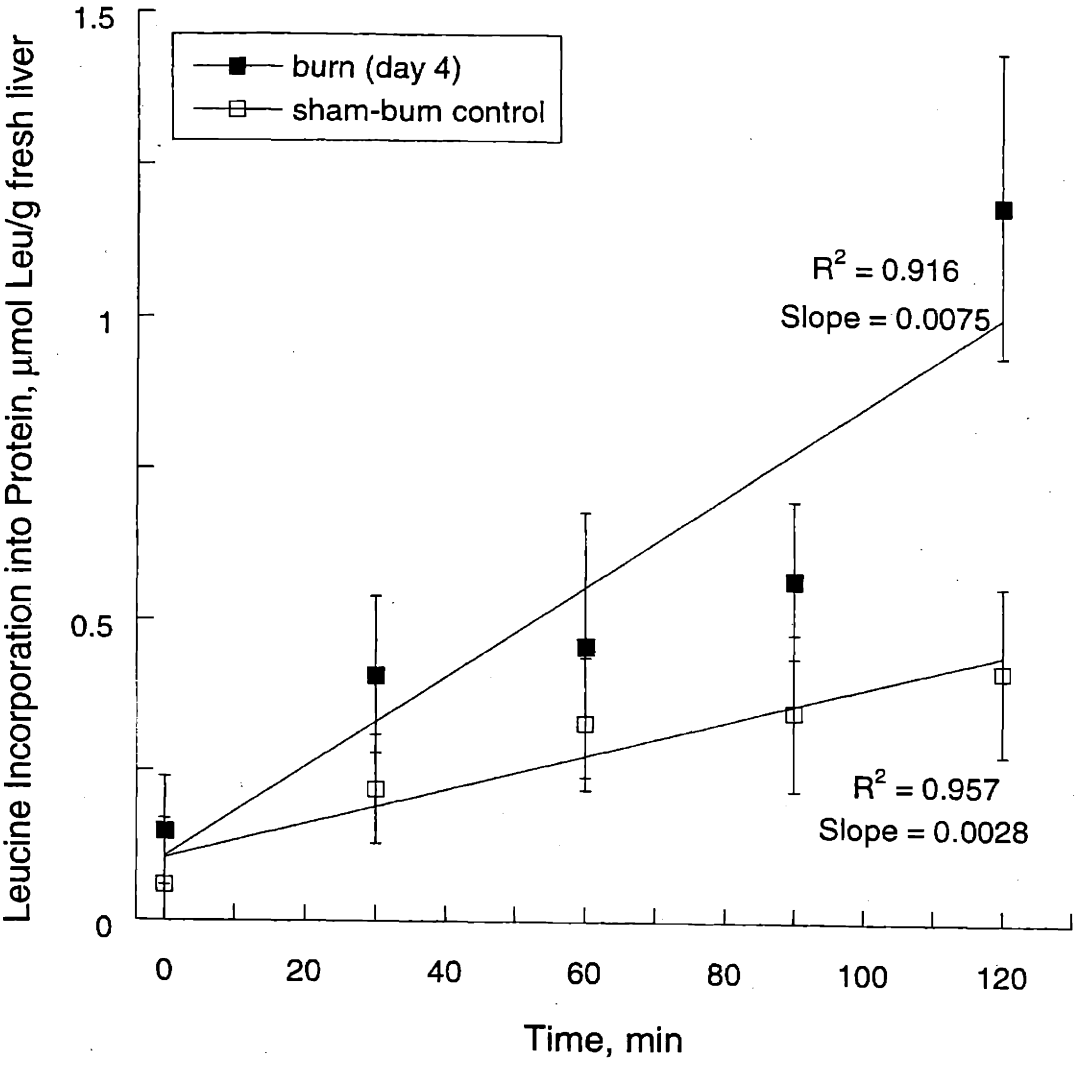

Figure 3-8. Secreted protein synthesis by the perfused liver.
Concentration profiles of labeled protein accumulation in the perfusion medium reservoir. Data shown are averages for 5 burn (day 4) (■) and 6 sham-burn control (□) livers ± SE. Slopes were obtained from linear regression statistics generated on the averaged data using MS Excel.

Table 3-6. ATP Balance

Reaction. No.	ATP Flux, Day(s) After Treatment, μmol/g liver/hr					
	0 (Sham-burn)	1	2	3	4	7
	n = 12	n= 9	n = 4	n = 4	n = 5	n = 8
Predicted Demand	390 ± 30	412 ± 29	422 ± 52	504 ± 70	467 ± 58	474 ± 24
Gluconeogenesis	173 ± 9	146 ± 12	125 ± 10*	131 ± 17	170 ± 10	128 ± 9*
Urea Synthesis	58 ± 7	78 ± 5*	100 ± 6*	90 ± 7*	91 ± 12*	116 ± 6*
KB Synthesis	75 ± 8	55 ± 6	56 ± 10	92 ± 5	58 ± 11	66 ± 6
Predicted Production	534 ± 35	599 ± 35	566 ± 61	870 ± 81*	830 ± 70*	815 ± 31*
Mitoch. Production	305 ± 34	336 ± 29	306 ± 34	514 ± 44*	528 ± 43*	510 ± 23*
Predicted Gap	144 ± 18	188 ± 19	144 ± 31	366 ± 41*	363 ± 40*	341 ± 19*
Measured OUR	59.8 ± 4.1	62.4 ± 5.2	58.1 ± 1.9	92.5 ± 5.0*	98.3 ± 0.4*	92.9 ± 5.1*
Apparent P/O	3.26	3.30	3.63	2.72	2.38	2.55

ATP synthesis and consumptions rates were calculated from the fluxes shown in Tables 3-4 and 3-5. Values are reported as mean ± SE. Errors were estimated by Equation 3-14 as described in **Materials and Methods**. *Significantly different from sham-burn control group ($p < 0.05$) as analyzed by *t*-test using the estimated errors.

The observations regarding an apparent ATP gap, taken together with the activation of the PPP, which in the non-regenerating liver can indicate presence of oxidative stress, suggested that burn injury may induce the expression of redox sensitive uncoupling proteins, which then could lead to a lowered efficiency in the synthesis of ATP from substrate oxidation. One class of uncoupling proteins termed UCPs are found in a wide array of mammalian tissues and have recently been implicated in the metabolic adaptation to oxidative stress [193-196]. An initial screen by RT-PCR revealed that only one member of this family, UCP2, was present in detectable quantities in the liver, consistent with reports in the literature [197]. Subsequent Western blot analysis for UCP2 in liver tissue extracts showed that the respiratory uncoupler was present in burn livers on days 2, 3, 4, and 7, but neither in sham-burn control livers nor burn livers on day one (Figure 3-9). The largest amount of UCP2 protein was present in the liver on day 3 post-burn, which also coincides with the onset of the apparent ATP gap. Similar to the PPP profile, UCP2 expression gradually decreased over days 4 ~ 7 to the level found on day 2 post-burn.

3.4 Discussion

In these studies, we examined the progression of burn injury associated hepatic hypermetabolism during the first of week. Using previously developed experimental and mathematical models, we characterized the time course of changes to liver metabolite exchange and intracellular fluxes in isolation from systemic effects. Hierarchical clustering of the measured and calculated metabolic fluxes identified physiologically recognizable groups of reactions that showed correlated activation or repression profiles: fatty acid oxidation, TCA cycle, amino acid catabolism, urea cycle, PPP, and gluconeogenesis. These pathways were affected differentially by burn injury, which pointed to an apparent mismatch between predicted ATP production and demand, which was reflected in the rates of ATP synthesis and consumption calculated from the metabolic fluxes. The final set of experiments presented in this chapter explored the possibility that this mismatch was caused by activation of mitochondrial respiratory uncouplers.

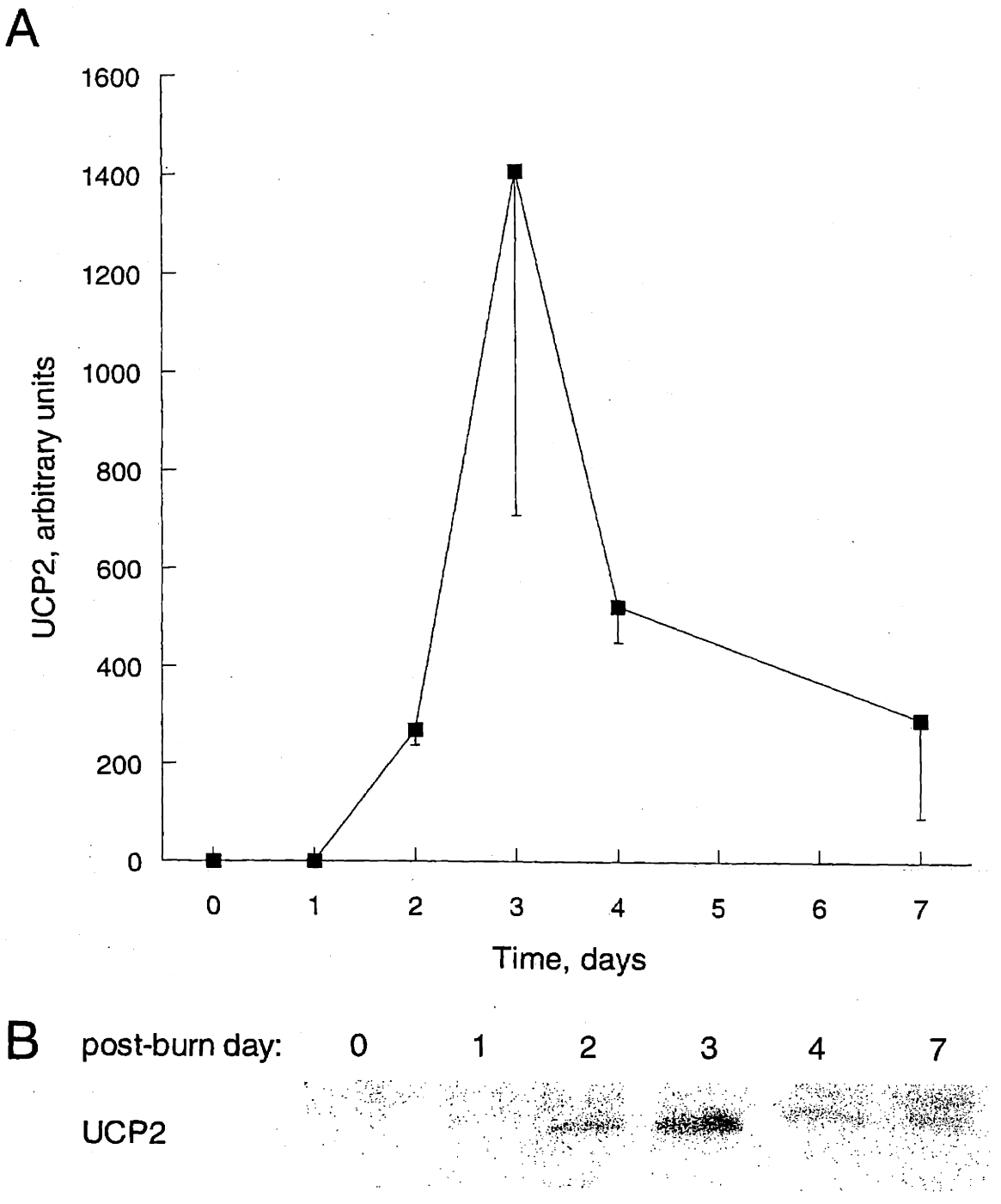

Figure 3-9. Induction of UCP2 expression by burn injury.
Volume analysis of UCP2 chemiluminescence captured from Western blots (A). Western blot of UCP2 in liver crude extracts (B). Data shown in (A) are averages for two Western blots ± SE, where each blot contained replicate lanes corresponding to two livers for each treatment group.

In deriving our flux estimates, we have assumed that the liver was in a metabolic steady state for the duration of the perfusion and that our model approximated the stoichiometric relationships of all major metabolic pathways in the fasted liver. The first assumption was justified by the observation that the metabolites accumulated in, or disappeared from, the medium in a linear fashion. With the second assumption, we recognize that the number of reactions included in our model was probably far less than the actual number of reactions participating in liver metabolism. However, metabolic reactions are known to vary in their quantitative contributions to metabolite turnover [49]. The present model was comprised of the major pathways of central carbon metabolism, which to the best of our knowledge were active in the fasted liver and accounted for most of the metabolite turnover examined in this study. Statistically, this approximation seemed valid, as application of the macroscopic balance test showed good consistency between the measurements and the assumed biochemistry. Thus the approximation represented an acceptable sacrifice of detail, which kept the number of required measurements within experimentally reasonable bounds, i.e. on the order of 10 to 100.

Further validation of the model flux estimates was obtained by experimentally measuring fluxes for selected pathways. In prior work, we have checked the calculated PPP fluxes against measurements obtained by radioisotope labeled tracer experiments and found good agreement [186]. In the present work, we tested the assumption that the amino acid flux into protein synthesis was negligible compared to the flux into pathways of central carbon metabolism. Using radio-labeled leucine, which is consistently present in most liver synthesized proteins, we measured the rate of amino acid incorporation into secreted protein synthesis in the perfused liver (Figure 3-8). Assuming, as in **Results**, that leucine accounts for roughly 10 % of the residues in secreted proteins, and an average nitrogen per residue score of 1.5, the expected nitrogen efflux from the liver via protein was 3 or 7 μmol/g liver/hr for the sham-burn or post-burn day 4 condition, respectively (Table 3-7). Compared to the corresponding nitrogen efflux via urea, 47 or 76 μmol/g liver/hr, respectively, this was smaller by one order of magnitude. Thus, we concluded that the omission of an equation for protein synthesis only negligibly impacted the calculation of the metabolic fluxes. This conclusion was also supported by drawing a nitrogen balance around the liver (Table 3-7), where the differences between nitrogen input and output varied from 1 to 34 % of the corresponding input fluxes, none of which were statistically significantly different from zero.

Table 3-7. Nitrogen Balance

	Nitrogen Flux, Day(s) After Treatment, μmol/g liver/hr					
	0 (Sham-burn) n = 12	1 n= 9	2 n = 4	3 n = 4	4 n = 5	7 n = 8
Uptake	50.2 ± 8.8	92.7 ± 10.7	100.1 ± 12.5	109.3 ± 27.8	106.4 ± 11.4	96.3 ± 8.6
Output	67.1 ± 8.8	86.1 ± 9.0	115.5 ± 1.9	73.7 ± 7.7	105.3 ± 19.3	123.3 ± 9.4
Net	16.9 ± 12.4	-6.6 ± 15.3	15.4 ± 7.6	-35.6 ± 25.9	-1.1 ± 29.1	27.0 ± 4.8
Net, % of uptake	34	-7	15	-33	-1	29
Protein	3				7	

Nitrogen and consumptions rates were calculated from the amino acid and urea exchange rate measurements shown in Table 1. Values are reported as mean ± SE. A negative net flux indicates that amino acids were taken up by the liver. In all cases, nitrogen uptake and output were not statistically significantly different ($p > 0.05$) as determined by ANOVA.

One series of observations made in these studies potentially inconsistent with published reports was that the glucose output by the perfused liver remained basically unchanged throughout the first week after the burn injury. Several investigators have observed that blood glucose levels are significantly elevated after burn injury [198-200]. Moreover, this elevation has been attributed to increased gluconeogenic activity by the liver [48, 201]. In order to verify that our observations regarding liver glucose production were not artifacts of the perfused liver, we compared the hepatic glucose gradient and blood flow between day 4 burn and sham-burned animals. The time of comparison after injury was chosen based on the observation that livers perfused day 4 post-burn showed the largest (albeit statistically insignificant) difference in glucose output compared to sham-burn control livers. The *in vivo* glucose gradient across the liver was determined by sampling the blood in the portal and hepatic veins and the blood flow rate into the liver was measured by an ultrasound method. The results of this validation experiment were consistent with the perfused liver findings, as neither hepatic blood flow nor glucose gradient was significantly altered by burn injury (Figure 3-10). There are several possible explanations that could reconcile our observations with the literature findings regarding glucose metabolism. One obvious candidate is that the source of the increased blood glucose concentration is not increased hepatic production, but instead the reduction in glucose uptake by the periphery, e.g. skeletal muscle, caused by insulin resistance, which has been extensively documented [202-205]. Another possible explanation is that the increased gluconeogenic activity measured by Wolfe et al. [48] in tracer experiments reflected increased futile cycling of substrates within the liver. Alternatively, the hyperglycemic response to burn injury could be species dependent. The studies in [198] were performed in guinea pigs, whereas these studies were conducted in rats. Other studies, including those performed by Jahoor et al. [206] and those referred by Wilmore [200], Waymack et al. [207], and Tredget et al. [129] were conducted in human patents. Lastly, the degree of hyperglycemia and the increase in hepatic glucose production could be proportionate to the burn size. In rats with 50 % total body surface area burns, a size significantly larger than the burns administered here, Yu et al. [199] observed increased blood glucose levels and hepatic glucose production rats.

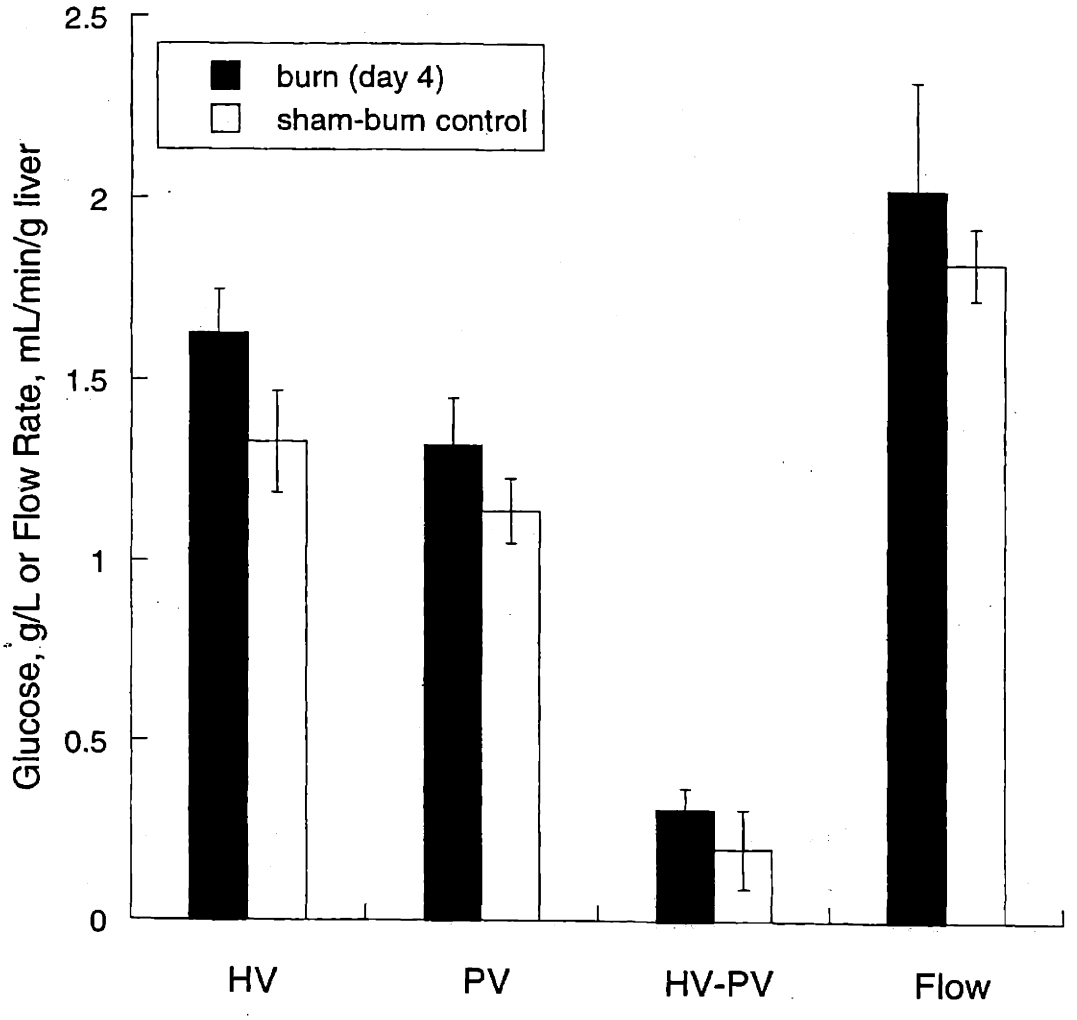

Figure 3-10. In vivo liver glucose gradient.
Glucose concentrations were measured in serum samples obtained from the hepatic and portal veins in anesthetized animals. Blood flow measurements were taken around both the portal vein and the hepatic artery and refer to the total volumetric rate of blood flow into the liver. Data shown are averages for 5 burn (day 4) and 6 sham-burn control animals ± SE.

A major finding from the analysis of this data was that metabolic pathways in the liver are activated or repressed differentially with respect to time after injury. The fatty acid oxidation, amino acid catabolism, and PPP fluxes reached maximal values between days 3 and 4 post-burn and declined thereafter. The urea cycle fluxes reached near maximal values by day 2 post-burn and remained elevated for the entire time. The TCA cycle reached maximal values by day 4 post-burn and remained elevated for the entire time. Finally, the gluconeogenic fluxes remained unaltered for the entire time.

An interesting corollary to the above finding was that a gap between the predicted ATP production and demand occurred 3 days after the initial insult. The cellular ATP level is known to remain relatively insensitive to environmental changes and the rate of ATP synthesis is typically regulated by demand [192]. Thus, it seemed unlikely that the predicted ATP over-production reflected actual conditions in the liver. One possible explanation for the predicted gap was that the calculated ATP demands, particularly for livers perfused 3, 4, and 7 days post-burn, were underestimates, and energetic requirements were indeed higher in these livers, perhaps due to the induction of futile cycles, whose presence after burn injury has been suggested by others [48]. Alternatively, the predicted rates for ATP production in Burn Day 3, 4, and 7 livers could be overestimates, which would be the case if there were a drop in the efficiency of ATP synthesis past 2 days post-burn. When calculating ATP synthesis rates, it was assumed that electron transfer from NADH to O_2 contributed to the electrochemical gradient across the inner mitochondrial membrane without any slippage or leakage. However, in recent years, endogenous respiratory uncouplers, whose expression effectively lowers the P/O ratio, have been found in a wide range of tissues including the liver, particularly during inflammatory states [197]. Thus, we hypothesized that the apparent over-production of ATP was an overestimate resulting from the partial uncoupling of oxidative phosphorylation and substrate oxidation. This hypothesis was at least partially confirmed by Western blot analysis of a liver specific uncoupler (UCP2), which showed that the induction of UCP2 strongly correlated with the onset of the predicted ATP gap (Figure 3-9).

It is thought that at least for the short term, hepatic hypermetabolism benefits the host by supporting the wound healing process via the synthesis of acute phase proteins and energy substrates, but in the long term, the persistence of this response harms the host by eroding the body lean mass and taxing the visceral organs [208, 209]. The findings reported here are

consistent with this etiology and may yield a biochemical explanation for the harmful consequences of prolonged hypermetabolism. Our results suggest that the liver is directed to increase amino acid uptake shortly (1 ~ 2 days) after the burn injury. This response is presumably hormone mediated and involves the induction of transporters, as a simple mass action effect or short term activation via chemical modifiers could not explain the differences observed between sham-burn and burn livers perfused with identical media. Experiments with membrane vesicles isolated from burned rat hepatocytes have shown that increased influx of amino acids into the liver one to 3 days after the injury is mediated by expression of additional transporter proteins [136]. Interestingly, the amino acid loading supported not only increased protein production (Figure 3-8), but also gluconeogenesis, as the increase in amino acid uptake was accompanied by a rise in the urea cycle fluxes.

As alluded to earlier, the increased flux through gluconeogenesis was diverted away from glucose output into the PPP, which suggested that the liver experienced a downward shift in the cellular NADPH to $NADP^+$ ratio. The lowered cellular reduction potential could have been caused by the oxidative burst of neutrophils, which have been shown to temporarily sequester in the liver ~ 3 hrs after burn injury for a period of 24 to 48 hrs. [210]. Increasing flux through the PPP allows increased turnover of NADPH, which in the non-regenerating, fasted liver is primarily used by the glutathione peroxidase-reductase system to maintain intracellular pools of reduced glutathione (GSH). GSH are important scavengers of reactive oxygen species (ROS) in the liver.

With the progression of the hypermetabolic response (3 ~ 4 days after the injury), substrate oxidation via the TCA cycle in the burn livers rose to significantly higher levels than sham-burn control livers, possibly contributing to conditions that lead to the mitochondrial generation of super oxide anions [178, 179]. Cells can limit this process by expressing uncoupling proteins, which increases respiratory chain activity and limits electron interaction with oxygen [211, 212]. The consequence of this partial uncoupling of ATP synthesis from electron transport is that the feedback regulation of substrate oxidation via the TCA cycle by ATP is also loosened. In the present case, one such uncoupler, UCP2, was found to be expressed in livers harvested on days 2 ~ 7 after the burn injury. Thus, the continued increase in liver oxygen consumption past day 2, beyond a level that can be accounted for by incremental metabolic demand, could be due to the action of the uncoupler. This could also explain the

decline in the flux through the redox sensing pathway PPP past day 4, when the fluxes in and around the TCA cycle reached near maximal values. The ROS limiting action of UCP2 could have improved the overall cellular redox balance, diminishing the demand for NADPH by the glutathione reductase-peroxidase system. On the other hand, the expression of UCP2 peaked on day 3, and declined gradually, but not completely, on days 4 and 7, while the increase in oxygen consumption by the liver was sustained over this period. It remains to be seen whether there was a threshold level of UCP2 that led to the increase in oxygen consumption, which could reconcile the UCP2 expression and the oxygen consumption profiles.

With a comprehensive set of metabolic measurements and an integrated analysis of the metabolite data, we have demonstrated that metabolic pathways in the liver are differentially activated or repressed during the first week of the injury. These results are consistent with the known etiology for the hypermetabolic response in the liver, and suggest a redox perturbation mechanism for the harmful consequences of sustained hypermetabolism, which in turn supported the multiple insult theory for organ dysfunction. Under this hypothesis, the first insult, in this case a severe burn, lowers or even depletes the cellular defenses against ROS, and a second insult, such as infection, causes irreversible damage to the weakened organ. One short-coming of the present study was that the size of the burn was too small to cause significant mortality, which prevented testing the efficacy of antioxidants in preventing organ dysfunction and mortality. However, studies by Lalonde et al. [137, 213] in burn and endotoxin treated rats showed that bolstering the liver antioxidant resources prevented mortality. Whether the hypermetabolic response caused the oxidative stress related liver dysfunction or merely represented the metabolic aspect of this stress remains to be elucidated in further studies.

CHAPTER 4. DIFFERENTIAL ACTIVATION OF METABOLIC PATHWAYS IN CULTURED HEPATOCYTES BY H_2O_2 AND GLUCAGON

4.1 Introduction

Inflammation is a coordinated systemic response involving a number of mediators that trigger metabolic as well as immune responses in the host. In addition to classical stress hormones and inflammatory cytokines, reactive oxygen species (ROS) are increasingly recognized to play an important role in mediating both types of responses. ROS include oxygen free radicals, which are oxygen containing chemicals that contain one or more unpaired electrons, and small molecular weight peroxides, which easily give rise to oxygen free radicals. Biologically relevant ROS include superoxide anion ($O_2^{-\bullet}$), hydroxyl radical ($HO^{\bullet}$), nitric oxide ($NO^{\bullet}$) and hydrogen peroxide (H_2O_2). They may be generated by a variety of endogenous mechanisms or by external stresses, such as toxic chemical challenge or UV irradiation. Endogenous mechanisms include autoxidation of flavins and quinones, enzyme catalysis, microsomal activity, and leakage from mitochondrial electron transport chain. ROS are also natural byproducts of aerobic metabolism, and relatively harmless in small amounts due to cellular defenses, which include both small molecules scavengers and enzymatic reduction systems [214]. In larger amounts, ROS overwhelm cellular defenses and, under certain conditions, cause irreversible damage to membrane lipids, nucleic acids, and other macromolecules [215]. It has been known for some time that phagocytic cells utilize this cytotoxic aspect of ROS to destroy engulfed foreign particles during inflammation [216].

More recently, ROS have also been implicated in cellular stress signaling with direct metabolic consequences. Mitochondrial ROS produced during hypoxia has been suggested to act as second messengers in oxygen sensing by cytochrome oxidase in cardiomyocytes [217]. Oxidatively modified low density lipoproteins (LDL) have be shown to modulate the DNA binding affinity of transcription factors that mediate cytokine and growth factor activity [218]. Exogenously added hydrogen peroxide has been observed to induce apoptosis by caspase action in a rat hepatocyte cell line RALA255-10G [219]. In Hep3B cells, another hepatocyte cell line, hypoxia triggered mitochondrial ROS production activated transcription of several gene products, including glycolytic enzymes aldolase and phosphoglycerate kinase. Other stress

pathways targeted by ROS include mitogen activated protein (MAP) kinase cascade [220] and nuclear factor kappaB (NFκB) activation [221].

ROS also directly affect intermediary metabolism by inducing defense pathways that synthesize and recycle antioxidant molecules, which require amino acid substrates and reducing equivalent NADPH. Prominent among cellular antioxidant defenses are the free radical scavenger glutathione (GSH) and its associated enzymes GSH peroxidase (GSHP) and reductase (GSHR). GSHP reduces potentially harmful H_2O_2 and other peroxides to water and alcohol. In the process, GSH is converted to the oxidized dimer GSSG. In order to continue peroxide reduction, GSSG has to be reduced to GSH by GSHR, which requires the cofactor NADPH. By way of this chain of reactions, ROS draw flux through the PPP, which is the main source of cytosolic NADPH. Another, recently discovered, metabolic pathway purported to be directly affected by ROS is mitochondrial respiration. Various analogs of mitochondrial uncoupling proteins, which partially detach ATP production from oxygen consumption and curtail release of unpaired electrons from the respiratory chain, have been reported in a variety of tissues under oxidative stress conditions, including UCP2 in the liver [194].

Results from studies detailed in the two previous chapters have shown that burn injury unregulated fluxes through pathways in the liver that indicate activation of the above mentioned two types of antioxidant defense mechanisms. Specifically, data in Chapters 2 and 3 showed increased flux through the PPP without obvious synthetic demand for NADPH as well as time dependent induction of UCP2 in livers isolated from burned animals. With this motivation, the studies in this chapter explore a possible role for ROS in mediating injury induced hepatic hypermetabolism. In order to precisely control the dose and timing of ROS stress, we used a well-defined cell culture system developed previously in our laboratory, which has been shown to exhibit long-term stable function [222]. Measured metabolic parameters were chosen to represent benchmark indices of hepatic hypermetabolism as determined in the perfused liver studies.

4.2 Materials and Methods

4.2.1 Reagents and culture media

The seeding medium (C+H) consisted of Dulbecco's modified Eagle medium (DMEM) supplemented with 10 % fetal bovine serum (FBS) by volume, 20 ng/mL EGF, 0.5 U/mL insulin, 2.0 nM glucagon, and 7.5 μg/mL hydrocortisone. The low hormone medium (LH) consisted of DMEM supplemented with 10 % FBS by volume, 100 μU/mL insulin, 0.1 nM glucagon, and 75 ng/mL hydrocortisone.

4.2.2 Cell culture

Hepatocytes were isolated from adult female Lewis rats weighing 150 – 200 g according to the two-step collagenase perfusion technique described by Seglen [223] as modified by Dunn et al. [222]. Prior to seeding, 0.5 or 1 mL of a collagen mixture consisting of 1 part concentrated (10×) DMEM and 9 part collagen solution (1 mg protein/mL) was distributed evenly over the culture plate or dish, respectively, which was then allowed to gel at 37° for 60 min. One or 2 million cells were seeded per well of a 6-well culture plate or 60 mm culture dish (P60) and incubated in one or 2 mL seeding (C+H) medium, respectively, in a humidified atmosphere of 90 % air and 10 % CO_2 at 37°. After 24 hrs, the medium was aspirated and the cells were overlaid with a second layer of the collagen mixture. After allowing the collagen mixture to gel for 60 min at incubator conditions, fresh C+H medium was added to the cultures. After an additional 24 hrs, the C+H medium was aspirated and one or 2 mL low hormone (LH) medium was added to the cultures. Cells were kept in LH medium for the next 3 days, during which time medium was replaced daily. Five days after seeding, cultures were randomly divided and treated with various media for 1 – 7 days, during which time medium was sample and replace daily. The various culture media used in these experiments are described in Table 4-1. At the termination of each culture, cells were detached from the collagen matrix by incubating in Krebs-Ringer bicarbonate buffer containing 0.1 % collagenase and 0.2 mg/mL $CaCl_2$. The detached cells were pelleted by centrifugation and stored at –20 °C until they were assayed for intracellular proteins. Figure 4-1 shows a schematic describing the cell seeding and culture schedule for these studies.

Table 4-1. Culture Media Contents

Medium	Contents	Significance
C+H	DMEM with 10 % by volume FBS, 20 ng/mL EGF, 0.5 U/mL insulin, 2.0 nM glucagon, and 7.5 μg/mL hydrocortisone	Cell seeding
LH	DMEM with 10 % by volume FBS, 100 μU/mL insulin, 0.1 nM glucagon, and 75 ng/mL hydrocortisone	Physiological levels of hormones
G	LH with 1.0 nM glucagon	Increased substrate loading
P	LH with 1.0 mM H_2O_2	Oxidative stress
GP	LH with 1.0 nM glucagon and 1.0 mM H_2O_2	Increased substrate loading and oxidative stress
GP+NAC	G with 5 mM N-acetylcysteine	GSH synthesis
GP+DHEA	G with 200 μM dehydroepianderosterone	PPP inhibition

4.2.3 Oxygen uptake measurement

Cells cultured in P60 dishes were used to measure the rate of oxygen uptake (OUR) by matrix attached hepatocytes at various time after treatment with various media. OUR was determined using a technique originally described by Foy et al. [224] and recently modified by Balis et al. [225]. At the time of measurement, the culture dish containing collagen-sandwiched hepatocytes was completely filled with medium and covered by a polycarbonate device that makes a seal with the top edge of the culture dishes The medium used to fill the culture dish was equilibrated with a 90 % air and 10 % CO_2 gas mixture prior to the addition. Care was taken so that the medium filled the chamber entirely and no air bubbles were present. A magnetic stir bar attached to the device kept the medium well mixed during the measurement period. The rate of decline of oxygen partial pressure in the chamber was measured with a polarographic oxygen electrode (Diamond-General, #731 MiniClark PO2, Ann Arbor, MI). The electrode was calibrated off-line using a 10% w/v sodium sulfite solution for the 0 mm Hg calibration point and culture medium equilibrated with 10% CO_2 and 90% air for the 143 mmHg calibration point. The rate of oxygen uptake by the hepatocytes was taken to be the slope of the linear portion of the oxygen partial pressure curve, which corresponds to saturating oxygen conditions. Oxygen uptake rates were normalized with respect to the number of cells seeded per dish.

4.2.4 Flux through PPP

Flux through the PPP in cultured hepatocytes was measured by a radioactive tracer method described for the perfused liver by Kuehn and Scholz [226] and adapted for the 6-well culture plate. At the time of measurement, 1 μCi of D-[1-^{14}C]glucose dissolved in 100 μL of 1× PBS was added to each well of the culture plate. After gently shaking, the culture plate was quickly covered with an adhesive plate sealer. Labeled carbon dioxide evolved from the decarboxylation of D-[1-^{14}C]glucose by glucose-6-phosphate dehydrogenase (G6PD) was trapped with potassium hydroxide solution (40 % w/v) soaked filter papers attached to the plate sealer. After incubating cells in the radioactive tracer medium for 2 hrs at 37 C, the filters were removed and placed in scintillation vials. The vials were completely filled with scintillation fluid

4.2.5 Western blot analysis

Cells previously frozen and stored at –20 °C were lysed by suspending in buffer for determination of intracellular proteins. After breaking up plasma and organelle membranes by sonication, centrifugation was used to pellet and remove the membrane debris from the cell lysate. The membrane free lysate was assayed for total protein concentration by a commercially available kit (BCA, Pierce). Proteins were separated on a 12 % Tris-HCl polyacrylamide gel (Bio-Rad, Hercules, CA) and transferred to polyvinylidine difluoride membranes (Bio-Rad). Membranes were blocked for 45 min. at room temperature in buffer containing Tris-buffered saline (TBS), 0.2 % Tween-20, and 5 % powdered milk (w/v). Membranes were then incubated with rabbit anti-mouse antibody to UCP2 (Chemicon, CA) in blocking buffer overnight at 4 °C. After 3 washes with TBS-Tween-20 (TBS-T), the membranes were incubated with goat anti-rabbit IgG conjugated with horseradish peroxidase (Santa Cruz Biotechnology, Santa Cruz, CA) for 1 hr. at room temperature. After washing again in TBS-T, the membranes were developed with a chemiluminescence enhancer (Pierce, Rockford, IL) and exposed on an imaging screen (Bio-Rad). Protein bands were quantified by image analysis and expressed in arbitrary units relative to background.

4.3 Results

In prior work, we had investigated the hepatic hypermetabolic response to burn injury using a perfused liver experimental model and a metabolite balance mathematical model. Using these tools, we characterized the effect of burn injury on liver metabolism on day 4 after burn injury, which corresponded to the peak activity level of the host metabolic response during the first week after the injury. Comparing livers from burn and sham-burn treated animals, we found that burn injury significantly increased the uptake of amino acids and the fluxes through several intracellular pathways, including the TCA cycle, urea cycle, and PPP. Given the sensitivity of the PPP to cellular antioxidant concentrations, these results hinted at a connection between oxidative stress and the increased uptake and oxidation of amino acids.

In this chapter, we examined the metabolic effects of oxidative stress during high substrate loading conditions using a sandwich configuration hepatocyte culture system developed previously in our laboratory [222]. Compared to the perfused liver, this stable cell culture system

offered the advantage of simplicity and greater experimental control, where it was possible to precisely regulate the addition and removal of stress hormones and oxidants over time. In all experiments, cells were seeded in DMEM supplemented with FBS and a milieu of hormones which previously had been shown to improve cell attachment and spreading over unsupplemented DMEM [222]. However, the metabolic hormones (insulin, glucagon, and hydrocortisone) in the seeding medium were present at pharmacological levels, making the seeding medium unfit for metabolic studies. Therefore, after the initial seeding period, cells were equilibrated for 72 hrs in a low hormone medium (LH) containing physiological levels of the metabolic hormones before exposure to the various treatment media (Figure 4-1).

Substrate loading into the cultured hepatocytes was increased by the addition of glucagon to the medium. Glucagon is a pancreatic hormone known to increase gluconeogenesis and amino acid uptake by the liver *in vivo*. Taking urea output as a marker for amino acid oxidation, the cultured hepatocytes responded to glucagon in a dose dependent manner within physiological ranges of the hormone (Figure 4-2). Increasing the hormone concentration beyond physiological (> 1 nM) doses did not appreciably increase urea production by hepatocytes. Results from previous work [186] suggested that in addition to catabolic hormones, oxidative stress played a significant role in up-regulating hepatic metabolism, especially amino acid oxidation. In order to determine whether oxidant molecules directly affected amino acid metabolism in hepatocytes, hydrogen peroxide (H_2O_2) was added to the medium in various amounts. Hydrogen peroxide is an endogenous oxidant formed from the byproducts of aerobic metabolism or released by activated immune cells and has been implicated in a range of oxidative stress related metabolic adaptations, including activation of redox sensitive transcription factors [227]. Unlike glucagon, H_2O_2 did not alter urea output by hepatocytes (Figure 4-2). When added together, glucagon affected urea output by hepatocytes in a dominant fashion, as the addition and removal of the hormone raised and lowered urea production rate, respectively, regardless of the presence of H_2O_2 (Figure 4-3).

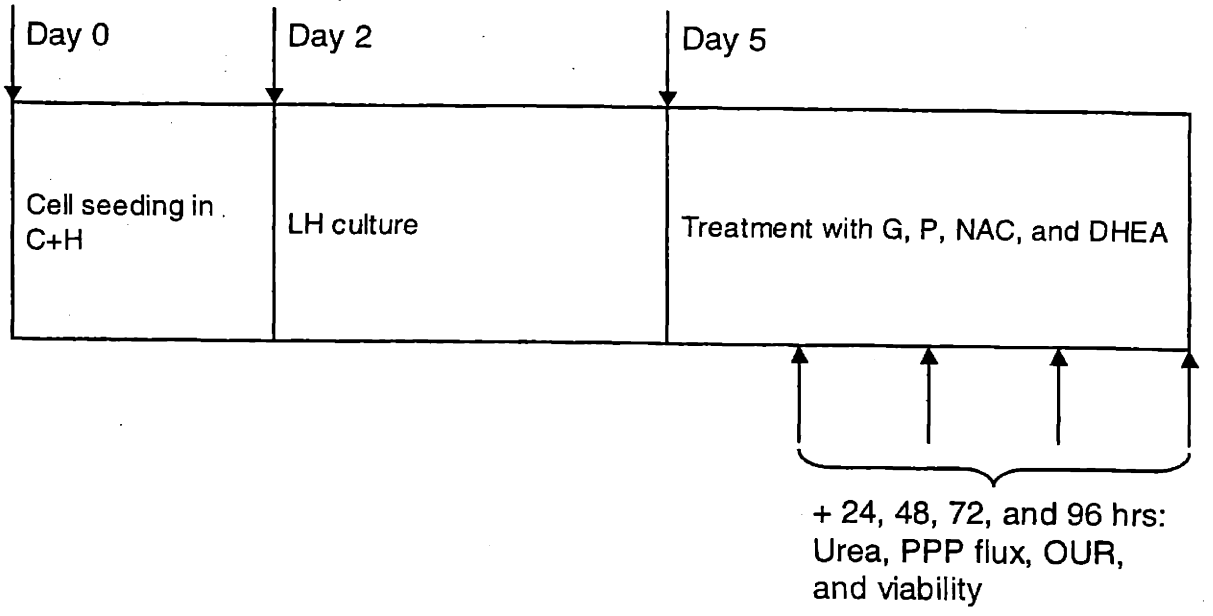

Figure 4-1. Cell culture schedule.

Cells were seeded in a serum containing medium supplemented with pharmacological levels of hormones and growth factors (C+H medium) previously shown to aid in cell attachment and spreading. Two days after seeding, cells were exposed to a serum containing medium containing physiological levels of hormones and substrates (LH medium). After equilibrating for 3 additional days, cells were divided into treatment groups, which were exposed to various media as defined in Table 4-1. Media were sampled daily at noon (± 2 hrs) and exchanged with fresh media.

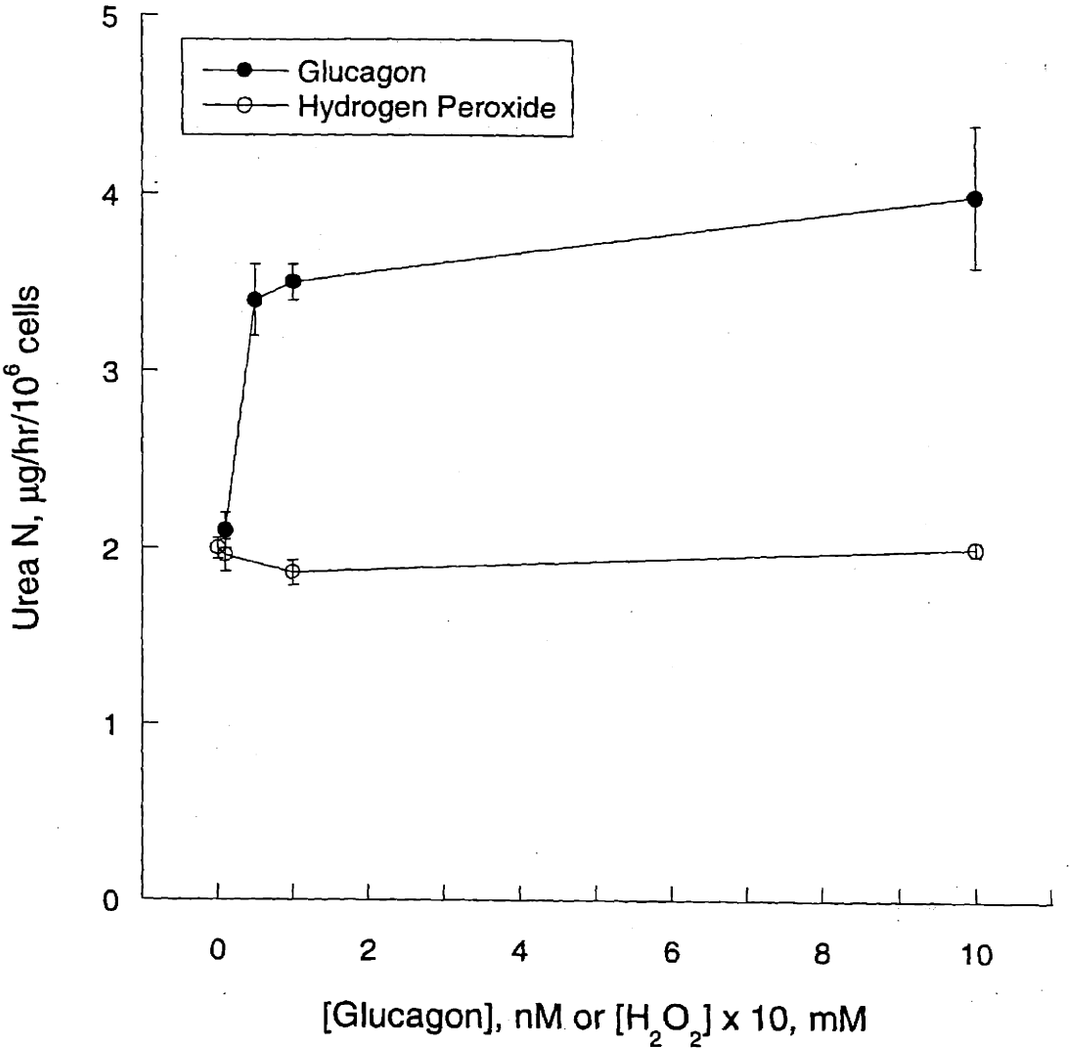

Figure 4-2. Hepatocyte dose respose to glucagon and hydrogen peroxide.
Hepatocytes cultured in the double-gel configuration for three days in basal physiological medium (see Figure 4-1 and Table 4-1) were exposed to varying doses of glucagon (0.1 to 10 nM) or hydrogen peroxide (0 to 1 mM). Dose ranges were guided by published literature values.

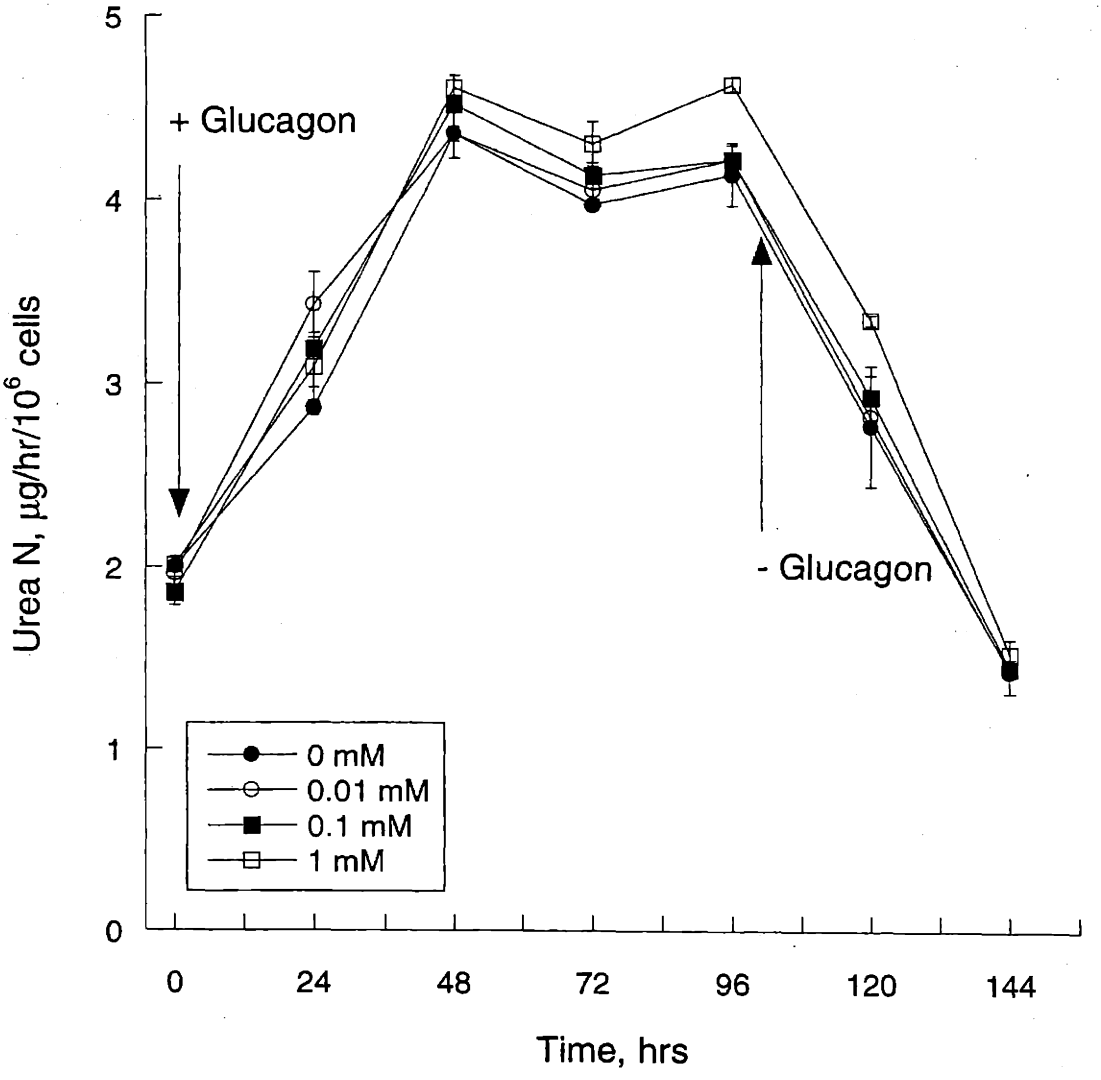

Figure 4-3. Combined effects of glucagon and hydrogen peroxide on urea production. Urea concentration was measured in medium supernatants collected at 0, 24, 48, 72, 96, 120, and 144 hrs after hepatocytes were expose to hydrogen peroxide and glucagon. Hydrogen peroxide was present (see figure legend) in the medium at varying doses throughout the experimental period. Glucagon (1.0 nM) was added to the cultures at 48 hrs and removed at 96 hrs. The basal level of glucagon in the medium was 0.1 nM.

In hepatocytes, one of the most sensitive pathways to oxidative stress is the pentose phosphate pathway (PPP), which in non-dividing cells is primarily responsible for maintaining cytosolic NADPH balance for lipid synthesis and glutathione turnover. The reduced form of glutathione (GSH) is the primary cytosolic defense molecule against reactive oxygen species (ROS), especially peroxides, and is regenerated from the oxidized dimer (GSSG) by glutathione reductase which requires NADPH as a co-factor. From Figure 4-4, it can be seen that the addition of H_2O_2 to the culture medium stimulated flux through the PPP as measured by the evolution of carbon dioxide (CO_2) via glucose 6-phophate dehydrogenase. The increase in PPP flux took place regardless of whether glucagon (1.0 nM) was present in the medium. Conversely, glucagon by itself failed to stimulate flux through the PPP. Interestingly, the increase in PPP flux by the extraneously added H_2O_2 was transient, lasting from 24 to 72 hrs after H_2O_2 was initially added, even though the oxidant was present continuously throughout the study period.

After observing that glucagon and H_2O_2, respectively, up-regulated amino acid oxidation and the PPP flux, their effects on the aerobic metabolism of cultured hepatocytes was assessed by oxygen uptake rate (OUR) measurements. The oxygen uptake experiments were conducted in cells cultured identically to those used for urea and PPP flux assays except that the culture vessels were P60 dishes instead of 6-well plates, as the OUR measurement device was designed to fit the P60 culture dish (see **Materials and Methods**). As shown in Figure 4-5, the addition of glucagon to the medium by itself failed to significantly affect the rate of oxygen uptake (OUR) by the hepatocytes. The addition of H_2O_2 alone decreased the OUR steadily over time, as the OUR of the peroxide treated cells were 42 % less than those maintained in the basal (LH) condition 96 hrs after continuous exposure. When the two stimulants were added together, the OUR increased by 25 % compared to the basal (LH) condition. Interestingly, this increase occurred 72 hrs after the initial exposure of the cells to H_2O_2 and glucagon, mirroring the time course of OUR increase observed in the perfused liver of burned animals (Chapter 3). The drop in OUR by the cells treated with H_2O_2 seemed to be due to the loss in cellular viability, in particular membrane integrity, as revealed by a fluorescence assay for cell death. In order to check the integrity of the cellular and nuclear membranes, cells were treated with EthD-1, which binds to the DNA and fluoresces in nuclei of cells with non-viable membranes. Figure 4-6 shows that H_2O_2 alone adversely affected cell viability, whereas glucagon had no appreciable effect.

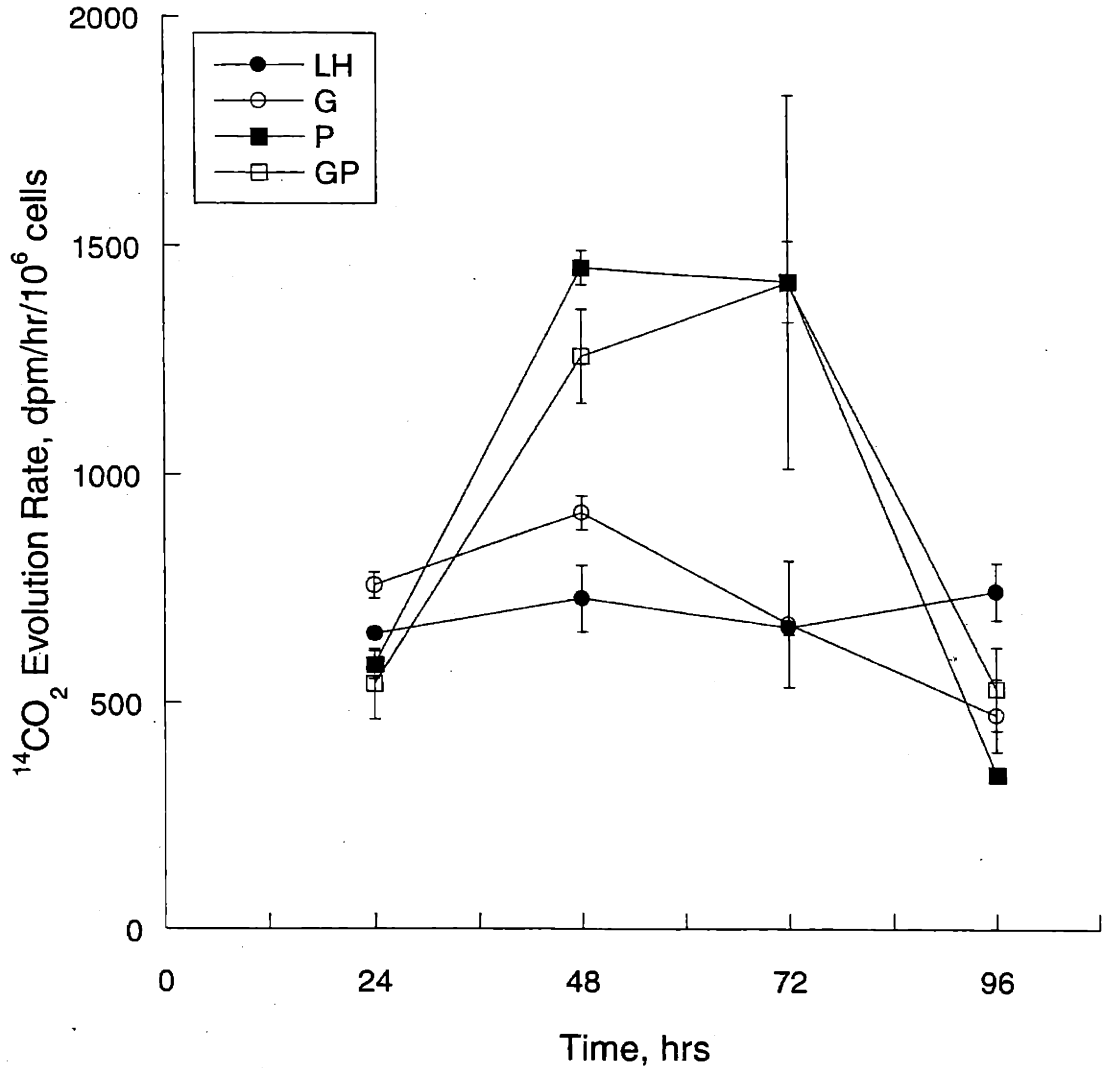

Figure 4-4. PPP activation by hydrogen peroxide.

After three days in basal physiological medium, cells were exposed to media containing 1.0 nM glucagon, 1.0 mM hydrogen peroxide, both, or kept in the basal medium. PPP flux was measured at 24, 48, 72, and 96 hrs using a radiometric assay method as described in **Materials and Methods**.

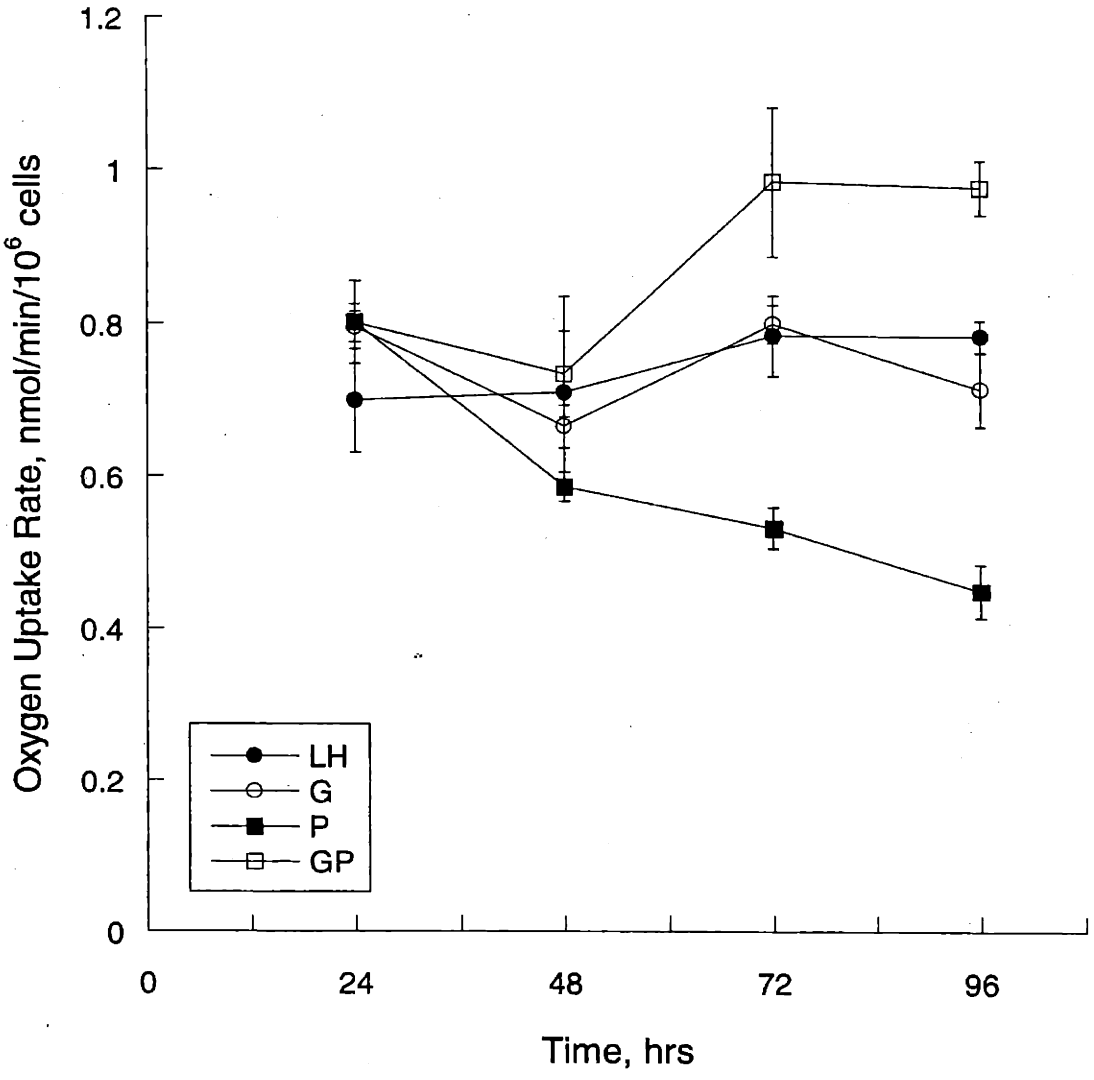

Figure 4-5. Effects of glucagon and hydrogen peroxide on oxygen uptake.
After three days in basal physiological medium, cells were exposed to media containing 1.0 nM glucagon, 1.0 mM hydrogen peroxide, both, or kept in the basal medium. Oxygen uptake was measured at 24, 48, 72, and 96 hrs using Clark-type electrodes as described in **Materials and Methods**.

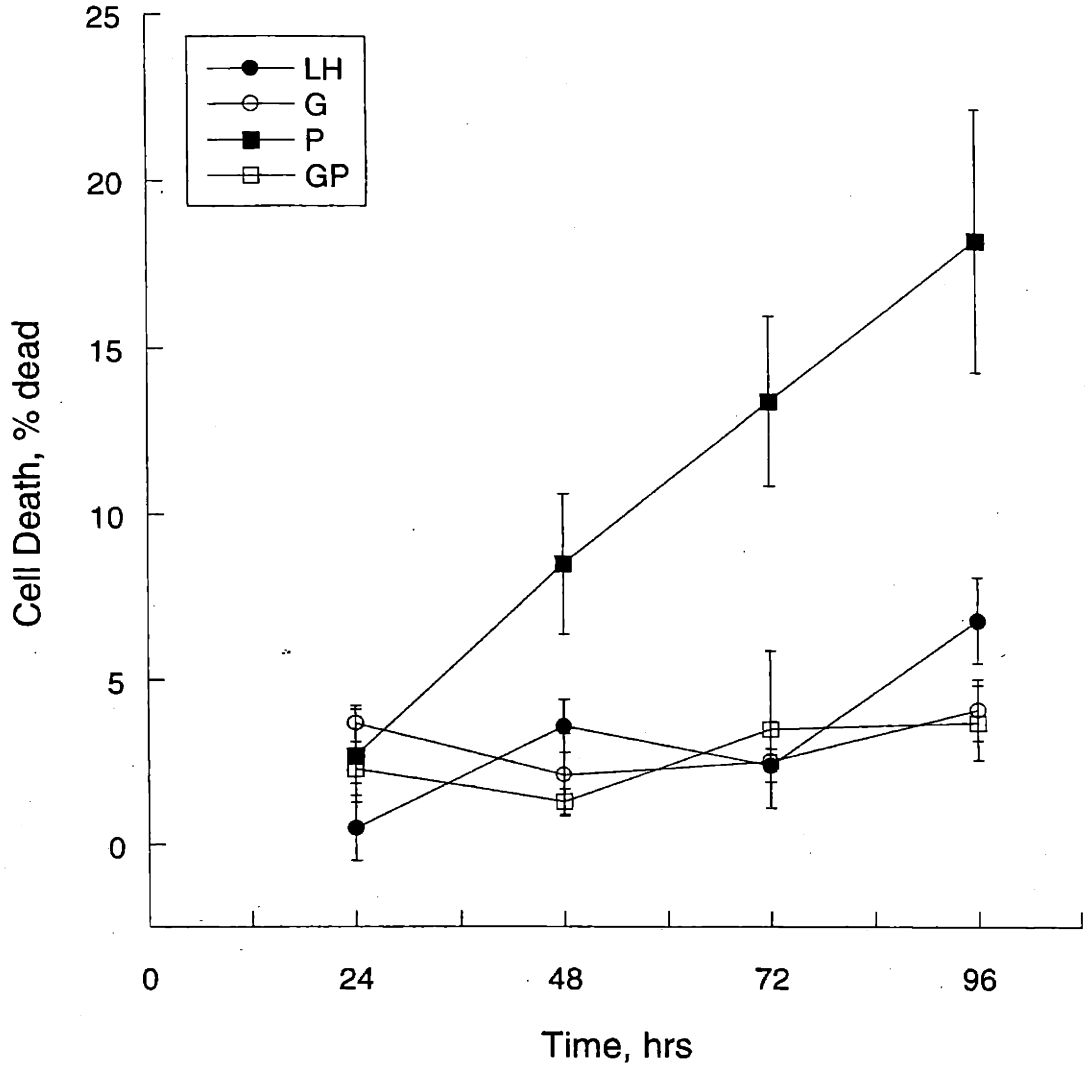

Figure 4-6. Hydrogen peroxide and cell death.

Cells cultured in parallel to those described by Figures 4-4 and 4-5 were checked for viability by fluorescence spectroscopy using EthD-1 as stain. Percent death was calculated by subtracting the live control from sample fluorescence intensities and normalizing the differences by the dead control fluorescence intensity. Live and dead control refer to cultures where most cells were determined to be either viable or dead, as determined by fluorescent microscopy. Live cells were kept in the seeding medium (C+H) until time of measurement. Cell death was induced by 24 hr exposure to 70 % v/v ethanol (aq).

On the other hand, when present alongside H_2O_2, glucagon seemed protect against the peroxide induced damage to the cellular membranes, as cells treated with both H_2O_2 or glucagon were able to maintain their membrane viability throughout the study period.

The above observations, in particular with respect to the sequential activation of the PPP and OUR, hinted at a possible connection between these two metabolic pathways. In order to explore this notion, we studied the effects of the general anti-oxidant N-acetyl cysteine (NAC) and the PPP inhibitor dehydroepianderosterone (DHEA) on urea production and OUR in cultures treated with glucagon and H_2O_2. In these experiments, the working concentrations of NAC and DHEA were determined from the published literature and by a dose response curve (Figure 4-7), respectively. In Figure 4-8, the urea production profiles of NAC and DHEA treated cultures (GP+NAC and GP+DHEA, respectively) are plotted alongside the profiles of glucagon (G) and glucagon and H_2O_2 (GP) cultures. All of the profiles were virtually identical for the entire study period, except for the last time point (96 hrs after the initial exposure) taken from the GP+DHEA culture, which showed a significant decrease in urea production. This decrease was not related to a loss in cellular viability, as the fraction of dead cells remained between 0 to 5 % for all conditions throughout the study period (Figure 4-10).

The OUR for GP+NAC and GP+DHEA cultures were measured only at the 72 and 96 hr time points, which corresponded to the period during which the GP culture showed significant OUR increase compared to the basal condition. Both NAC and DHEA decreased OUR in GP cultures, with DHEA having the greater effect. Seventy-two hrs after the initial exposure, the general antioxidant NAC was unable to significantly reduce OUR, whereas the PPP inhibitor DHEA decreased OUR to a level comparable to the basal (LH) condition. Both NAC and DHEA further decreased OUR by 96 hrs, to 16 and 37 %, respectively, below the GP condition.

In the final set of experiments of this study, we explored the possibility of induction of respiratory uncouplers as a potential molecular level mechanism underlying the increase in OUR by glucagon and H_2O_2. A likely candidates was UCP2, which belongs to a class of mitochondrial uncoupling proteins found in the liver [193] and in cultured hepatocytes [194], which have been found to increase state 4 relative to state 3 respiration. UCP2 is normally dormant in adult rodent liver, but has been found to be expressed under oxidative stress conditions [228].

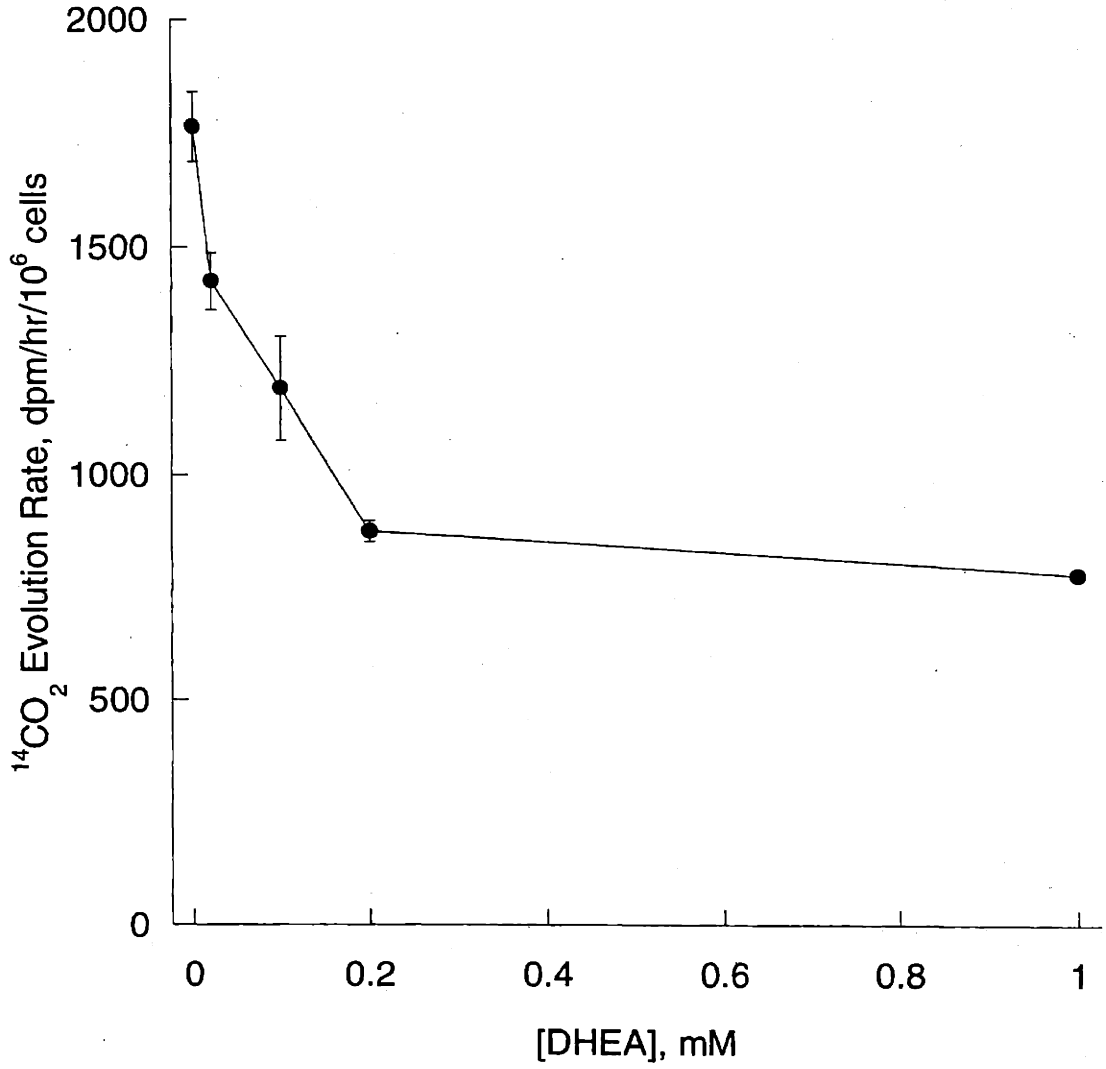

Figure 4-7. Hepatocyte dose respose to dehydroxyepianderosterone (DHEA).
Hepatocytes cultured in the double-gel configuration for three days in basal physiological medium (for culture protocol and medium definition, see Figure 4-1 and Table 4-1) were exposed to varying doses of DHEA and assayed for PPP activity using a radiometric method. Dose ranges were guided by published literature values.

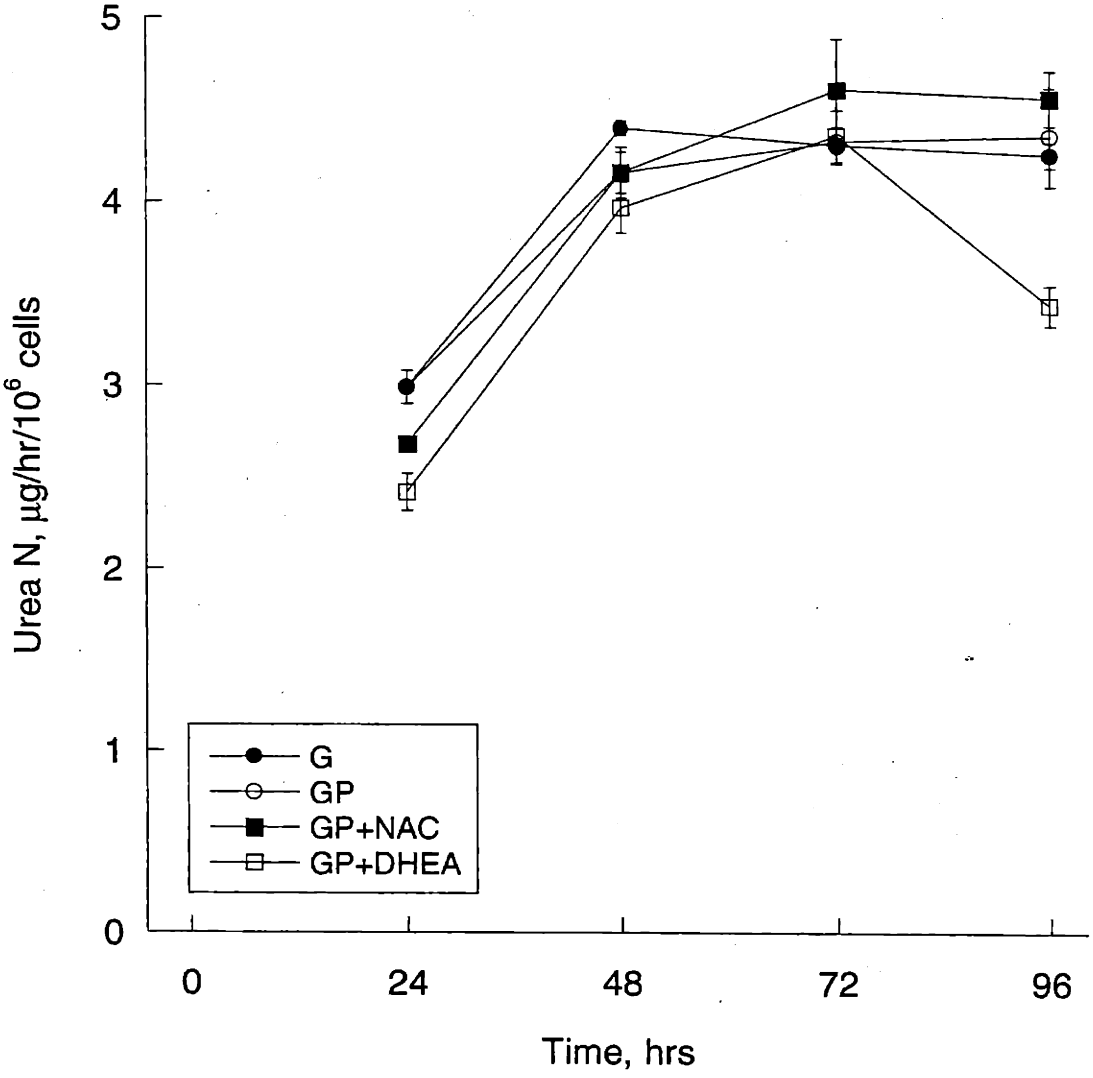

Figure 4-8. PPP flux and hepatocyte urea production.

After three days in basal physiological medium, cells were exposed to media containing 1.0 nM glucagon (G), 1.0 nM glucagon and 1.0 mM hydrogen peroxide (GP), GP and 5 mM N-acetylcysteine (GP+NAC), or GP and 200 µM DHEA (GP+DHEA). NAC stimulates glutathione synthesis, thereby reducing the need for glutathione recycling via the NADPH dependent reductase-peroxidase system. DHEA is a specific inhibitor of glucose-6 phosphate dehydrogenase, which is the first step of the PPP. Medium samples were taken at 24, 48, 72, and 96 hrs and assayed for urea.

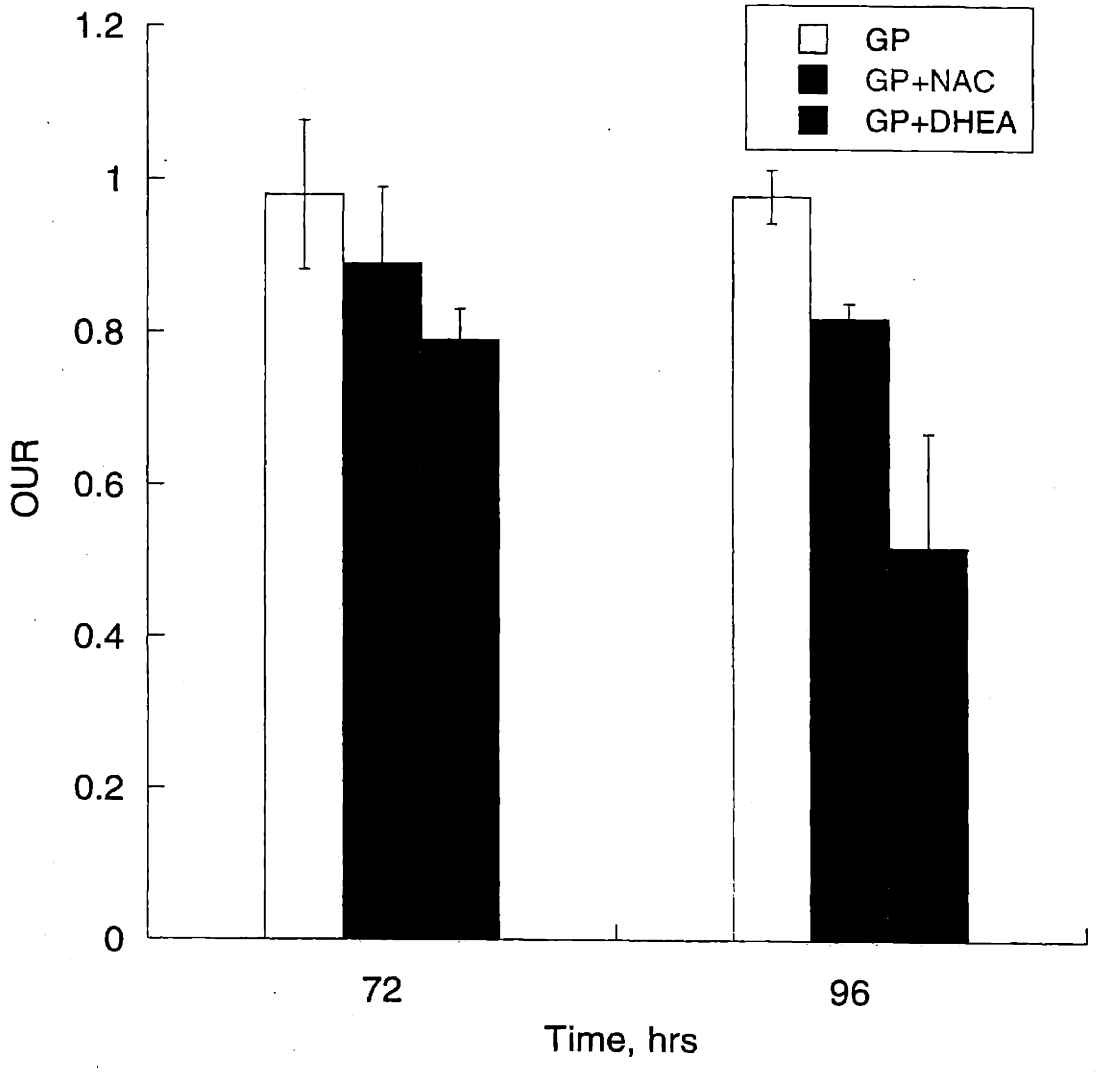

Figure 4-9. Oxidative stress, PPP flux, and hepatocyte oxygen consumption.
After three days in basal physiological medium, cells were exposed to media containing 1.0 nM glucagon (G), 1.0 nM glucagon and 1.0 mM hydrogen peroxide (GP), GP and 5 mM N-acetylcysteine (GP+NAC), or GP and 200 μM DHEA (GP+DHEA). Oxygen uptake was measured at 24, 48, 72, and 96 hrs using Clark-type electrodes as described in **Materials and Methods**.

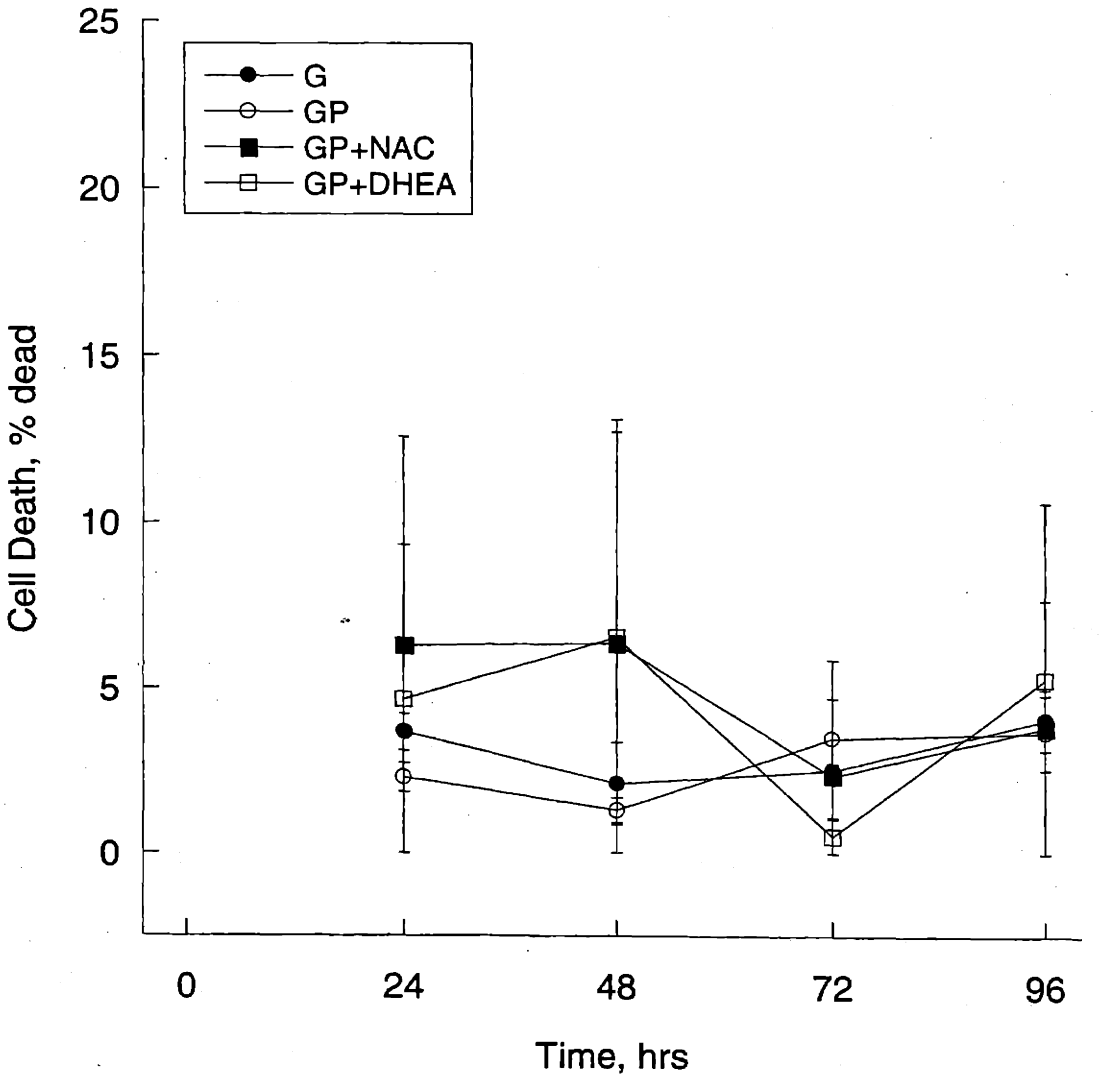

Figure 4-10. NAC and DHEA effects on cell death.
Cells cultured in parallel to those described by Figures 4-8 and 4-9 were checked for viability by fluorescence spectroscopy using EthD-1 as stain. Percent death was calculated as described in the Figure 4-6 legend.

We used Western blots to assay for UCP2 in cellular extracts collected at the 96 hr time period from G, GP, GP+NAC, and GP+DHEA cultures. Cells not subjected to extraneously introduced oxidative stress (G culture) expressed the least amount of UCP2. Cells fed media containing the peroxide (GP) expressed the uncoupler most strongly (data not shown). Interestingly, cells fed the GP medium but also treated with either NAC or DHEA expressed a greater amount of the uncoupler than those fed the G medium, but to a lesser degree than those fed only the GP medium (data not shown).

4.4 Discussion

The experiments in this chapter built on previous work (Chapters 2 and 3) to examine the role of ROS in mediating hepatic hypermetabolism after burn injury. In Chapter 2, MFA of fasted rat livers perfused 4 days after burn or sham-burn treatment revealed that flux through the PPP was significantly increased in the burn condition. Moreover, the uptake of most amino acids was also substantially increased. As the PPP is responsible for NADPH production, and lipid synthesis in the fasted liver is repressed, these results hinted at activation of the NADPH consuming antioxidant defense system GSHP-GSHR cycle, which in turn indicated that the liver was oxidatively stressed. In Chapter 3, these findings were corroborated by an expanded study involving liver perfusions at various times during the first week of injury. Flux through the PPP was significantly elevated by day 2 post-burn and remained above the sham-burn control level throughout the study period, although declining slightly by day 7 post-burn. It was also shown that metabolic pathways in the liver were differentially activated or repressed with respect to extent and time after injury. In particular, the TCA cycle fluxes were increased disproportionately with respect to the major energy requiring processes, suggesting either ATP overproduction or lowered oxidative phosphorylation efficiency. The latter possibility was at least partially substantiated by detecting uncoupling protein 2 (UCP2) induction in livers isolated from burned rats, where UCP2 is a mitochondrial respiratory uncoupler with putative antioxidant properties.

These above mentioned findings suggested that ROS may mediate some of the hypermetabolic features observed in the liver after burn injury. Therefore, we investigated the effects of a model ROS compound, H_2O_2, on urea production, oxygen consumption, PPP flux,

and cell viability in a previously developed stable hepatocyte culture system. In hepatocytes, H_2O_2 is produced endogenously by superoxide dismutase from byproduct of aerobic metabolism. Hydrogen peroxide is also released by activated immune cells, which have been shown to sequester in the liver shortly after injury [210]. In the present study, H_2O_2 was added exogenously at a dose low enough not to cause immediate cell death, but high enough to elicit biological activity. In order to simulate high substrate loading conditions found during hypermetabolism, glucagon was added to the culture medium at a physiological dose that elicited near maximal urea production by the cultured hepatocytes. Urea production was measured as a marker for amino acid conversion to glucogenic precursors. PPP flux was measured to assess degree of cytoplasmic oxidative stress. Oxygen uptake was measured to assess overall metabolic activity and evaluated with respect to induction of the respiratory uncoupler UCP2. General antioxidant NAC and specific PPP inhibitor DHEA were used to probe the relationship between cytoplasmic redox potential, oxidative stress, and respiration.

One significant result of the current chapter is that the two aforementioned types of stressors, oxidative and hormonal, differentially affected amino acid processing and aerobic metabolism in hepatocytes. Glucagon potently increased urea synthesis, more than doubling urea output in less than 48 hrs. This phenomenon was also fully reversible, as removal of glucagon from the medium returned the urea output to the basal level. In contrast, H_2O_2 had almost no effect on urea production. Conversely, PPP flux was virtually unaffected by glucagon while strongly activated by H_2O_2. Interestingly, oxygen uptake was only significantly increased when both H_2O_2 and glucagon were added to the medium. Moreover, this change took place several days (72 hrs) after the initial stress, suggesting an inductive mechanism involving *de novo* protein synthesis. Taking urea output as a marker for substrate uptake and processing, PPP for oxidative stress, and oxygen uptake for global activity index of central carbon metabolism, and in the context of the discussions presented in Chapters 2 and 3, the above observations point to a potential push-pull mechanism for hepatic hypermetabolism, where substrate loading by glucagon is the push and oxidative stress by H_2O_2 is the pull. The potential molecular link between these stresses is provided by mitochondrial respiratory uncouplers.

Albeit faint signals due to the low affinity of the mouse antibody for the rat protein and small absoulte amounts expressed in hepatocytes, it could be seen that there was clear correlation between oxidative stress and UCP2 induction. UCP2 was not detected in cells treated with only

glucagon, consistent with literature reports that transcription of the protein is dormant in normal adult hepatocytes [228]. However, UCP2 was visible in Western blots of cell crude extracts formed from cultures treated with both glucagon and H_2O_2. Moreover, the uncoupler expression was partially inhibited by addition of the general antioxidant NAC. Partial downward modulation was also accomplished by addition of DHEA, a specific PPP inhibitor, suggesting a induction mechanism involving ROS sensing via PPP flux.

The effects of NAC and DHEA on UCP2 expression were mirrored by their effects on oxygen consumption. When added to cultures exposed to glucagon and H_2O_2, both agents reduced the oxygen uptake rate (OUR), with DHEA having the larger effect. After a 96 hr exposure to DHEA, hepatocyte OUR remained at levels comparable to those seen for the basal LH medium cultures. The reduction in OUR, or inhibition of pathways leading to the upregulation of OUR, was not a result of decreased viability, as the fraction of dead cells remained low (less than 8 %) regardless of the presence of NAC or DHEA. On the other hand, glucagon had a protective effect on cell viability, as there was a significantly higher fraction of nonviable cells in cultures exposed to H_2O_2 without a high dose of glucagon. In this regard, the high substrate loading may prevent ROS mediated cell death by contributing to gluconeogenesis, which in turn supplies phosphorylated hexose units (glucose 6-P and fructose 6-P) for the PPP. The protective role of PPP against ROS mediated cell injury has already been described in the introduction of this chapter. Along the same vein, increased UCP2 expression and concomitant OUR upregulation could constitute another defense mechanism whereby cells limit endogenous production of ROS during high substrate loading conditions.

In conclusion, the studies in this chapter show that while glucagon and H_2O_2 differentially affect intracellular pathways in hepatocytes, both stressors are needed to globally influence central carbon metabolism. A noteworthy and useful aspect of this feature is that this experimental system represents an *in vitro* model of hepatic hypermetabolism exhibiting both increased oxygen consumption as well as urea production, which, to the best of the author's knowledge, is reported here for the first time. Moreover, the time course of the metabolic changes observed in these studies mirrors that found in perfused livers of burned animals (Chapter 3), corroborating a ROS mediated mechanism for the hepatic metabolic response to injury. Finally, the results from this chapter support a push and pull notion for upregulating cellular aerobic metabolism, where the push and pull stresses are potentially linked by a

mitochondrial respiratory uncoupler. Further studies are warranted in order to validate this hypothesis by elucidating the molecular underpinnings, which is beyond the scope of this thesis.

CHAPTER 5. METABOLIC PROFIIING: DEFINITION AND USE IN PHYSIOLOGICAL STATE CLASSIFICATION

5.1 Introduction

With the recent progress in high-throughput methods for detecting gene and protein expression levels, these two types of molecules have received much attention as important determinants in characterizing and understanding cellular physiology. Gene expression profiling, or simultaneous analysis of large-scale gene expression data, has been applied to classifying normal and cancer cells based on their molecular characteristics, discovering novel subtypes of tumors, identifying potential biomarkers for cancer prognosis, testing tissue drug response, delineating gene families by function, and improving general understanding of genetic regulation. Nevertheless, recent experiments in yeast [229] and human liver cells [230] and have shown that there is no obvious correlation between mRNA and protein expression levels in these systems, suggesting that mRNA abundance is not always a good indicator of the corresponding protein levels. Expression levels of a protein depend not only on transcription rates of the corresponding gene, but also on nuclear export and mRNA localization, transcript stability, translational regulation, and protein degradation [231]. It follows that complementing genomic with proteomic analysis will lead to even better description of cellular physiology, allowing finely stratified classification of normal and diseased cells based on functional characteristics as well as targeted development of patient-specific therapeutics. Moreover, protein expression data obtained directly by two-dimensional (2D) gel electrophoresis or mass spectrometry (MS) contain biochemical information not available from mRNA measurements alone, especially with regards to phenotypical changes resulting from multigenic phenomena such as aging, stress, and disease.

In this regard, a third class of biological molecules, small molecule metabolites, can be thought of as constituting another useful dimension for describing cell physiology [232]. Metabolites refer to the intermediates of biochemical reaction pathways which convert nutrient fuel to energy, maintain cellular homeostasis, eliminate harmful chemicals, and provide building blocks for biosynthesis. Therefore, metabolites partake in some of the most essential cellular activities. Furthermore, many metabolic intermediates are in constant exchange with the

extracellular medium, and employing appropriate models, changes in pathway activity may be correlated with extracellular metabolite concentrations. In contrast, the multiple layers of regulatory interactions as well as transport limitation across the cellular membrane prohibit direct mapping of changes at the mRNA or protein expression levels to observable biochemical function [233]. For these reasons, metabolites can be thought as the most immediate descriptors of the biochemical state in a cell, which is the basic notion behind metabolic profiling. Here, in analogy to gene and protein expression profiling, metabolic profiling is defined as a methodology whereby biochemical function or metabolic phenotype is assigned to cells, tissues, organs, and organisms based on simultaneous measurement of concentrations of many metabolites, fractional enrichments of isotopic tracers, and derived quantities, such as metabolic fluxes. In recent applications, metabolic profiling has been used to study shifts in metabolism resulting from overexpression of a yeast enzyme in transgenic potato [234], describe phenotypical differences between *Arabidopsis* mutants [233], and discover novel biomarkers for a specific type of muscular dystrophy [232]. A role for metabolic profiling in the discovery of novel genes and their annotation in the context of the source organism has also been suggested [235].

Metabolite profiling also has obvious applications to the medical field, especially with respect to the investigation of metabolic disorders. The potential for developing clinical diagnostic protocols based on metabolite profiling has been recognized for some time, especially in the context of tissue biopsy characterization [236]. However, the early efforts concentrated on analyzing just few markers [237] while neglecting information contained in the correlations among metabolites that would result from a comprehensive analysis of small molecules in tissue and bodily fluids. In recent years, increasingly sensitive methods for rapid detection of metabolites have become available, particularly in the form of GC-MS [238]. In order to extract useful biological information from the growing volume of data, models and methodologies will be needed to systematically evaluate the correlations between large numbers of metabolites and pathways. Like genetic circuits and signal cascades, cellular metabolism has a built-in network structure that arises from shared intermediates in the form of common reactants and products, allosteric effectors, reducing equivalents, and other cofactors. Fortunately, the stoichiometry of most major metabolic reactions has been thoroughly elucidated, and well-established

methodologies are available for quantifying the relationships between metabolites using conservation equations and network models of metabolism [2, 35, 239].

In this paper, the above concepts are applied to two sets of metabolite data obtained in liver models of injury. The first set, previously published by Arai et al. [240] describes the metabolic differences between livers isolated from normal and hepatotoxin D-galactosamine challenged rats. The second set, described in detail in Chapter 3, was obtained in perfused rat liver experiments performed at various times during the first week after sham-burn or burn treatment. Drawing upon statistical formalism, recasting the original data to an array form convenient for manipulation and analysis, and implementing a well-established discrimination algorithm, metabolic profiles were constructed for each liver sample obtained from the aforementioned studies. Using these profiles, we set out to 1) assess the observability of distinct physiological states by modeling metabolite data, 2) demonstrate the utility of statistical projection methods in discriminating between different physiological states, and, most importantly, 3) identify key metabolites in the development of liver failure (in the case of the D-galactosamine study) or hypermetabolism (burn study).

5.2 Materials and Methods

5.2.1 Animals

Male Sprague-Dawley rats (Charles River Laboratories, Boston, MA) weighing 150 ~ 200 g were housed in a temperature (25 °C) and light-controlled room (12-hour light-dark cycle). The animals were cared for in accordance with the National Research Council guidelines. Experimental protocols were approved by the Subcommittee on Research Animal Care, Committee on Research, Massachusetts General Hospital. Water and rat chow were provided *ad libitum*. Animals were individually housed and allowed to adjust to their new surroundings for at least 2 days before receiving treatment.

The initiation of fulminant hepatic failure (FHF) by D-galactosamine injection and the induction of hepatic hypermetabolism by burn injury have been described in detail in previous publications. Briefly, FHF was caused by intraperitonealy administering D-galactosamine dissolved in normal saline at a dose of 1.4 g /kg to fasted rats 12 and 24 hrs after beginning the fast. The mortality rate of the D-galactosamine treatment was 25 % at 48 hrs and 83 % at 168 hrs

after the initial injection. Control rats were fasted, but did not receive D-galactosamine injections. The FHF study rats were fasted for a total of 36 hrs prior to the perfusion (12 hrs before and 24 hrs after first D-galactosamine injection). The burn injury and perfusion protocols have already been described in Chapter 2.

5.2.2 Metabolites and fluxes

Metabolite measurement methods have been described in Chapter 2. For each perfusion study, metabolite exchange rates were calculated by linear regression of the perfusate reservoir metabolite concentration data. The derived exchange rates were arranged into $N \times P$ data matrices $\boldsymbol{M}$, where the element m_{ij} holds the flux of metabolite j into or out of liver sample i. In the FHF study, $P = 27$ metabolite exchange rates were determined for a total of $N = 12$ livers (6 failure and 6 control). In the burn experiments, $P = 25$ metabolite exchange rates were observed for $N = 42$ livers, which were perfused 1, 2, 3, 4, or 7 days after the burn or sham-burn treatment. All sham-burn livers, regardless of the time elapsed between the perfusion and the treatment, were classified into a single "control" group, resulting in a total of $K = 6$ treatment groups: control (group sample size $n = 13$), day 1 post-burn ($n = 9$), day 2 post-burn ($n = 4$), day 3 post-burn ($n = 4$), day 4 post-burn ($n = 5$), and day 7 post-burn ($n = 8$). Using these data, intracellular fluxes were calculated by metabolite balancing. A network model of hepatic central carbon metabolism was constructed from known reaction stoichiometry and used with minor modification in both the FHF study and the burn study. For reference, a graph of this model is shown in Figure 3-2. Derivation of the stoichiometric balance equations, solution by least-squares, and error analysis have been described in Chapters 2 and 3. The calculated and measured fluxes (metabolite exchange rates) were pooled and arranged in $N \times Q$ flux matrices $\boldsymbol{F}$ analogous to the metabolite data matrices, where $Q = 58$ for the FHF study, and $Q = 60$ for the burn experiments.

5.2.3 Discriminant analysis

The data and flux matrices were subjected to discriminant analysis based on Fisher's technique as outlined by Dillon and Johnson [191, 241]. For a data set comprised of X samples divided into K groups observed over Y variables, Fisher's discriminant analysis (FDA) seeks linear combinations of the variables that define a new set of coordinate axes so that the

separation between groups are maximized when the samples are projected into the new coordinate space. The linear combinations are obtained by multiplying (i.e. projecting) the original data matrix by a projection matrix V, which is obtained by solving the following optimization problem:

$$\max_{V} \Lambda = \frac{V^{T} B V}{V^{T} W V} \tag{5-1}$$

In the above defined objective function, W and B denote the matrices of within-group and between-group variances, respectively. The within-group variance W_i for the ith group is found as follows:

$$W_i = \sum_{j=1}^{N_i} (X_{ij} - \bar{x}_i)(X_{ij} - \bar{x}_i)^{T} \tag{5-2}$$

where N_i denotes the number of member objects (livers samples) in the ith group, X_{ij} the jth object (liver sample) in group i, and $\bar{x}_i$ the vector mean of the variables (metabolite fluxes) observed for the objects (liver samples) X_{ij} averaged across the ith group. After calculating W_i, W is found by the summation of W_i over all K groups:

$$W = W_1 + W_2 + \ldots W_K \tag{5-3}$$

The between-group variance matrix B is found by subtracting W from the total variance matrix T:

$$B = T - W \tag{5-4}$$

$$T = \sum_{i=1}^{K} \sum_{j=1}^{N_i} (X_{ij} - \bar{x})(X_{ij} - \bar{x})^{T} \tag{5-5}$$

where $\bar{x}_i$ is the vector mean of the variables (metabolite fluxes) averaged acros the entire range of objects (liver samples). The solution to the maximization problem in Equation 5-1 is obtained by the eigenvalue decomposition (ED) of $W^{-1}B$. Alternatively, the solution to the maximization problem can be obtained by the singular value decomposition (SVD) of the matrix $(W^{-1}B)^{T}\, W^{-1}B$. Here, SVD was used instead of ED, because it resulted in a better overall separation, as determined by the Wilks-Lamda likelihood-ratio criterion, defined as:

$$\Lambda = \frac{|W|}{|W + B|} \tag{5-6}$$

If the eigenvalues of $\boldsymbol{W}^{-1}\boldsymbol{B}$ are distinct, there are *K-1* or *P* (whichever is smaller) possible linear composites (i.e. projection axes), because $\boldsymbol{B}$ has rank equal to the minimum of *P* and *K-1*. The relative magnitudes of the eigenvalues λ_j ($j = 1, 2, \ldots, K\text{-}1$ or *P*) give a descriptive index of the importance of the discriminant axes defined by the corresponding eigenvectors $\boldsymbol{V}_j$. The number of statistically significant linear composites (i.e. discriminant axes) is determined by using Bartlet' *V* statistic, given by:

$$V_j = -\{(n-1) - \frac{1}{2}(P+K)\}\ln(1+\lambda_j) \qquad (5\text{-}7)$$

where V_j measures the significance of the *j*th eigenvalue λ_j of $\boldsymbol{W}^{-1}\boldsymbol{B}$. The statistic V_j is distributed approximately as a chi-square (χ^2) random variable. As expected for a two group problem ($K = 2$), discriminant analysis of the FHF study data yielded one significant axis. The burn study data, which included six treatment groups, yielded five significant discriminant axes, three of which accounted for 99 % of the variance in the data.

5.3 Results

In prior work [240], we had characterized in detail the metabolic alterations occurring in the liver during the onset of fulminant hepatic failure (FHF) using D-galactosamine challenge in conjunction with a perfused rat liver model. As described in detail in Chapter 3, we also studied the metabolic response of the liver to severe burn during the first week of injury. In both studies, measurements were obtained for an array of metabolic intermediates of hepatic central carbon pathways. From these data, we calculated the effects of the aforementioned insults on hepatic central carbon fluxes using metabolite balancing. Key findings of the FHF and burn studies were, respectively, that D-galactosamine strongly inhibited starvation induced gluconeogenesis by lowering ATP production and that burn injury differentially activated or repressed the pathways of central carbon metabolism. These results demonstrated the utility of metabolite measurements in understanding physiological changes in terms of changes in biochemical pathway fluxes. In this final chapter, we examined the converse situation, where the biochemical data was used to define changes to physiological states.

5.3.1 Class separation by FDA

As a first step toward constructing metabolic profiles, the aforesaid metabolites measurements were arranged into multidimensional data arrays. A common approach to identifying subgroups within multivariate data is dimensionality reduction. By forming weighted linear combinations of the data array elements, in this case metabolite measurements, the original higher-dimensional data may be presented in a lower-dimensional space while retaining the essential features of the original data. This procedure not only facilitates visualization, but also provides a means for systematically ordering variables according to their importance in discriminating, or assigning classes to, the source objects, in this case liver samples. One frequently used technique for data dimensionality reduction and classification is principal component analysis (PCA) [242], which finds new axes directions, or principal components, so that projection of the data along these axes maximizes the covariance among the variables. PCA is especially useful when the objective is to describe most of the variance in the data with a minimal number dimensions. In other words, PCA efficiently visualizes subset shapes without any prior knowledge regarding the number or membership of the subsets. However, when *a priory* information regarding subsets is available, another technique, called Fisher's discriminant analysis (FDA), yields better discrimination between the subsets. In FDA, *a priori* knowledge regarding group assignments is used to define linear combinations, or classification functions, which maximize the between-group variances with respect to the within-group variances in the projected sample space. These ideas are illustrated in Figure 5-1, which compares two-dimensional projections formed by PCA (panel A) and FDA (panel B) using the same set of metabolite data taken from the FHF study. By inspection, it is clear that both PCA and FDA separated the projected samples into two groups, corresponding to normal and D-galactosamine challenged livers. Presumably, this reflects the metabolically distinct nature of the two groups. It is also obvious that separation by FDA was superior, as the projected samples clustered more tightly around each other in the FDA space than the PCA space.

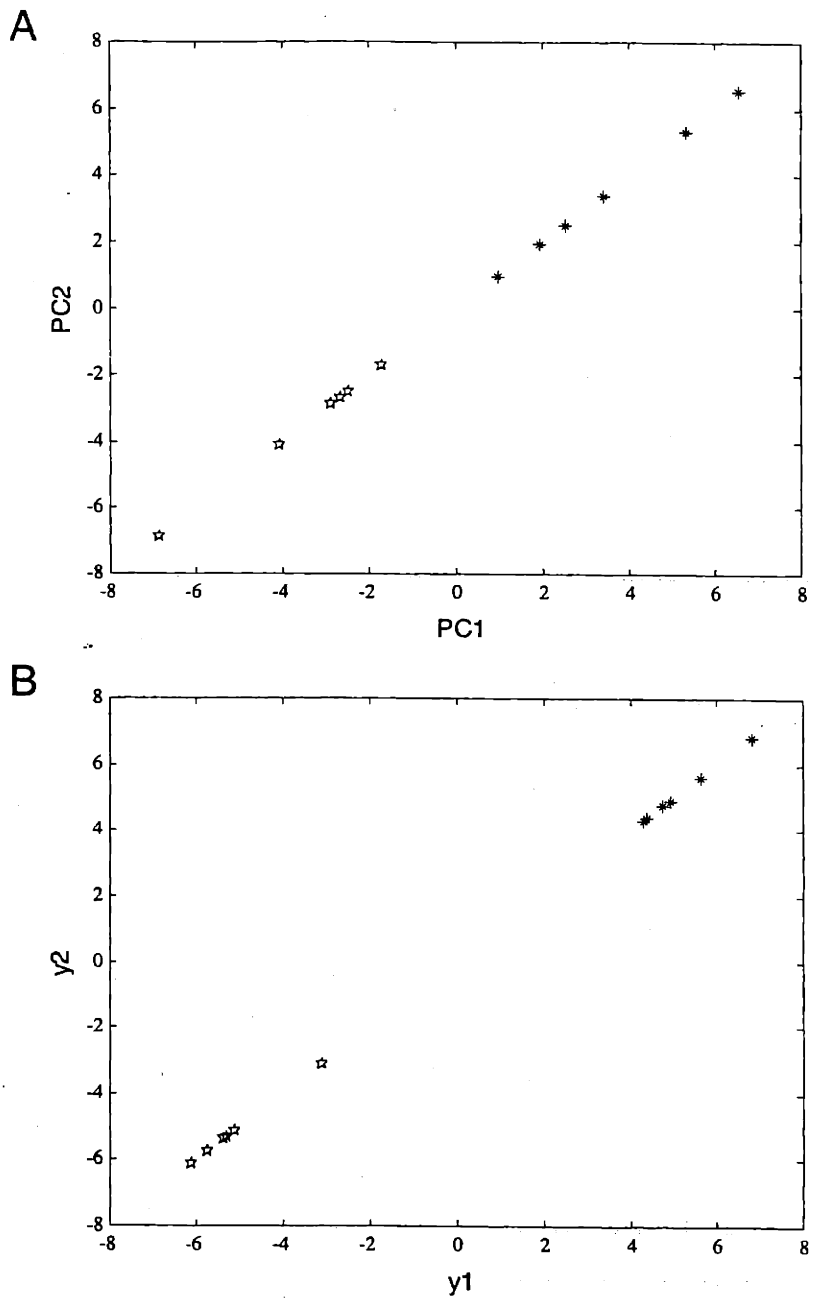

Figure 5-1. Comparison between PCA and FDA projections of FHF study data. Twenty–eight metabolites observed across 6 normal and D-galactosamine treated livers were projected into two dimensions using principal component analysis (PCA) and Fisher's discriminant analysis (FDA). Both projections correctly separated liver samples into normal (upper right corner) and D-galactosamine (lower left corner) treated groups. However, separation by FDA was superior, as the samples projected into more tightly clustered groups.

An important additional utility of FDA is that the projection vector (V) elements often have physiological meaning. These elements, called "discriminant loadings (DL)," are coefficient multipliers of variables in the linear combinations which define the FDA axes directions. For example, in Figure 5-1 the $y1$ FDA space coordinate for sample i was formed as follows:

$$y_{i1} = a_{i1}m_{i1} + a_{i2}m_{i2} + a_{i3}m_{i3} + ...a_{ip}m_{ip} \quad (5\text{-}8)$$

where $a_{i1} \ldots a_{ip}$ and $m_{i1} \ldots m_{ip}$ refer to discriminant loadings and metabolite measurements, respectively. The loadings measure the contribution of the corresponding variables, in this case metabolites, to discriminating the source objects, in this case livers. They can be interpreted by simply considering V, or a modified version V^*, which is computed by rotating V about the corresponding correlation (R) and variance (D) matrices:

$$V^* = RD^{1/2}V \quad (5\text{-}9)$$

It has been shown that V^* is less subject to instability caused by intercorrelations of the variables and tend to be more useful for interpretation than the standard discriminant loadings [191]. In the present analysis, the modified discriminant loadings identified two groups of metabolites useful for characterizing the distinct aspects of the normal and D-galactosamine challenged livers. Comparing Figures 5-1B and 5-2, it is easy to note the correspondence between sample and discriminant loading projections. Referring to Table 5-1, it can bee seen that larger (more positive or less negative) values of oxygen uptake (symbol number 27 in Figure 4), lactate consumption (number 2), and glucose production (number 1) were characteristic of the normal fasted liver, while smaller (more negative or less positive) values of alanine (number 7), valine (number 12), and tyrosine (number 17) uptake were characteristic of the D-galactosamine challenged liver. As alluded to earlier, gluconeogenesis and ATP synthesis were suppressed by D-galactosamine treatment, and thus these biochemical changes were correctly reflected by the discriminant loadings. Furthermore, our previous work showed that D-galactosamine strongly inhibited uptake of gluconeogenic and branched chain amino acids, also correctly reflected in the discriminant loading analysis.

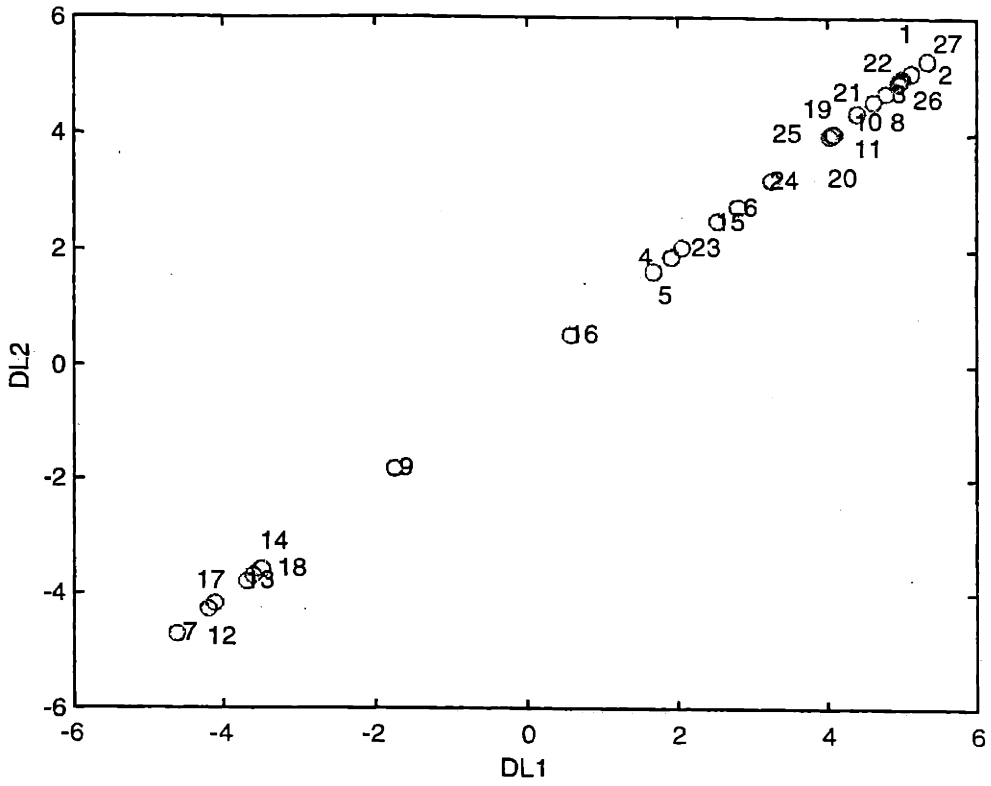

Figure 5-2. FDA projection of discriminant loadings for FHF study data.
Rotated discriminant loadings were calculated for the FHF study data as described by Equation 5-9. The loadings were projected into two-dimensional FDA space analogous to the samples. Metabolites were indexed by the numbering schedule shown in Table 5-1.

Table 5-1. FHF Study Metabolite Data

Metabolite	No.	Exchange Rate, *μmol/g dry liver/hr*	
		Normal	FHF
Glucose	1	55.4 ± 22.8	-33.2 ± 25.4
Lactate	2	16.2 ± 3.3	-66.0 ± 25.9
Urea	3	201.2 ± 23.4	130.5 ± 20.6
Arg	4	58.8 ± 14.7	48.3 ± 17.3
Ammonia	5	-3.1 ± 16.7	-10.4 ± 6.3
Ornithine	6	49.7 ± 13.5	35.9 ± 12.6
Ala	7	-7.5 ± 3.2	1.6 ± 3.1
Ser	8	5.5 ± 2.2	-1.3 ± 2.7
Cys	9	0.0 ± 0.3	0.4 ± 0.7
Thr	10	0.5 ± 2.5	-4.5 ± 1.9
Gly	11	1.2 ± 4.8	-5.9 ± 2.1
Val	12	-2.1 ± 2.3	3.6 ± 2.7
Ile	13	-2.5 ± 1.6	0.2 ± 1.6
Leu	14	0.5 ± 2.2	3.1 ± 1.3
Lys	15	1.5 ± 2.9	-2.1 ± 4.5
Phe	16	5.5 ± 1.3	5.3 ± 0.9
Tyr	17	-0.5 ± 1.1	2.9 ± 2.1
Glu	18	1.7 ± 2.5	5.7 ± 2.5
Gln	19	18.8 ± 8.4	-2.3 ± 12.6
Pro	20	2.9 ± 1.3	0.2 ± 1.5
His	21	2.1 ± 1.2	-1.4 ± 1.3
Met	22	1.0 ± 0.5	-0.4 ± 0.3
Asp	23	-1.6 ± 1.8	-2.5 ± 0.7
Asn	24	13.4 ± 3.8	6.8 ± 5.8
Acac	25	63.7 ± 12.0	42.2 ± 10.2
3-OH-Bt	26	110.5 ± 12.0	59.8 ± 13.7
Oxygen	27	317.8 ± 17.4	189.3 ± 13.4

It was interesting to note that the exchange rates of some compounds used as clinical markers for FHF, such as ammonia [243], glutamate [244], leucine and phenylalanine [245], ranked low in terms of their contribution to discriminating between normal and D-galactosamine treated livers (Table 5-2). In order to visualize the spread in the data, probability density functions (PDFs) were computed using mean and standard deviations obtained in the FHF study (Figure 5-3). By inspection, it is clear that the PDFs of ammonia, glutamate, and phenylalanine exchange rates overlap for normal and D-galactosamine conditions. In contrast, the PDFs of the metabolites determined by FDA to rank 1 ~ 3 in terms of their discriminatory contribution did not show significant overlap even between 99 % confidence regions (Figure 5-3, Table 5-2). These results suggested that metabolite selection was important in ensuring reliable discrimination between physiological states by metabolic profiling. Therefore, we next turned our attention to the effect of variable composition, in this case number and type of metabolites, on FDA performance.

Table 5-2. Contribution of Metabolites to Discrimination between Normal and FHF Livers

Rank	Type I Error Probability	Metabolite	
		Individual	*Composite*
1	1 %	27	27
2		2	2
3		26	22
4		22	1
5		1	26
6		3	3
7		7	7
8		8	21
9		21	8
10		10	10
11		12	12
12		17	17
13		19	11
14		11	25
15		25	20
16		20	19
17	5 %	13	13
18		18	18
19		14	14
20	Overlap		24
21			6
22			15
23			23
24			4
25			9
26			5
27			16

Type I error refers to the probability that the null hypothesis is rejected when it is true, i.e. means for normal and D-galactosamine conditions are deemed different when they are equal. Individual discriminatory power ranking was determined by mean hypothesis test p value. Composite contribution to discrimination was determined by the percent of the total variance accounted by a particular metabolite as calculated by FDA.

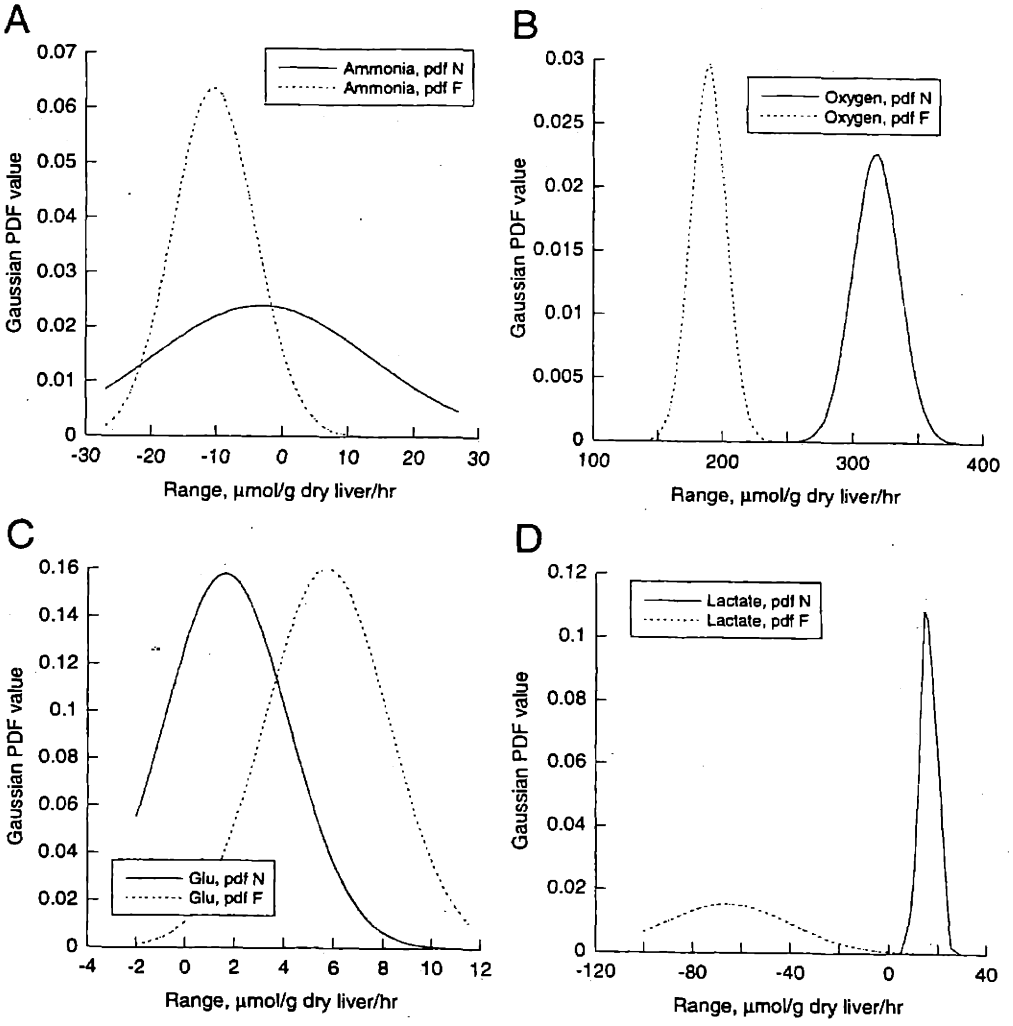

Figure 5-3. Metabolite PDF.

PDFs were computed for selected metabolites using means and standard deviations obtained in the FHF study assuming a Gaussian distribution. Clinically relevant markers ammonia (A), glutamate (C), and phenylalanine (E) all show signficant overlap between normal and D-glactosamine PDFs. PDFs of oxygen (B), lactate (D), and methionine (F) ranked 1 ~ 3 as composite discriminators by FDA, show far less overlap.

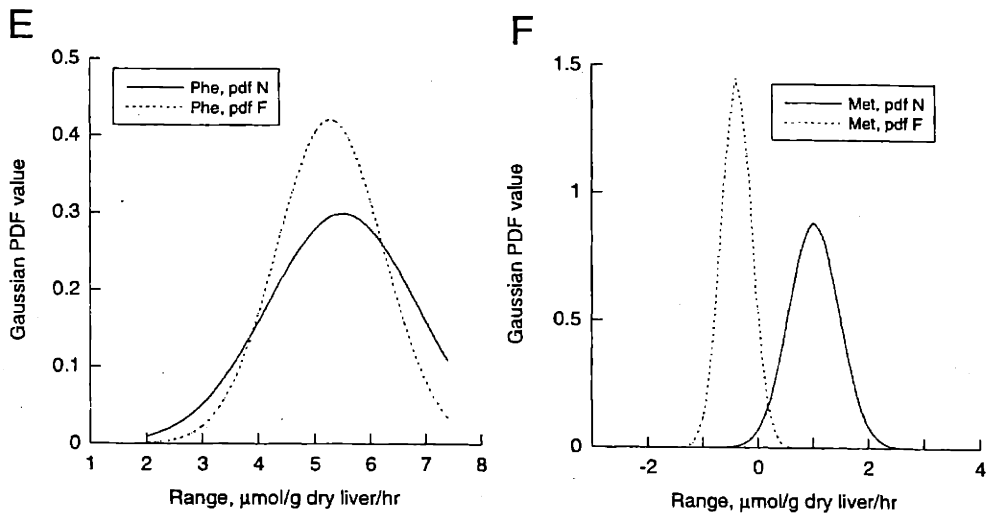

Figure 5-3. continued.

5.3.2 Successive addition of metabolites

In order to assess the effect of metabolite selection on class discrimination, FDA projections were formed using the following four sets of metabolites from the burn study: (A) 7 clinically relevant markers (B) 10 randomly chosen metabolites, (C) the clinical markers of (A) plus 6 metabolites with the highest discriminatory power, and (D) all 28 measured metabolites (Figure 5-4). The worst separation between classes resulted when the fewest number (seven) of metabolites were employed (panel A), even though these metabolites represented the clinically most relevant markers [129, 184, 246]. All of the projected samples gathered into one region of the FDA space, and clear boundaries between sample groups could not be established. Using 10 randomly chosen metabolites (panel B) as the basis for the FDA projections resulted in a slight improvement over the case presented in panel A. In particular, projections of the day 7 post-burn samples clustered into a clearly discriminated group without any visible overlap with the other treatment groups. Further improvement was achieved when projections were formed using a slightly larger subset comprised of the six individually most discriminating metabolites and the set of seven clinical markers. In addition to the day 7 post-burn samples, the day 4 post-burn samples also clustered into a clearly discriminated group (panel C). The best discrimination between samples belonging to different treatment groups was achieved when all 28 measured metabolites were employed in forming the projections (panel D). In this projection, samples from post-burn days 2, 3, 4, and 7 were clearly separated, with no overlap between the treatment groups. The improvements from panel A to D can also be noted by examining the Wilks-Lamda criterion (Λ), which decreased dramatically. The only groups which could not be satisfactorily discriminated from each other were control and day 1 post-burn, which showed overlap both in the *y1-y2* as well as *y1-y3* coordinate planes of the FDA space (Figure 5-5A).

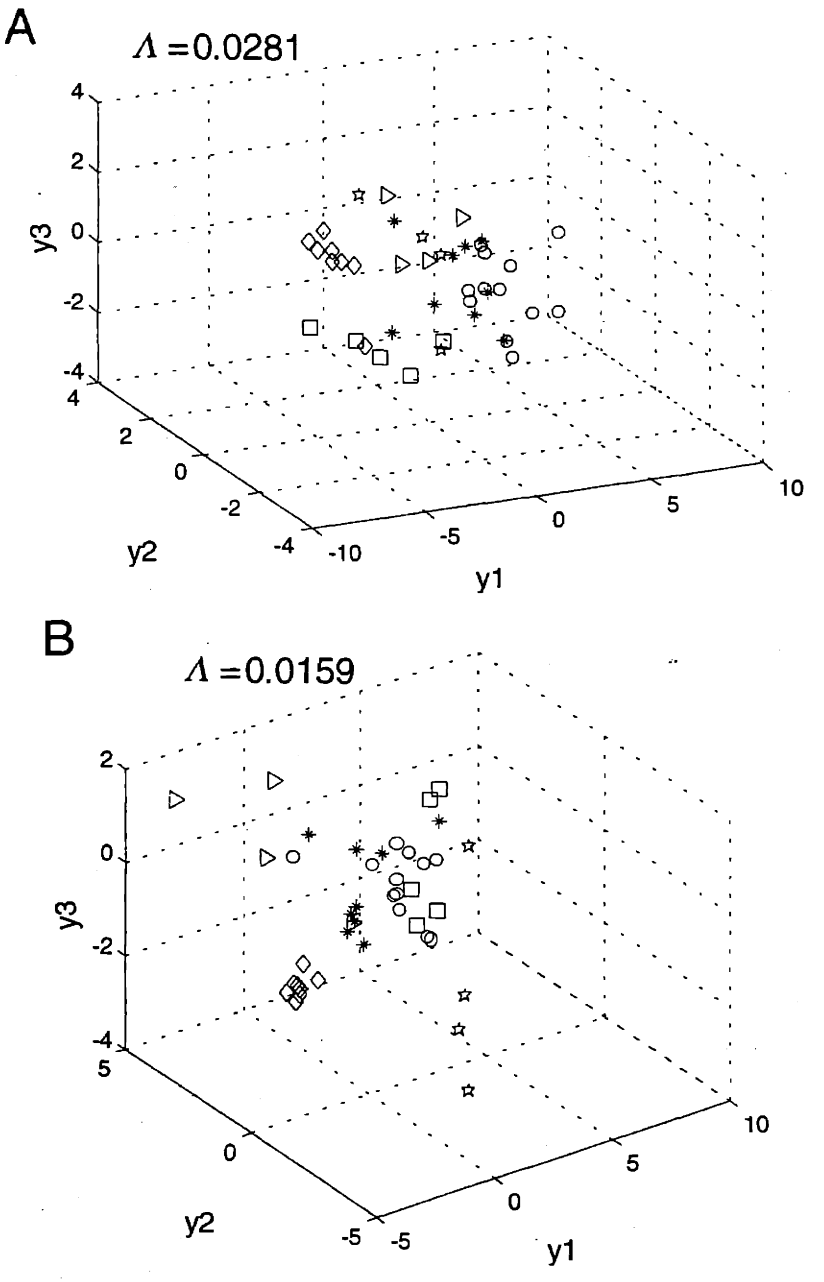

Figure 5-4. Metabolite selection and class discrimination by FDA.
In order to assess the effect of the number and type of metabolite measurements used on FDA performance, projections were formed employing the following sets of metabolite measurements taken from the burn study data: seven commonly used clinical markers (glucose, urea, lactate, 3-hydroxybutrate, acetoacetate, O_2, and CO_2) (A), ten randomly chosen metabolites (CYS, PRO, ACAC, AMM, ASP, MET, ALA, ASN, urea, THR) (B),

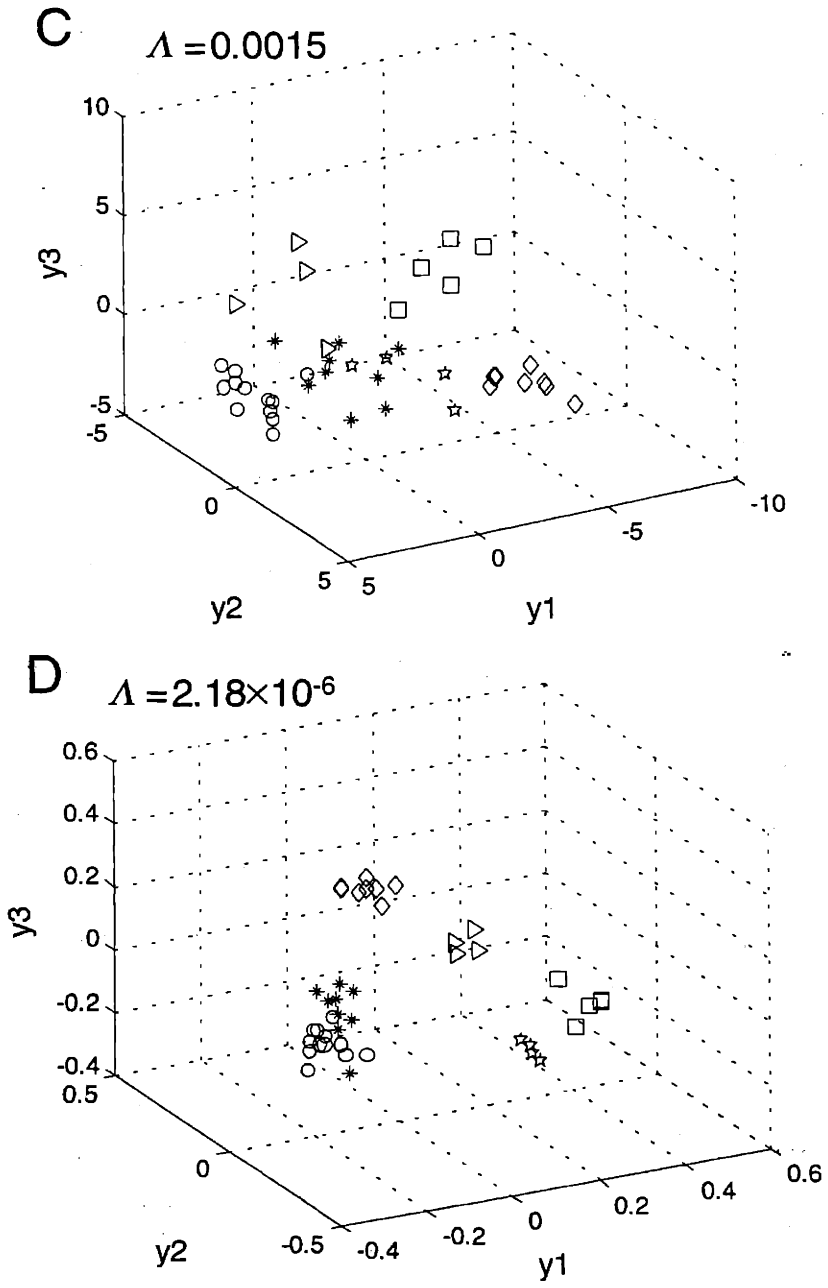

Figure 5-4. continued.

thirteen metabolites comprised of the clinical markers and six individually most discriminating metabolites (C), all twenty-eight measured metabolites (D). Classification performance improved as more metabolites were added, even if the added metabolite had low individual discriminatory power. Symbols denote liver sample treatment group membership: ○, sham-burn control; ✳, day 1 post-burn; ▷, day 2 post-burn; ✱, day 3 post-burn; □, day 4 post-burn; and ◇, day 7 post-burn.

5.3.3 Introduction of intracellular fluxes

The improvement in FDA performance by successive addition of metabolites hinted at the possibility that significant discriminatory information was contained not only in the actual metabolite exchange rates, but also in the correlations between these variables. It followed that by explicitly modeling these correlations, even more discriminatory information may be extracted from the data. One way to assign structure to the correlations is to take advantage of the well-established stoichiometric relationships between the reactions and intermediates of central carbon metabolism. Rates of change of extracellular metabolite concentration can be used to calculate intracellular fluxes based on a network model intermediary metabolism using mass balance constraints derived from the stoichiometry of reactions included in the model. The calculated fluxes have been presented elsewhere (Arai et al. [240] and Chapter 3, corresponding to FHF and burn studies, respectively). The effect of including the derived fluxes on FDA performance was evaluated visually (Figure 5-5). Comparing Figures 5-5A with 5-5B and Figures 5-5C with 5-4D, it is apparent that the extra variables generated by metabolite balancing altered the resulting projection in FDA space and improved the separation between classes. In particular, the separation between centroids of "control" and "day 1 post-burn" treatment groups improved significantly, as judged by the increased distance between the centroids and reduced scatter within the group cluster.

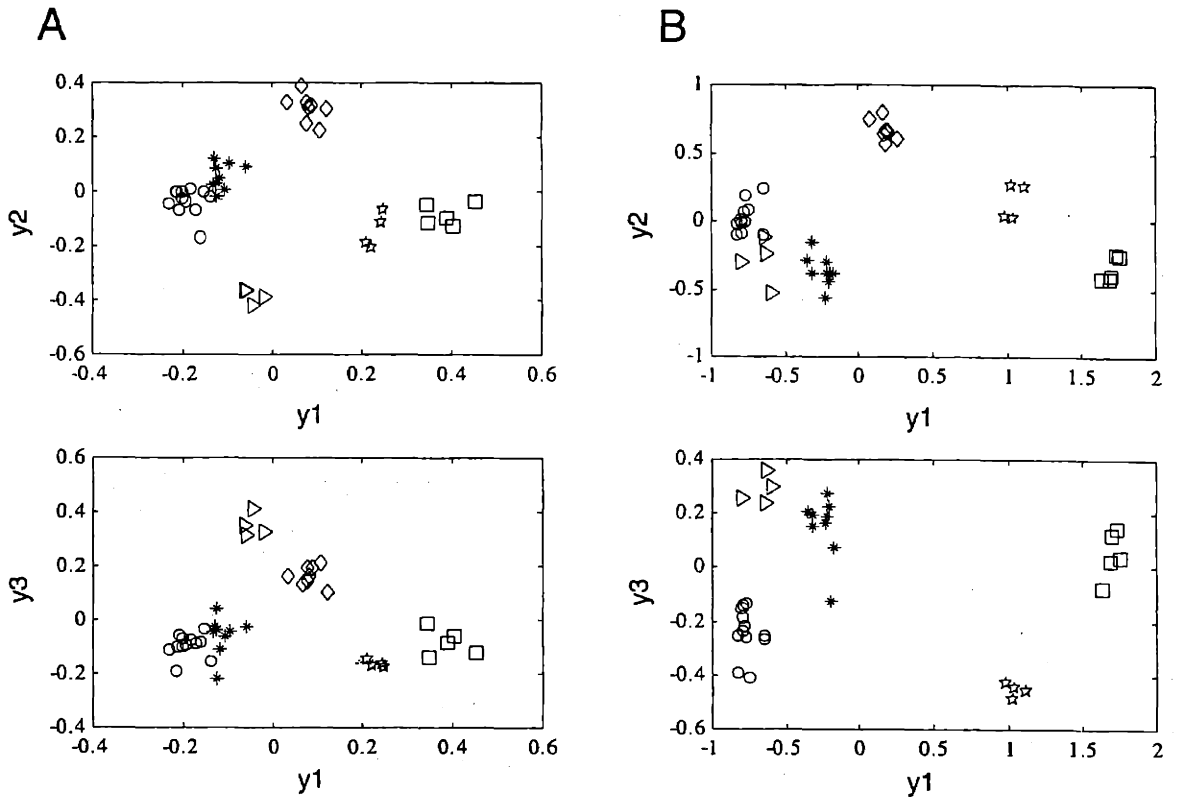

Figure 5-5. Comparison of flux and metabolite based FDA projections using burn study data. Intracellular fluxes calculated by Equation 3-12 were combined with the metabolite data and projected into three-dimensional FDA space (C). For comparison's sake, two-dimensional sections are shown for both the flux plus metabolite (B) and metabolite only (A) projections. Note the improved discrimination between sham-burn control and day 1 post-burn samples in both the y1-y2 and y1-y3 planes. Symbols denote liver sample treatment group membership: ○, sham-burn control; ✳, day 1 post-burn; ▷, day 2 post-burn; ✱, day 3 post-burn; □, day 4 post-burn; and ◇, day 7 post-burn.

C

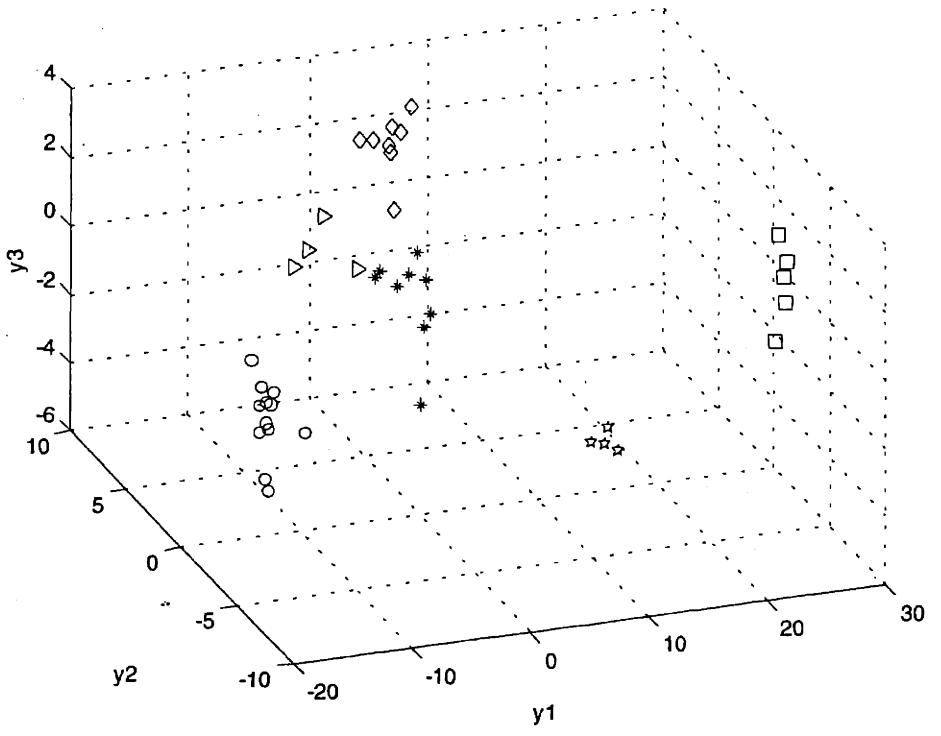

Figure 5-5. continued.

In order to explore an algebraic explanation for the additional discriminatory information, a singular value decomposition (SVD) analysis was performed on the matrix multipliers in the burn study which related the calculated fluxes to the measured metabolite exchange rates. First, the matrix multipliers were combined into a single matrix, yielding the following simplified version of Equation 3-12:

$$v_c = Av_m \tag{5-10}$$

where A replaced $-(S_c^T S_c)^{-1} S_c^T S_m$. SVD of A and substitution into Equation 13 yields:

$$v_c = (ULV^T)v_m \tag{5-11}$$

where U and V are unitary matrices and L a diagonal matrix with nonnegative diagonal elements. A unitary matrix performs an orthonormal change of basis by taking a vector space and rigidly rotating and reflecting its basis vectors. Therefore, a unitary matrix does not distort the lengths or relative angles between the basis vectors. In Equation 5-10, the operation Av_m first rotates and then reflects v_m to a new basis. In this basis, the nonunitary elements of L stretch v_m along the corresponding axes. Then U takes this result and rotates/reflects it again to give the final answer. The SVD of A produced 18 non-zero diagonal elements in L, or singular values. Of these, 9 singular values were larger than one, leading to elongation of the rotated basis vectors, and 9 singular values less than one, leading to their contraction (Table 5-3). In this regard, the additional discrimination afforded by the calculated fluxes could be due to the elongations and contractions of the data set resulting from the linear combinations as prescribed by the assumed structure of the model metabolic network.

Table 5-3. Singular Value Decomposition of the Flux Transformation Matrix

Statistic		Significance
Rank of $\boldsymbol{A}$ (number of non-zero singular values)	18	Number of independent linear relationships among the measured metabolites
Number of non-zero singular values larger than one	9	Elongation along the corresponding eigenvector directions
Number of non-zero singular values less than one	9	Contraction along the corresponding eigenvector directions

Matrix $\boldsymbol{A}$ transforms metabolite exchange rates into intracellular fluxes. The SVD of $\boldsymbol{A}$ provides insight into the transformation of the data structure underlying this operation. Eighteen independent linear transformations, defined by a corresponding number eigenvectors, characterize the operation of matrix $\boldsymbol{A}$. Nine linear combinations elongate the data structure in the measured rate space along the corresponding nine eigenvectors in mapping into the flux space, while the remaining nine linear combinations contract the data structure.

5.3.4 Discriminant loadings and metabolite clusters

As alluded to earlier, FDA systematically assesses the contribution to overall discrimination by each variable, in this case metabolite or intracellular flux. Unlike in the FHF study, projection of V^* for the burn study did not yield cleanly distinguishable metabolite clusters which corresponded to the six sample clusters, presumably due to the added complexity introduced by the time dimension (Figure 5-6). Thus, only a subset of the projected DL could be uniquely assigned to corresponding samples groups. Referring to Table 5-4A and sample group boundaries drawn on Figure 5-6B, the unique correspondences were: asparagine and arginine to sham-burn control; glycine, isoleucine, lysine, proline, and valine to day 1 post-burn; glutamine and acetoacetate to day 2 post-burn; carbon dioxide to day 4 post-burn; and glutamate to day 7 post-burn. The remaining metabolites were common discriminators for two or more sample groups, depending on their location in the DL plane. For example, oxygen (number 27), located in the upper right quadrant (DL1 > 0, DL2 > 0) roughly equidistant from sample clusters 3, 4, and 7, is a common discriminator for these three groups (Figure 5-7A). Elevated output of glutamate (number 8), located in the upper left quadrant between sample clusters 1 and 7, but closer to 7, is characteristic of all group 7 livers and one group 1 liver (Figure 5-7B). In contrast, increased output of carbon dioxide (number 28) was distinctively characteristic of sample group 4 (Figure 5-7C).

The above observations and the proximity of some sample clusters in the *y1-y2* FDA plane suggested that a natural grouping of the metabolite clusters may be afforded by considering the DL plane in terms of quadrants. Table 4B summarizes the quadrant associations between sample clusters and metabolites. Quadrants III and IV contain metabolites whose altered exchange rates characterize the transition from the basal to initial injury response state in the liver. This group of metabolites included all of the amino acids except ornithine, a urea cycle intermediate, and cysteine, a thiol residue carrier. Quadrant II is composed of acetoacetate, cysteine, and carbon dioxide, and delineates further changes in metabolite exchange characteristic of days 3 and 4 post-burn. Quadrant I metabolites, together with Quadrant II components, delineate altered exchange of reactants and products of major central carbon pathways in the liver, such as urea cycle and respiration.

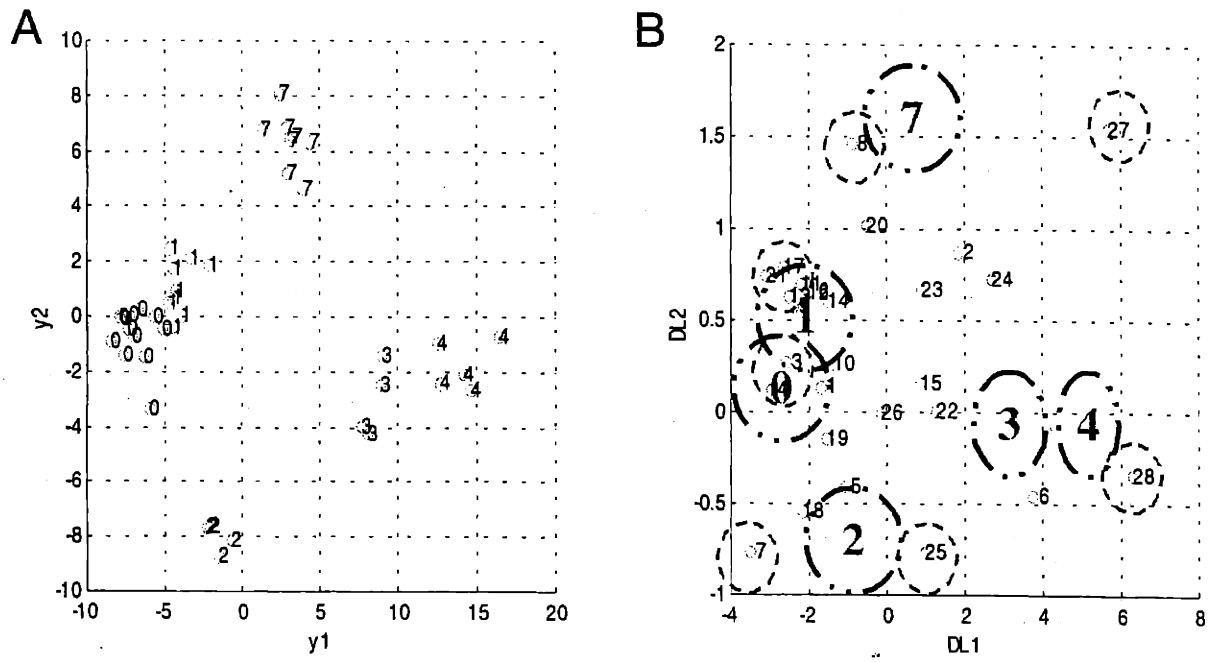

Figure 5-6. Discriminant loadings for the burn study metabolite data.
Rotated discriminant loadings calculated by Equation 16 for the burn study metabolite data is plotted in two dimensions (B) and compared to sample projections in the *y1-y2* plane (A). Corresponding sample boundary locations are sketched in (B) as dotted black circles. Each metabolite with a unique sample group correspondence is circumscribed with a dotted red circle.

Table 5-4A. Burn Study Metabolite Clusters

No.	Metabolite	Corresponding Sample (Time) Cluster(s)
1	Ala	0, 1
2	Ammonia	3, 4, 7
3	Arg	0
4	Asn	0
5	Asp	0, 2
6	Cys	3, 4
7	Gln	2
8	Glu	7
9	Gly	1
10	His	0, 1
11	Ile	1
12	Leu	1
13	Lys	1
14	Met	0, 1
15	Ornithine	3, 4, 7
16	Phe	1
17	Pro	1
18	Ser	0, 2
19	Thr	0, 2
20	Tyr	0, 1, 7
21	Val	1
22	Glucose	0, 1, 3, 4
23	Lactate	3, 4, 7
24	Urea	3, 4, 7
25	Acetoacetate	2
26	3-OH-Bt.	0, 1, 2, 3, 4, 7
27	Oxygen	3, 4, 7
28	Carbon dioxide	4

Table 5-4B. Burn Study Metabolite and Sample Quadrants

	Quadrant I DL1 > 0, DL2 > 0	Quadrant II DL1 > 0, DL2 < 0	Quadrant III DL1 < 0, DL2 < 0	Quadrant IV DL1 < 0, DL2 > 0
Sample Groups	3, 4, 7	3, 4	0, 1, 2	0, 1
Metabolites	Ammonia	Cys	Asp	Ala
	Ornithine	Acetoacetate	Gln	Arg
	Lactate	Carbon dioxide	Ser	Asn
	Urea		Thr	Glu
	Oxygen			Gly
				His
				Ile
				Leu
				Lys
				Met
				Phe
				Pro
				Tyr
				Val

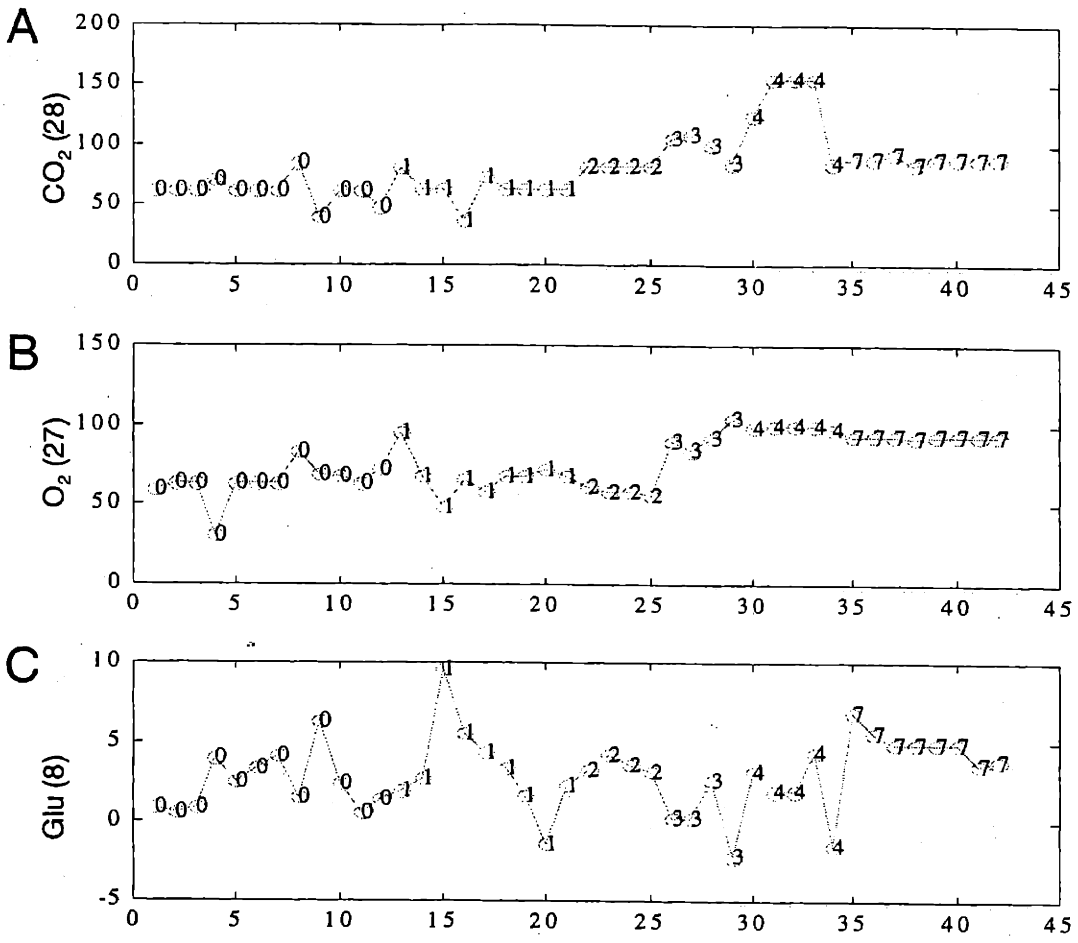

Figure 5-7. Selected metabolite exchange profiles.

These profiles illustrate the correspondences between metabolites in the DL plot and the sample group clusters in the *y1-y2* plane (Figure 5-6). The numbers inside plot symbols indicate source sample group assignment. Output of carbon dioxide (metabolite 28 in Table 5-4A), located in the DL plot within sample group 4 boundary, is consistently more elevated in this group (A) than in all others. Uptake of oxygen (metabolite 27), located halfway between sample group 3, 4, and 7 boundaries, is more elevated in these groups than the others (B). Output of glutamate (metabolite 8), located between group 1 and 7 boundaries, but closer to the group 7 boundary, is higher in one group 1 member and most of group 7 members (C).

Interestingly, the sequence of changes in metabolite exchange approximated the pathway activation sequence determined by hierarchical clustering of the pooled metabolite exchange rates and intracellular fluxes in Chapter 3. Referring to Table 3-2, the reaction time profiles in Figure 3-6 showed that after burn injury, liver amino acid uptake was increased first (panel C), followed by transient increases in fluxes through urea cycle, pentose phosphate pathway, fatty acid oxidation, which peaked between days 2 and 3 post-burn (panels D, E, and A, respectively). TCA cycle fluxes continued to increase past day 3, and remained elevated for the duration of the study (panel B).

5.4 Discussion

In this work, an emerging framework for multi-dimensional biological data analysis, namely metabolic profiling, was applied to metabolite measurement and flux data obtained using models of liver injury. We began by illustrating the utility of a multivariate statistical analysis tool, called FDA, in building and interpreting metabolic profiles with a discussion on the simpler FHF study data set. FDA efficiently discriminated normal and D-galactosamine treated livers into two clearly visible clusters in the projection space, performing superior to PCA in this respect. Furthermore, projection of rotated discriminant loadings revealed two well-discriminated metabolite clusters, corresponding to the liver sample clusters. Thus, FDA also grouped metabolites according to their contributions to discriminating either the normal or D-galactosamine treated livers. Moving on to a more complex scenario involving time series data from the burn study, we demonstrated the advantage of employing many metabolites over a few in improving the quality of discrimination between liver samples, and consequently, reliability of class discrimination. Discriminatory information resided not only in actual metabolite exchange values, but also in the correlations between these values. This was clearly shown by explicitly modeling the relationship between metabolites by MFA. Incorporating the calculated intracellular fluxes into the metabolite data further improved class separation by FDA, especially in the burn study case. Finally, comparing the rotated DLs with sample projections, we arrived at a sequence of changes in metabolite exchange patterns that potentially delineates hepatic interaction with whole-body circulation at the substrate level during the first week of burn injury.

The linear combinations defining the sample projections in FDA space essentially constitute a classification function which separates samples (in this case livers) based on a composite criterion involving multiple variables (in this case metabolites and fluxes). The classification functions, i.e. sample projections, presented thus far were derived using all of the available data, and their success in discriminating the source livers was assessed by visual inspection of the resulting projections. We also performed a more rigorous validation trial, where classification functions were calculated by from a partial data set consisting of the full set minus a randomly selected sample. After building the classification functions, percent errors were calculated by counting the number of times the random sample was misclassified during a set of 100 trials. In order to render a scenario with potential clinical relevance, a two-step classification strategy was devised, where the first (gating) step discriminated between sham-burn and burn samples, and the second step discriminated between samples isolated at different times post-burn. The small size of the resulting errors (Table 5-5) show that this strategy was successful with respect to distinguishing sham-burn from burn liver samples, but less so with respect to identifying the post-burn isolation time. Nevertheless, these validation trials further underlined the advantage of incorporating the calculated fluxes into the variable space, as this reduced the classification errors for both steps.

One significant result of the present chapter is that classification of physiological states by metabolic profiling gains in quality when larger numbers of metabolite measurements are used. Conversely, attempting to discriminate between physiological states using a small number of measurements leads to poor outcomes. In a clinical context, this result implies that diagnosing or monitoring progression of metabolic disorders should be best conducted using as many measurements as possible. As, there is significant information contained in the correlations between measurements, the probability of correctly discriminating between normal and disease states or various stages of disease progression improves with the number of measurements used. Furthermore, employing a basket of metabolites, rather than one or a few markers, lowers the chance for misdiagnosis or misclassification. These ideas were illustrated by the case study involving liver samples isolated at various times after burn injury, where samples closely related with respect to time were inseparable when only a few markers were employed.

Table 5-5. Model Classification Errors, Burn Study Data

Trial	% Error, Metabolite Data		% Error, Metabolite and Flux Data	
	Burn vs. Sham-burn	Treatment Time	Burn vs. Sham-burn	Treatment Time
1	8	32	28	0.005
2	6	28	25.5	0
3	7.5	34	30	0.01
4	2.5	33.5	23	0.005
5	4.5	28.5	24	0
Mean	5.7	31.2	26.1	0.004

A corollary to the above observation is that physiologically useful conclusions may be drawn from the projected sample distances in FDA space. Intuitively, physiologically distinct states are easier to discriminate than those similar to each other. This was seen in Figures 6 and 7, where day 7 post-burn liver samples could be separated from sham-burn control samples by using only 7 markers, whereas day 1 post-burn samples could be separated from sham-burn control samples only after incorporating calculated intracellular fluxes. Thus, the distance between sample clusters correlated with degree of distinction between physiological state in the context of metabolite measurement descriptors. Presumably, the physiological state at day 7 post-burn, when hepatic hypermetabolism is fully established, is very different from the sham-burn state, whereas the state at day 1 post-burn, when hypermetabolism has just begun to develop, is not so different, as judged by aggregate differences in metabolite exchange rates and their correlations.

Physiological interpretations existed also for the projection loadings. The initial stage of hepatic hypermetabolic response during the first week of burn injury was best characterized by changes in amino acid exchange. Similarly, the second, intermediate stage was defined by alterations to the inputs and outputs for intracellular pathways whose regulation was presumably more complex and therefore slower to be affected by the systemic injury. The third and final stage was delineated by changes to inputs and outputs for respiration whose regulation was even more convoluted and required more involved coordinate modifications to all central carbon pathways.

In conclusion, this chapter has shown that metabolic profiling as outlined here, is a promising methodology for clinical diagnosis as well as a useful research tool for investigating disease progression. Applying a projection based classification method, we reaffirmed the benefit of the comprehensive, integrative approach to investigating cellular metabolism, in this case defining physiological states. It was also shown that the information content of metabolite measurements is significantly upgraded by explicitly modeling naturally existing correlations between the metabolites. One way to accomplish this was by using MFA, which takes advantage of the well-established stoichiometric relationships between metabolic intermediates. Thus, considering many metabolites, rather than a few, and examining correlations between metabolites heightens the sensitivity and adds robustness to physiological state classification by metabolite profiling. These results, and others presented in this dissertation, call for continued

work in developing tools for formulating, validating, and analyzing larger, more complex metabolic network models, as well as robust techniques for high-throughput detection of large arrays of metabolites and their isotopomers.

BIBLIOGRAPHY

1. Bailey, J.E., *Toward a science of metabolic engineering.* Science, 1991. **252**(5013): p. 1668-75.
2. Stephanopoulos, G., *Metabolic fluxes and metabolic engineering.* Metab Eng, 1999. **1**(1): p. 1-11.
3. Nielsen, J., *Metabolic engineering.* Applied Microbiology and Biotechnology, 2001. **55**(3): p. 263-283.
4. Cameron, D.C. and I.T. Tong, *Cellular and metabolic engineering. An overview.* Appl Biochem Biotechnol, 1993. **38**(1-2): p. 105-40.
5. Ikeda, M., A. Ozaki, and R. Katsumata, *Phenylalanine production by metabolically engineered Corynebacterium glutamicum with the pheA gene of Escherichia coli.* Appl Microbiol Biotechnol, 1993. **39**(3): p. 318-23.
6. Deanda, K., et al., *Development of an arabinose-fermenting Zymomonas mobilis strain by metabolic pathway engineering.* Appl Environ Microbiol, 1996. **62**(12): p. 4465-70.
7. Ramos, J.L., et al., *Redesigning metabolic routes: manipulation of TOL plasmid pathway for catabolism of alkylbenzoates.* Science, 1987. **235**(4788): p. 593-6.
8. Furukawa, K., et al., *Efficient degradation of trichloroethylene by a hybrid aromatic ring dioxygenase.* J Bacteriol, 1994. **176**(7): p. 2121-3.
9. Timmis, K.N., R.J. Steffan, and R. Unterman, *Designing microorganisms for the treatment of toxic wastes.* Annu Rev Microbiol, 1994. **48**: p. 525-57.
10. Madison, L.L. and G.W. Huisman, *Metabolic engineering of poly(3-hydroxyalkanoates): from DNA to plastic.* Microbiol Mol Biol Rev, 1999. **63**(1): p. 21-53.
11. Ohta, K., et al., *Genetic improvement of Escherichia coli for ethanol production: chromosomal integration of Zymomonas mobilis genes encoding pyruvate decarboxylase and alcohol dehydrogenase II.* Appl Environ Microbiol, 1991. **57**(4): p. 893-900.
12. Ohta, K., et al., *Metabolic engineering of Klebsiella oxytoca M5A1 for ethanol production from xylose and glucose.* Appl Environ Microbiol, 1991. **57**(10): p. 2810-5.
13. Kao, C.M., L. Katz, and C. Khosla, *Engineered biosynthesis of a complete macrolactone in a heterologous host.* Science, 1994. **265**(5171): p. 509-12.
14. Hershberger, C.L., *Metabolic engineering of polyketide biosynthesis.* Curr Opin Biotechnol, 1996. **7**(5): p. 560-2.

15. Khosla, C. and J.E. Bailey, *Heterologous expression of a bacterial haemoglobin improves the growth properties of recombinant Escherichia coli.* Nature, 1988. **331**(6157): p. 633-5.

16. Aristidou, A.A., K.Y. San, and G.N. Bennett, *Modification of Central Metabolic Pathway in Escherichia-Coli to Reduce Acetate Accumulation by Heterologous Expression of the Bacillus-Subtilis Acetolactate Synthase Gene.* Biotechnology and Bioengineering, 1994. **44**(8): p. 944-951.

17. Yanagimachi, K.S., et al., *Metabolic flux analysis and characterization of indene bioconversion in Rhodococcus sp.* Abstracts of Papers of the American Chemical Society, 2000. **219**: p. 115-BIOT.

18. Stafford, D.E., et al., *Characterization of indene bioconversion in Rhodococcus sp continuous cultures using radioactive tracers and multichannel flow cytometry.* Abstracts of Papers of the American Chemical Society, 2000. **219**: p. 69-BIOT.

19. Aldor, I. and J.D. Keasling, *Metabolic engineering of poly(3-hydroxybutyrate-co-3-hydroxyvalerate) composition in recombinant Salmonella enterica serovar typhimurium.* Biotechnol Bioeng, 2001. **76**(2): p. 108-14.

20. Daae, E.B., et al., *Metabolic modeling as a tool for evaluating polyhydroxyalkanoate copolymer production in plants.* Metab Eng, 1999. **1**(3): p. 243-54.

21. Slater, S., et al., *Metabolic engineering of Arabidopsis and Brassica for poly(3-hydroxybutyrate-co-3-hydroxyvalerate) copolymer production.* Nat Biotechnol, 1999. **17**(10): p. 1011-6.

22. Nerem, R.M., *Tissue engineering in the USA.* Med Biol Eng Comput, 1992. **30**(4): p. CE8-12.

23. Sahhar, A., et al., *Cerebral neurons, skeletal myoblasts, and cardiac muscle cells cultured on macroporous beads.* Biotechnol. Bioeng., 1994. **43**(8): p. 826-831.

24. Naughton, B.A., et al., *Stereotypic culture systems for liver and bone marrow: evidence for the development of functional fissue in vitro and following implantation in vivo.* Biotechnol. Bioeng., 1994. **43**(8): p. 810-825.

25. Tziampazis, E. and A. Sambanis, *Tissue engineering of a bioartificial pancreas: modeling the cell environment and device function.* Biotechnol. Prog., 1995. **11**(2): p. 115-126.

26. Foy, B.D., et al., *Engineering organ perfusion protocols: NMR analysis of hepatocyte isolation from perfused rat liver.* Biotechnol. Bioeng., 1994. **43**(7): p. 661-672.

27. Fussenegger, M., et al., *Controlled proliferation by multigene metabolic engineering enhances the productivity of Chinese hamster ovary cells [In Process Citation].* Nat. Biotechnol., 1998. **16**(5): p. 468-72.

28. Boyce, S.T., et al., *Topical nutrients promote engraftment and inhibit wound contraction of cultured skin substitutes in athymic mice.* J. Invest. Dermatol., 1995. **104**(3): p. 345-9.

29. Naughton, G., J. Mansbridge, and G. Gentzkow, *A metabolically active human derman replacement for the treatment of diabetic foot ulcers.* Artif. Organs., 1997. **21**(11): p. 1203-1210.

30. Pincus, D.W., et al., *Neural stem and progenitor cells: a strategy for gene therapy and brain repair.* Neurosurgery, 1998. **42**(4): p. 858-867.

31. Naik, S., et al., *Isolation and culture of porcine hepatocytes for aritifical liver support.* Cell Transplant., 1996. **5**(1): p. 107-115.

32. Minuth, W.W., M. Sittinger, and S. Kloth, *Tissue engineering: generation of differentiated artificial tissues for biomedical applications.* Cell Tissue Res., 1998. **291**(1): p. 1-11.

33. Xie, L. and D.I.C. Wang, *High cell density and high monoclonal antibody production through medium design and rational control in a bioreactor.* Biotechnol. Bioeng., 1996. **51**(6): p. 725.

34. Stephanopoulos, G. and A.J. Sinskey, *Metabolic engineering--methodologies and future prospects.* Trends. Biotechnol., 1993. **11**(9): p. 392-6.

35. Stephanopoulos, G., A.A. Aristidou, and J. Nielsen, *Metabolic engineering : principles and methodologies.* 1998, San Diego: Academic Press. xxi, 725.

36. Papoutsakis, E.T., *Equations and calculations for fermentations of butyric acid bacteria (Reprinted from Biotechnology and Bioengineering, vol 26, pg 174-187, 1984).* Biotechnology and Bioengineering, 2000. **67**(6): p. 813-826.

37. Varma, A. and B.O. Palsson, *Metabolic flux balancing: basic concepts, scientifc, and practical use.* Biotechnology (N Y), 1994. **12**(10): p. 994.

38. Holms, W.H., *The central metabolic pathways of Escherichia coli: relationship between flux and control at a branch point, efficiency of conversion to biomass, and excretion of acetate.* Curr. Top. Cell Regul., 1986. **28**: p. 69-105.

39. Vallino, J.J. and G. Stephanopoulos, *Metabolic flux distribution in corynebacterium glutamicum during growth and lysine overproduction.* Biotechnol. Bioeng., 1993. **41**(6): p. 633.

40. Vallino, J.J. and G. Stephanopoulos, *Carbon flux distribution at the glucose-6-phosphate branch point in corynebacterium glutamicum during lysine overproduction.* Biotechnol. Prog., 1994. **10**(3): p. 327.

41. Stephanopoulos, G. and J.J. Vallino, *Network rigidity and metabolic engineering in metabolite overproduction.* Science, 1991. **252**(5013): p. 1675-81.

42. Joergensen, H., et al., *Metabolic flux distribution in Penicilium chrysogenum during fed-batch cultivations.* Biotechnol. Bioeng., 1995. **46**(2): p. 117.

43. Pons, A., et al., *Metabolic flux distribution in Corynebacterium melassecola.* Biotechnol. Bioeng., 1996. **51**(2): p. 177.

44. Stryer, L., *Biochemistry*. 4th ed. ed. 1995, New York: W.H. Freeman. 1064.

45. Bonarius, H.P.J., G. Schmid, and J. Tramper, *Flux analysis of underdetermined metabolic networks: the quest for the missing constraints.* Trends. Biotechnol., 1997. **15**(8): p. 308-314.

46. Kalderon, B., et al., *Glucose recycling and production in children with glycogen storage disease type I, studied by gas chromatography/mass spectrometry and (U- 13C)glucose.* Biomed. Environ. Mass. Spectrom., 1988. **16**(1-12): p. 305-8.

47. Des Rosiers, C., et al., *Isotopomer analysis of citric acid cycle and gluconeogenesis in rat liver. Reversibility of isocitrate dehydrogenase and involvement of ATP- citrate lyase in gluconeogenesis.* J. Biol. Chem., 1995. **270**(17): p. 10027-36.

48. Wolfe, R.R., et al., *Effect of severe burn injury on substrate cycling by glucose and fatty acids.* N Engl J Med, 1987. **317**(7): p. 403-8.

49. Reich, J.G., *Energy metabolism of the cell: a theoretical treatise*. 1981, Lodon: Academic Press. 345.

50. Fell, D.A., *Metabolic control analysis: a survey of its theoretical and experimental development.* Biochem. J., 1992. **286**(Pt 2): p. 313-30.

51. Wang, N.S. and G. Stephanopoulos, *Application of macroscopic balances to the identification of gross measurement errors.* Biotechnol. Bioeng., 1983. **25**: p. 2177-2208.

52. Bertsimas, D. and J.N. Tsitsiklis, *Introduction to linear optimization.* Athena scientific series in optimization and neural computation. 1997, Belmont, MA: Athena Scientific.

53. Savinell, J.M. and B.O. Palsson, *Network analysis of intermediary metabolism using linear optimization. II. Interpretation of hybridoma cell metabolism.* J. Theor. Biol., 1992. **154**(4): p. 455-73.

54. Savinell, J.M. and B.O. Palsson, *Network analysis of intermediary metabolism using linear optimization. I. Development of mathematical formalism.* J. Theor. Biol., 1992. **154**(4): p. 421-54.

55. Weinman, E.O., E.H. Strisower, and I.L. Chaikoff, *Conversion of fatty acids to carbohydrate. Applications of isotopes to this problem and the role of the Krebs cycle as a synthetic pathway.* Physiol. Rev., 1957. **37**: p. 252-272.

56. Rognstad, R. and J. Katz, *Gluconeogenesis in the kidney cortex. Quantitative estimation of carbon flow.* J. Biol. Chem., 1972. **247**(19): p. 6047-54.

57. Kelleher, J.K., *Analysis of tricarboxylic acid cycle using [14C]citrate specific activity ratios.* Am. J. Physiol., 1985. **248**(2 Pt 1): p. E252-60.

58. Kelleher, J.K. and B.M.d. Bryan, *A 14CO2 ratios method for detecting pyruvate carboxylation.* Anal. Biochem., 1985. **151**(1): p. 55-62.

59. Cohen, D.M. and R.N. Bergman, *SYNTAX: a rule-based stochastic simulation of the time-varying concentrations of positional isotopomers of metabolic intermediates.* Comput. Biomed. Res., 1994. **27**(2): p. 130-47.

60. Cohen, D.M. and R.N. Bergman, *Prediction of positional isotopomers of the citric acid cycle: the syntactic approach.* Am. J. Physiol., 1994. **266**(3 Pt 1): p. E341-50.

61. Cohen, D.M. and R.N. Bergman, *Estimation of TCA cycle flux, aminotransferase flux, and anaplerosis in heart: validation with syntactic model.* Am. J. Physiol., 1995. **268**(3 Pt 1): p. E397-409.

62. Chance, E.M., et al., *Mathematical analysis of isotope labeling in the citric acid cycle with applications to 13C NMR studies in perfused rat hearts.* J. Biol. Chem., 1983. **258**(22): p. 13785-94.

63. Chatham, J.C., et al., *Calculation of absolute metabolic flux and the elucidation of the pathways of glutamate labeling in perfused rat heart by 13C NMR spectroscopy and nonlinear least squares analysis.* J. Biol. Chem., 1995. **270**(14): p. 7999-8008.

64. Yu, X., et al., *Kinetic analysis of dynamic 13C NMR spectra: metabolic flux, regulation, and compartmentation in hearts.* Biophys. J., 1995. **69**(5): p. 2090-102.

65. Yu, X., et al., *Subcellular metabolite transport and carbon isotope kinetics in the intramyocardial glutamate pool.* Biochemistry, 1996. **35**(21): p. 6963-8.

66. Yu, X., N.M. Alpert, and E.D. Lewandowski, *Modeling enrichment kinetics from dynamic 13C-NMR spectra: theoretical analysis and practical considerations.* Am. J. Physiol., 1997. **272**(6 Pt 1): p. C2037-48.

67. Gavva, S.R., et al., *A 13C isotopomer n.m.r. method for monitoring incomplete beta-oxidation of fatty acids in intact tissue.* Biochem. J., 1994. **303**(Pt 3): p. 847-53.

68. Cohen, S.M., J.G. Werrmann, and M.R. Tota, *13C NMR study of the effects of leptin treatment on kinetics of hepatic intermediary metabolism.* Proc Natl Acad Sci U S A, 1998. **95**(13): p. 7385-90.

69. Shulman, R.G. and D.L. Rothman, *13C NMR of intermediary metabolism: implications for systemic physiology.* Annu Rev Physiol, 2001. **63**: p. 15-48.

70. Sherry, A.D., et al., *Effects of aminooxyacetate on glutamate compartmentation and TCA cycle kinetics in rat hearts.* Am J Physiol, 1998. **274**(2 Pt 2): p. H591-9.

71. Schmidt, K., et al., *13C tracer experiments and metabolite balancing for metabolic flux analysis: comparing two approaches.* Biotechnol Bioeng, 1998. **58**(2-3): p. 254-7.

72. Wittmann, C. and E. Heinzle, *Modeling and experimental design for metabolic flux analysis of lysine- producing Corynebacteria by mass spectrometry.* Metab Eng, 2001. **3**(2): p. 173-91.

73. Zupke, C. and G. Stephanopoulos, *Modeling of isotope distributions and intracellular fluxes in metabolic networks using atom mapping matrices.* Biotechnol. Prog., 1994. **10**(5): p. 489.

74. Zupke, C., et al., *Numerical isotopomer analysis: estimation of metabolic activity.* Anal. Biochem., 1997. **247**(2): p. 287-93.

75. Fernandez, C.A. and C. Des Rosiers, *Modeling of liver citric acid cycle and gluconeogenesis based on 13C mass isotopomer distribution analysis of intermediates.* J. Biol. Chem., 1995. **270**(17): p. 10037-42.

76. Schmidt, K., et al., *Modeling isotopomer distributions in biochemical networks using isotopomer mapping matrices.* Biotechnol. Bioeng., 1997. **55**(6): p. 831.

77. Vogt, J.A., et al., *A general model for analysis of the tricarboxylic acid cycle with use of [13C]glutamate isotopomer measurements.* Am. J. Physiol., 1994. **266**(6 Pt 1): p. E1012-22.

78. Schmidt, K., et al., *Quantification of intracellular metabolic fluxes from fractional enrichment and 13C-13C coupling constraints on the isotopomer distribution in labeled biomass components.* Metab Eng, 1999. **1**(2): p. 166-79.

79. Dolezal, J., J. Fidler, and I.F.f.I. Processing. *System modeling and optimization: proceedings of the seventeenth IFIP TC7 conference on system modeling and optimization.* in *IFIP Conference on System Modeling and Optimization.* 1995. Prague, Czech Republic: Chapman and Hall.

80. Wiechert, W. and A.A. de Graaf, *In vivo stationary flux analysis by 13C labeling.* Adv. Biochem. Eng. Biotechnol., 1996. **54**: p. 109.

81. Wiechert, W. and A.A. de Graaf, *Bidirectional reaction steps in metabolic networks I.* Biotechnol. Bioeng., 1997. **55**(1): p. 101.

82. Reder, C., *Metabolic control theory - a structural approach.* J. Theor. Biol., 1988. **135**(2): p. 175-201.

83. Szyperski, T., *Biosynthetically directed fractional 13C-labeling of proteinogenic amino acids. An efficient analytical tool to investigate intermediary metabolism.* Eur. J. Biochem., 1995. **232**(2): p. 433-48.

84. Christensen, B. and J. Nielsen, *Isotopomer analysis using GC-MS.* Metab Eng, 1999. **1**(4): p. 282-90.

85. Wolfe, R.R., *Tracers in metabolic research: radioisotope and stable isotope/mass spectrometric analysis.* 1984, New York: A.R. Liss. 287.

86. Wolfe, R.R., *Radioactive and stable isotope tracers in biomedicine: principles and practice of kinetic analysis.* 1992, New York: Wiley-Liss. 471.

87. Hellerstein, M.K., et al., *Altered fluxes responsible for reduced hepatic glucose production and gluconeogenesis by exogenous glucose in rats.* Am. J. Physiol., 1997. **272**(1 Pt 1): p. E163-72.

88. Kalderon, B., A. Gopher, and A. Lapidot, *A quantitative analysis of the metabolic pathways of hepatic glucose synthesis in vivo with 13C-labeled substrates.* FEBS Lett., 1987. **213**(1): p. 209-14.

89. Kalderon, B., et al., *Estimation of glucose carbon recycling in children with glycogen storage disease: A 13C NMR study using [U-13C]glucose.* Proc. Natl. Acad. Sci. U. S. A., 1989. **86**(12): p. 4690-4.

90. Kalderon, B., et al., *Glucose recycling and production in glycogenosis type I and III: stable isotope technique study.* Am. J. Physiol., 1989. **257**(3 Pt 1): p. E346-53.

91. Strong, J.M., et al., *A novel approach to the analysis of mass spectrally assayed stable isotope-labeling experiments.* J. Biol. Chem., 1985. **260**(7): p. 4276-81.

92. Hellerstein, M.K., et al., *Use of mass isotopomer distributions in secreted lipids to sample lipogenic acetyl-CoA pool in vivo in humans.* Am. J. Physiol., 1991. **261**(4 Pt 1): p. E479-86.

93. Hellerstein, M.K., *Relationship between precursor enrichment and ratio of excess M2/excess M1 isotopomer frequencies in a secreted polymer.* J. Biol. Chem., 1991. **266**(17): p. 10920-4.

94. Hellerstein, M.K., et al., *Measurement of de novo hepatic lipogenesis in humans using stable isotopes.* J. Clin. Invest., 1991. **87**(5): p. 1841-52.

95. Hellerstein, M.K. and R.A. Neese, *Mass isotopomer distribution analysis: a technique for measuring biosynthesis and turnover of polymers.* Am. J. Physiol., 1992. **263**(5 Pt 1): p. E988-1001.

96. Lee, W.N., et al., *In vivo measurement of fatty acids and cholesterol synthesis using D2O and mass isotopomer analysis.* Am. J. Physiol., 1994. **266**(5 Pt 1): p. E699-708.

97. Lee, W.N., et al., *Measurement of fractional lipid synthesis using deuterated water (2H2O) and mass isotopomer analysis.* Am. J. Physiol., 1994. **266**(3 Pt 1): p. E372-83.

98. Landau, B.R., *Estimating gluconeogenic rates in NIDDM.* Adv. Exp. Med. Biol., 1993. **334**: p. 209-20.

99. Neese, R.A., et al., *Gluconeogenesis and intrahepatic triose phosphate flux in response to fasting or substrate loads. Application of the mass isotopomer distribution analysis technique with testing of assumptions and potential problems.* J. Biol. Chem., 1995. **270**(24): p. 14452-66.

100. Previs, S.F., et al., *Limitations of the mass isotopomer distribution analysis of glucose to study gluconeogenesis. Substrate cycling between glycerol and triose phosphates in liver.* J. Biol. Chem., 1995. **270**(34): p. 19806-15.

101. Kharroubi, A.T., et al., *Isotopomer spectral analysis of triglyceride fatty acid synthesis in 3T3-L1 cells.* Am. J. Physiol., 1992. **263**(4 Pt 1): p. E667-75.

102. Kelleher, J.K., et al., *Isotopomer spectral analysis of cholesterol synthesis: applications in human hepatoma cells.* Am. J. Physiol., 1994. **266**(3 Pt 1): p. E384-95.

103. Holleran, A.L., G. Fiskum, and J.K. Kelleher, *Quantitative analysis of acetoacetate metabolism in AS-30D hepatoma cells with 13C and 14C isotopic techniques.* Am. J. Physiol., 1997. **272**(6 Pt 1): p. E945-51.

104. Lligona-Trulla, L., et al., *Acetyl-L-carnitine flux to lipids in cells estimated using isotopomer spectral analysis.* J. Lipid. Res., 1997. **38**(7): p. 1454-62.

105. Portais, J.C., et al., *Metabolic flux determination in C6 glioma cells using carbon-13 distribution upon [1-13C]glucose incubation.* Eur J Biochem, 1993. **217**(1): p. 457-68.

106. Portais, J.C., et al., *Glucose and glutamine metabolism in C6 glioma cells studied by carbon 13 NMR.* Biochimie, 1996. **78**(3): p. 155-64.

107. Bouzier, A.K., et al., *Glucose and lactate metabolism in C6 glioma cells: evidence for the preferential utilization of lactate for cell oxidative metabolism.* Dev Neurosci, 1998. **20**(4-5): p. 331-8.

108. Malloy, C.R., A.D. Sherry, and F.M. Jeffrey, *Analysis of tricarboxylic acid cycle of the heart using 13C isotope isomers.* Am J Physiol, 1990. **259**(3 Pt 2): p. H987-95.

109. Laplante, A., et al., *Effects and metabolism of fumarate in the perfused rat heart. A 13C mass isotopomer study.* Am. J. Physiol., 1997. **272**(1 Pt 1): p. E74-82.

110. Sumegi, B., et al., *Lipoamide influences substrate selection in post-ischaemic perfused rat hearts.* Biochem J, 1994. **297**(Pt 1): p. 109-13.

111. Cohen, S.M., *13C and 31P NMR study of gluconeogenesis: utilization of 13C-labeled substrates by perfused liver from streptozotocin-diabetic and untreated rats.* Biochemistry, 1987. **26**(2): p. 563-72.

112. Cohen, S.M., *13C NMR study of effects of fasting and diabetes on the metabolism of pyruvate in the tricarboxylic acid cycle and the utilization of pyruvate and ethanol in lipogenesis in perfused rat liver.* Biochemistry, 1987. **26**(2): p. 581-9.

113. Cohen, S.M., *Effects of insulin on perfused liver from streptozotocin-diabetic and untreated rats: 13C NMR assay of pyruvate kinase flux.* Biochemistry, 1987. **26**(2): p. 573-80.

114. Peroni, O., et al., *Glucose production and gluconeogenesis in postabsorptive and starved normal and streptozotocin-diabetic rats.* Metabolism, 1997. **46**(11): p. 1358-63.

115. Tayek, J.A. and J. Katz, *Glucose production, recycling, and gluconeogenesis in normals and diabetics: a mass isotopomer [U-13C]glucose study.* Am. J. Physiol., 1996. **270**(4 Pt 1): p. E709-17.

116. Landau, B.R., et al., *Estimates of Krebs cycle activity and contributions of gluconeogenesis to hepatic glucose production in fasting healthy subjects and IDDM patients.* Diabetologia, 1995. **38**(7): p. 831-8.

117. Gopher, A., et al., *Determination of fructose metabolic pathways in normal and fructose-intolerant children: a 13C NMR study using [U-13C]fructose.* Proc Natl Acad Sci U S A, 1990. **87**(14): p. 5449-53.

118. Di Donato, L., et al., *Rates of gluconeogenesis and citric acid cycle in perfused livers, assessed from the mass spectrometric assay of the 13C labeling pattern of glutamate.* J. Biol. Chem., 1993. **268**(6): p. 4170-80.

119. Magnusson, I., et al., *Noninvasive tracing of Krebs cycle metabolism in liver.* J. Biol. Chem., 1991. **266**(11): p. 6975-84.

120. Jones, J.G., et al., *13C NMR measurements of human gluconeogenic fluxes after ingestion of [U-13C]propionate, phenylacetate, and acetaminophen.* Am J Physiol, 1998. **275**(5 Pt 1): p. E843-52.

121. Follstad, B.D. and G. Stephanopoulos, *Effect of reversible reactions on isotope label redistribution-- analysis of the pentose phosphate pathway.* Eur. J. Biochem., 1998. **252**(3): p. 360-71.

122. Sherry, A.D., et al., *13C isotopomer analyses in intact tissue using [13C]homonuclear decoupling.* Magn. Reson. Med., 1994. **31**(4): p. 374-9.

123. Wykes, L.J., F. Jahoor, and P.J. Reeds, *Gluconeogenesis measured with [U-13C]glucose and mass isotopomer analysis of apoB-100 amino acids in pigs.* Am. J. Physiol., 1998. **274**(2 Pt 1): p. E365-76.

124. Marx, A., et al., *Determination of the fluxes in the central metabolism of Corynebacterium glutamicum by nuclear magnetic resonance spectroscopy combined with metabolite balancing.* Biotechnol. Bioeng., 1996. **49**(2): p. 111-129.

125. Eisenreich, W., et al., *Retrobiosynthetic analysis of carbon fixation in the phototrophic eubacterium Chloroflexus aurantiacus.* Eur. J. Biochem., 1993. **215**(3): p. 619-32.

126. Crawford, J.M. and J.J. Blum, *Quantitative analysis of flux along the gluconeogenic, glycolytic and pentose phosphate pathways under reducing conditions in hepatocytes isolated from fed rats.* Biochem. J., 1983. **212**(3): p. 585-98.

127. Ekiel, I., I.C. Smith, and G.D. Sprott, *Biosynthetic pathways in Methanospirillum hungatei as determined by 13C nuclear magnetic resonance.* J. Bacteriol., 1983. **156**(1): p. 316-26.

128. Cuthbertson, D.P., *The disturbance of metabolism produced by bony and non-bony injury, with notes on certain abnormal conditions of bone.* Biochem. J., 1930. **24**: p. 1244-1254.

129. Tredget, E.E. and Y.M. Yu, *The metabolic effects of thermal injury.* World J Surg, 1992. **16**(1): p. 68-79.

130. Khorram-Sefat, R., et al., *Long-term measurements of energy expenditure in severe burn injury.* World J Surg, 1999. **23**(2): p. 115-22.

131. Cerra, F.B., *Hypermetabolism, organ failure, and metabolic support.* Surgery, 1987. **101**(1): p. 1-14.

132. Cerra, F.B., *Multiple organ failure syndrome.* Dis Mon, 1992. **38**(12): p. 843-947.

133. Wang, S., S.E. Wolf, and B.M.J. Evers, *Differential activation of the Stat signaling pathway in the liver after burn injury.* Am J Physiol, 1997. **273**(5 Pt 1): p. G1153-9.

134. Wolfe, R.R. and J.F. Burke, *Effect of burn trauma on glucose turnover, oxidation, and recycling in guinea pigs.* Am J Physiol, 1977. **233**(2): p. E80-5.

135. Wolfe, R.R., *Burn injury and increased glucose production.* J Trauma, 1979. **19**(11 Suppl): p. 898-9.

136. Lohmann, R., et al., *Stimulation of rat hepatic amino acid transport by burn injury.* Metabolism, 1998. **47**(5): p. 608-16.

137. LaLonde, C., et al., *Energy charge potential and glutathione levels as predictors of outcome following burn injury complicated by endotoxemia.* Shock, 1998. **9**(1): p. 27-32.

138. Beal, A.L. and F.B. Cerra, *Multiple Organ Failure Syndorme in the 1990s.* JAMA, 1994. **271**(3): p. 226 - 233.

139. Carter, E.A., et al., *Nitric oxide production is intensely and persistently increased in tissue by thermal injury.* Biochem J, 1994. **304**(Pt 1): p. 201-4.

140. Yamaguchi, Y., et al., *Effect of burn injury on glucose and nitrogen metabolism in the liver: preliminary studies in a perfused liver system.* Surgery, 1997. **121**(3): p. 295-303.

141. Yarmush, D.M., et al., *Cutaneous burn injury alters relative tricarboxylic acid cycle fluxes in rat liver.* J Burn Care Rehabil, 1999. **20**(4): p. 292-302.

142. Pilkis, S.J. and D.K. Granner, *Molecular physiology of the regulation of hepatic gluconeogenesis and glycolysis.* Annu Rev Physiol, 1992. **54**: p. 885-909.

143. Hellerstein, M.K., J.M. Schwarz, and R.A. Neese, *Regulation of hepatic de novo lipogenesis in humans.* Annu Rev Nutr, 1996. **16**: p. 523-57.

144. Gabay, C. and I. Kushner, *Acute-phase proteins and other systemic responses to inflammation.* N Engl J Med, 1999. **340**(6): p. 448-54.

145. Dickson, P.W., D. Bannister, and G. Schreiber, *Minor burns lead to major changes in synthesis rates of plasma proteins in the liver.* J Trauma, 1987. **27**(3): p. 283-6.

146. Nielsen, J., *Metabolic engineering: techniques for analysis of targets for genetic manipulations.* Biotechnol Bioeng, 1998. **58**(2-3): p. 125-32.

147. Lee, K., et al., *Metabolic Flux Analysis: A Powerful Tool for Monitoring Tissue Function.* Tissue Eng, 1999. **5**(4): p. 347-368.

148. Kuehn, A. and R. Scholz, *Rates of flux through the pentose cycle in perfused rat liver.* Eur J Biochem, 1982. **124**: p. 611-617.

149. Gaines, D.W., L. Friedman, and R.C. Braunberg, *Facilitated micromethod for measurement of metabolically generated 14CO2, with application to measurement of ornithine decarboxylase.* Anal Biochem, 1989. **178**(1): p. 52-6.

150. Zupke, C., A.J. Sinskey, and G. Stephanopoulos, *Intracellular flux analysis applied to the effect of dissolved oxygen on hybridomas.* Appl Microbiol Biotechnol, 1995. **44**(1-2): p. 27-36.

151. Nogueira, M., et al., *Regulation of the pentose phosphate cycle. Cofactor that controls the inhibition of glucose-6-phosphate dehydrogenase by NADPH in rat liver.* Biochem J, 1986. **239**(3): p. 553-8.

152. Reed, D.J., *Regulation of reductive processes by glutathione.* Biochem Pharmacol, 1986. **35**(1): p. 7-13.

153. Newman, J.J., et al., *Altered muscle metabolism in rats after thermal injury.* Metabolism, 1982. **31**(12): p. 1229-1233.

154. Goldstein, S.A. and D.H. Elwyn, *The effects of injury and sepsis on fuel utilization.* Annu Rev Nutr, 1989. **9**: p. 445-73.

155. Petit, F., G.J. Bagby, and C.H. Lang, *Tumor necrosis factor mediates zymosan-induced increase in glucose flux and insulin resistance.* Am J Physiol, 1995. **268**: p. E219-E228.

156. Kirsch, R.E. and J.J. Franks, *Fibrinogen synthesis in the isolated perfused rat liver: stimulation by a humoral factor associated with trauma.* Hepatology, 1982. **2**(2): p. 205-208.

157. Peavy, D.E., J.M. Taylor, and L.S. Jefferson, *Correlation of albumin production rates and albumin mRNA levels in livers of normal, diabetic, and insulin-treated diabetic rats.* Proc. Natl. Acad. Sci. USA, 1978. **75**(12): p. 5879-5883.

158. Peters, T., *Serm albumin.* Adv. Protein Chem., 1985. **37**: p. 161-215.

159. Morgan, E.H. and T. Peters, *The biosynthesis of rat serum albumin. Effect of protein depletion and refeeding on albumin and transferrin synthesis.* J. Biol. Chem., 1971. **246**: p. 3500-3507.

160. Jeejeebhoy, K.N., et al., *Protein turnover.* Ciba Found. Symp., 1973. **9**: p. 217-238.

161. Brigelius, R., *Glutathione oxidation and activation of pentose phosphate cycle during hydroperoxide metabolism. A comparison of livers from fed and fasted rats.* Hoppe Seylers Z Physiol Chem, 1983. **364**(8): p. 989-96.

162. Large, V., et al., *Use of labeling pattern of liver glutamate to calculate rates of citric acid cycle and gluconeogenesis.* Am. J. Physiol., 1997. **272**(1 Pt 1): p. E51-8.

163. Harper, M.-E. and M.D. Brand, *The quantitative contributions of mitochondrial proton leak and ATP turnover reactions to the changed respiration rates of hepatocytes from rats of different thyroid status.* J Biol Chem, 1993. **268**(20): p. 14850-14860.

164. Scholz, R. and T. Bucher, *Hemoglobin-free perfusion of rat liver*, in *Control of Energy Metabolism*, B. Chance, Editor. 1965, Academic Press: New York. p. 393-414.

165. Wolfe, R.R., in *Radioactive and stable isotope tracers in biomedicine: principles and practice of kinetic analysis*. 1992, Wiley-Liss: New York. p. 293-299.

166. Sabate, L., et al., *A model of the pentose phosphate pathway in rat liver cells.* Mol Cell Biochem, 1995. **142**: p. 9-17.

167. Smith, P.F., D.W. Alberts, and G.F. Rush, *Role of glutathione reductase during menadione-induced NADPH oxidation in isolated rat hepatocytes.* Biochem Pharmacol, 1987. **36**(22): p. 3879-84.

168. Smith, P.F., D.W. Alberts, and G.F. Rush, *Menadione-induced oxidative stress in hepatocytes isolated from fed and fasted rats: the role of NADPH-regenerating pathways.* Toxicol Appl Pharmacol, 1987. **89**(2): p. 190-201.

169. Sies, H., R. Brigelius, and P. Graf, *Hormones, glutathione status and protein S-thiolation.* Adv Enzyme Regul, 1987. **26**: p. 175-89.

170. Spolarics, Z., A.P. Bautista, and J.J. Spitzer, *Primed pentose cycle activity supports production and elimination of superoxide anion in Kupffer cells from rats treated with endotoxin in vivo.* Biochim Biophys Acta, 1993. **1179**(2): p. 134-40.

171. Spolarics, Z. and J.J. Spitzer, *Augmented glucose use and pentose cycle activity in hepatic endothelial cells after in vivo endotoxemia.* Hepatology, 1993. **17**(4): p. 615-20.

172. Demling, R., et al., *Fluid resuscitation with deferoxamine prevents systemic burn-induced oxidant injury.* J. Trauma, 1991. **31**(4): p. 538-43.

173. Sabeh, F., C.R. Baxter, and S.J. Norton, *Skin burn injury and oxidative stress in liver and lung tissues of rabbit models.* Eur J Clin Chem Clin Biochem, 1995. **33**(6): p. 323-8.

174. Brand, M.D., et al., *The causes and functions of mitochondrial proton leak.* Biochim Biophys Acta, 1994. **1187**(2): p. 132-9.

175. Kehrer, J.P., *Free radicals as mediators of tissue injury and disease.* Crit Rev Toxicol, 1993. **23**(1): p. 21-48.

176. Augustin, W., et al., *Role of endogenous and exogenous antioxidants in the defence against functional damage and lipid peroxidation in rat liver mitochondria.* Mol Cell Biochem, 1997. **174**(1-2): p. 199-205.

177. Turrens, J.F. and A. Boveris, *Generation of superoxide anion by the NADH dehydrogenase of bovine heart mitochondria.* Biochem J, 1980. **191**(2): p. 421-7.

178. Beyer, R.E., *The participation of coenzyme Q in free radical production and antioxidation.* Free Radic Biol Med, 1990. **8**(6): p. 545-65.

179. Naqui, A., B. Chance, and E. Cadenas, *Reactive oxygen intermediates in biochemistry.* Annu Rev Biochem, 1986. **55**: p. 137-66.

180. Dong, Y.-L., et al., *Metabolic abnormalities of mitochondrial redox potential in postburn multiple system organ failure.* Burns, 1992. **18**(4): p. 283-286.

181. Wolfe, R.R., J.H. Shaw, and M.J. Durkot, *Energy metabolism in trauma and sepsis: the role of fat.* Prog Clin Biol Res, 1983. **111**: p. 89-109.

182. Bessey, P.Q., et al., *Posttraumatic skeletal muscle proteolysis: the role of the hormonal environment.* World J Surg, 1989. **13**(4): p. 465-70; discussion 471.

183. Chiolero, R., J.P. Revelly, and L. Tappy, *Energy metabolism in sepsis and injury.* Nutrition, 1997. **13**(9 Suppl): p. 45S-51S.

184. Demling, R.H. and P. Seigne, *Metabolic management of patients with severe burns.* World J Surg, 2000. **24**(6): p. 673-80.

185. Hart, D.W., et al., *Persistence of muscle catabolism after severe burn.* Surgery, 2000. **128**(2): p. 312-9.

186. Lee, K., et al., *Metabolic flux analysis of postburn hepatic hypermetabolism.* Metab Eng, 2000. **2**(4): p. 312-27.

187. Sax, H.C., et al., *Increased synthesis of secreted hepatic proteins during abdominal sepsis.* J Surg Res, 1988. **44**(2): p. 109-16.

188. Zhao, G. and A.L. Maclean, *A comparison of canonical discriminant analysis and principal component analysis for spectral transformation.* Photogramm Eng Rem, 2000. **66**(7): p. 841-7.

189. Drake, A.W., *Fundamentals of applied probability theory.* McGraw-Hill series in probability and statistics. 1967, New York,: McGraw-Hill. 283.

190. Eisen, M.B., et al., *Cluster analysis and display of genome-wide expression patterns.* Proc Natl Acad Sci U S A, 1998. **95**(25): p. 14863-8.

191. Dillon, W.R. and M. Goldstein, *Multivariate analysis : methods and applications.* Wiley series in probability and mathematical statistics. Applied probability and statistics. 1984, New York: Wiley. xii, 587.

192. Lehninger, A.L., D.L. Nelson, and M.M. Cox, *Principles of biochemistry.* 2nd ed. 1993, New York, NY: Worth Publishers. xli, 1013, [77].

193. Yang, S., et al., *Mitochondrial adaptations to obesity-related oxidant stress.* Arch Biochem Biophys, 2000. **378**(2): p. 259-68.

194. Cortez-Pinto, H., et al., *Lipids up-regulate uncoupling protein 2 expression in rat hepatocytes.* Gastroenterology, 1999. **116**(5): p. 1184-93.

195. Lee, F.Y., et al., *Tumor necrosis factor increases mitochondrial oxidant production and induces expression of uncoupling protein-2 in the regenerating mice [correction of rat] liver.* Hepatology, 1999. **29**(3): p. 677-87.

196. Cortez-Pinto, H., et al., *Bacterial lipopolysaccharide induces uncoupling protein-2 expression in hepatocytes by a tumor necrosis factor-alpha-dependent mechanism.* Biochem Biophys Res Commun, 1998. **251**(1): p. 313-9.

197. Ricquier, D. and F. Bouillaud, *The uncoupling protein homologues: UCP1, UCP2, UCP3, StUCP and AtUCP.* Biochem J, 2000. **345 Pt 2**: p. 161-79.

198. Wolfe, R.R., H.I. Miller, and J.J. Spitzer, *Glucose and lactate kinetics in burn shock.* Am J Physiol, 1977. **232**(4): p. E415-8.

199. Yu, C.C., H.A. Hua, and C. Tong, *Hyperglycaemia after burn injury.* Burns, 1989. **15**(3): p. 145-6.

200. Wilmore, D.W., *Carbohydrate metabolism in trauma.* Clin Endocrinol Metab, 1976. **5**(3): p. 731-45.

201. Rose, J.G. and D.F. Heath, *The effects of stress and injury on the activity of phosphoenolpyruvate carboxykinase in the liver of the rat.* Biochem J, 1986. **233**(1): p. 239-44.

202. Turinsky, J., et al., *Dynamics of insulin secretion and resistance after burns.* J Trauma, 1977. **17**(5): p. 344-50.

203. Thomas, R., N. Aikawa, and J.F. Burke, *Insulin resistance in peripheral tissues after a burn injury.* Surgery, 1979. **86**(5): p. 742-7.

204. Jenkins, R.C. and R.J. Ross, *Growth hormone therapy for protein catabolism.* Qjm, 1996. **89**(11): p. 813-9.

205. Ikezu, T., et al., *Analysis of thermal injury-induced insulin resistance in rodents. Implication of postreceptor mechanisms.* J Biol Chem, 1997. **272**(40): p. 25289-95.

206. Jahoor, F., D.N. Herndon, and R.R. Wolfe, *Role of insulin and glucagon in the response of glucose and alanine kinetics in burn-injured patients.* J Clin Invest, 1986. **78**(3): p. 807-14.

207. Waymack, J.P. and D.N. Herndon, *Nutritional support of the burned patient.* World J Surg, 1992. **16**(1): p. 80-6.

208. Jeschke, M.G., R.E. Barrow, and D.N. Herndon, *Insulinlike growth factor I plus insulinlike growth factor binding protein 3 attenuates the proinflammatory acute phase response in severely burned children.* Ann Surg, 2000. **231**(2): p. 246-52.

209. Wilmore, D.W., *Alterations in protein, carbohydrate, and fat metabolism in injured and septic patients.* J Am Coll Nutr, 1983. **2**(1): p. 3-13.

210. Baskaran, H., M.L. Yarmush, and F. Berthiaume, *Dynamics of tissue neutrophil sequestration after cutaneous burns in rats.* J Surg Res, 2000. **93**(1): p. 88-96.

211. Skulachev, V.P., *[Nonphosphorylating respiration as the mechanism preventing the formation of active forms of oxygen].* Mol Biol (Mosk), 1995. **29**(6): p. 1199-209.

212. Skulachev, V.P., *Uncoupling: new approaches to an old problem of bioenergetics.* Biochim Biophys Acta, 1998. **1363**(2): p. 100-24.

213. LaLonde, C., et al., *Excessive liver oxidant stress causes mortality in response to burn injury combined with endotoxin and is prevented with antioxidants.* J Burn Care Rehabil, 1997. **18**(3): p. 187-92.

214. Fernandez, V. and L.A. Videla, *Biochemical aspects of cellular antioxidant systems.* Biol Res, 1996. **29**(2): p. 177-82.

215. Martinez-Cayuela, M., *Oxygen free radicals and human disease.* Biochimie, 1995. **77**(3): p. 147-61.

216. Shepherd, V.L., *The role of the respiratory burst of phagocytes in host defense.* Semin Respir Infect, 1986. **1**(2): p. 99-106.

217. Duranteau, J., et al., *Intracellular signaling by reactive oxygen species during hypoxia in cardiomyocytes.* J Biol Chem, 1998. **273**(19): p. 11619-24.

218. Maziere, C., et al., *Oxidized LDL activates STAT1 and STAT3 transcription factors: possible involvement of reactive oxygen species.* FEBS Lett, 1999. **448**(1): p. 49-52.

219. Jones, B.E., et al., *Role of caspases and NF-kappaB signaling in hydrogen peroxide- and superoxide-induced hepatocyte apoptosis.* Am J Physiol Gastrointest Liver Physiol, 2000. **278**(5): p. G693-9.

220. Beltman, J., et al., *C3 toxin activates the stress signaling pathways, JNK and p38, but antagonizes the activation of AP-1 in rat-1 cells.* J Biol Chem, 1999. **274**(6): p. 3772-80.

221. Wesselborg, S., et al., *Activation of transcription factor NF-kappaB and p38 mitogen-activated protein kinase is mediated by distinct and separate stress effector pathways.* J Biol Chem, 1997. **272**(19): p. 12422-9.

222. Dunn, J.C., et al., *Hepatocyte function and extracellular matrix geometry: long-term culture in a sandwich configuration.* Faseb J, 1989. **3**(2): p. 174-7.

223. Seglen, P.O., *Preparation of isolated rat liver cells.* Methods Cell Biol, 1976. **13**: p. 29-83.

224. Foy, B.D., et al., *A device to measure the oxygen uptake rate of attached cells: importance in bioartificial organ design.* Cell Transplant, 1994. **3**(6): p. 515-27.

225. Balis, U.J., et al., *Oxygen consumption characteristics of porcine hepatocytes.* Metab Eng, 1999. **1**(1): p. 49-62.

226. Kuehn, A. and R. Scholz, *Rates of flux through the pentose cycle in perfused rat liver. A procedure for the calculation of rates of substrate flux from 14CO2 production from [1-14C]glucose.* Eur J Biochem, 1982. **124**(3): p. 611-7.

227. Sen, C.K. and L. Packer, *Antioxidant and redox regulation of gene transcription.* Faseb J, 1996. **10**(7): p. 709-20.

228. Kimura, K., et al., *Induction of uncoupling protein (UCP) 2 in primary cultured hepatocytes.* FEBS Lett, 1999. **457**(1): p. 75-9.

229. Gygi, S.P., et al., *Correlation between protein and mRNA abundance in yeast.* Mol Cell Biol, 1999. **19**(3): p. 1720-30.

230. Anderson, L. and J. Seilhamer, *A comparison of selected mRNA and protein abundances in human liver.* Electrophoresis, 1997. **18**(3-4): p. 533-7.

231. Pradet-Balade, B., et al., *Translation control: bridging the gap between genomics and proteomics?* Trends Biochem Sci, 2001. **26**(4): p. 225-9.

232. Griffin, J.L., et al., *Metabolic Profiling of Genetic Disorders: A Multitissue (1)H Nuclear Magnetic Resonance Spectroscopic and Pattern Recognition Study into Dystrophic Tissue.* Anal Biochem, 2001. **293**(1): p. 16-21.

233. Fiehn, O., et al., *Metabolite profiling for plant functional genomics.* Nat Biotechnol, 2000. **18**(11): p. 1157-61.

234. Roessner, U., et al., *Metabolic Profiling Allows Comprehensive Phenotyping of Genetically or Environmentally Modified Plant Systems.* Plant Cell, 2001. **13**(1): p. 11-29.

235. Trethewey, R.N., *Gene discovery via metabolic profiling.* Curr Opin Biotechnol, 2001. **12**(2): p. 135-8.

236. Goodman, S.I., et al., *Organic acid profiles of human tissue biopsies by capillary gas chromatography-mass spectrometry.* J Chromatogr, 1977. **142**: p. 497-503.

237. Jellum, E., *Profiling of human body fluids in healthy and diseased states using gas chromatography and mass spectrometry, with special reference to organic acids.* J Chromatogr, 1977. **143**(5): p. 427-62.

238. Fiehn, O., et al., *Identification of uncommon plant metabolites based on calculation of elemental compositions using gas chromatography and quadrupole mass spectrometry.* Anal Chem, 2000. **72**(15): p. 3573-80.

239. Christensen, B. and J. Nielsen, *Metabolic network analysis. A powerful tool in metabolic engineering.* Adv Biochem Eng Biotechnol, 2000. **66**: p. 209-31.

240. Johnson, R.A. and D.W. Wichern, *Applied multivariate statistical analysis.* 3rd ed. 1992, Englewood Cliffs, N.J.: Prentice Hall. xiv, 642.

241. Arai, K., et al., *Intrahepatic amino acid and glucose metabolism in a D-galactosamine-induced rat liver failure model.* Hepatology, 2001. **34**(2): p. 360-71.

242. Hart, D.W., et al., *Determinants of skeletal muscle catabolism after severe burn.* Ann Surg, 2000. **232**(4): p. 455-65.

APPENDIX. SUPPLEMENTARY MATERIAL FOR CHAPTERS 2 AND 3

A.1 Matlab Implementation of the Metabolite Balance Model

A.1.1 Main function

```
function mfa(S,M)
% MFA
%
% Last modified 3/20/2001
% Variable definitions
% S: stoichiometric matrix
% M: measurement matrix
% M has the following format:
% Column 1: index vector specifying measured reactions.
% Columns 2 to k: measurements
% Column k + 1: measurement mean
% Column k + 2: measurement errors (SD)

% [filename,path] = uigetfile('*.txt','Select Stoichiometric Matrix');
% cd(path);
%l oad(filename);
% disp('Loaded file:');
% filename
% S = input('Type filename without file extension.\n>');

% [filename,path] = uigetfile('*.txt','Select Measurement Matrix');
% cd(path);
%l oad(filename);
% disp('Loaded file:');
% filename
% M = input('Type filename without file extension.\n>');

% Get data size
[data_rows,data_columns] = size(M);
num_groups = data_columns-3;

% Partition S (or G) matrix
list = M(:,1);
Gc = S;
Gc(:,list) = [];
Gm = S(:,list);

% Here allow choice between 1) Moore-Penrose pseudo-inverse and 2) Tsai and Lee, etc.
user = input('1: Moore-Penrose?\n2: Tsai and Lee?\n3: both?\n4: Zupke?\n5: CI?\n>');
```

```
switch user
case 1,
  output = [];
  for i = 1:(num_groups+1)
    vm = M(:,i+1);
    temp = mppi(Gc,Gm,vm,S,M);
    output = [output,temp(:,2)];
  end;
  sd = M(:,data_columns);
  var_vm = power(sd,2);
  Gc_pi = inv(Gc.'*Gc)*Gc.';
  B = -Gc_pi*Gm;
  [B_row,B_col] = size(B);
  for i = 1:B_row
    coeff = B(i,:);
    coeff_2 = power(coeff,2);
    var_vc(i) = coeff_2*var_vm;
  end;
  var_vc = var_vc.';
  var_top = [compidx(S,M(:,1)),var_vc];
  var_bottom = [list,var_vm];
  var = [var_top;var_bottom];
  var = sortrows(var,1);
  sd = power(var(:,2),0.5);
  output = [output,sd];
  figure(1);
  plot(output), hold on, plot(output(:,num_groups+1),'ko'), title('Moore-Penrose'), hold off;
case 2,
  output = [];
  % F is the variance-covariance matrix for the residuals of both the
  % measured fluxes and the pseudo-steady state assumptions.
  noise = input('Use SD info for variance-covariance marix?\n>','s');
  for i = 1:(num_groups+1)
    vm = M(:,i+1);
    temp = eq820(Gc,Gm,vm,S,M,noise);
    output = [output,temp(:,2)];
  end;
  figure(2);
  plot(output), hold on, plot(output(:,num_groups+1),'o'), title('Tsai-Lee'), hold off;
case 3,
  output = [];
  output1 = output;
  output2 = output;
  noise = input('Use SD info for variance-covariance marix?\n>','s');
  for i = 1:(num_groups+1)
    vm = M(:,i+1);
```

```
  temp1 = mppi(Gc,Gm,vm,S,M);
  temp2 = eq820(Gc,Gm,vm,S,M, noise);
  output1 = [output1,temp1(:,2)];
  output2 = [output2,temp1(:,2)];
 end;
 output = [output1,output2];
 for i = 1:length(output)
   ratio(i) = output2(i,num_groups+1)/output1(i,num_groups+1);
 end;
 figure(3);
 subplot(2,2,1), plot(output1), title('Moore-Penrose');
 subplot(2,2,2), plot(output2), title('Tsai-Lee');
 subplot(2,2,3), plot(output1,output2), title('Tsai-Lee vs. Moore-Penrose');
 subplot(2,2,4), plot(ratio), title('Tsai-Lee over Moore-Penrose');
case 4,
  output = [];
  for i = 1:(num_groups+1)
    vm = M(:,i+1);
    temp = zupke(Gc,Gm,vm,S,M);
    output = [output,temp(:,2:3)];
  end;
  figure(4);
  plot(output), hold on, plot(output(:,2*num_groups+1),'ko'), title('Zupke et al.'), hold off;
 case 5,
   h_vect = [];
   Rr = reduced(S,M(:,1));
   D = M(:,data_columns);
   D = num_groups*power(D,2);
   F = diag(D);
   for i = 1:(num_groups+1)
     vm = M(:,i+1);
     temp = CI_value(Rr,vm,F);
     h_vect = [h_vect,temp];
   end;
   h_vect(1,:).'
   choice = input('Apply deletion algorithm? yes or no.\n>','s');
   if strcmp(choice,'no') == 0
     output = [];
     for i = 1:(num_groups+1)
       vm = M(:,i+1);
       temp = best_CI(h_vect(1,i),S,vm,M(:,1),D);
       output = [output,temp];
     end;
     output
   else
     disp('Deletion not applied.');
```

```
    output = h_vect(1,:).'
  end;
otherwise,
  disp('Choice not recognized.');
end;

% Save?
save = input('Save? yes or no.\n>','s');
while (strcmp(save,'yes') | strcmp(save,'no')) == 0
  save = input('Invalid response. Enter yes or no.\n>','s');
end;
if strcmp(save,'no') == 0
  [fname, pathname] = uiputfile('*.txt','Save Fit Results As');
  cd(pathname);
  mwrite(output,fname);
  disp('Fit results saved.')
else
  disp('Fit results not saved.')
end;
```

A.1.2. Moore-Penrose pseudo inverse

```
function solution = mppi(Gc,Gm,vm,S,M)
% MPPI(Gc,Gm,vm,S,M)
% Created 3/6/01
% Modified 3/25/01

Gc_pi = inv(Gc.'*Gc)*Gc.';
vc = -Gc_pi*Gm*vm;

% Reconstructing the flux vector
solution_top = compidx(S,M(:,1));
solution_top = [solution_top,vc];
solution_bottom = M(:,1);
solution_bottom = [solution_bottom,vm];
solution = [solution_top;solution_bottom];
solution = sortrows(solution,1);
```

```
function list = compidx(S,meas_index)
% COMPIDX
% Given a matrix and an index, calculates the complementray index.
% That is, if the matrix has columns 1 through n and the index has
% 1, 2, 9, and 10, the new index will have all the numbers from 1 thorugh n
% except 1, 2, 9, and 10.
total_var = max(size(S));
remove_list = meas_index;
temp = ones(total_var,1);
```

```
temp(remove_list) = 0;
list = find(temp == 1);
```

A.1.3. Tsai-Lee method

```
function solution = eq820(Gc,Gm,vm,S,M,noise);
% EQ820(Gc,Gm,vm,S,M,noise)
% Created 3/6/01

% Reformulate into the form T*v = (vm / 0) = (v1 / v2),
% where vm and v1 are NOT necessarily equal
% First, calculate the dimensions of T:
[G_row,G_col] = size(S);
T_row = length(vm)+G_row;
T_col = G_col;
% Second, pad T with zeros
T = zeros(T_row,T_col);
% Now construct T from I, O, and S
% Upper left
T(1:length(vm),1:length(vm)) = eye(length(vm));
% Upper right
T(1:length(vm),(length(vm)+1):T_col) = zeros(length(vm),T_col-length(vm));
% Lower left
T(length(vm)+1:T_row,1:length(vm)) = Gm;
% Lower right
T(length(vm)+1:T_row,(length(vm)+1):T_col) = Gc;

% F is the variance-covariance matrix for the residuals of both the measured fluxes and the
% pseudo-steady state assumptions.
% F is by definition a square matrix, therefore m = n
% The number of columns in F has to equal the number of rows in T

if strcmp(noise,'yes') == 1
  [M_row,M_col] = size(M);
  f1 = M(:,M_col);
  f1 = power(f1,2);
  f2 = ones(G_row,1);
else
  f1 = ones(length(vm),1);
  f2 = ones(G_row,1);
  f2 = 0.1*f2;
end;
d = [f1;f2];
F = diag(d);
rhs = [vm;zeros(G_row,1)];
v = inv(T.'*inv(F)*T)*T.'*inv(F)*rhs;
```

```
% Now reconstruct the solution vector
solution = zeros(length(v),2);
solution(1:length(vm),1) = M(:,1);
unknown = compidx(S,M(:,1));
solution(length(vm)+1:length(v),1)=unknown;
solution(:,2) = v;
solution = sortrows(solution,1);
```

A.1.4. Weighted least-squares method

```
function solution = zupke(Gc,Gm,vm,S,M)
% ZUPKE(Gc,Gm,vm,S,M)
% Created 3/23/01

unk_list = compidx(S,M(:,1));
[Gc_row,Gc_col] = size(Gc);
[M_row,M_col] = size(M);
sd = abs(vm*0.15);
% var = power(sd,2);
r = -1*Gm*vm;
% var_r = abs(-1*Gm*var);
% sd_r = sqrt(var_r);
sd_r = sqrt(M_col-2)*abs(-1*Gm*sd);
b = zeros(length(r),1);
% Now the equation is Gc*x = r
% calculating re-scaled Gc and r veactor
for i = 1:Gc_row
  if sd_r(i) == 0
    b(i) = r(i)/0.001;
  else
    b(i) = r(i)/sd_r(i);
  end;
  for j = 1:Gc_col
    if sd_r(i) == 0
      D(i,j) = Gc(i,j)/0.001;
    else
      D(i,j) = Gc(i,j)/sd_r(i);
    end;
  end;
end;
vc = inv(D.'*D)*D.'*b;
vc_var = diag(inv(D.'*D));
vc_sd = sqrt(vc_var);

solution_top = [compidx(S,M(:,1)),vc];
solution_top = [solution_top,vc_sd];
solution_bottom = [M(:,1),vm];
```

```
solution_bottom = [solution_bottom,sd];
solution = [solution_top;solution_bottom];
solution = sortrows(solution,1);
```

A.1.5. Consistency index

```
function Rr = reduced(S,meas_index)
% REDUCED(Stoichiometric_matrix,meas_index)
% The output is the reduced redundancy matrix.

[S_row, S_col] = size(S);
index = compidx(S,meas_index);
dimension = length(index);

Rr = arrange(S,index);
[Rr_row,Rr_col] = size(Rr);
elcol = S_col-dimension+1;
while Rr_col > (S_col-dimension)
  [pivot, pivotrow] = findpiv(Rr,elcol);
  Rr = pivop(Rr,pivotrow,elcol,pivot);
  [Rr_row,Rr_col] = size(Rr);
end;
```

```
function R = arrange(X, IND)
% ARRANGE
% Cuts index columns of X and pastes them to the end of the matrix.
% The rearranged matrix is returned in R. INDEX is a horizontal vector
% with integer elements.
indexlength = length(IND);
[row, col] = size(X);
for i = 1:indexlength
  T(:,i) = X(:,IND(i));
end
X(:,IND) = [];
R = X;
R(:,(col-indexlength+1):col) = T;
```

```
function [y,z] = findpiv(M, column)
% FINDPIV
% Finds pivot in column, given matrix M.
% Pivot is defined as the first non-zero element.
[row, col] = size(M);
for i = 1:row
  p = M(i,column);
  if p ~= 0
    r = i;
    break;
```

```
  end;
end;
y = p;
z = r;
```

```
function Y = pivop(matrix, row_num, col_num, pivot)
% PIVOP
% Used in eliminating variables from a matrix. The calling function is present in the file
% "reduce.m"
[row, col] = size(matrix);
Y = matrix;
for r = 1:row
  factor = matrix(r,col_num)/pivot;
  add = matrix(row_num,:);
  if r == row_num
    Y(r,:) = 0;
  else
    Y(r,:) = (matrix(r,:)-factor*add);
  end;
end;
Y(row_num,:) = [];
Y(:,col_num) = [];
```

```
function h_and_delta = CI_value(Rr,vm,F);
% CI_VALUE(reduced_matrix,measurement_vector,variance_matrix)

P = Rr*F*Rr.';
delta = F*Rr.'*inv(P)*Rr*vm;
epsilon = Rr*delta;
h = epsilon.'*inv(P)*epsilon;
delta = vm+delta;
h_and_delta = [h;delta];
```

```
function output = best_CI(h0,S,vm0,index0,SD0);
% BEST_CI(S,vm,index0,SD)

h_current = h0;
delta_current = [];
deleted = 0;
for i = 1:length(vm0)
  index = index0;
  index(i) = [];
  vm = vm0;
  vm(i) = [];
  SD = SD0;
  SD(i) = [];
```

```
  SD = power(SD,2);
  F = diag(SD);
  Rr = reduced(S,index);
  P = Rr*F*Rr.';
  delta = F*Rr.'*inv(P)*Rr*vm;
  epsilon = Rr*delta;
  h = epsilon.'*inv(P)*epsilon;
  if h < h_current
    h_current = h;
    deleted = i;
    delta_current = delta;
  end;
end;
vm_adj = vm0;
vm_adj(deleted) = [];
vm_adj = vm_adj-delta_current;
output = [h_current;index0(deleted)];
output = [output;vm_adj];
```

A.1.6. Input and output functions

```
function mwrite(X,fname)
% MWRITE(X,fname)
% Opens a file called "fname" and writes X.
fid = fopen(fname,'w');
[X_row,X_col] = size(X);
for i = 1:X_row
  for j = 1:X_col
    fprintf(fid, '%f\t', X(i,j));
  end;
  fprintf(fid, '\n');
end;
fclose(fid);
```